DOE/BC/14600-23
Distribution Category UC-122

MODIFICATION OF CHEMICAL AND PHYSICAL FACTORS IN STEAMFLOOD TO INCREASE HEAVY OIL RECOVERY

Annual Report for the Period
October 1, 1990 through September 30, 1991

DOE/BC/14600--23

DE92 001034

By
Y.C. Yortsos

April 1992

Work Performed Under Contract No. DE-FG22-90BC14600

Prepared for
U.S. Department of Energy
Assistant Secretary for Fossil Energy

Thomas B. Reid, Project Manager
Bartlesville Project Office
P. O. Box 1398
Bartlesville, OK 74005

Prepared by
University of Southern California
Department of Chemical Engineering
Petroleum Engineering Program
Los Angeles, CA 90089-1211

MASTER

Contents

List of Figures vi

List of Tables xi

ACKNOWLEDGEMENTS xii

ABSTRACT xiii

1 INTRODUCTION 1

2 PERCOLATION MODELS FOR BOILING AND BUBBLE GROWTH IN POROUS MEDIA AT LOW SUPERHEATS 4

2.1 INTRODUCTION 4

2.2 PHASE EQUILIBRIA IN POROUS MEDIA 5

2.3 NUCLEATION 9

2.4 BUBBLE GROWTH 12

2.4.1 Dimensionless Parameters 14

2.4.2 Governing Equations 15

2.4.3 Low Superheats 17

2.4.4 Moderate and Large Superheats 18

2.5 PERCOLATION MODELS 19

2.5.1 Ordinary Percolation with Nucleation 19

2.5.2 Percolation with Superheat Depletion 24

2.5.3 Gradient Percolation with Nucleation 24

2.6 CONCLUSIONS 28

3 VISUALIZATION EXPERIMENTS ON STEAM INJECTION IN HELE-SHAW CELLS 29

3.1 INTRODUCTION 29

3.2 EXPERIMENTAL 31

3.3 RESULTS AND DISCUSSION 31

3.4 DISPLACEMENT IN HORIZONTAL HELE-SHAW CELLS 32

3.4.1 Gravity Effects 39

3.5 CONCLUSIONS 43

4 EFFECTS OF HETEROGENEITY ON VAPOR-LIQUID COUNTERFLOW IN POROUS MEDIA 46
4.1 INTRODUCTION 46
4.2 FORMULATION 48
4.3 CONCLUSIONS 71

5 VISUALIZATION OF IMMISCIBLE DISPLACEMENT IN MICROMODEL FRACTURED SYSTEMS 73
5.1 INTRODUCTION 73
5.2 EXPERIMENTS 75
5.3 RESULTS 76
5.3.1 Primary Imbibition 76
5.3.2 Primary Drainage 81
5.3.3 Secondary Imbibition 88

6 NUMERICAL CONSTRUCTION AND FLOW SIMULATION IN NETWORKS OF FRACTURES USING FRACTAL GEOMETRY 94
6.1 INTRODUCTION 94
6.2 NUMERICAL SYNTHESIS OF FRACTAL NETWORKS OF FRACTURES . . 96
6.2.1 Fragmentation and Fractals 96
6.2.2 Generation of Fractal Networks of Fractures 97
6.3 FLUID FLOW SIMULATION 107
6.3.1 Flow Conductivity Matrix 107
6.3.2 Pressure Transients 108
6.4 CONCLUSIONS 116

7 A THEORETICAL ANALYSIS OF VERTICAL FLOW EQUILIBRIUM 119
7.1 INTRODUCTION 119
7.2 ASYMPTOTIC ANALYSIS 120
7.3 LAYERED RESERVOIRS 125
7.4 EFFECTS OF CAPILLARITY AND GRAVITY 128
7.5 MISCIBLE DISPLACEMENT 130
7.6 TRACER DISPERSION 132
7.7 GRAVITY SEGREGATED FLOW 134
7.8 THE DUPUIT AND DIETZ APPROXIMATIONS 135

7.9 CAPILLARITY-GRAVITY SEGREGATION 138
7.10 SUMMARY 139

8 PARALLEL FLOW IN HELE-SHAW CELLS 141
8.1 INTRODUCTION 141
8.2 THEORY 143
8.2.1 Linear Analysis 145
8.2.2 Weakly Non-Linear Analysis 147
8.2.3 Numerical Method 154
8.3 EXPERIMENTAL 155
8.4 RESULTS AND DISCUSSION 157
8.4.1 Symmetric Case 157
8.4.2 $M < 1$ 157
8.4.3 $M \sim 1$ 166
8.4.4 $M > 1$ 166
8.4.5 Non-Symmetric Case 168
8.5 CONCLUDING REMARKS 171

9 FLOW OF POWER-LAW FLUIDS IN POROUS MEDIA 173
9.1 INTRODUCTION 173
9.2 POWER-LAW FLUIDS 174
9.2.1 Effective Medium Averages 175
9.2.2 Critical Path Analysis 178
9.2.3 Flow Patterns 180
9.3 TWO-PHASE FLOW 185
9.4 VISCOELASTIC EFFECTS 188

SUMMARY AND FUTURE WORK 192

REFERENCES 196

List of Figures

1 Schematic of a "bubble" in a porous medium 6

2 Schematic of equilibrium and supersaturations 7

3 Stability of a vapor-liquid interface in a converging geometry 9

4 Schematic of a nucleation site in a pore body 10

5 Bubble radius-volume equilibrium for the hydrophobic cavity of Figure 4 11

6 Bubble growth in percolation from nucleation sites in a square latice at three different stages of growth (p=0.221, 0.555 and 0.9988, respectively) 20

7 Relative permeabilities as a function of β 22

8 Critical gas saturation as a function of β ($\kappa = 0.1$) 23

9 Supersaturation paths for adiabatic depletion: (a) Pressure, (b) Temperature 25

10 Vapor-liquid equilibrium in a temperature gradient using gradient percolation for different values of β : (a) β= 0.2, (b) $\beta = 0.5$ 27

11 Schematic of the experimental apparatus 32

12 Initial stage of displacement 33

13 A typical steam displacement snapshot 34

14 Close-up of steam front 34

15 Snapshot after water breakthrough 35

16 Evidence of emulsification of oil 36

17 Finger thinning after breakthrough 37

18 Typical fingering pattern for oil displacement by water 38

19 Snapshot of mineral oil displacement by steam 38

20 Steam zone during displacement by steam of a Long Beach crude 40

21 A different snapshot of steam zone displacement of Long Beach crude oil 40

22 Close-up of steam zone during steam displacement 41

23 Updip steam injection 42

24 Downdip steam injection 42

25 Steam displacement in a vertical cross-section 43

26 Close-up of steam zone during displacement in a vertical cross-section 44

27 Snapshot after water breakthrough 44

28 Steam gravity override 45
29 Schematic of a special heterogeneity profile: (a) Permeability increase; (b) Permeability decrease 49
30 Schematic of saturation response for the profile of Figure 29a 51
31 The capillary heterogeneity function $\omega(S)$ 52
32 Saturation profiles for integration from right-to-left: (a) $S_1 < S_{VH}$; (b) $S_{VH} < S_1 < S_{LH}$; (c) $S_{LH} < S_1$ 54
33 Saturation profiles for integration from left-to-right: (a) $S_{LH} < S_o$; (b) $S_{VH} < S_o < S_{LH}$; (c) $S_o < S_{VH}$ 56
34 Schematic of vertical counterflow 58
35 Steady-state selection in homogeneous heat pipes : (a) Integration upwards, $S_1 < S_{LG}$, (b) Integration upwards, $S_1 > S_{LG}$, (c) Integration downwards, $S_o > S_{VG}$, (d) Integration downwards, $S_o < S_{VG}$ 60
36 Weak heterogeneity (a) τ profile, (b) LD regime, $\omega = 23.0$, (c) VD regime, $\omega = 25.0$ 63
37 Capillary pressure gradient corresponding to Figure 36b 64
38 Weak heterogeneity for larger heat fluxes: (a) LD regime, $\omega = 24.0$, (b) VD regime, $\omega = 28.0$ 66
39 The VD regime corresponding to Figure 36a for $\omega = 0.6$ 67
40 Normal heterogeneity: (a) τ profile, (b) LD regime, $\omega = 0.02$, (c) VD regime, $\omega = 0.02$ 68
41 Capillary pressure corresponding to Figure 40a 69
42 Normal heterogeneity for larger heat fluxes: (a) LD regime, $\omega = 0.2$, (b) VD regime, $\omega = 0.2$ 70
43 The pore network and fracture pattern 75
44 Primary imbibition (water-air) showing roughness flow. 79
45 Primary imbibition (water-air) at $N_{ca} = 2 \times 10^{-8}$, showing both pore invasion and channel filling. 79
46 Primary imbibition (water-air) at $N_{ca} = 10^{-8}$, showing a rough shape of the displacement front. 80
47 Primary imbibition (water-air) at $N_{ca} = 10^{-7}$, showing a flat shape of the front. . . . 80

48 Primary drainage (air-water) at $N_{ca} = 3.6 \times 10^{-10}$, showing that air moves to the fracture only. 83
49 Primary drainage (air-water) at $N_{ca} = 3.6 \times 10^{-8}$, showing that air moves to the fracture only. 83
50 Primary drainage (air-water) at $N_{ca} = 3.6 \times 10^{-6}$, showing that air may also invade the matrix. 84
51 Primary drainage (air-water) at $N_{ca} = 2.8 \times 10^{-5}$, showing that air invades the matrix in a ramified fashion. 84
52 Primary drainage (kerosene-water) at $N_{ca} = 3.2 \times 10^{-7}$, showing that kerosene enters the fracture only. 85
53 Primary drainage (kerosene-water) at $N_{ca} = 6.3 \times 10^{-6}$, showing that kerosene invades the matrix. 85
54 Primary drainage (kerosene-water) at $N_{ca} = 1.2 \times 10^{-5}$, showing that kerosene invades the matrix after entering the fracture. 86
55 Primary drainage (kerosene-water) at $N_{ca} = 3.2 \times 10^{-5}$, showing that kerosene invades most of the matrix after entering the fracture. 86
56 Primary drainage (oil-water) at $N_{ca} = 4.1 \times 10^{-5}$, showing that viscous oil invades both the fracture and the matrix. 87
57 Secondary imbibition (water-air) at $N_{ca} = 2 \times 10^{-8}$. 90
58 Secondary imbibition (water-kerosene) at $N_{ca} = 4 \times 10^{-8}$. 90
59 Secondary imbibition (water-kerosene) at $N_{ca} = 4 \times 10^{-7}$. 91
60 Secondary imbibition (water-kerosene) at $N_{ca} = 4 \times 10^{-6}$. 91
61 Secondary imbibition (water-heavy oil) at $N_{ca} = 4 \times 10^{-8}$. 92
62 Secondary imbibition (water-heavy oil) at $N_{ca} = 4 \times 10^{-7}$. 92
63 Secondary imbibition (water-heavy oil) at $N_{ca} = 4 \times 10^{-6}$. 93
64 Secondary imbibition (water-heavy oil) at $N_{ca} = 4 \times 10^{-5}$. 93
65 (a) Modified Sierpinski gasket (11 generations) with self-similar IFS. Positions A (square) and B (circle) (b) Corresponding box counting(*), fracture length (solid line) and fragment size (dashed line) distributions. 99

66 (a) Modified Sierpinski gasket (11 generations) with self-affine IFS. (b) Corresponding box counting(*), fracture length (solid line) and fragment size (dashed line) distributions. 100

67 (a) Modified Sierpinski gasket (11 generations) with non-linear IFS. (b) Corresponding box counting(*), fracture length (solid line) and fragment size (dashed line) distributions. 101

68 (a) Fracture network (11 generations) using a quadrilateral initiator and $p_f = 1$. (b) Corresponding box counting(*), fracture length(o) and fragment size (x) distributions. 103

69 (a) Distorted fracture network (11 generations) using a quadrilateral initiator and $p_f = 1$. (b) Corresponding box counting (*), fracture length(o) and fragment size (x) distributions. 104

70 (a) Fracture network (11 generations) as in Figure 68 with $p_f = 0.90$. (b) Corresponding box counting(*), fracture length(o) and fragment size (x) distributions. . . 105

71 (a) Fracture network (11 generations) as in Figure 68 with $p_f = 0.80$. (b) Corresponding box counting(*), fracture length(o) and fragment size (x) distributions. . 106

72 Pressure transient response for a homogeneous network. (a) Pressure (solid line), pressure derivative (dashed line). (b) Corresponding slopes. (c) Radial fracture mass plot. 111

73 The response for the modified Sierpinski gasket of Figure 65a with well at A. (a), (b) Pressure transients. (c) Radial fracture mass plot for position A. 112

74 The response of the modified Sierpinski gasket (9 generations) with well at A. (a), (b) Pressure transients. (c) Radial fracture mass plot. 114

75 The response of the modified Sierpinski gasket of Figure 65a with well at B. (a), (b) Pressure transients. (c) Radial fracture mass plot for position B. 115

76 (a), (b) Pressure transient response for the network of Figure 70. (c) Radial fracture mass plot. 117

77 (a), (b) Pressure transient response for the network of Figure 71. (c) Radial fracture mass plot. 118

78 Schematic of heterogeneous reservoir for VFE. 121

79 Schematic of viscous fingering in VFE. 121
80 Schematic of gravity segregated displacement. 122
81 Schematic of layered reservoir for VFE. 126
82 Schematic of air-water system for Dupuit assumption. 136
83 Flow geometry for (a) Non-symmetric and (b) Symmetric case 144
84 Counterflow of the two fluids in a moving frame of reference 152
85 M vs. λ_1 diagram for formation of solitons 153
86 Experimental set up 155
87 Single solitary wave (a) Initial condition (b) and (c) Subsequent stages 158
88 Numerical simulation of figure 87c. Inset: Profile in different scales 159
89 Two solitary waves at two different stages 161
90 Numerical simulation of figure 89 Inset: profile in different scales 162
91 Two solitary waves (a) Before and (b) After interaction 163
92 Numerical simulation of figure 91 Inset: Profile in different scales 164
93 Short wave initial disturbance and subsequent stage 165
94 Experiment with $\lambda < 1/2$ and positive initial disturbance 167
95 The non-symmetric case: Single soliton at two different stages 169
96 Numerical Simulation of Figure 95 170
97 Effective conductances for power-law fluids for a uniform pore size distribution in [0.9-1.1] 176
98 Effective conductances for power-law fluids for a uniform pore size distribution in [0.4-1.6] 177
99 Effective conductances for power-law fluids for a uniform pore size distribution in [0.01-1.99] 177
100 Test of critical path analysis for a uniform pore size distribution in [0.4-1.6] 179
101 Test of critical path analysis for a uniform pore size distribution in [0.01-1.99] 180
102 Flow Pattern for n=1 181
103 Flow Pattern for n=0.2 182
104 Flow Pattern for n=0.07 183
105 Flow Pattern for n=5 184

106 Simulation of drainage for n=0.2 at three different times (N_{ca}=0.03)(1 denotes injected and 0 denotes displaced fluids) 187
107 Simulation of drainage for n=2.0 at three different times (N_{ca}=0.03)(1 denotes injected and 0 denotes displaced fluids) 188
108 Flow behavior of viscoelastic fluids in porous media (from [61]) 190
109 Typical model geometries studied in [61] 190

List of Tables

1 Typical values of parameters 13

2 Conditions for various primary imbibition experiments. 77

3 Conditions of various primary drainage experiments. 81

4 Conditions for various secondary imbibition experiments. 89

ACKNOWLEDGMENTS

The research reported in this volume was supported by the U.S. Department of Energy under Contract FG22-90BC14600 subcontracted from Stanford University. We would like to express our gratitude to Tom Reid, our DOE Project Manager, for his steady support and commitment. Thanks are also due to Dr. Louis Castanier of SUPRI for his continuing interest and help in administering the subcontract. The works on vertical flow equilibrium and on fractal fracture networks were partly supported by the USC Center for Oil Recovery Research, sponsored by the California State Land Commission, Oryx, Shell E & P, Unocal, and Texaco. All these sources of support are greatfully acknowledged.

ABSTRACT

The study of vapor-liquid flow in porous media continued. Three aspects were addressed: (*i*) The further development of percolation and pore network models for phase change (boiling) in porous media; (*ii*) Visualization of steam injection in Hele-Shaw cells; and (*iii*) Macroscopic modeling of countercurrent steam- water flow in porous media.

We analyzed the liquid-to-vapor phase change in single-component fluids in porous media at low superheats. Conditions typical to steam injection in porous media were taken. We examined nucleation, phase equilibria and their stability and the growth of vapor bubbles. Effects of pore structure were emphasized. It was shown that at low superheats, bubble growth can be described as a percolation process. A modification was also proposed in the case of spatial temperature gradients, when solid conduction predominates.

Visualization experiments on steam injection in Hele-Shaw cells continued. Both synthetic and natural heavy oils were used under a variety of conditions, including effects of gravity. The experiments were conducted at low pressures. The results demonstrate the intreplay between steam injection, steam condensation, viscous fingering, heat transfer and steam distillation effects. The experiments reveal that steam fronts are neither smooth nor flat, but undergo constant rearrangement as a result of condensation and injection. These dynamics are substantially different from a typical immiscible displacement. The injected steam was found to follow the path of condensed water, which set the general fingering pattern. A viscoelastic response of the displaced heavy oil was also identified.

The macroscopic modeling of countercurrent vapor-liquid flow also continued. Based on a continuum description, the effect of permeability heterogeneity was analyzed. It was found that the capillary heterogeneity induced acts as a body force that enhances or diminishes gravity effects. Selection rules that determine the particular steady states reached in homogeneous, gravity-driven heat pipes were formulated. It is shown that the two-phase zone terminates only if a substantial increase in permeability, in the direction of increasing depth, occurs somewhere in the medium. Weak heterogeneity affects only slightly gravity-driven flows, but strong variations in permeability may give rise to substantial capillary effects.

Substantial efforts were made in the area of reservoir heterogeneity. These can be classified in two categories: (*i*) Studies related to fractured systems and (*ii*) Parallel flow in long and narrow

reservoirs.

Experimental studies were conducted to classify the displacement behavior in model systems. We considered a glass micromodel taken to represent a fracture separating two matrix blocks. While the ultimate goal is to study the effect of steam injection, it was realized that even simple, immiscible displacement in such systems is poorly understood. We carried out a series of primary imbibition, primary drainage and secondary imbibition experiments for a variety of mobility ratio and capillary number values. The flow mechanisms pertaining to the various conditions were classified. Conditions for the penetration of the matrix block were derived.

In the same category, we investigated the numerical construction of fractal networks of fractures. The method is based on the IFS technique and allows for great flexibility in the development of patterns. Numerical techniques were developed to simulate unsteady single-phase flow in these networks. It was found that the pressure transients behave according to the theoretical predictions provided that there exists a power-law in the mass- radius relationship around the test well location. Otherwise, finite size effects become significant and interfere severely with the identification of the underlying fractal structure.

Regarding fluid flow in long and narrow reservoirs we performed a theoretical analysis of the Vertical Equilibrium assumption. The latter is often applied to the modeling and displacement of various flow processes in porous media. However, the existing methodology is rather intuitive. In our work, we developed a rigorous asymptotic analysis, based on which a series of models are obtained. In the absence of strong gravity effects, we generalized previous works on immiscible and miscible displacements. When gravity is strong, such that fluids become fully segregated, conditions for flow segregation were proved and previous approximations were justified and generalized. Effects of capillarity and transverse dispersion were also included.

In the second study related to parallel flow, we considered the dynamics of motion of interfaces in parallel flow when viscous forces predominate. The particular application involves immiscible fluids in a Hele-Shaw cell. The evolution of disturbances on the interface was studied both experimentally and theoretically. It was found that such interfaces support wave motion, the amplitude of which for long waves is governed by the celebrated KdV equation. The waves are dispersive provided that the fluids have different viscosities. Experiments conducted in a long and narrow Hele-Shaw cell appear to validate the theory for both the symmetric and the non-symmetric cases.

Finally, work continued in the area of additives for mobility control. This year, we completed the experimental study on foam propagation in porous media. A detailed report and a PhD Thesis were published on this subject. Because of this availability, they will not be presented in this volume. Work on foams currently continues. We also extended our previous study on non- Newtonian fluid flow in porous media by using computer simulation to test theoretical predictions on the effective permeability of power-law fluids. It was found that the critical path analysis can be effectively used to model the permeability provided that the power law exponent is not too small. Preliminary work is also reported on the properties of the displacement of a Newtonian fluid by a non-Newtonian fluid and the effects of rheology on the displacement. Rheological effects are important on their own right, but also because many heavy oils of interest to this work are likely to have a non-Newtonian behavior.

1 INTRODUCTION

This report covers work performed in the area related to the physicochemical factors for the improvement of the oil recovery efficiency in steamfloods. In this context, three general areas are studied: (*i*) The understanding of vapor-liquid flow in porous media, whether the flow is internal (boiling), external (steam injection) or countercurrent (as in vertical heat pipes). (*ii*) The effect of reservoir heterogeneity, particularly as it regards fractured systems and long and narrow reservoirs (which are typical of oil reservoirs). (*iii*) The flow properties of additives for the improvement of recovery efficiency, in particular the properties of foams.

The study of the mechanisms of vapor-liquid flow reported here involves all three research tools, analysis, computation and experiments. We have focused on pore level modeling using pore networks and on flow visualization using Hele-Shaw cells. Questions that need to be answered include the following: to what degree the dynamics of steam-water or steam-oil interfaces differ from a typical isothermal, immiscible, two-component displacement? and how do temperature gradients and heat transfer affect the displacement pattern? Pore network simulation of moving interfaces and visualization experiments, as described in Chapters 2 and 3 of this report, help provide some insight on these questions. Ultimately, we aim at scaling up pore network level phenomena to model vapor-liquid flow at the macroscale. It is for this reason that the simple theories of Chapter 2, such as percolation and gradient percolation or other variations, may be of great utility.

Despite the apparent simplicity of the geometry, Hele-Shaw cells provide a great deal of information on the dynamics of steam- liquid interfaces. Chapter 3 describes our efforts in this direction. During the past year we experimented with a variety of fluids and conditions. An important, unexpected result was found owing to the viscoelastic behavior of the various heavy oils used. We are in the process of understanding this behavior. Current work also involves the use of glass beads in a packed Hele-Shaw cell in order to examine effects of geometric disorder.

In parallel, we are studying macroscopic flows, particularly countercurrent steam-water flow. In view of the potential of horizontal wells in thermal recovery, countercurrent steam-water flows are likely to be of importance. Prototypes of such behavior are heat pipes. In fact, a heat pipe description is typically used to represent boiling in porous media. Despite their significance, however, many important questions have not been answered. By introducing permeability and capillary gradients, we have formulated a theory presented in Chapter 4 based on which various flows are

analyzed rigorously. We classify the various emerging regimes and propose rules for the selection of steady- states.

The second important area of study in this work is reservoir heterogeneity. We are particularly interested in fractured systems, as well as in general, macroscopic (field) scale heterogeneity effects. While our ultimate interest is on steam displacement, we have realized that any meaningful progress requires that simpler, immiscible, isothermal displacement be analyzed first, particularly as it regards fractured systems. This is the reason that we proceeded with simple imbibition and drainage studies in the micromodel fracture geometries described in Chapter 5. We should point out that preliminary steam injection was indeed performed in these micromodels. However, a thorough analysis must await the successful resolution of the isothermal immiscible displacement. Injection of steam will commence soon after the successful completion of these experiments.

For large scale application the characterization of the fracture network in fractured systems is also necessary. It is well known that typical double porosity systems, currently used routinely, suffer from the inability to describe more than two scales of heterogeneity. Experimental observations suggest that many naturally fractured reservoirs are multiply fractured and contain a cascade of length scales. Using the novel tool of fractal geometry, we have proposed the use of fractals for the representation of networks of fractures. Chapter 6 describes our efforts in the past year. We have developed a novel technique for the synthetic construction of such networks and for the numerical simulation of single-phase flow. Based on the progress to be made in the fracture-block interaction, as described in Chapter 5, we hope to be able to provide a simulation of steam injection in fractured systems in the near future.

In relation to reservoir heterogeneity, we have also addressed the issue of flow in long and narrow reservoirs. This configuration has been used often in practice for the development of pseudofunctions, under the common assumption of Vertical Flow Equilibrium. Despite its success, however, it has lacked a fundamental justification. We embarked in a study of this problem in order to provide the formalism that will enable the extension of the approach to many EOR processes, such as steam injection. Chapter 7 provides the details of this approach. In the same context, we have completed our work on the parallel flow of two immiscible fluids. The work is both experimental and theoretical. We have studied the dynamics of lateral interfaces and found that they support wave motion. Chapter 8 describes the results obtained. As it addresses primarily viscous coupling

effects, the analysis should be also of interest to fully developed viscous fingers.

The final area of our work described in this report pertains to the injection of chemical additives. Over the past several years we have been studying the flow properties of foam. This effort has culminated with the completion of a Ph. D Thesis on experimental aspects of foam flow. Work on foam flow continues in an effort to interpret and to extend the findings of the experimental part. In parallel, we continued our research on the flow of non-Newtonian fluids in porous media. In addition to their generic interest, non-Newtonian fluids are likely to model heavy oils. We have alluded above to the novel behavior displayed in the displacement of heavy oils. Chapter 9 describes our research of the past year on the permeability of power-law fluids and on methods for its estimation. Also briefly discussed are the properties of a displacement, where both Newtonian and non- Newtonian (power-law) fluids are involved.

2 PERCOLATION MODELS FOR BOILING AND BUBBLE GROWTH IN POROUS MEDIA AT LOW SUPERHEATS

C. Satik and Y. C. Yortsos

2.1 INTRODUCTION

The liquid-to-vapor phase change in porous media is a process fundamental to many phenomena, such as drying and boiling, and it is common to diverse applications, such as geothermal, enhanced oil recovery and nuclear waste disposal. Despite its demonstrated significance, however, it is at present poorly understood. With few exceptions, most of the available studies are of a phenomenological nature, relying on the conventional extension of Darcy's law and on the use of relative permeability and capillary pressure functions, typically borrowed from the literature on gas-liquid displacement. Examples abound in the respective applications [119],[106],[37],[6]. Lacking, in particular, is the understanding of the interplay between phase equilibria and phase change, the degree and rate of change of supersaturation, the heat transfer and the pore structure. The latter introduces aspects different than for phase change in the bulk [121],[103],[102]. This is especially true for porous media of moderate-to-low permeability, where capillary phenomena can be significant.

Although recent publications in the Russian literature peripherally touch on some of these issues [123],[129],[70], concerted efforts to address various problems were made by Udell [135], who attempted to describe vapor-liquid equilibria in porous media, and by Parlar and Yortsos [99], who proposed a percolation model for steam-water relative permeabilities. Both approaches were incomplete, however, in that the first largely ignored the pore structure, while the second neglected any heat transfer or supersaturation considerations. It must be pointed out that the model of Parlar and Yortsos [99] for drainage did indeed corroborate the experimental findings of Sanchez and Schechter [116] for concurrent flow. Nevertheless, additional work is necessary to support their findings and to describe the process for other flow configurations. Recently, Yortsos and Parlar [148] made significant advances on the related problem of solution gas-drive. The system considered was two-component, two-phase, with the bubble growth controlled by solubility, pressure decline and mass transfer. The authors considered various aspects of the process including phase equilibria and nucleation, and proposed a percolation model for bubble growth from many nucleation sites.

The work in [148] is the first to analyze systematically the bubble growth process, although

specific solutions were derived only for rather special cases. Since the two problems share many common aspects we can apply a similar approach to describe the phase change and the subsequent bubble growth of a single-component system driven by an imposed superheat. This forms the main objective of this chapter. In the context of boiling in porous media, we will address equilibria of vapor-liquid interfaces, issues of heterogeneous nucleation, the subsequent bubble growth and effects of superheat and heat transfer. The analysis is intended to probe the validity of the conventional approach, to derive constraints on its applicability and to illustrate growth patterns. A key element in our models is the representation of the porous medium in terms of a connected (but uncorrelated) network of pore throats and pore bodies of variable size. With the assumption of lack of spatial correlations, we are in a position to take advantage of novel statistical tools, such as percolation theory, to describe the growth process. This allows us to demonstrate clearly the difference between bubble growth in a porous medium and that in the bulk.

Although a general analysis is attempted, specific results are obtained only for the case of low superheats (slow growth). Under such conditions, expected to be valid for steam injection processes in oil recovery or for geothermal reservoirs, temperature and pressure gradients are small, thus relative permeabilities are only saturation (and history) dependent. As will become apparent, nucleation effects significantly influence the macroscopic properties. We will illustrate two applications, one in which spatial temperature gradients are negligible and the heating is uniform, and another in which heat conduction through the solid matrix dominates the distribution of phases. Although progress is made in both directions, significant work still remains to be done, as will be pointed out below.

2.2 PHASE EQUILIBRIA IN POROUS MEDIA

We consider a vapor bubble in equilibrium with a liquid in a porous medium (Figure 1). We assume that nucleation has ceased and that individual interface menisci in pores are spherical (although macroscopic shapes are certainly not spherical). At conditions of equilibrium, temperature, liquid and vapor pressures are all spatially uniform. Thermodynamics dictate that the Laplace equation is satisfied, thus relating fluid pressures to the radius of curvature of any vapor-liquid meniscus

$$P_V - P_L = \frac{2\gamma}{r} \tag{1}$$

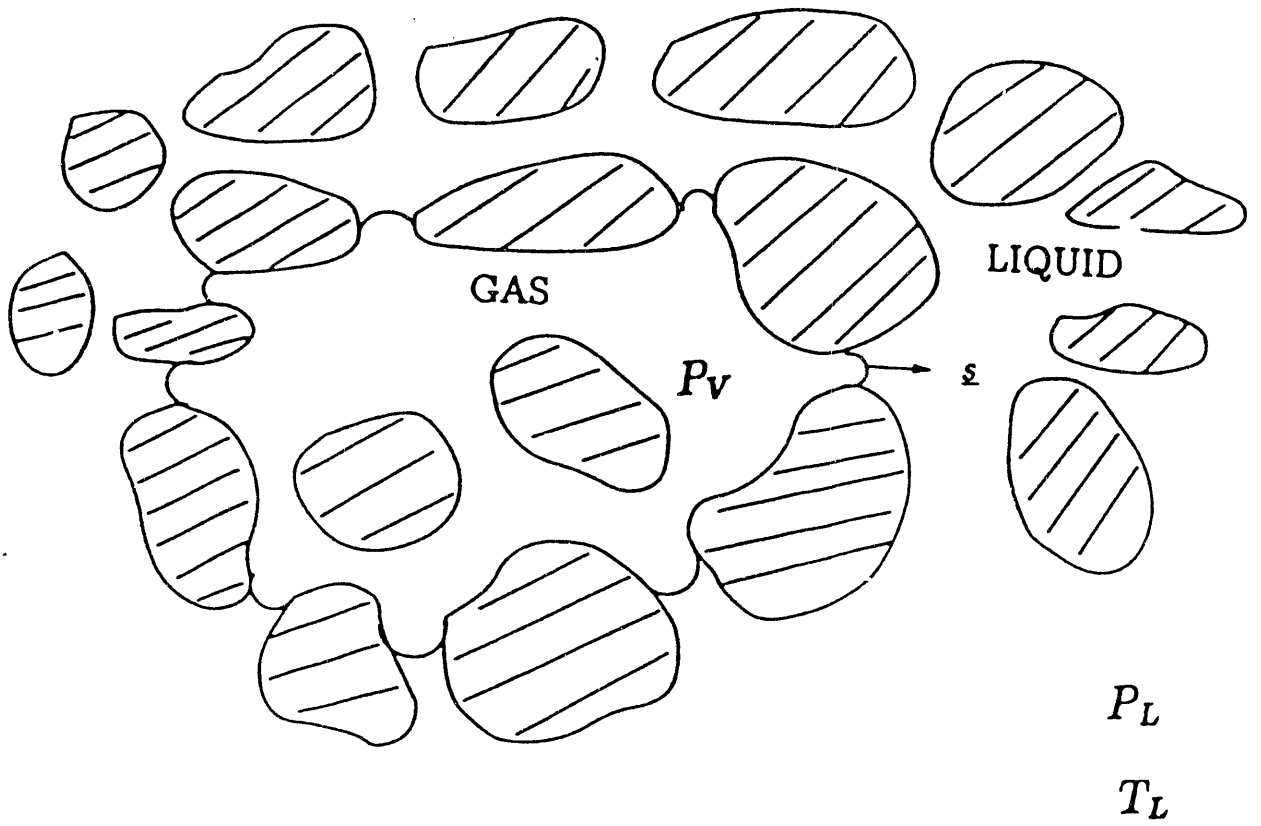

Figure 1: Schematic of a "bubble" in a porous medium

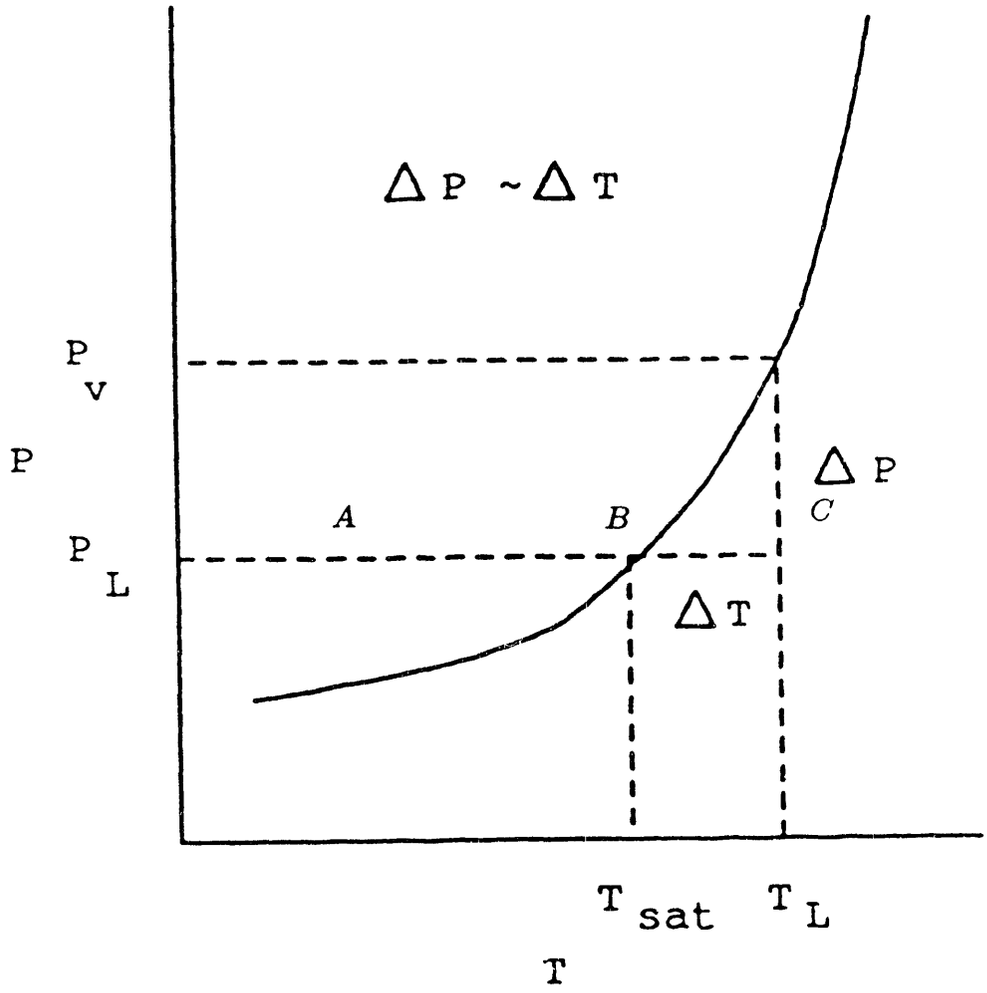

Figure 2: Schematic of equilibrium and supersaturations

where γ is the surface tension. For simplicity, we neglect Kelvin effects and assume that the pressure in the vapor phase, P_V, is equal to the saturation vapor pressure at T_L, e.g., as given by the Clausius-Clapeyron equation

$$P_V = P_{VO}(T_L) \tag{2}$$

It is worth pointing out that the importance of Kelvin effects has been exaggerated in the previous literature (e.g. [135],[99]). In a recent study [118], using a conventional macroscopic description we have shown that, except for very tight porous media (with permeability on the order of microdarcies), or for very low liquid saturation values, Kelvin effects are generally of secondary significance.

Phase change and phase equilibria in a porous medium may be schematically interpreted as in Figure 2. The system, initially in the liquid state (point A), is slowly heated at constant pressure,

until the equilibrium curve is reached (point B). Further increase in temperature leads to the superheat $\Delta T = T_L - T_{sat}$, where T_{sat} is the saturation temperature at P_L. In a liquid in the bulk, the appearance of the first bubble theoretically occurs at the onset of homogenous nucleation, which requires substantial amounts of superheat. In a porous medium, on the other hand, the onset of phase change is facilitated by heterogeneous nucleation. Given that a bubble has formed (point C), the pressure in the vapor phase at equilibrium is given by (2). Mechanical equilibrium of the vapor-liquid interfaces in the porous media "bubble" (Figure 1) requires spherical shape menisci of constant mean curvature H_0

$$P_{VO}(T_L) - P_L = 2\gamma H_0 \tag{3}$$

The RHS in the above is a measure of the capillary pressure and it is set by the porous medium.

Contrary to processes in the bulk, where unbounded growth ensues, pore walls in porous media stabilize interfaces, thus vapor-liquid equilibria are possible. The stability of gas-liquid interfaces in porous media for two-component, two-phase systems was summarized by Hirasaki et. al. [57]. It was shown that interfaces residing on converging pore geometries are stable, while these on diverging geometries are unstable. Yortsos and Parlar [148] extended their analysis to account for mass transfer by diffusion in the case of two-component, vapor-liquid systems. They found that the stability of menisci on converging pore geometries is enhanced by mass transfer. Analogous results should apply for the system under consideration here. In the following, we adapt the qualitative part of their argument to show equivalent effects for the single-component, vapor-liquid system of interest to boiling. The mathematical details are similar, but generally complex, and we refer the reader to Appendix A of [148].

Consider a small perturbation in the curvature of a spherical, vapor-liquid interface located in a converging pore element (from pore body-to-pore throat, Figure 3). For this interface to advance, the mean cuvature must increase. For a constant liquid pressure, this requires an increase in the vapor pressure, or equivalently, in the interface temperature. This increase sets, in turn, a temperature gradient, and a concommitant heat flux away from the vapor towards the liquid, which results in condensation, thus in a retraction of the interface to its original position. An equivalent argument applies if the initial perturbation is in the oposite direction. One is led to conclude that the equilibrium of a vapor-liquid meniscus in a conveging pore geometry is additionally stabilized

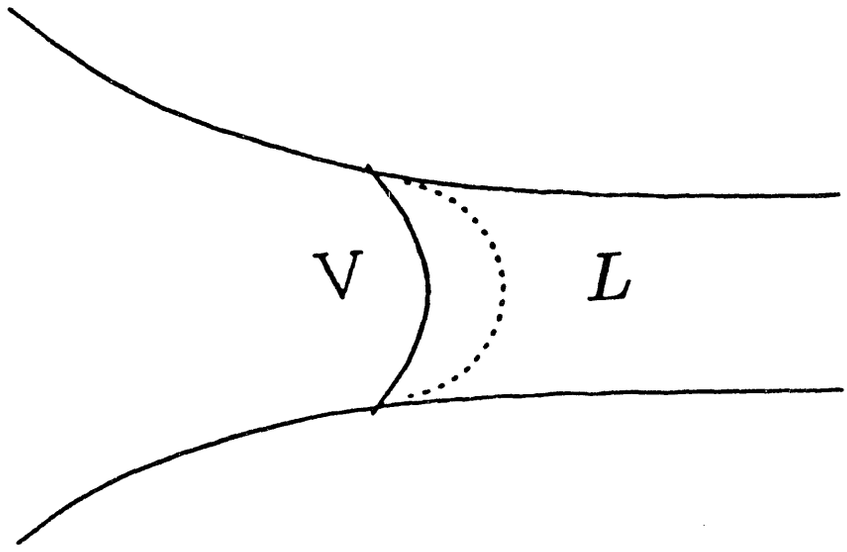

Figure 3: Stability of a vapor-liquid interface in a converging geometry

by heat transfer and phase equilibria. This is not the case for a diverging geometry, where stable equilibria are not possible, much like the case of vapor bubbles in the bulk. The existence of stable interfaces in pore geometries is fundamental to heterogeneous nucleation, an issue to which we turn next.

2.3 NUCLEATION

Nucleation processes in porous media are quite complex and there are still several questions that remain unanswered. However, some reasonable progress has been made. It is evident that in the majority of cases we can discard homogeneous nucleation as a plausible mechanism because of its restrictive conditions of perfectly smooth and liquid wet solid surfaces, the absence of trapped gases, and the unrealistically high supersaturations (of the order of several thousand psi for the solution gas-drive example of Yortsos and Parlar [148]). All these conditions are not likely to be met in many instances. Instead, heterogeneous nucleation is the mechanism likely to dominate the phase change process.

Heterogeneous nucleation has been analyzed by Yortsos and Parlar [148], who proposed a conventional nucleation model. It is based on the assumption that there exist pore surface irregularities

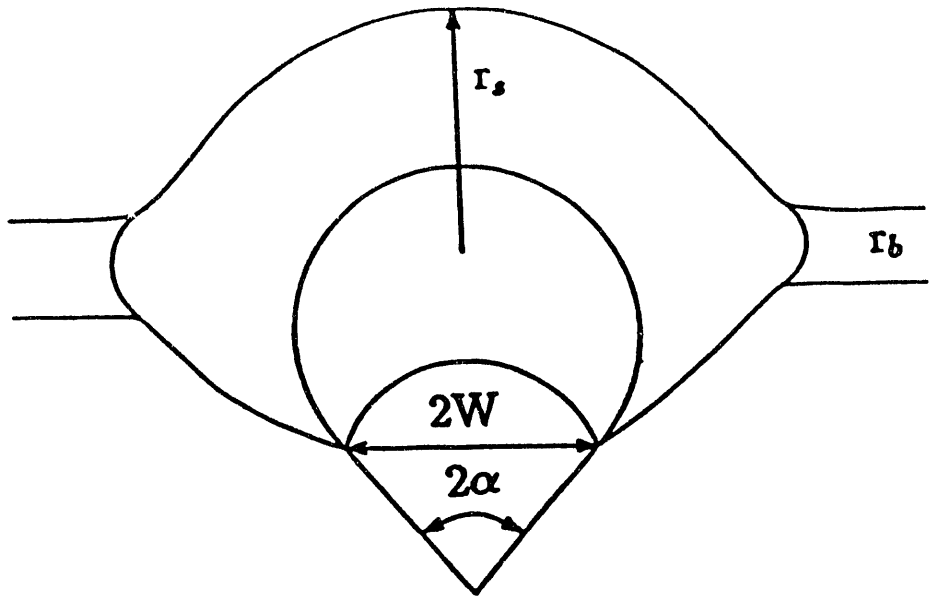

Figure 4: Schematic of a nucleation site in a pore body

(cracks, scratches, pits), which are not liquid wet and which contain pre-existing or trapped gases, that act as nucleation sites. For convenience in calculations, the sites were assumed of a conical shape (Figure 4). Because of the premise of heterogeneous mechanism, the issue of nucleation rates does not arise. Instead, sites are activated and a pore body is allowed to be occupied by vapor when the vapor-liquid meniscus in the cavity loses stability. As shown below, this occurs when the interface reaches the cavity mouth.

To examine the nucleation mechanism, we consider a hydrophobic conical cavity and evaluate the variation of the radius of curvature of the liquid-vapor interface with the volume of the vapor (Figure 5). Calculations of such configurations were made by Forrest [47]. As previously pointed out, stable interfaces correspond to configurations such that $dr/dv < 0$, i.e. the radius of curvature decreases with an increase in the volume of the gas phase. Note that a negative radius of curvature implies an interface concave to the liquid phase. ¿From the schematic in Figure 5 it follows that until the radius r reaches the pit mouth (and $r = W$), the equilibrium state is stable, suggesting that the vapor is confined in the cavity. When the cavity mouth is reached, however, a further increase in the supersaturation (superheat) renders the equlibrium state unstable. The bubble would grow in a non-equilibrium fashion, much like in the bulk, until its radius of curvature equals

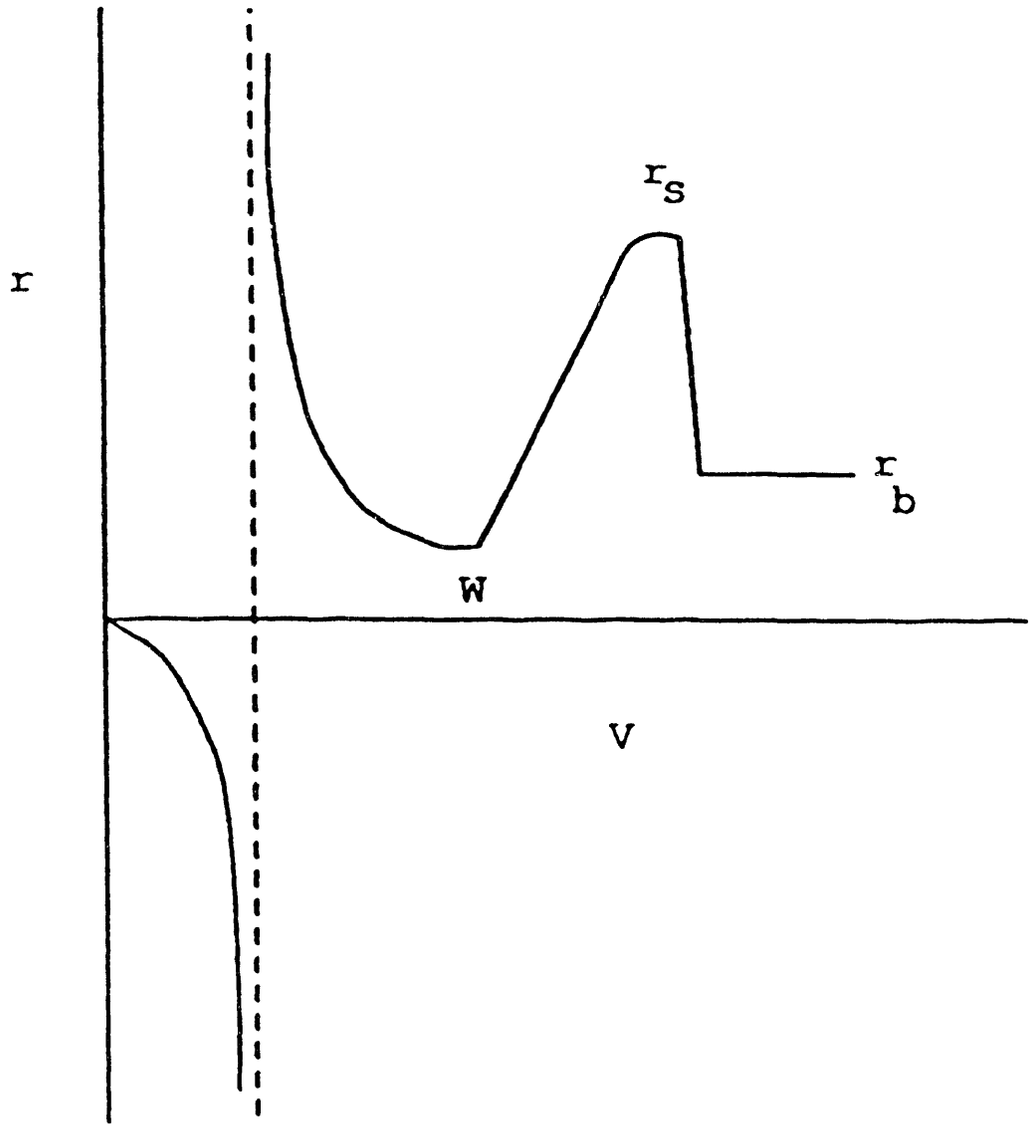

Figure 5: Bubble radius-volume equilibrium for the hydrophobic cavity of Figure 4

the host pore body radius r_s. Due to the pore wall constraints, further increase in the volume causes a decrease in the radius of curvature. This step is also stable, although it may not necessarily be an equilibrium one at the particular supersaturation (its radius may be larger than W), in which case the bubble may further grow.

By contrast, a vapor bubble in the bulk liquid is in unstable mechanical equilibrium, that enforces continuous growth or collapse. The fact that due to pore wall stabilization, a vapor bubble can exist in stable equilibrium with a superheated liquid, is a major difference between porous media and bulk. With W denoting the cavity mouth radius, we conclude that the onset of nucleation of a site occurs when

$$P_{VO}(T_L) - P_L = \frac{2\gamma}{W} \tag{4}$$

To express this condition in terms of the host pore body radius, we adopt from Yortsos and Parlar [148] the geometric factor $\beta = W/r_s$, which is the ratio of cavity mouth radius to pore body radius. Given the latter, equation (4) expresses the condition for a pore body of a given size to nucleate (be occupied by vapor). If β is assumed constant, larger pores are more likely to nucleate first. Of course this may not necessarily be the case and, in fact, it is more likely that β is randomly distributed. However, the assumption, of constant β considerably facilitates the calculations, while it does not detract qualitatively from the conclusions to be reached, particularly regarding the growth pattern. Of course, other expressions can also be used (see Parlar and Yortsos [98]).

In the above, it was also assumed that no bubble detachment due to gravity occurs. A condition for the validity of the latter was obtained by balancing surface and gravity forces, [148]. For the typical values listed in Table 1, we calculate that gravity-induced detachment will not take place in any pore with size smaller than $571.59\sqrt{\beta}\mu m$.

2.4 BUBBLE GROWTH

Having previously described phase equilibria and nucleation, we may proceed to formulate bubble growth in the pore space. The latter is controlled by surface, inertia, pressure and viscous forces, the driving parameter being the externally imposed superheat in the liquid. For simplicity, we consider first a single vapor "bubble" in an infinitely large porous medium otherwise occupied by liquid (Figure 1). In a later section, the model is extended to consider growth from multiple

$$c_p = 1.059\ Btu/lbm/^oF$$

$$H_o^{-1} = 15\mu m$$

$$k = 1darcy$$

$$L_v = 841.75\ Btu/lbm$$

$$M = 18lb/mol$$

$$P_L = 202.819psi$$

$$T_L = 383^oF$$

$$\alpha_L = 6.7113 * 10^{-3} ft^2/h$$

$$\gamma = 60.0\ dynes/cm^2$$

$$\lambda_L = 0.386Btu/h/ft/^oF$$

$$\xi_d = 1$$

$$\rho_L = 54.31\ lbm/ft^3$$

$$\phi = 0.35$$

Table 1: Typical values of parameters

"bubbles". In the present context, "bubbles" are not spherical, although individual menisci have locally spherical shape.

2.4.1 Dimensionless Parameters

To discuss the growth process, the dimensionless groups that control the growth regimes are, first, introduced. We follow Szekely and Martins [130] who studied the growth of a spherical gas bubble in a supersaturated bulk liquid. Typical parameter values correspond to a steam injection process for oil recovery and they are listed in Table 1.

As in Yortsos and Parlar [148], the variable Φ expresses the importance of capillarity with respect to supersaturation

$$\Phi = \frac{2\gamma H_0}{\Delta P} \tag{5}$$

where H_0 is a reference mean curvature of the menisci. For the heat transfer problem of interest here, we can alternatively use the imposed superheat ΔT to get

$$\Phi = \frac{\Delta T^{**}}{\Delta T} \tag{6}$$

where

$$\Delta T^{**} = 2\gamma H_0 \frac{T_L^2}{\kappa P_L} \tag{7}$$

and

$$\kappa = \frac{L_v M}{R} \tag{8}$$

Here, L_v, M and R are latent heat of vaporization, the molecular weight and the ideal gas constant, respectively. For the values in Table 1, $\Delta T^{**} = 0.53\ ^oF$. Depending upon the magnitude of ΔP (or ΔT), growth is described by different regimes. At low superheat values, Φ is $O(1)$ or larger. Capillary-controlled growth occurs at $\Phi \gtrsim O(1)$, in which case ΔP is of the order $2\gamma H_0$. The latter can be significant for small permeabilities.

Another measure of bubble growth is the Jacob number

$$Ja = \frac{\rho_L c_p \Delta T}{\rho_V L_v} \tag{9}$$

where ρ_L, c_p and ρ_V are liquid density, liquid specific heat capacity and vapor density, respectively. By using the ideal gas law and after some manipulation, the Jacob number can be related to the

superheat

$$Ja = \frac{\Delta T}{\Delta T^*} \tag{10}$$

where

$$\Delta T^* = \frac{1}{\rho_L c_p} \frac{\kappa P_L}{T_L} \tag{11}$$

and for the typical values of Table 1, ΔT^*=6.204 ^oF. This is also inversely proportional to Φ

$$Ja = \frac{\Phi^*}{\Phi} \tag{12}$$

where

$$\Phi^* = (2\gamma H_0)(\rho_L c_p)\frac{T_L^3}{(\kappa P_L)^2} \tag{13}$$

Clearly, important parameters which control the magnitudes of of Ja and Φ are liquid pressure and temperature in the far field.

Finally, a measure of inertia forces is given by the growth rate parameter

$$B = \frac{Ja^2}{\sqrt{G}} \tag{14}$$

where

$$G = \frac{R_0^2}{\rho_L \alpha_L^2}\Delta P \tag{15}$$

and where R_0 and α_L are initial bubble radius and thermal diffusivity of the liquid, respectively. Following Szekely and Martins [130], $B \ll 1$ would imply heat transfer-controlled growth, while $B \gg 1$ implies inertia-controlled growth. In our subsequent applications, $Ja \ll 1$, thus the growth process is heat transfer-controlled only and inertia forces are, therefore, not considered. This is certainly not the case in rapid bubble growth (flash boiling).

2.4.2 Governing Equations

To express the energy balance in the liquid-occupied space we use the dimensionless notation

$$\theta = \frac{T_L - T_{sat}}{\Delta T}, \tag{16}$$

$$\tau = \frac{\alpha_L t Ja}{R_0^2}, \tag{17}$$

$$\underline{\xi} = \frac{\underline{r}}{R_0} \tag{18}$$

to find

$$Ja(\frac{\partial\theta}{\partial\tau} + \underline{\nu_L}.\nabla\theta) = \nabla^2\theta \tag{19}$$

where

$$\underline{\nu_L} = \frac{R_0\underline{u_L}}{\alpha_L Ja} \tag{20}$$

In the above, $\underline{u_L}, \underline{x}$ and t are liquid velocity, spatial distance and time, respectively, while T_{sat} corresponds to the far-field liquid pressure. An energy balance at the vapor-liquid interface reads

$$\nu_s = \frac{\partial\theta}{\partial s} \tag{21}$$

The energy balance in the solid obeys the heat conduction equation. In dimensionless form we have

$$Ja\frac{\partial\Theta}{\partial\tau} = \psi\nabla^2\Theta \tag{22}$$

where

$$\Theta = \frac{T_s - T_{sat}}{\Delta T} \tag{23}$$

and T_s and ψ are the solid temperature and the ratio of solid to liquid thermal diffusivities, respectively. At the solid-liquid interface, continuity of thermal energy yields

$$\frac{\partial\theta}{\partial s} = \mu\frac{\partial\Theta}{\partial s} \tag{24}$$

where μ is the ratio of solid to liquid conductivities.

At the vapor-liquid interface, and for low superheats, inertia and viscous forces are negligible and the momentum balance simply reads

$$\Pi = \Phi\eta \tag{25}$$

where

$$\Pi = \frac{P_V - P_L}{\Delta P} \tag{26}$$

and

$$\eta = \frac{H}{H_0} \tag{27}$$

where H is the mean curvature. Alternatively, Π at the interface can be related to θ by the Clausius-Clapeyron equation. We note that at the low Re regime, fluid flow is described by Stokes equation, which is commonly approximated for porous media by a Laplace equation,

$$\nabla^2 p = 0 \tag{28}$$

Appropriate boundary and initial conditions are

$$\theta = 1 \qquad at \qquad \underline{\xi} \rightarrow \infty \qquad or \qquad \tau = 0 \tag{29}$$

and

$$\underline{\nu_L} = 0 \qquad at \qquad \underline{\xi} \rightarrow \infty \tag{30}$$

The problem is, in principle, completely specified by the above. However, a full solution will not be attempted here. Instead, some special, and quite limiting, cases are considered that allow for a simpler description. In all cases described below low superheats are assumed.

2.4.3 Low Superheats

At conditions of low superheats, then $Ja \ll 1$, and both balance equations above reduce to the Laplace equation, (provided also that $Ja \ll \psi$),

$$\nabla^2\theta = 0 \tag{31}$$

$$\nabla^2\Theta = 0 \tag{32}$$

At such conditions, the temperature fields in both liquid and solid are quasi-static. This facilitates considerably the analysis. Simple solutions are possible for two cases depending on the magnitude of Φ.

(a) When $\Phi \tilde{>} O(1)$, capillary forces solely control the growth and the process is of the percolation (ordinary or invasion) type, which has been well studied. The rules for the occupancy of pores by the vapor phase given in Yortsos and Parlar [148] can be used with minor modifications. Percolation (ordinary or invasion) growth patterns are applicable to quasi-static fields and the above are valid only if the temperature increase rate is small, to allow for equilibrium to be established. Yortsos and Parlar [148] developed a constraint for the case of pressure depletion in solution gas-drive systems. It is straightforward to modify their result for the case of boiling in porous media. We obtain the following condition on the heating rate

$$Q \ll \frac{\Delta T^*}{\tau^*} Ja^3 \tag{33}$$

where

$$\tau^* = \frac{\xi_d^2 k}{\phi \alpha_L} \tag{34}$$

and ξ_d, k and φ are the dimensionless correlation length in the percolation process, permeability and porosity, respectively. Taking $Ja \sim 10^{-3}$ and substituting $\Delta T^* = 6.204\ ^oF$ in the condition above, gives $Q \ll 32.497\ ^oF/day$ for percolation growth patterns to be valid. This constraint is likely to be violated for typical, laboratory scale boiling processes where heating rates are generally high. On the other hand, it is well within the limits of applications involving steam injection for oil recovery or geothermal systems, where processes are slow and equilibrium can be reached.

(b) When $\Phi \ll 1$, capillarity is not important, and in the absence of solid conduction, the process is of the DLA (Diffusion-Limited-Aggregation) type. In this case, equilibrium states are not possible and there is continous growth until full occupancy of the porous medium by vapor. Clearly, at least for this case, classical concepts such as relative permeabilities need to be reexamined.

2.4.4 Moderate and Large Superheats

Before proceeding we should briefly comment on the case of larger superheats. Now Ja is $O(1)$ or larger. Under the condition $B \ll 1$, inertia and viscous forces are still negligible. Therefore, the growth process is heat transfer-controlled, but now the temperature field is no longer quasi-static. This problem is quite complex, requiring for its solution the consideration of both convection and unsteady state terms. Finally, at very large superheat, $Ja \gg 1$, while also $B \gg 1$, implying that inertia controlls growth. This is the case of explosive growth, which is outside the present scope.

The above pertained to growth of a single "bubble" in porous media. In the remaining, we shall consider growth of "bubbles" from multiple sites, as a result of the activation of many nucleation sites. Growth from multiple sites was studied by Yortsos and Parlar [148] who modified ordinary percolation in infinite Bethe lattices. Their results are in closed-form expressions. Here, we present numerical results for the boiling case by considering the same percolation problem but in a square lattice. The model in [148] was developed for infinite systems, where there is no depletion of supersaturation. Here, we shall also consider the adiabatic case, where the available energy is finite.

We should point out that an important difference with the solution gas-drive problem is the participation of the solid matrix to transport. In general, three different regimes can be distinguished according to the ratio of conductivities ($\mu = \lambda_s/\lambda_L$):

$\mu \ll 1 \rightarrow$ where only the liquid is conducting

$\mu \sim 1 \rightarrow$ where both solid and liquid participate in the conduction

$\mu \gg 1 \rightarrow$ where only the solid is conducting

Each of these three cases finds many applications. The solution gas-drive model in Yortsos and Parlar [148] pertains to the first limit, where the solid conductivity is small and its participation to heat transfer is negligible. Many boiling applications in porous media lie closer to the third limit, with the ratio μ as high as 10. To account for this, a variant of gradient percolation is developed.

2.5 PERCOLATION MODELS

We consider bubble growth from multiple nucleation sites corresponding to low superheats (or to $\Phi \sim 1$), where the growth process is of the percolation type. In this case, infinitesimally small ΔT steps corresponding to a slow heating rate are imposed, such that the supersaturation is always balanced by capillary pressure. Three cases are considered: The first case is slow, uniform heating at an increased superheat, the second corresponds to adiabatic expansion, although at spatially uniform temperature and pressure, while the third involves static vapor-liquid distributions in the presence of a temperature gradient. Main objectives are to find the distributions of the vapor and liquid phases in the pore space, for each process, so that classical continuum concepts, such as relative permeabilities, can be calculated. This is, by no means, a trivial exercise. As previously implied, the present models mostly address effects of nucleation on these properties.

We use both bond and site distributions. The rules for the activation of the nucleation sites and the occupancy of pore space by the vapor are simple. Given a superheat $\Delta T = T_L - T_{sat}$, pores with throat radius

$$r_b \geq R^* = \frac{2\gamma T_{sat}}{\rho_V L_v \Delta T} \tag{35}$$

are occupied by the vapor phase if they are already connected to vapor-occupied sites or to nucleation sites. New nucleation sites are activated if the host pore bodies have a large enough radius

$$r_s \geq \frac{R^*}{\beta} \tag{36}$$

An important difference between this model and ordinary percolation is nucleation. Classical percolation is recovered in the limit $\beta = 1$.

2.5.1 Ordinary Percolation with Nucleation

Simulation results are shown in Figure 6, for square (30x30) lattice network at three different

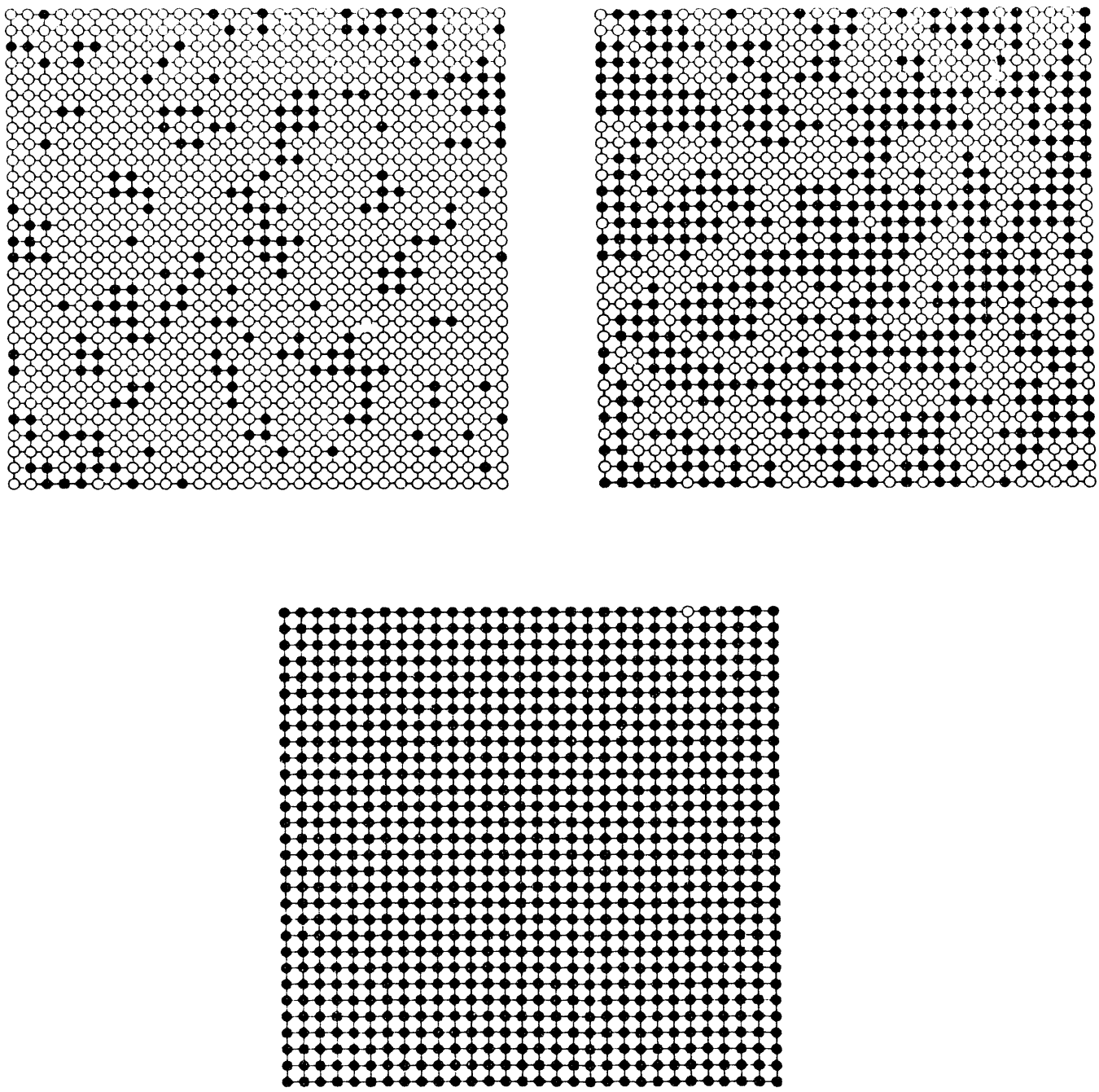

Figure 6: Bubble growth in percolation from nucleation sites in a square latice at three different stages of growth (p=0.221, 0.555 and 0.9988, respectively)

stages of growth corresponding to increasing superheats. Pore body and throat sizes were randomly assigned from a uniform distribution. In Figure 6, gray denotes vapor-occupied sites, black denotes nucleation sites and white denotes liquid-occupied sites. It is apparent that all vapor-occupied pores are connected to a nucleation site. In this model of unlimited supply of supersaturation, more nucleation sites are activated as the supersaturation increases. However, not all nucleation sites have expanded, particularly at low superheats. Since no temperature gradients are considered, no frontal structures (spatial gradients) develop. The predictions from this model are similar to those from the analytical study of Yortsos and Parlar [148]. In particular, a critical supersaturation exists for the onset of bulk vapor flow, and relative permeabilities can be calculated as a function of the nucleation parameter β. We refer the reader to [148] for details. Figure 7 shows relative permeability results reprinted from [148].

Since the process is of the percolation type, the onset of bulk vapor flow occurs when an "infinite" cluster forms, corresponding to the supersaturation

$$\Delta P_c = \frac{2_\tau}{r_{dc}} \tag{37}$$

where r_{dc} solves

$$\int_{r_{dc}}^{\infty} \alpha_b(r)dr = p_c \tag{38}$$

Here, $\alpha_b(r)$ is the bond size distribution, and p_c is the percolation threshold. The critical vapor saturation S_{gc} is obtained by adding to the "infinite cluster" the contribution of vapor-occupied sites that are connected to nucleation sites but do not belong to the percolation cluster. It is apparent that the latter value would increase as nucleation is more facilitated. Equivalently, the relative permeability to vapor would decrease as the nucleation fraction increases. These features are clearly evident in Figure 7. We should point out that when the ratio $\kappa = \frac{r_{dc}}{r_{s,max}}$ is not zero it is possible that although sufficient superheat is available for bond percolation, vapor occupancy has not yet occured, because of lack of nucleation sites ($\beta < \kappa$). Percolation then takes place when the first site is nucleated, with superheat corresponding to the radius $\beta r_{s,max}$, thus resulting into large values of S_{gc}. Figure 8 taken from [148] shows this dependence.

Conditions for the validity of this model were developed above. As pointed out, this process is a slow, spatially uniform heating of the liquid in the porous medium. Clearly, this is only an approximation to the actual process. One possible modification regards the depletion of superheat.

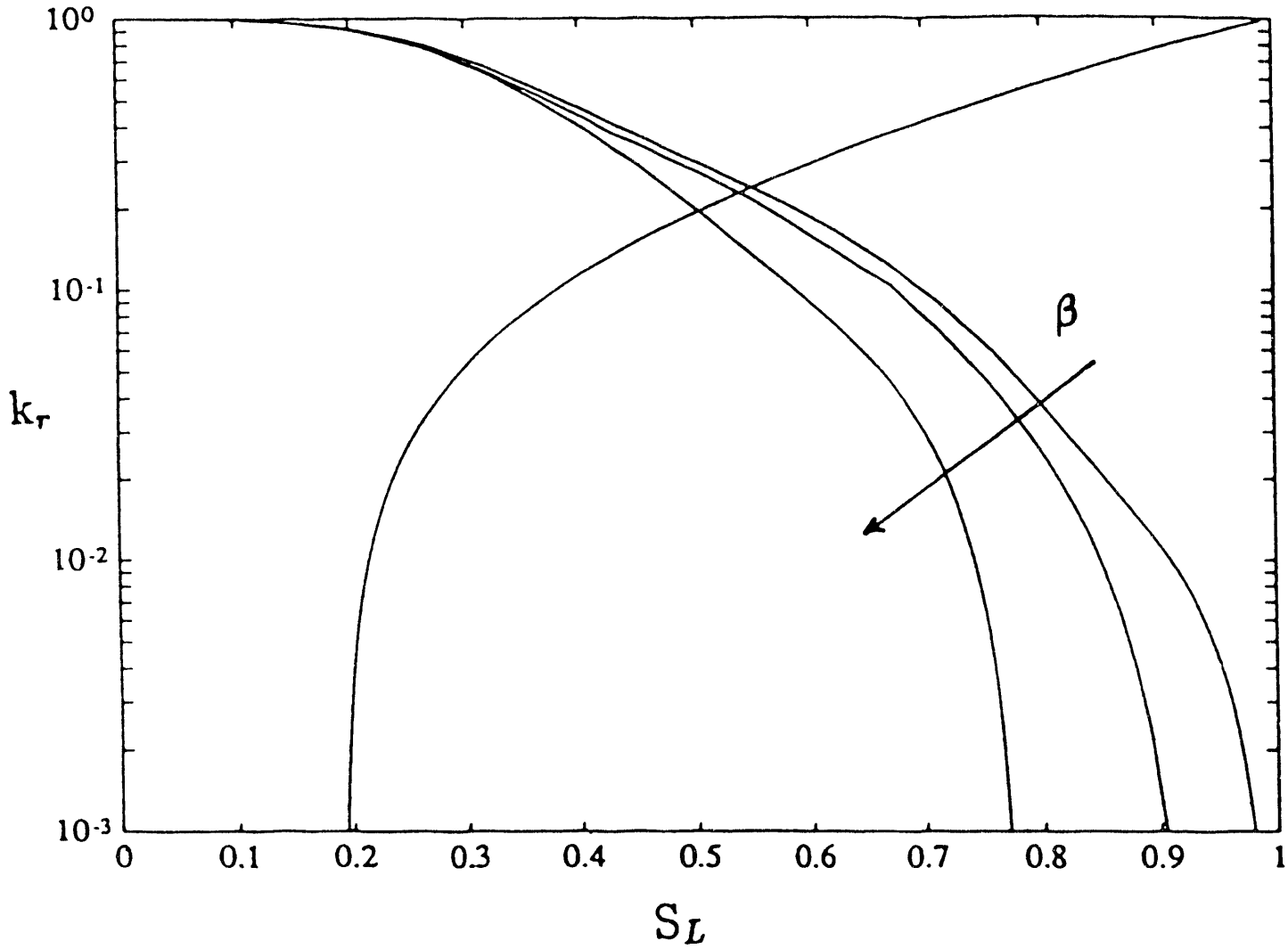

Figure 7: Relative permeabilities as a function of β

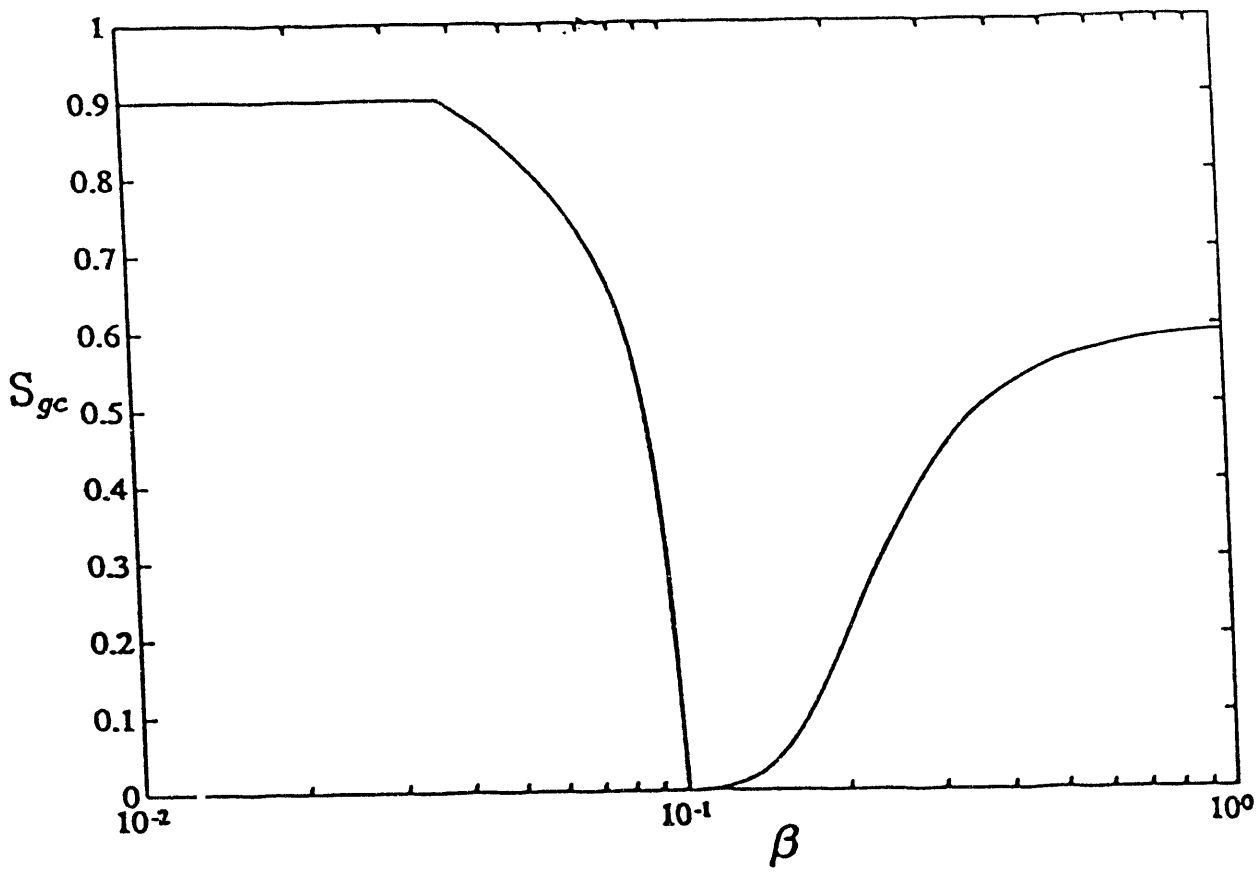

Figure 8: Critical gas saturation as a function of β ($\kappa = 0.1$)

2.5.2 Percolation with Superheat Depletion

To model this process, we have simulated vapor growth by pressure reduction in an adiabatic system. Contrary to the previous, the available superheat here is finite. Since vapor expands and displaces liquid which leaves the system, the available amount of initial entalphy is constantly reduced. Further growth can thus occur only by further pressure depletion. We must note that although supeerheat is depleted, competition for growth among the various bubbles is still absent, because of the assumption of uniform temperatures. Results are shown in Figure 9 for conditions identical to the previous. At the end of the process, the pressure has been reduced from 202.8 psi to 185 psi, while the temperature reduction is somewhat less, from 383 ^oF to 375.9 ^oF. Although the amount of supersaturation or superheat changes, one can nevertheless show that the growth pattern still remains identical to the previous percolation type. This is to be expected, since spatial gradients are not included. One concludes that consideration of finite volume and adiabatic conditions does not change the previous results as far as flow parameters (e.g. relative permeabilities, etc.) is concerned.

Both of the above were modifications of ordinary percolation, corresponding to the case where solid matrix participation is of no relevance. The last section considers gradient percolation which involves mainly heat conduction by the solid.

2.5.3 Gradient Percolation with Nucleation

A final modification involves the case where a fixed temperature gradient is assumed across the sample. The assumption is that solid conduction dominates the heat transfer ($\mu \gg 1$), thus, a spatial temperature gradient can be sustained, regardless of pore space occupancy. We make use of the previous rules for vapor occupancy of a site, for both nucleation and growth. Note, however, that fluid flow, particularly countercurrent flow, is not considered. This is a substantial limitation: A temperature gradient in the vapor phase requires a corresponding pressure gradient, thus vapor flow. At steady state, this must be counterbalanced by liquid flow in the opposite direction. We are currently investingating the effects of this approximation in a study of heat pipes using pore network models.

Allowing for a spatial gradient gives rise to gradient percolation. This concept has been introduced in recent years as a variation of classical percolation. It is recalled that in ordinary

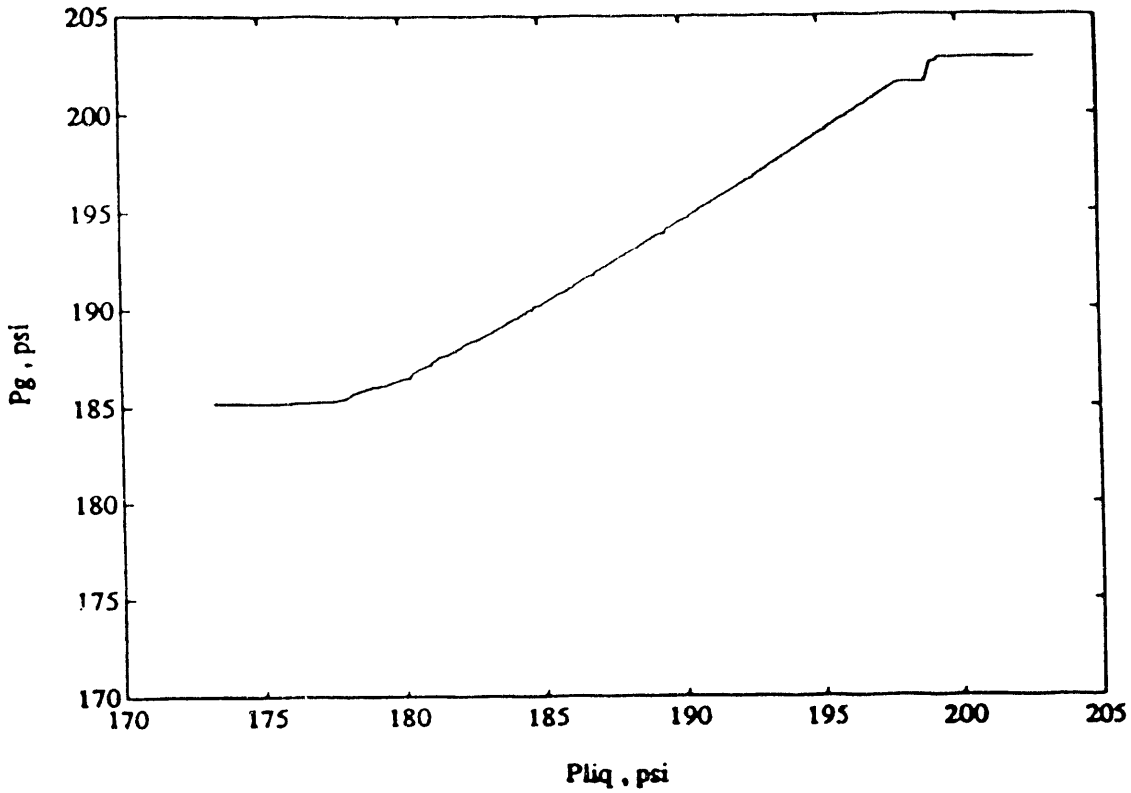

(*a*)

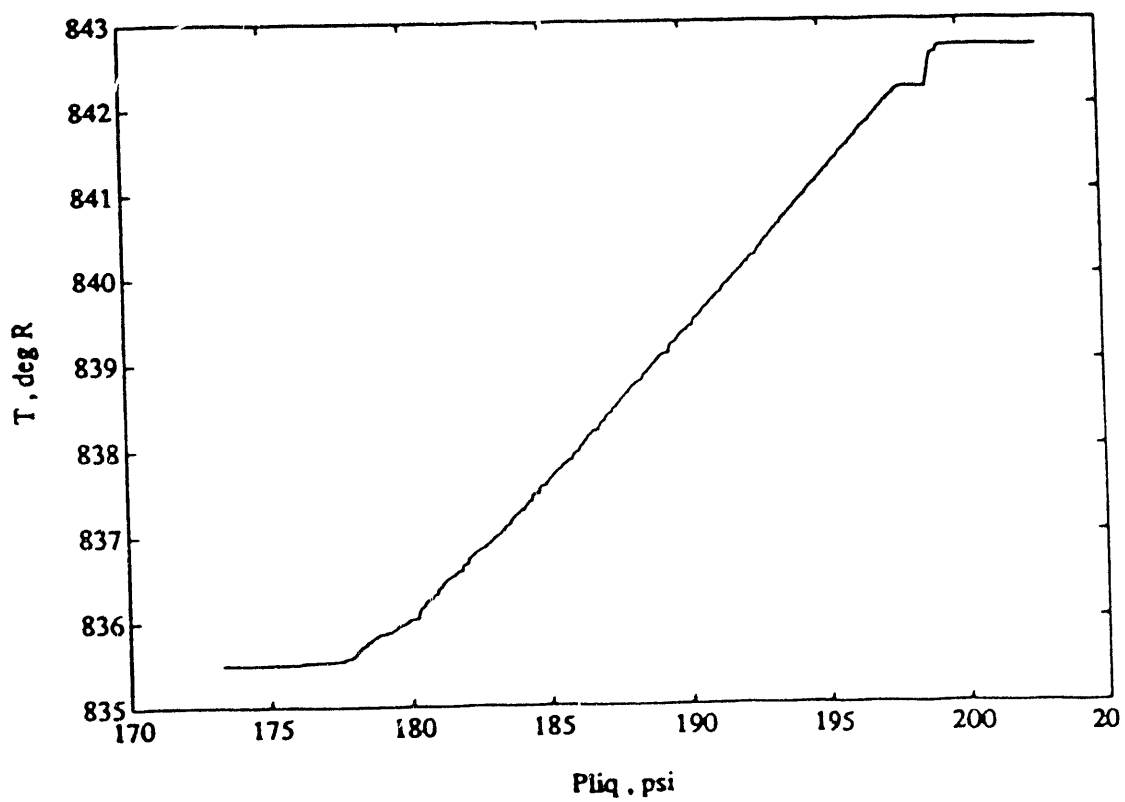

(*b*)

Figure 9: Supersaturation paths for adiabatic depletion: (a) Pressure, (b) Temperature

percolation the probability for the occupation of a site is spatially uniform. For gradient percolation, on the other hand, it is given by a specified function which is variable in space. This difference substantially changes the pattern of growth from that of classical percolation. In particular, fronts can be delineated.

Gouyet et al. [108] introduced gradient percolation in their study of diffusion in solids. They used the complementary error function to describe the probability distribution in space, for two-dimensional, square and triangular lattice networks. Using certain clustering and occupation rules, they examined the nature of the diffusion front created. They found out that this front is fractal (with dimension 1.75), while the probability value at the mean position of this front is related to the percolation threshold of ordinary percolation. In a subsequent study of 3-d cubic lattices, (Gouyet et al. [109]) they observed significant differences between 2-d and 3-d simulations. In particular, the shape of the density profile at the frontier changed. Furthermore, the probability density value at the mean frontier position was different than p_c. Nevertheless, many scaling properties were found (Rosso et al. [52]).

Concerning bubble growth in porous media, when solid conduction predominates ($\mu \gg 1$), the application of gradient percolation is appealing. At such conditions, the temperature field is decoupled from the occupancy scheme, which it actually dictates. For application to boiling, we have modified gradient percolation by adding bond statistics and nucleation effects. We consider uniform size distributions for sites and bonds, and a linear temperature profile. The parameters affecting the occupancy are pore and bond size distributions, the values of β and the imposed gradient ΔT. Growth patterns for modified gradient percolation models are shown in Figure 10 for two different values of the nucleation parameter β. Gray denotes vapor-occupied sites, while black denotes the interface which separates the infinite clusters of liquid-occupied sites and vapor-occupied sites. As β increases, more nucleation sites are available and this results in higher occupancy of pores by vapor. This increase in β shifts the interface toward the liquid side. Comparison between Figures 6 and 10 shows that the two patterns are quite different. A steam front is clearly distinguishable in the gradient percolation case. However, when spatial gradients are involved the definition of continuum quantities becomes problematic. Further progress requires additional research which is currently in progress in our laboratory.

(a)

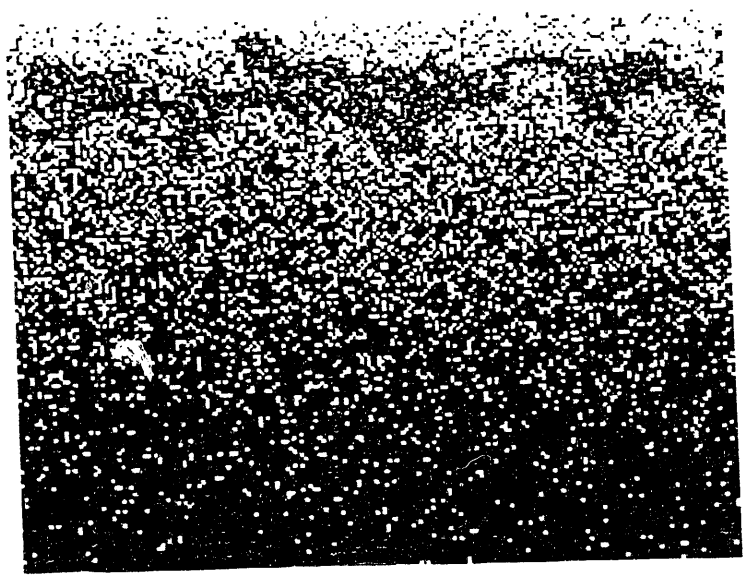

Figure 10: Vapor-liquid equilibrium in a temperature gradient using gradient percolation for different values of β : (a) $\beta = 0.2$, (b) $\beta = 0.5$

2.6 CONCLUSIONS

In this chapter we applied the general methodology developed by Yortsos and Parlar [148] for solution gas-drive processes, to the case of boiling in porous media. Phase equilibria and stability, nucleation, pore level microstructure and bubble growth were considered. At conditions of low superheat where the temperature field is quasi-static, the growth problem was shown to be similar to a drainage displacement process, with the addition of growth from activated nucleation sites. The case of uniform heating was described using a percolation approach, under the constraint that the heating rate must be significantly lower than 32.49 ^oF/day. Field cases relevant to steam injection or geothermal processes may obey this constraint. If such conditions prevail, relative permeability functions and critical saturation values can be employed in a modified form to account for nucleation. To account for temperature gradients in case where conduction in the solid dominates the heat transfer, and in the absence of flow, we have modified gradient percolation. Although an improvement over the uniform percolation model, these modifications are still tentative. We are currently involved in an effort to resolve many of the important issues left unanswered, including the effect of the rate of superheat and the competition between nucleation sites for growth.

3 VISUALIZATION EXPERIMENTS ON STEAM INJECTION IN HELE-SHAW CELLS

X. Kong, M. Haghighi and Y.C. Yortsos

3.1 INTRODUCTION

Flow visualization experiments have been successfully employed in reservoir engineering research for many years [24, 33, 59, 137, 141]. Typically, they make use of transparent Hele-Shaw cells, glass bead packs and glass micromodels. Although such geometries lack important 3-D aspects and particularly they do not accout for effects of gravity in the case of a horizontal arrangement, they are nevertheless valuable for the insight they offer on the micromechanics of the displacement. This is particularly important for displacement processes in constricted pore geometries, where an accurate description of the dynamics of the moving interfaces is paramount to a proper understanding of the process.

Most of the visualization work has been done on simple immiscible displacements (drainage or imbibition). A great deal of valuable information has been obtained regarding the various regimes that govern these processes, such as percolation, DLA (Diffusion-Limited-Aggregation), and other aspects of viscous fingering [76]. Studies with micromodels have been instrumental in identifying the pertinent flow mechanisms, particularly in secondary imbibition. Some visualization experiments with glass micromodels have also been carried out to study more complex phenomena, such as solution gas-drive, foam propagation, condensing-gas drive and other applications [2, 25, 31, 94, 80]. An excellent recent summary can be found in [19].

Surprisingly, visualization of steamfloods, which constitute a major part of current EOR methods for heavy oil, has not been attempted to date (although a preliminary investigation was indeed conducted in our laboratory several years ago). Reasons for the lack of success in this direction include the difficulties associated with an adequate control of the heat transfer and operational problems at higher temperatures and pressures. In a some what related context, the application of CT scanning to steamfloods in sandpacks was recently proposed with encouraging preliminary results [34]. Flow imaging using CT scanning accounts for important 3-D effects. However, the scale of resolution is still too large to allow for a meaningful pore-level analysis, although important laege scale heterogeneity effects can indeed be detected. At present, direct flow visualization appears to remain an essential and inexpensive tool for studies at the pore-level.

Even in the absence of heat transfer control, steam displacement visualization can be very valuable. For example, while much work has been done on steamfloods in laboratory cores and on partly scaled models [36, 122, 125], the results obtained are typically of the input-output type and provide very limited understanding of the interactions at the pore-level. A thorough investigation of the latter is important for the validation of many premises used in current theories, for the refinement and improvement of models, for instance those pertaining to relative permeabilities and capillary pressure, and for process simulation. It should be pointed out that the current state of the art in thermal recovery relies on the direct application of two-phase flow concepts from immiscible displacement analogues [99], the validity of which, however, for condensing-evaporating drives is quite questionable.

Motivated by the above, we have undertaken experimental studies with a main objective the visualization of steam injection processes in Hele-Shaw cells and in glass micromodels. The study of Hele-Shaw geometries is expected to shed light on the displacement of heavy oils by steam in planar geometries. To some degree, this geometry parallels that of a fracture, hence the study would also find direct application to fractured systems. More generally, flow in Hele-Shaw cells provides many clues about flow behavior in porous media. It should be recalled that flow in Hele-Shaw cells at low Reynolds numbers is potential and can be approximated by Darcy's law, which governs porous media flow, although in the absence of microstructure ("noise"). Hence, Hele-Shaw studies of steamfloods offer a good approximation of condensing/evaporating flows in "porous media" geometries. On the other hand, because of the lack of microstructure, which is an integral part of porous media, the analogy between Hele-Shaw and porous media displacement is also tenuous. This deficiency can be partially remedied by studies in glass micromodels, which allow for effects of pore structure to be investigated in great detail. Such an investigation will be reported in a future communication.

This chapter is organized as follows: First, a brief description of the experimental procedure is presented. Results of visualization experiments are subsequently discussed. Two different geometries are analyzed, one horizontal and another vertical, in order to isolate gravity effects.

3.2 EXPERIMENTAL

The Hele-Shaw cell used for steam displacement was constructed from pyrex glass. The cell was of dimensions 24.5in.×12in.×.035in. and consisted of two glass plates of 1/2" thickness. Three types of oil were used, a synthetic oil (Dutrex 739), taken as a representative of heavy oil, a mineral oil, taken as a representative of light oil, and a Long Beach crude oil. The mineral oil used was Newtonian, with a room temperature viscosity of 189 cp, while both the Long Beach crude oil and the synthetic oil exhibited non-Newtonian behavior with a room temperature shear viscosity of $1.35 \times 10^4 cp$ and $10^5 cp$, respectively. The shear viscosity for Dutrex 739 was significantly reduced by an increase in temperature [36]. A similar sensitivity was expected, but it was not measured, for the Long Beach crude. Non-Newtonian rheology, although complicating the interpretation of experiments, is certainly a prominent, although typically neglected, feature of heavy oils.

Variable water injection rates and temperatures were used, typically in the range 0.1-5 cc/min. Injection temperatures fluctuated to within a few ^oF around a mean value of 250 ^oF. In most runs, the injected steam was superheated. The Hele-Shaw cell was not insulated or otherwise equipped with heat loss control, which occured by heat conduction through the glass to the surroundings. The lack of heat transfer control certainly presents important problems that may affect the quantitative, although not the qualitative, analysis of our results. A separate, but equally important, problem regards the low injection pressure typically used (in order to prevent fracturing of the glass). We are currently experimenting with ways to resolve both these problems. More than 30 runs were conducted. Most of the experiments were run with the cells in the horizontal position. Effects of gravity were investigated by tilting the cell at various angeles and also by carrying injection in the configuration of a planar vertical cross-section. A schematic of the experimental set up is shown in Figure 11.

3.3 RESULTS AND DISCUSSION

We shall discuss in the following two sets of experimental results pertaining to: (i) Displacement in horizontal Hele-Shaw cells and (ii) Effects of gravity.

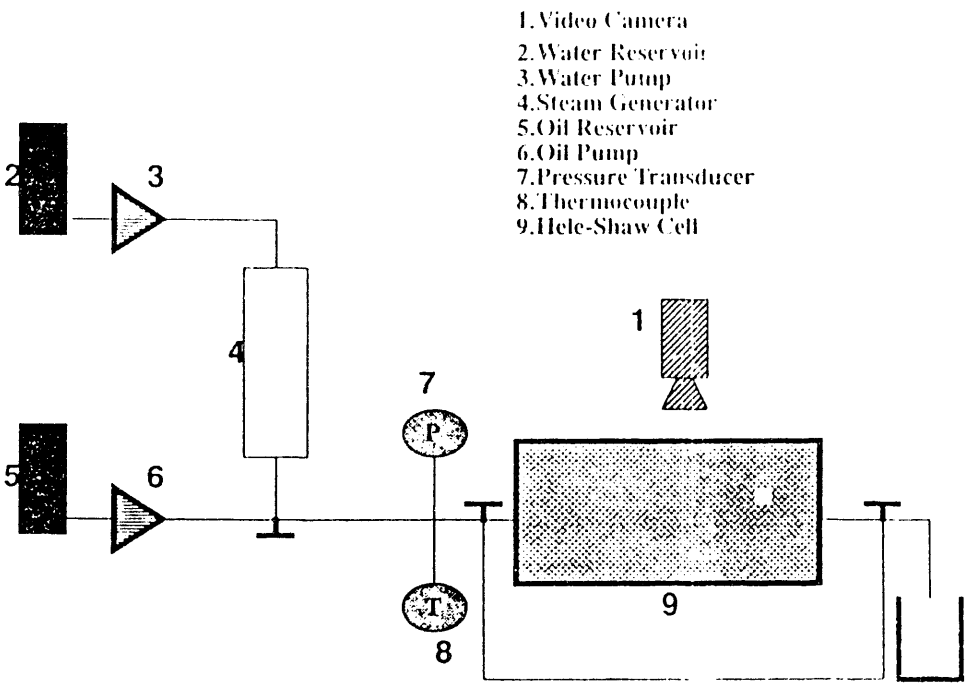

Figure 11: Schematic of the experimental apparatus

3.4 DISPLACEMENT IN HORIZONTAL HELE-SHAW CELLS

We consider as base case the displacement of Dutrex 739 by steam at the rate of 3 cc/min and an injection temperature of 230 ^{o}F. In the subsequent pictures, taken from a still videotape, displacement is from left to right. One injection and one production ports were used. In the colored pictures, red is the color of the original oil, and bright white is steam. Condensed water typically flows between residual yellow oil films attached to the two glass plates and left behind after water displacement.

Figure 12 shows the initial part of the displacement. Due to the rapid heat losses and the contact with the initially cold oil, steam is shown to condense rapidly. Thus, the original displacement of oil is by condensed water only. Because of the unfavorable mobility contrast, this displacement is unstable [145] and produces viscous fingers in a manner very similar to the case of isothermal displacement, although the overall pattern is slightly different. Nonetheless, repeated tip splitting was observed, as is common with highly unstable displacement [58]. We point out that the pattern laid by the advancing condensed water is of crucial importance, because it dictates the paths to be followed by the injected steam. After a certain period of injection, a rather irregular steam

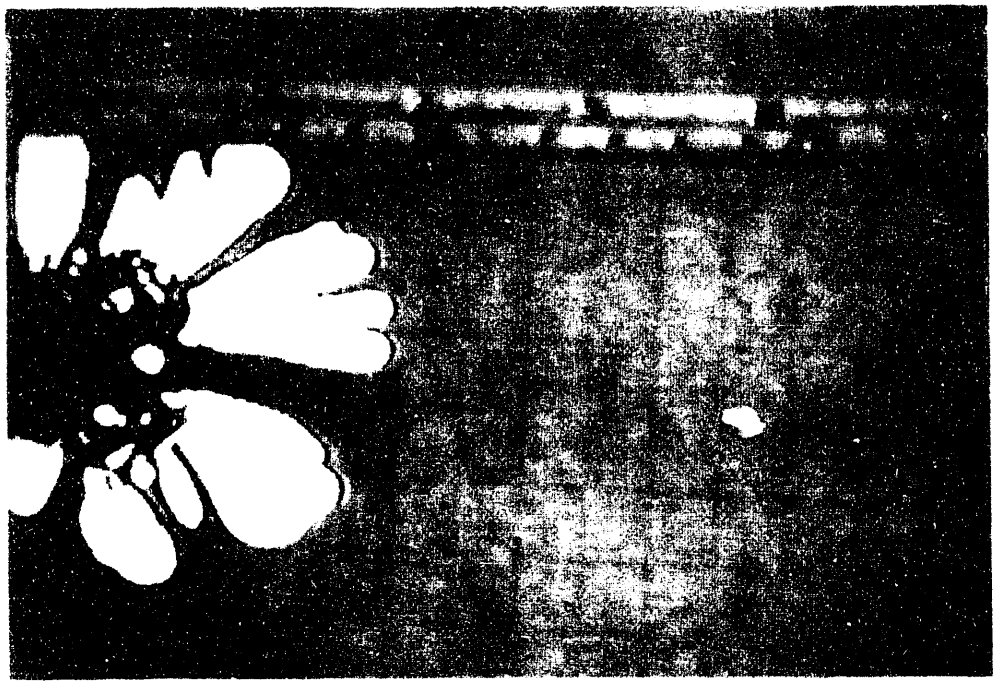

Figure 12: Initial stage of displacement

zone is established near the injection port (Figure 13). Vapor and liquid phases can be visually separated. Upon displacement of oil, liquid water is covered on both sides by yellow, residual oil films which coat the glass plates. Upon contact with vapor, these films rapidly diminish in thickness and eventually disappear, perhaps as a result of a steam distillation mechanism. A close up of the steam zone is shown in Figure 14. One can distinguish traces of what appear to be light oil components. Even after the glass plates are clean, vapor and liquid can be visually separated by the meniscus, the motion of which can be clearly followed.

Most interesting are the shape and properties of the steam front. We recall that in a typical immiscible displacement in a Hele-Shaw cell, interfaces advance smoothly, provided that the plates are smooth. This was indeed the case for the displacement of oil by the advancing condensed water (Figure 15). The thin films of oil left behind are predicted from Bretherton's theory for displacement [49], which postulates that their thickness increase with an increas in the capillary number $N_{ca}(= q\mu/\gamma)$. The dynamics of vapor-liquid interfaces are quite different, however. Typically, two kinds of water vapor-liquid interfaces were observed, a steam-oil and a steam-water interface (Figure 15). The steam-oil front was almost stationary and moved very slowly (if at all). Disconnected and trapped steam bubbles were frequently observed. By contrast, the steam-water interace was in a

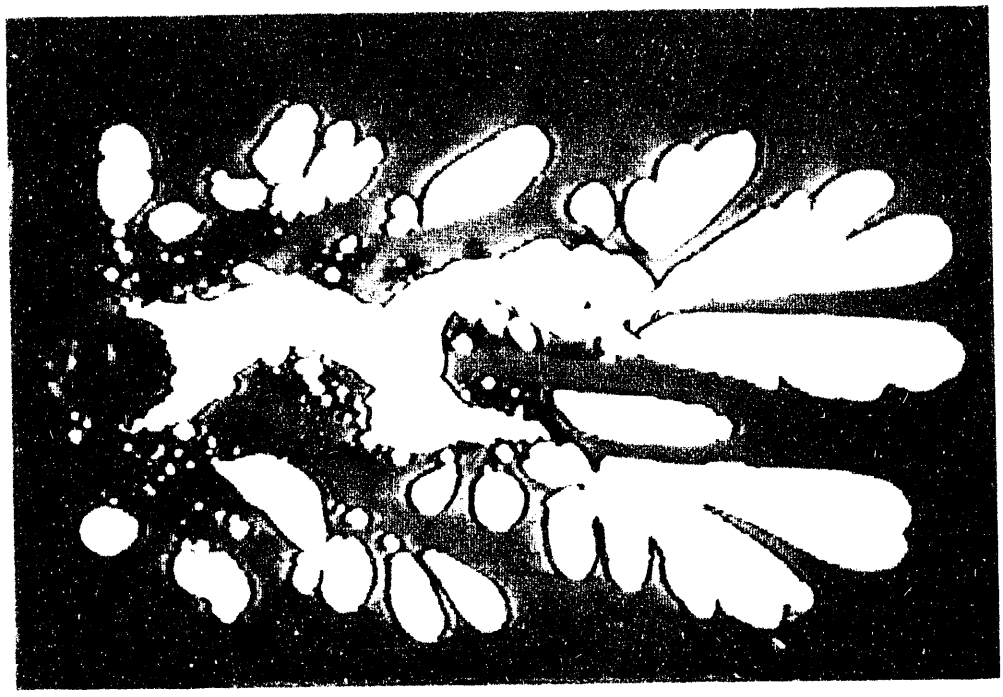

Figure 13: A typical steam displacement snapshot

Figure 14: Close-up of steam front

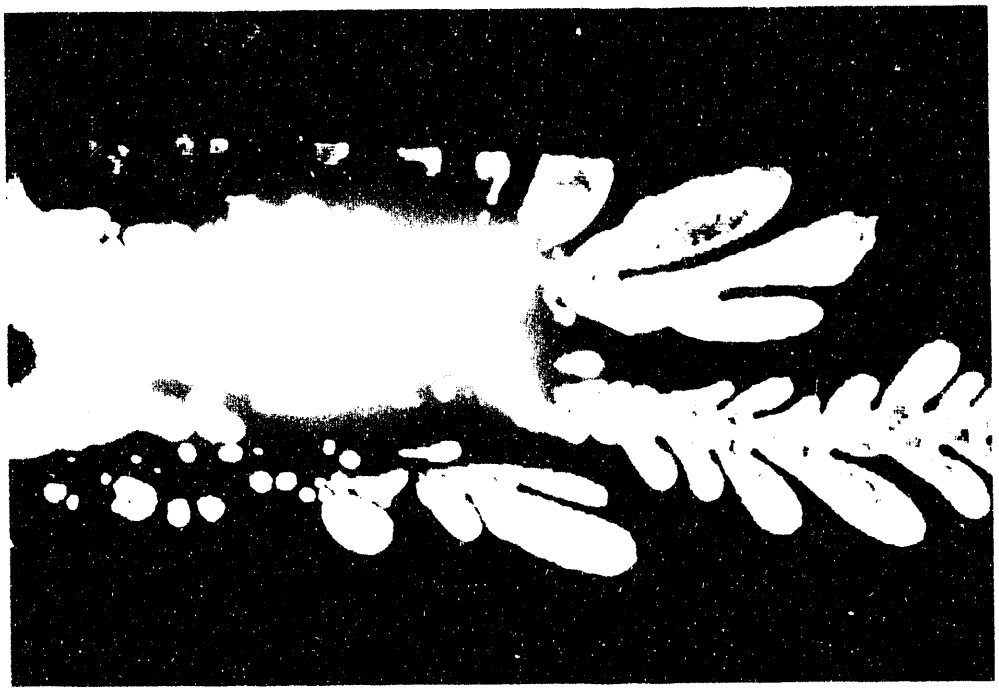

Figure 15: Snapshot after water breakthrough

state of perpetual fluctuation, which eventually resulted into a net but slow advancement. This was explained as follows:

The advancement of the steam front led to a rapid condensation of a sizeable part of the steam zone, as a result of heat losses. Shortly therafter, this was followed by a rapid burst of vapor-influx, which essentially restored to vapor occupation the previously condensed part. This cycle of advancement-vapor condensation-vapor replacement was repeated continuously and appeared to be the general mechanism for the growth of the steam zone. In no instance did we observe a smooth frontal displacement of the typical water-oil intersace. Also, in contrast to what typically assumed, steam fronts were neither smooth nor "flat", but they had a finger-like appearence, as they followed the flow paths of the condensed water. This complex process is of course controlled by heat transfer, vicosity reduction, injection rates and pressure, the end result being quite different than ordinary Hele-Shaw displacements. Indeed, it is possible that condensation and vapor growth phenomena in the above cycles are rapid enough for inertia effects not to be negligible. This complex mechanism is currently under investigation.

Water breakthrough occurs when the fastest among the competing fingers reaches the production end. Important observations during this period were the following: Steam flowed mostly along

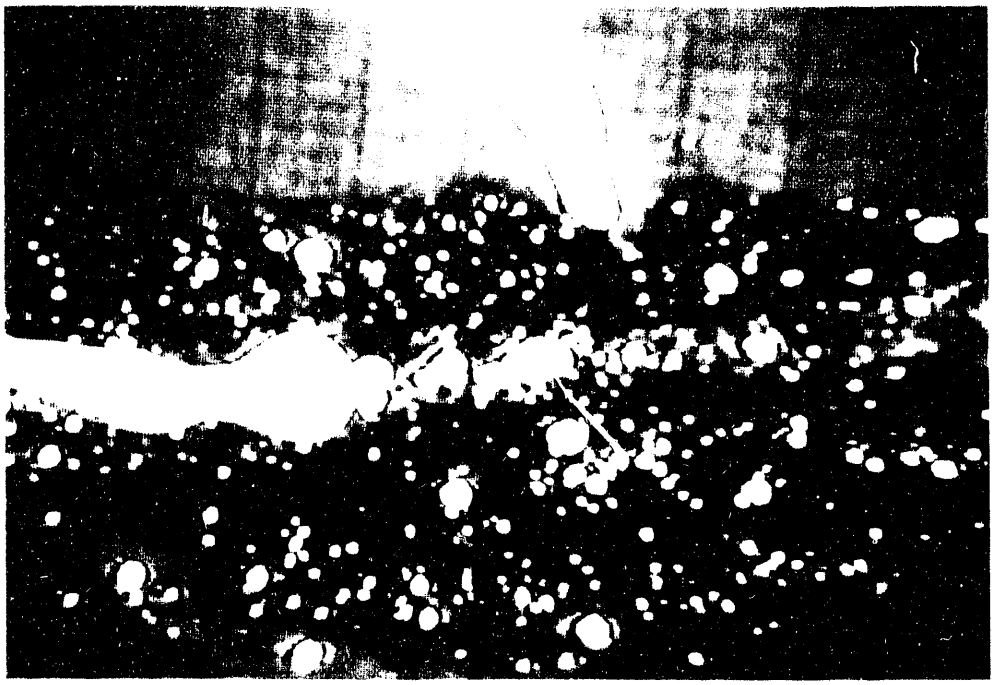

Figure 16: Evidence of emulsification of oil

the paths connected to the production well. Water fingers connected to the steam zone that did not breakthrough, occasionally became disconnected from the steam zone due to condensation events. Flow of steam was not smooth but involved the condensation -advancement cycle. During this process, substantial emulsification of the oil also occured (Figure 16). After breakthrough, a large fraction of the oil produced was in the form of water emulsion. We suspect that emulsification was enhanced by the following rather unusual rheological response of Dutrex. Soon after water breakthrough, the connected finger started to continuously thin, until it eventually fragmented at one or several points and lost connection to the producing port (Figure 17). A different finger then started growing following a usual displacement process, until breakthrough of that path was also reached. Soon after, the process of thinning commenced, once again, to follow the previous route until disconnection and so on. These phenomena are not due to steam injection, but they are attributed to the particular oil, as they were also observed during an ordinary waterflood.

A possible explanation for this behavior can be provided if we assume that Dutrex 739 is viscoelastic. Before water breakthrough, the fluid pressure is relatively high due to the high viscosity. Upon water breakthrough, the oil responds to the resulting pressure decrease by expanding following a relaxation, time-dependent process. This results into the thinning and shrinkage of the producing

Figure 17: Finger thinning after breakthrough

water finger until total disconnection occurs. The process is then repeated. This rough qualitative argument explains the gross behavior observed, although for a more convincing interpretation, a model is necessary.

A comparison between steam and cold water displacement is shown in Figure 18 for the same mass injection rates. Typical finger patterns before breakthrough show the characteristic tip-splitting. Upon breakthrough, the same response previously described sets in. Significant differences with the steam injection runs involved the presence of residual oil films and the lack of emulsification in the case of water injection. Effects of injection rate were also considered, by carrying a steam injection run at the lower rate of 1 cc/min. As anticipated, the decrease in the rate results into a smaller steam zone area, which did not propagate significantly far into the cell. Otherwise, phenomena qualitatively similar to the previous were observed.

For comparison, the results of steam displacement of light (mineral) oil at the same rate of 3 cc/min and a temperature of $230^o F$ are shown in Figure 19. Several significant differences with the heavy oil were noted: The degree of tip splitting was considerably less, as anticipated due to the lesser viscosity contrast in the light oil case. No significant residual oil films were detected in the displacement by either water liquid or by steam. This observation was verified by the cold water

Figure 18: Typical fingering pattern for oil displacement by water

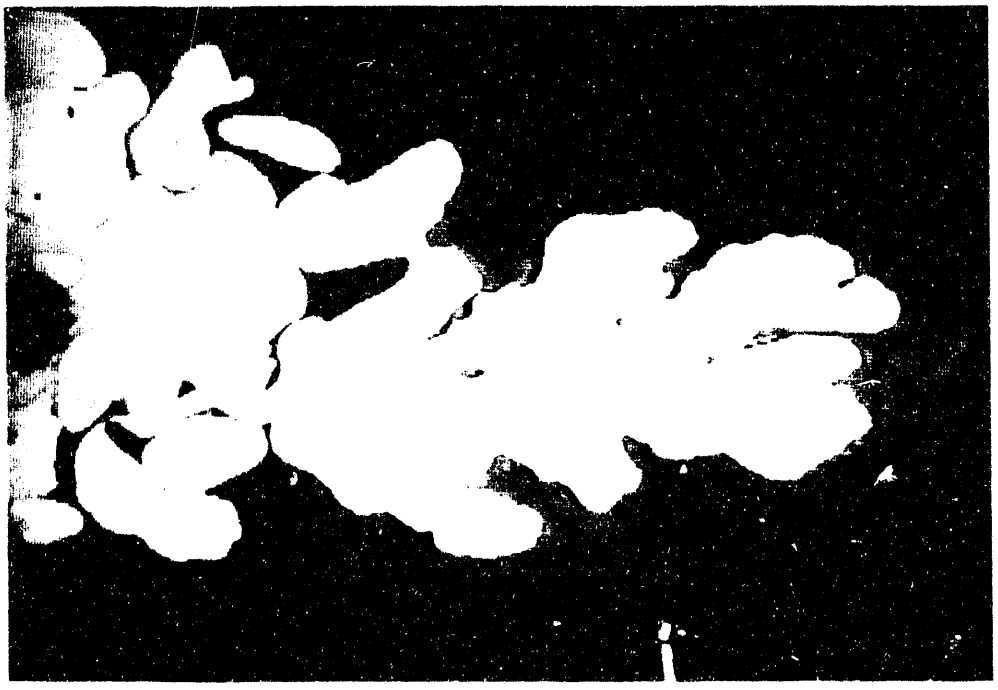

Figure 19: Snapshot of mineral oil displacement by steam

injection experiments also. In contrast to the heavy oil case, the steam front did not necessarily follow the path of the condensed water fingers. Instead, the steam zone expanded almost uniformly. This behavior can be attributed to the higher mobility of the light oil, and it is consistent with currently available theories. The behavior of the mineral oil was Newtonian throughout the process. Upon breakthrough, the water finger width remained essentially constant and provided the main flow path for the injected steam.

Steam displacement of the Long Beach crude oil resulted into a behavior qualitatively similar to the displacement of Dutrex 739. Severe fingering by condensed water (Figure 20), residual oil films after waterflood (Figure 21), steam front oscillation, propagation of steam zone along the condensed water path (Figure 21) and finger thining after breakthrough were all observed. It appeared that the crude oil shared with Dutrex 739 a similar non-Newtonian rheology. A significant difference was noted, however, regarding water vapor-oil interaction. The almost instantaneous removal of the residual oil film upon steam contact, observed during displacement of Dutrex 739, did not occur in the case of crude oil. Instead, a process resembling extraction of light ends (perhaps steam distillation) set in at the vapor-oil interface (Figure 22). The extracted components did not partition in the water phase, but were instead convected along with the fllowing vapor. The extraction process, continued for the duration of the experiments and appeared to be a primary mechanism for the recovery of the crude oil.

3.4.1 Gravity Effects

The next set of experiments investigated effects of gravity following two different geometrical configurations, one with the Hele-Shaw cell tilted at a small angle with respect to horizontal, and another with the cell rotated parallel to the gravity vector (vertical cross-section).

In the first configuration we probed effects of formation dip. Steam was injected from the bottom (updip) or from the top (downdip). For updip injection, steam displacement occured along a rather narrow strip, the density difference acting to destabilize the front. The oscillation phenomena of the front were well pronounced and steam zone breakthrough occured in a short time (Figure 23). In direct contrast, a flat and stable steam front was observed in the case of downdip injection (from top). This front advanced very slowly, due to the heat loss, most of the displacement occuring by the condensed water (Figure 24). Both these observations are generally

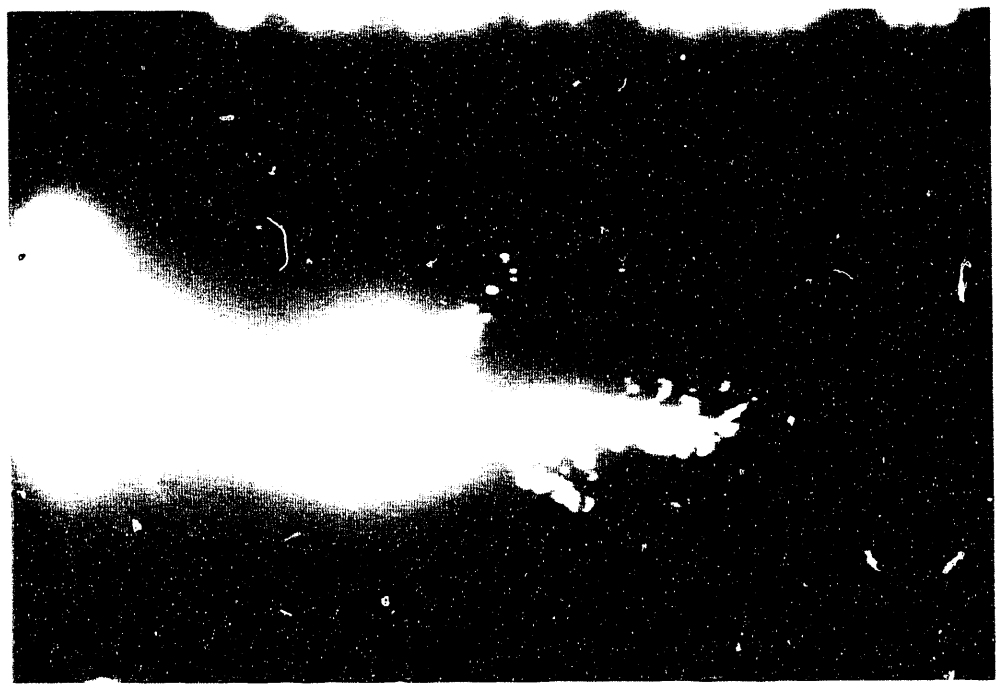

Figure 20: Steam zone during displacement by steam of a Long Beach crude

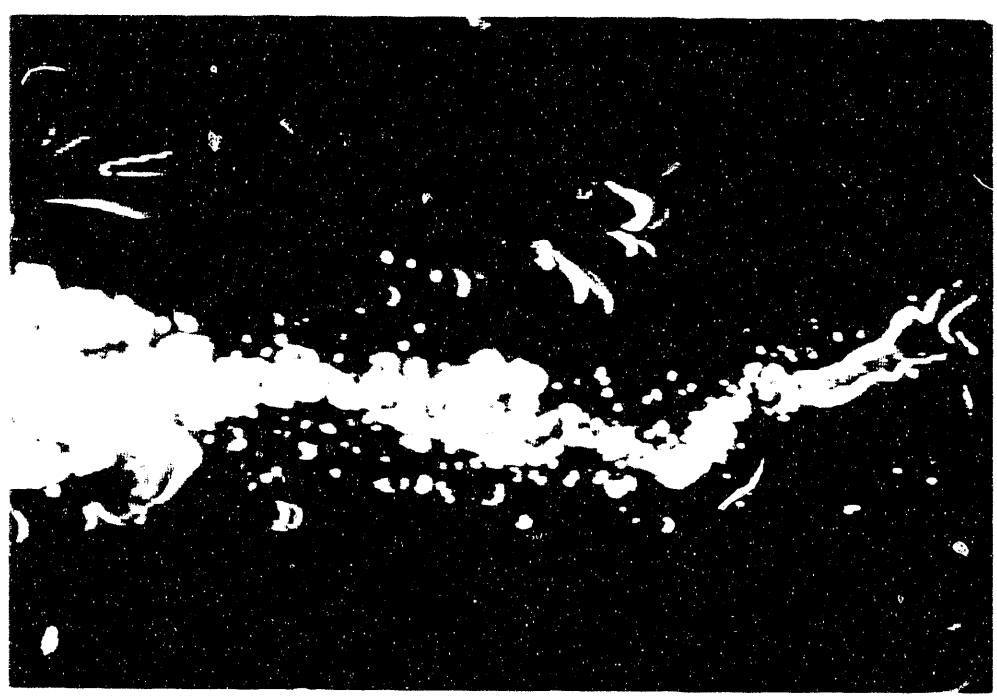

Figure 21: A different snapshot of steam zone displacement of Long Beach crude oil

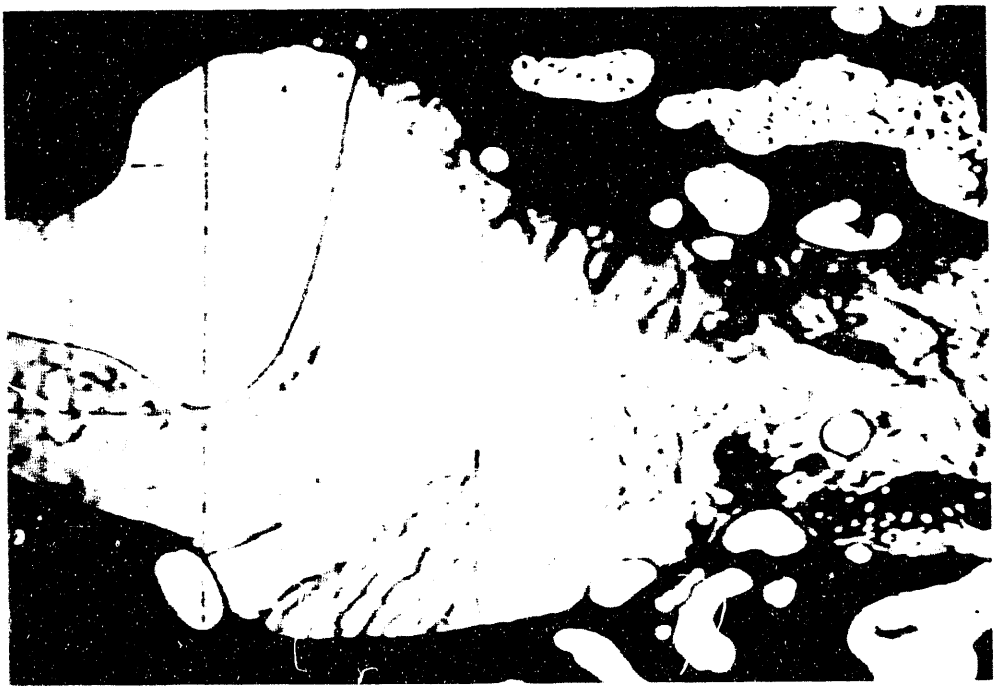

Figure 22: Close-up of steam zone during steam displacement

consistent with conventional theories on the effect of gravity on displacement fronts.

In the second configuration we probed effects of gravity override, for both Dutrex 739 and Long Beach crude oil steamfloods. The most significant difference with the prevrious involved the interplay between gravity, condensation and heat transfer. Typically, the injected steam migrated upwards to form a rather stationary steam zone. Condensed water flowed downwards in the direction of a water finger at the bottom of the steam zone, which developed at the onset of the experiment and displaced oil towards the production well (Figure 25). Most of the oil displacement occured as a result of this mechanism, although the extraction process was also very much evident (Figure 26). After water finger breakthough, steam flow ensued along the finger path, much like in the case of horizontal displacement (Figure 27). As in the previous case, the non-Newtonian response of the heavy oils eventually resulted into finger thinning. Now, however, when the connection to the production part is lost, the steam zone at the top starts growing. Condensed water creates a finger originating from the upper part of the steam zone, resulting into a displacement along the top, in a mechanism similar to the horizontal case (Figure 28). After this finger reaches breakthrough, the cycle sets on again and a different branch may be selected. The process continues until the displacement is completed. We observed that the steam zone volume depends significantly

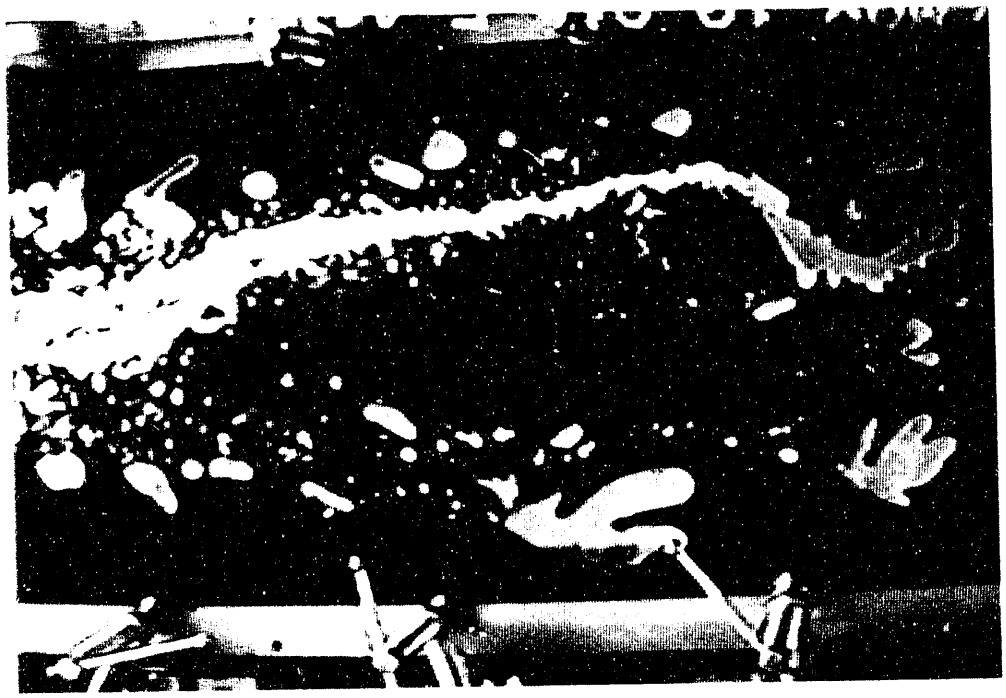

Figure 23: Updip steam injection

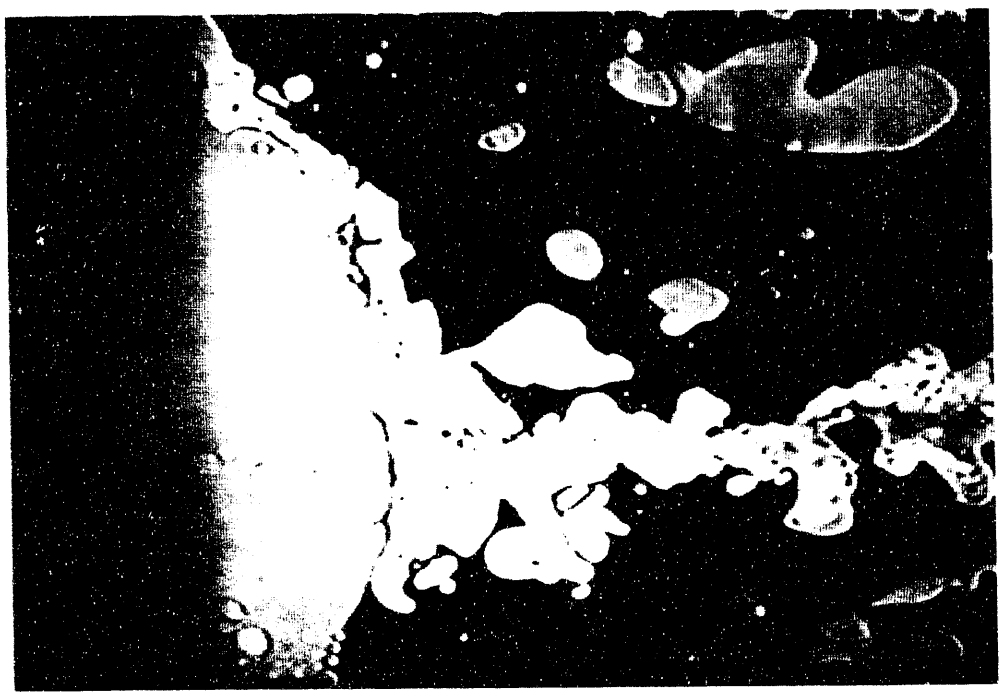

Figure 24: Downdip steam injection

Figure 25: Steam displacement in a vertical cross-section

on whether it is connected to a finger that has already reached breakthrough or not. In the former case, due to the prevailing lower pressure, steam zone volume is much larger than when the water finger is not at breakthrough conditions.

3.5 CONCLUSIONS

The preliminary experiments reported above have probed a part of the complicated process of steam displacement. One of the most interesting results, common to all runs, was the unsteady, almost flickering state of the steam front, and the mode of advancement by the cycle penetration-condensation-restoration. This is certainly to be affected by injection rate, heat transfer and flow mobilities. Our current work is aimed at the understanding of this process.

For the low pressure, relatively high rate conditions of our experiments, injected steam was found to follow the path of the condensed water. The latter set the general displacement pattern, which in the case of heavy oil was highly fingered. It should be evident, that this result is a consequence of the particular combination of fluid flow and heat transfer in our experiments, thus any extrapolation must be done with caution. We identified a rather unusual non-Newtonian behavior for Dutrex 739, a chemical taken to represent heavy oil,and for Long Beach crude oil.

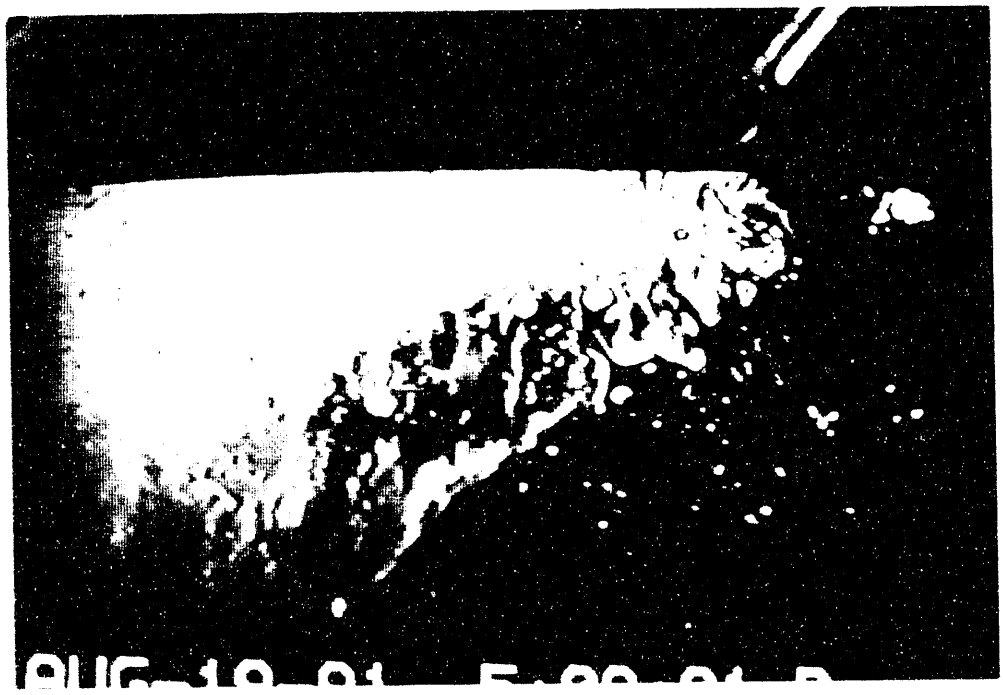

Figure 26: Close-up of steam zone during displacement in a vertical cross-section

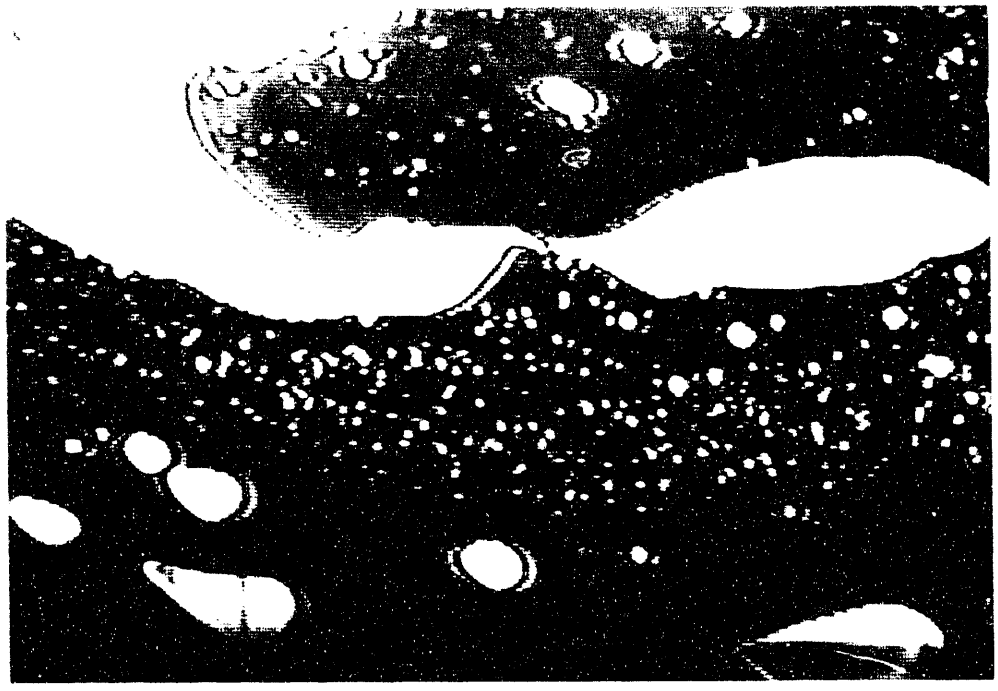

Figure 27: Snapshot after water breakthrough

Figure 28: Steam gravity override

Regardless of the particular aspects of the response observed, one may reasonably conclude that the non-Newtonian rheology of many heavy oils is likely to lead to similarly complex behavior. This subject is further to be explored.

We have observed direct evidence of a steam extraction of oil components from a crude oil, a process that has direct relevance to the oil recovery. Effects of gravity were also examined. While the mode of injection (updip or downdip) was found consistent with currently available theories on frontal displacement, the detailed visualization of frontal motion revealed additional aspects. In particular, the growth of the steam zone in a vertical cross-section displacement was found to be affected significantly from the condensation and flow phenomena ahead of it. Much of this behavior is novel and requires further investigation.

4 EFFECTS OF HETEROGENEITY ON VAPOR-LIQUID COUNTERFLOW IN POROUS MEDIA

A. K. Stubos, C. Satik and Y. C. Yortsos

4.1 INTRODUCTION

Countercurrent vapor-liquid flows in porous media have been the subject of many recent studies due to their relevance to geothermal processes, boiling, thermal methods for oil recovery and nuclear waste disposal [126],[127],[136],[106],[38]. Of particular interest are steady state heat pipes driven by gravity. The theoretical analysis shows that when the system is homogeneous, an infinitely long two-phase zone of nearly constant saturation develops if the heating rate is low enough (below a critical value). Furthermore, under the same operating conditions, two such states are predicted, one coresponding to low liquid saturation (vapor-dominated, VD) and one corresponding to high liquid saturation (liquid-dominated, LD). In a recent note [128], using the detailed analysis described in a previous paper [118], we have proposed that the selection of the particular solution only depends on the past history of the system. For instance, in boiling applications which involve bottom heating, it is the LD branch that is followed. While, in the case of condensation of a superheated vapor (top cooling), it is the VD branch that is selected. In either of the two cases, capillarity is necessary to connect the constant saturation profiles to the subcooled or dry regions, respectively.

In practice, of course, all systems are finite and heterogeneous. The two-phase zone must terminate at a finite location, thus, the "infinite" extent predictions of the heat pipe formalism cannot hold indefinitely. Termination of the two-phase zone must be obtained by smoothly merging the two-phase region with a subcooled liquid or a dry region, in the LD or VD cases, respectively (otherwise, non-zero vapor and liquid fluxes would exist at the impermeable boundary of the medium [128]). Although the various studies conveniently avoid further elaboration on this issue, the implicit assumption is that this can be accomplished with the use of heterogeneities. Analogous problems arise in the gravitational stability of counterflow vapor-liquid systems, when a vapor-rich region underlies a subcooled liquid layer. Even if we accept the suitability of the various base states used in the analysis [120],[107] (the validity of which is questionable), the present consensus is that unconditional stability is possible only if a heterogeneity is present somewhere in the two-phase region.

Heat pipe instability, but in a much different context, and more precisely as it regards the sensitivity of steady, 1D profiles to the boundary conditions, was considered in a recent study [91]. It was suggested that, under certain conditions, a VD solution is unconditionally "unstable" and must revert to a "stable" LD configuration, or vice versa, if the boundary conditions are reversed. While not immediately apparent, this problem is really related to heterogeneity, as shown below. We recall that boundary end effects in immiscible displacement can be considered as special cases of heterogeneity, when the change in permeability is abrupt and very large [147].

Effects of heterogeneity on vapor-liquid concurrent flow were studied in [100]. These authors generalized previous works on the steady state, two-phase flow of non-condensing fluids [147]. With the exception of a rather preliminary analysis [27], however, heterogeneity effects on countercurrent vapor-liquid flows have not been addressed in much detail and they are currently poorly understood. Cases in point are the previously mentioned questions on the termination of the theoretically "infinite" two-phase zone, on the gravitational instability and on the sensitivity to boundary conditions. This chapter aims at resolving some of these issues. We theoretically investigate effects of heterogeneity under various configurations. We find that permeability (capillary) heterogeneity acts in reality as a body force (e.g. gravity), with the important additional property that it is also spatially varying. Heterogeneity may thus enhance or counterbalance gravity effects, depending on magnitude, form and direction of change.

The chapter is organized as follows: We first study the simpler, but quite useful, horizontal case, which allows for an exact solution to be developed. Then, we apply the results obtained to interpret effects of gravity when the heat flux is below critical. Next, we address problems involving both heterogeneity and gravity at conditions of slow and fast permeability variation. In all these cases, heat conduction is not significant, and it is not considered. Throughout the chapter, the formalism of [118] is followed. The description is thus traditional, based on continuum assumptions, and employs the concepts of equilibrium, saturation-dependent only, relative permeability and capillary pressure functions. Whether this formalism is adequate for rapidly varying permeabilities, is not questioned in this chapter, the conclusions of which are therefore subject to this important hypothesis. It is conceivable that, at least in the case of sharp heterogeneities, some of the results may need further support, e.g. from more detailed pore network-level analysis.

4.2 FORMULATION

We proceed with the assumption that the main heterogeneous variable is permeability [147],[100]. Contrary to 2D flows, where viscous effects dominate, an important parameter which is affected in the present case of 1D counterflow is capillary pressure. This is a result of the Leverett J-function representation:

$$P_c = \frac{\sigma J(S)}{\sqrt{k}}$$

The function J (as well as the relative permeabilities) may also be taken as weakly varying, although it is the dimensional $\sqrt{k}$-dependence that basically controls the capillary variation (see also [147] for a more detailed discussion).

The importance of conduction is expressed through the following dimensionless group [118]:

$$KR_m = \frac{kL_v^2 M_w P_o \rho_v}{\mu_v \lambda R T_o^2}$$

For large values of the latter, conduction is negligible. This is the case typically in heat pipes, where KR_m is large (equal to 5184 for the conditions in [136]). Conduction must be retained in systems with low k or very high λ values, although, such cases may be of limited practical interest (although see [128]). When the flow configuration is different, conduction may be important, e.g. in the geothermal systems of the type discussed by Schubert & Straus [119], where its consideration is necessary in order to sustain counterflow. Regardless of the application, however, the relevance of conduction to a study of *heterogeneity* should be small. Indeed, for the former to have some impact requires substantially large variations in the vapor pressure [128],[118]. Such are not likely to occur if the regions of continuous permeability increase (or decrease) are not very long. Therefore, capillarity is likely to predominate over conduction, the effects of which we shall neglect henceforth.

In the absence of heat conduction, we can formulate the problem in a straightforward fashion, because saturation and temperature are decoupled from each other and the solution is obtained by simple means. Following [118], a straightforward manipulation of mass, momentum and energy balances yields the simple equation:

$$\tau J' \frac{dS}{d\xi} - J \frac{d\tau}{d\xi} = \omega \frac{(k_{r\ell} + \beta k_{rv})}{k_{r\ell} k_{rv}} + sin\theta \, \tau^2 \tag{39}$$

Here $\tau \equiv \sqrt{k/k^*}$ is the heterogeneity variable which is spatially varying, k^* denotes a constant reference permeability and superscript $'$ indicates derivatives with respect to S. The notation is

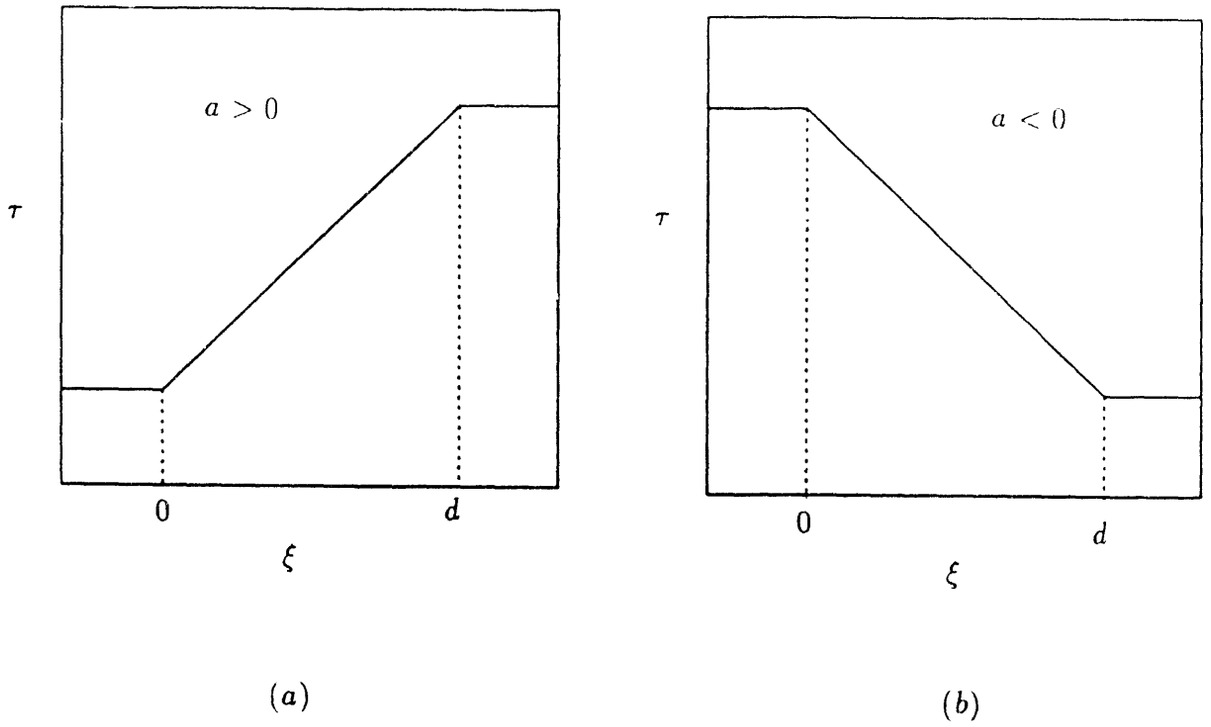

Figure 29: Schematic of a special heterogeneity profile: (a) Permeability increase; (b) Permeability decrease

identical to [118] except for τ, which here does not denote temperature. The coordinate ξ increases in the direction from the liquid to the vapor, such that the liquid velocity is positive, while the dimensionless heat flux $\omega = q\mu_v/k^* L_v g \Delta\rho\rho_v$ is normalized with a reference permeability. In this notation, therefore, different permeability regions have the same value of ω, but not the same critical values (see also below). Equation (39) must be generally solved numerically. Preliminary insight can be obtained by an analytical solution, which is possible for a special case in horizontal counterflow.

A. Horizontal Counterflow

In a horizontal system ($\theta = 0$) counterflow is driven by capillarity only [38]. Then (39) yields:

$$\tau J' \frac{dS}{d\xi} = \omega \frac{(k_{r\ell} + \beta k_{rv})}{k_{r\ell} k_{rv}} + J \frac{d\tau}{d\xi} \tag{40}$$

Consider, without loss, $\omega > 0$. Very useful results are obtained in the special case, when τ is piecewise linear (Figure 29):

$$\tau = \begin{cases} 1 \quad ; \quad \xi < 0 \\ a\xi + 1 \quad ; \quad 0 < \xi < d \\ \tau_+ \quad ; \quad d < \xi \end{cases} \tag{41}$$

where $\tau_+ \equiv ad + 1$. Here, the spatial extent of the heterogeneity is denoted by $d > 0$, while a indicates the direction of change ($a > 0$ for an increase, $a < 0$ for a decrease of τ in the ξ direction). Outside this region, $\xi < 0$ or $d < \xi$, the system is homogeneous and the solution is a continuously decreasing saturation profile, $S(\xi)$, of the general form:

$$\int^S \frac{k_{r\ell}k_{rv}J'dS}{(k_{r\ell} + \beta k_{rv})} = \omega\xi \quad \left(or \quad \frac{\omega\xi}{\tau_+}\right) + const.$$

Inside the heterogeneity, $0 < \xi < d$, the saturation satisfies:

$$\frac{k_{r\ell}k_{rv}J'dS}{\omega(k_{r\ell} + \beta k_{rv}) + k_{r\ell}k_{rv}a\ J} = \frac{d\xi}{a\xi + 1} \tag{42}$$

This can be readily integrated. Because of the qualitatively different responses, two different cases are separately considered:

1. $a > 0$ (*Figure 29a*)

Here, the permeability is increasing, and from (42) we obtain the straightforward result:

$$\int_{S_o}^S \frac{k_{r\ell}k_{rv}J'dS}{\omega(k_{r\ell} + \beta k_{rv}) + k_{r\ell}k_{rv}a\ J} = \frac{1}{a}ln(a\xi + 1) \tag{43}$$

where S_o is the saturation at 0 (presently unknown). Because of $a > 0$, the saturation decreases steadily also within the region of heterogeneity (Figure 30). The downstream value S_1 satisfies:

$$\int_{S_o}^{S_1} \frac{k_{r\ell}k_{rv}J'dS}{\omega(k_{r\ell} + \beta k_{rv}) + k_{r\ell}k_{rv}a\ J} = \frac{1}{a}ln\tau_+ \tag{44}$$

provided that a solution to the latter exists. This requires:

$$\int_0^1 \frac{k_{r\ell}k_{rv}(-J')dS}{\omega(k_{r\ell} + \beta k_{rv}) + k_{r\ell}k_{rv}a\ J} \geq \frac{1}{a}ln\tau_+ \tag{45}$$

Otherwise, single-phase flow conditions develop inside the heterogeneity region. The particular saturation profile depends on the conditions imposed away from the heterogeneity. If the location of the subcooled liquid boundary on the left is known, then integration occurs from left to right, and S_o, S_1 etc. can be determined sequentially. The reverse applies if it is the location of the dry region on the right which is known.

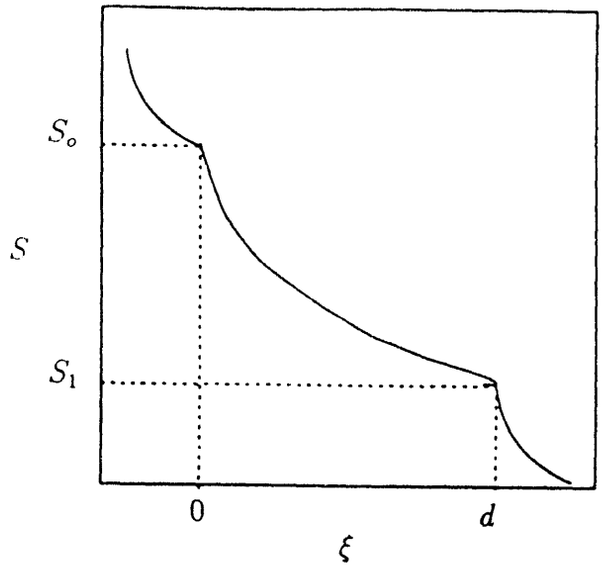

Figure 30: Schematic of saturation response for the profile of Figure 29a

Of special interest is the case of a sharp discontinuity ($a \gg 1$). Then, (44) yields:

$$\frac{J(S_1)}{J(S_o)} = \tau_+ = \sqrt{\frac{k_1}{k_o}} \tag{46}$$

which is nothing else but the condition of constant capillary pressure, implying a saturation jump across the discontinuity. This is the static (no flow) condition, which differs from the case $a < 0$, as shown below, as well as from the case of concurrent flow [147]. In the latter, a build-up of the wetting phase saturation is necessary before a high permeability region is entered.

2. $a < 0$ (*Figure 29b*)

While the previous are straightforward, non-trivial effects arise in the case of a permeability decrease. When $a < 0$, the denominator in (43) may vanish, if ω is small enough. For this to occur, the following equation must admit a real solution:

$$\omega = -a\ J \frac{k_{r\ell} k_{rv}}{k_{r\ell} + \beta k_{rv}} \tag{47}$$

The RHS of (47) is schematically plotted in Figure 31. We note that there exists a critical value,

$$\omega_{cr,H} = (-a) \max_S \left(\frac{J k_{r\ell} k_{rv}}{k_{r\ell} + \beta k_{rv}} \right) \tag{48}$$

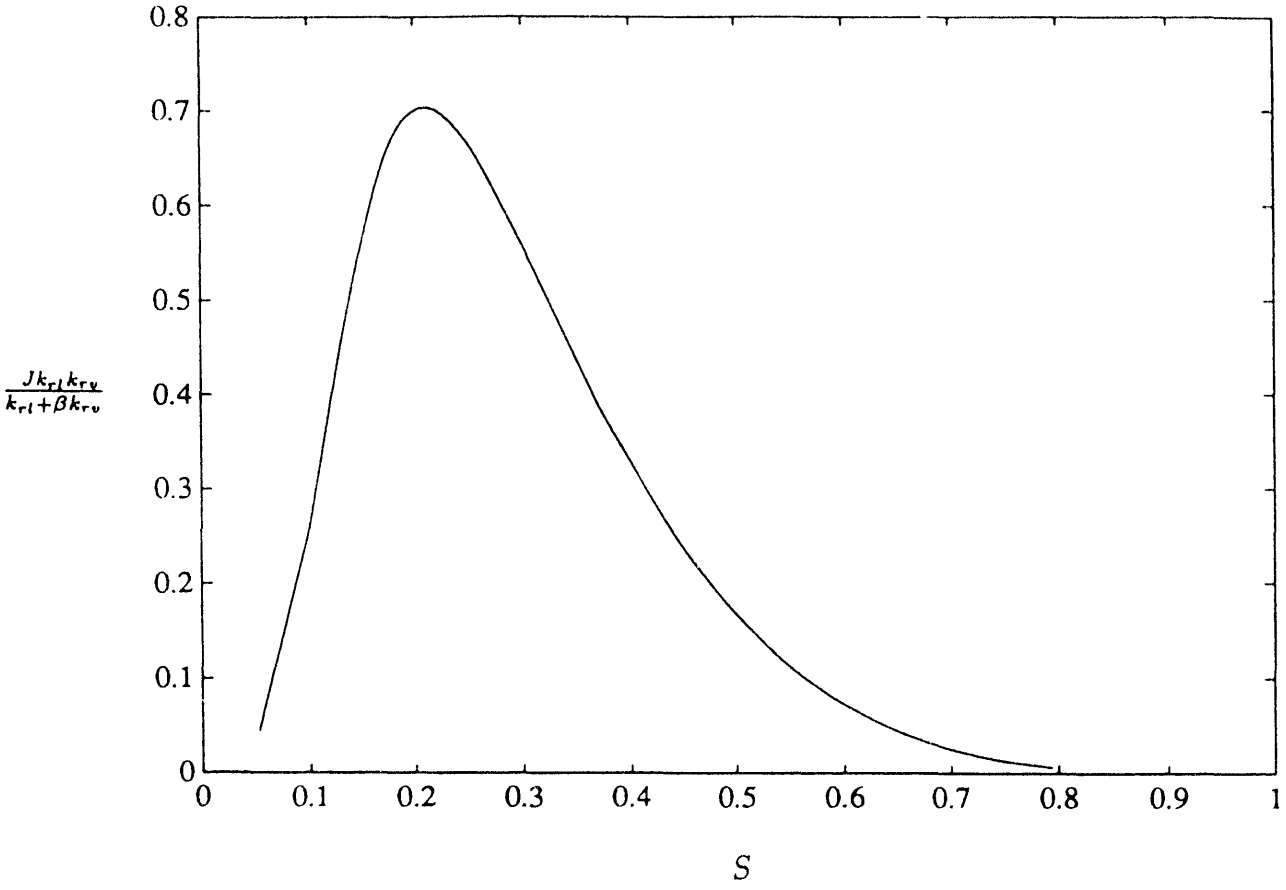

Figure 31: The capillary heterogeneity function $\omega(S)$

above which a real solution to (47) does not exist. In dimensional notation we obtain:

$$q_h \propto \frac{\sigma L_v \rho_v}{\mu_v}\left(-\frac{d\sqrt{k}}{dx}\right) \tag{49}$$

Thus, sharper changes in permeability result into larger critical flux values. The system response depends on the relative value of ω: (i) For $\omega > \omega_{cr,H}$, equation (47) has no solution. Then, the effect of heterogeneity is identical to the previous ($a > 0$), the solution being described by (42), (43) and (44), as schematically plotted in Figure 30. (ii) For $\omega < \omega_{cr,H}$, on the other hand, equation (47) has two roots, denoted by S_{VH} and S_{LH} ($0 < S_{VH} < S_{LH} < 1$), in very close analogy with the vapor-dominated and liquid-dominated regimes, respectively, of gravity-driven heat pipes. The similarity with the latter is very interesting. Indeed, as in heat pipes, the saturation integral diverges at the two saturations, thus nearly flat saturation profiles (either VD or LD) develop to span the region of heterogeneity. Here, however, it is capillary heterogeneity, with the permeability decreasing in the direction of liquid flow, and not gravity, that sustains the constant saturation profiles.

In retrospect, the analogy between capillary heterogeneity and gravity is not unexpected. In capillary-controlled displacements in pore networks, effects of either gravity or pore size heterogeneity can both be successfully described by the gradient percolation approach of [117]. In terms of continuum models, the analogy between capillary heterogeneity and gravity was noted in the concurrent flow study of [147]. In the latter case, however, the curve corresponding to $\omega(S)$ (which represented an augmented fractional flow curve) admits only one root, therefore there was stable attraction to a single root only. In [147], steady state saturation profiles were obtained by backwards integration starting from the outlet end (opposite to the flow direction), since the solution is ill-posed and rapidly diverges if integration started from the opposite end. In the present case of countercurrent flow, both sides can be used as starting points for the integration. As shown below, however, which end is taken is decisive on the selection of the particular solution. This was implicitly contained also in [91].

Consider, first, integration from the vapor side (Figure 32). This requires that superheated vapor exists somewhere on the right so that we may start integrating from the location $S = 0$ in the negative ξ direction. The saturation, S_1, reached when the heterogeneity is entered, $\xi = d$, dictates how the solution behaves inside the heterogeneity: - If $S_1 < S_{VH}$, then $dS/d\xi < 0$, and the solution is rapidly attracted to the asymptotic value S_{VH} (compare with (43)) as shown in Figure 32a. This is a vapor-dominated regime as in gravity-driven heat pipes. Outside the heterogeneity, $\xi < 0$, the

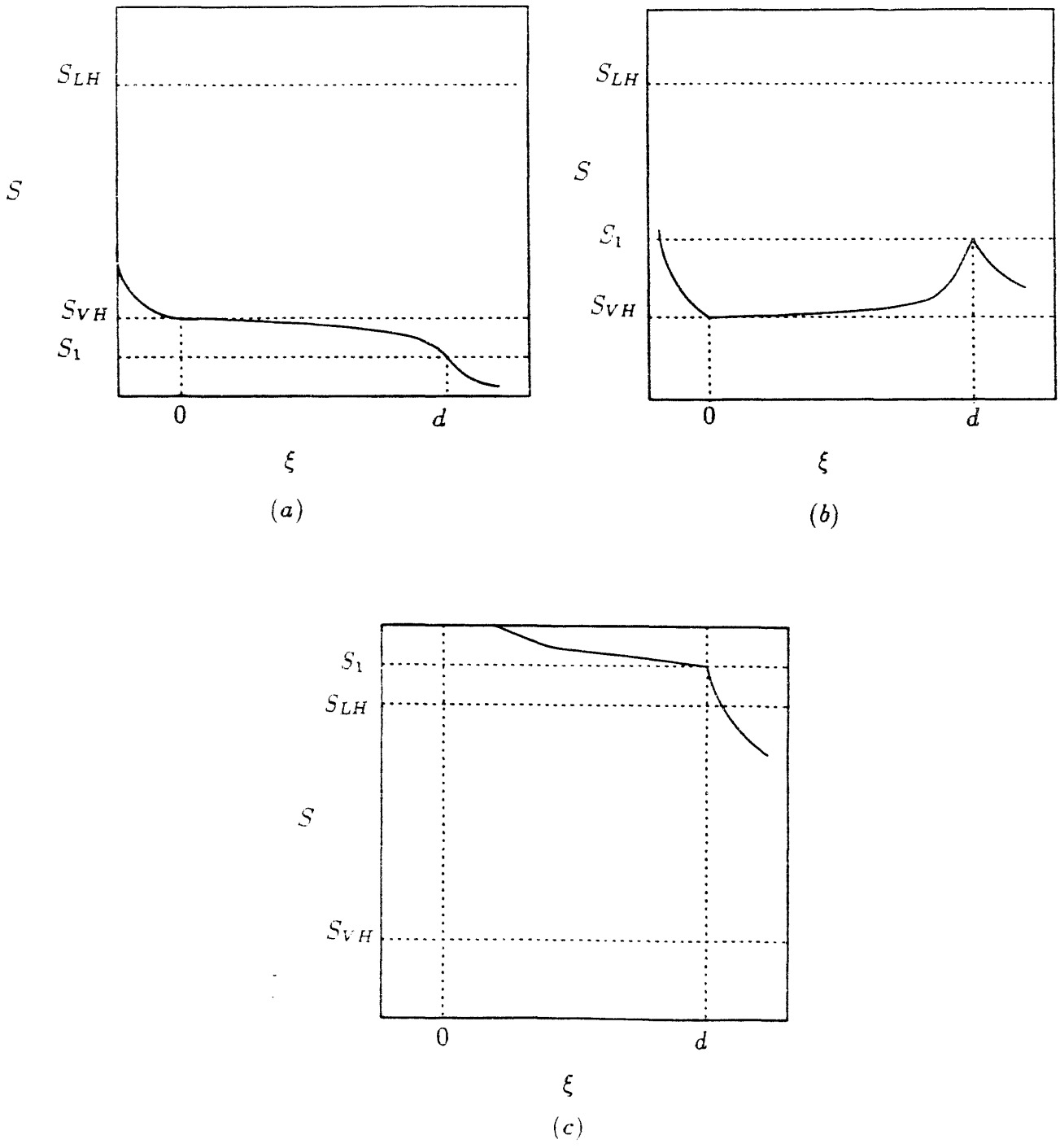

Figure 32: Saturation profiles for integration from right-to-left: (a) $S_1 < S_{VH}$; (b) $S_{VH} < S_1 < S_{LH}$; (c) $S_{LH} < S_1$

integration is straightforward:

$$\int_{S_{VH}}^{S} \frac{k_{r\ell} k_{rv} J' dS}{(k_{r\ell} + \beta k_{rv})} = \omega \xi \tag{50}$$

This solution applies until conditions of subcooled liquid are reached ($S = 1$). - If $S_{VH} < S_1 < S_{LH}$, then $dS/d\xi > 0$, and the solution is again asymptotic to S_{VH}, except that the saturation is now decreasing in the short region before the asymptote is reached (Figure 32b). - Finally, if $S_{LH} < S_1$, then $dS/d\xi < 0$, but the solution cannot be now attracted to a flat profile. The latter does not develop, instead the saturation is described with the previous equations (43)-(45), much like the case A.1 (Figure 32c).

Consider, next, integration from the liquid side. We assume that subcooled liquid exists somewhere on the left, such that we can proceed integrating from the location $S = 1$ in the positive direction. If we denote by S_o the saturation at $\xi = 0$, the following options are possible: - If $S_{LH} < S_o$, then $dS/d\xi < 0$, and the solution is attracted to the liquid-dominated regime with value S_{LH} (Figure 33a). After exiting the heterogeneity, further integration proceeds normally, much like in (50) until superheated vapor conditions are eventually reached ($S = 0$). - If $S_{VH} < S_o < S_{LH}$, then $dS/d\xi > 0$, and the solution is attracted to the same liquid-dominated asymptote, except that now the saturation increases in the short region before this asymptote is reached (Figure 33b). - Finally, if $S_o < S_{VH}$, then $dS/d\xi < 0$, but the solution is not attracted to a flat profile. Instead, it decreases relatively fast, much like in the homogeneous case (Figure 33c).

Thus, depending on the direction of integration, two different solutions (a VD and an LD) are found to satisfy the system. This feature is particular to vapor-liquid steady state counterflow. We contend that the selection of the particular paths (for example, whether it is the profiles in Figure 32 or those in Figure 33) is strictly determined from the past history of the system, which therefore attributes a hysteresis effect, albeit on a large scale [128]. The VD solutions of Figure 32 correspond to steady states reached by a system which is initially vapor-occupied and subsequently cooled from the left, while superheated conditions are maintained somewhere on the right. This is a condensation process (akin to imbibition). The LD solutions of Figure 33, on the other hand, correspond to steady states reached by an initially liquid-occupied system which is subsequently heated from the right, while subcooled conditions are maintained somewhere on the left. This corresponds to a boiling process (akin to drainage). Thus, the particular history imposed on the system decisively determines the final steady state. Hysteresis effects, but at the pore level, are

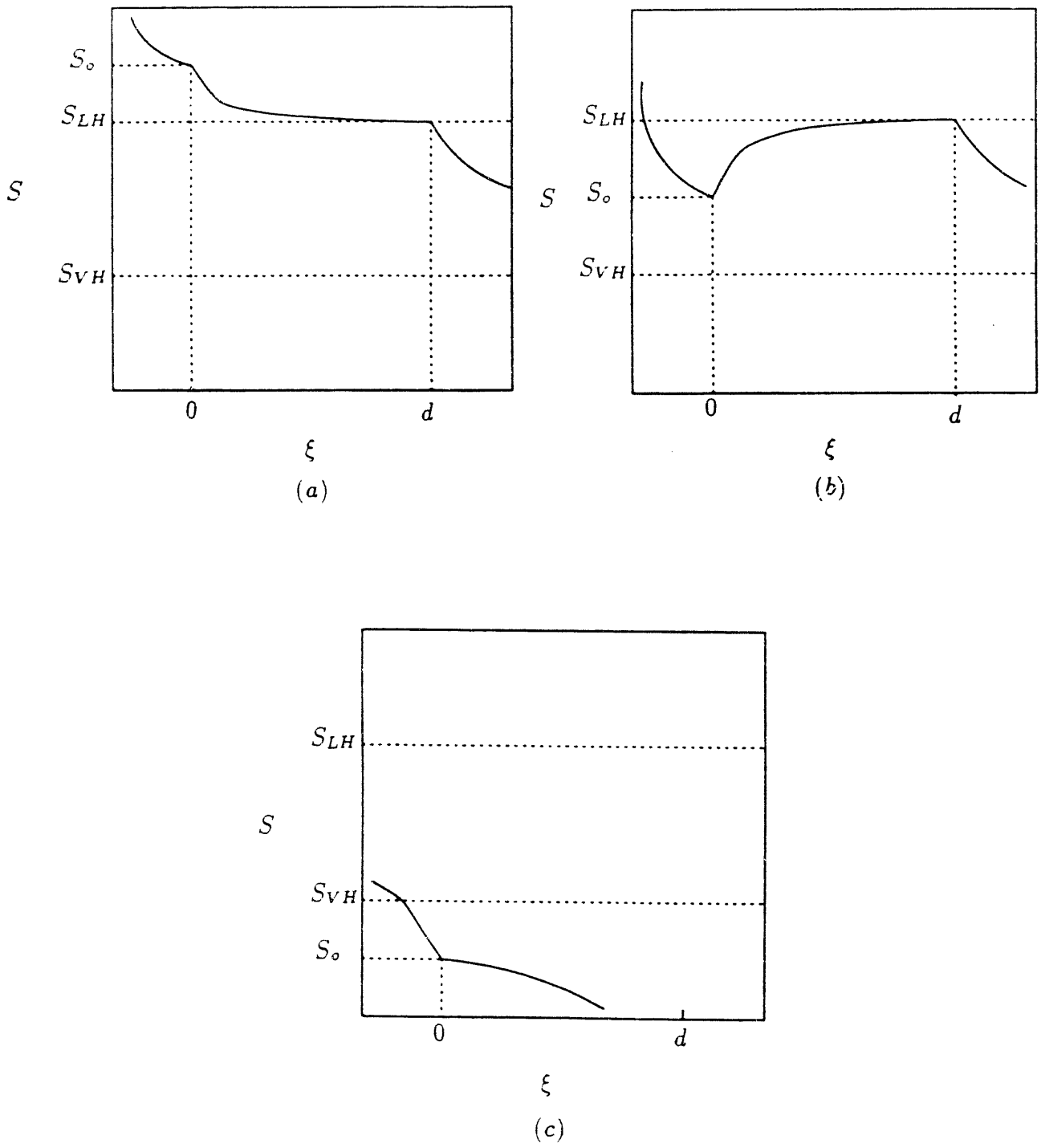

Figure 33: Saturation profiles for integration from left-to-right: (a) $S_{LH} < S_o$; (b) $S_{VH} < S_o < S_{LH}$; (c) $S_o < S_{VH}$

routine in typical displacement processes. For vapor-liquid counterflow, however, the hysteresis (evaporation - condensation) also involves large scale aspects (indeed, in the present work $k_{rv}, k_{r\ell}$ and J were taken invariant to direction).

Before we proceed further, it is worthwhile to consider the limit of a large discontinuity ($a < 0$ and $|a| \gg 1$). It is readily confirmed that in this case the two roots, S_V and S_L, approach the respective limits $S_V \to 0$ and $S_L \to 1$. Because of the latter, and in view of the previous analysis, singularities are not encountered, thus one may formally take the limit of (43) at large $|a|$. The result is the previous condition of capillary pressure continuity (46), provided that the predicted saturation value does not lie close to either of the two extremes, 0 or 1. Otherwise, the term $\omega(k_{r\ell} + \beta k_{rv})/k_{r\ell}k_{rv}$ can become comparable to $-aJ$ and the saturation jumps do not correspond to capillary pressure continuity alone (see also below). This behavior is different from both the $a > 0$ and the concurrent flow cases.

We close by noting that the above analysis also applies when the heterogeneity is slowly varying. As shown below, the solution is still a VD or LD branch, now of variable saturations. When the τ profiles are arbitrary, however, a numerical solution is necessary, as discussed later.

B. Vertical Counterflow

The above pertained to counterflow in the absence of gravity. We consider, next, the case of vertical counterflow (Figure 34). Here, two generic configurations are possible, heating from the top ($\theta = \pi/2$, $sin\theta > 0$), and heating from the bottom ($\theta = 3\pi/2$, $sin\theta < 0$). Because it is more commonly encountered, we address the bottom heating case first.

1. *Bottom Heating*

Under this condition, equation (39) yields:

$$\tau\, J' \frac{dS}{d\xi} = \omega \frac{(k_{r\ell} + \beta k_{rv})}{k_{r\ell}k_{rv}} - (\tau^2 - Ja) \tag{51}$$

where $a(\xi)$ is the heterogeneity gradient, $a \equiv d\tau/d\xi$. In the homogeneous case ($\tau \equiv const.$, $a \equiv 0$), the RHS above vanishes for the two saturation values S_{VG} and S_{LG} that solve the equation:

$$\omega = \frac{\tau^2 k_{r\ell}k_{rv}}{k_{r\ell} + \beta k_{rv}} \tag{52}$$

provided that $\omega < \omega_{cr,G}$. The critical value $\omega_{cr,G}$ is constant for a homogeneous system of a given permeability (e.g. equal to 0.3063 for $\tau = 1$, [136]). The two steady states of gravity-driven homogeneous heat pipes were investigated in [91], where a theory of heat pipe instability was developed.

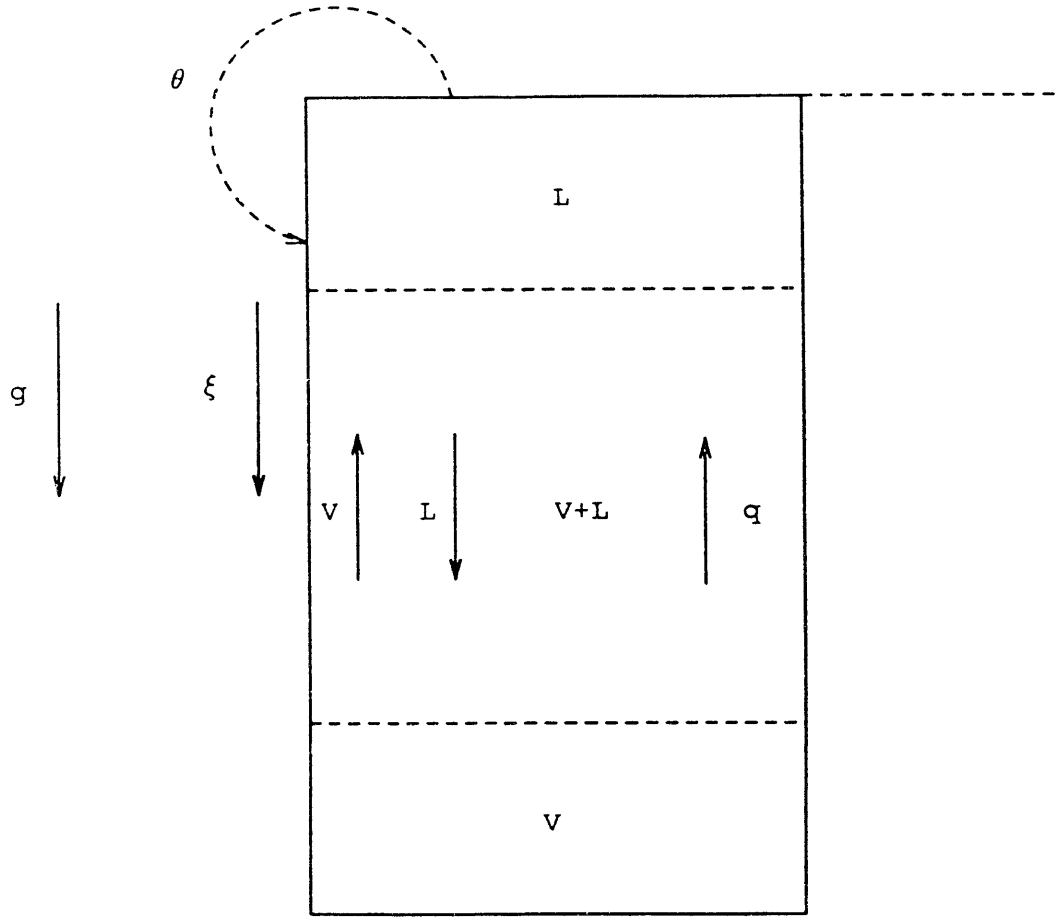

Figure 34: Schematic of vertical counterflow

We recall that an identical multiplicity was also encountered in heterogeneous, horizontal counterflow. Because of this similarity, we contend below that, in a strict sense, instability is not really relevant and that the selection mechanisms of the horizontal case are much more appropriate. The analysis follows closely the arguments for the horizontal case, except that the medium is now homogeneous. As in [91], a crucial role is played by the boundary conditions imposed. However, both here and in [128], these boundary conditions are related to the past history of the system.

(i) Homogeneous Systems : Steady State Selection

When the integration proceeds from the bottom (the "vapor side") upwards, it is the VD branch S_{VG} which is selected, if the starting saturation S_1 lies to the left of S_{LG}, $S_1 < S_{LG}$ (Figure 35a). This would be the case if superheated vapor existed somewhere below, as in the bottom curve of Figure 35a (note also that because of (46), any desired saturation value is possible as a starting point, see top curve of Figure 35a). In the interpretation of [128] this case could result from an initially superheated system that partly condenses due to top cooling. If $S_1 > S_{LG}$, on the other hand, a flat profile does not develop and the saturation rapidly converges to $S = 1$ (Figure 35b).

By contrast, when the integration proceeds from the top (the "liquid side") downwards, it is the LD branch, S_{LG}, which is selected, if the starting saturation S_o lies to the right of S_{VG}, $S_o > S_{VG}$ (Figure 35c). This is the case of subcooled liquid somewhere at the top, a typical application being boiling [128]. If $S_o < S_{VG}$, a flat profile does not develop, the saturation rapidly approaching the dry regime, $S = 0$ (Figure 35d). We readily conclude that it is the past history of the system that determines the steady state solution. Evidently, all such saturation profiles are intrinsically stable.

(ii) Sharp Discontinuity : Termination of an "Infinite" Two – Phase Zone

Next, we proceed with the discussion of effects of heterogeneity. For convenience, we consider first the special case of an abrupt discontinuity ($|a| \gg 1$). This analysis is necessary to explain how VD or LD saturation profiles can merge with subcooled liquid or superheated vapor, respectively, thus how an "infinite" two-phase zone can terminate in practice.

In the case of large $|a|$, the contribution of aJ on the RHS of (51) overwhelms that of τ^2. For this to occur requires:

$$|\Delta\tau/\Delta\xi| \gg \tau^2 \tag{53}$$

and, in dimensional notation,

$$|\Delta\sqrt{k}/\Delta x| \gg \Delta\rho\ g\ k/\sigma \equiv N_B \tag{54}$$

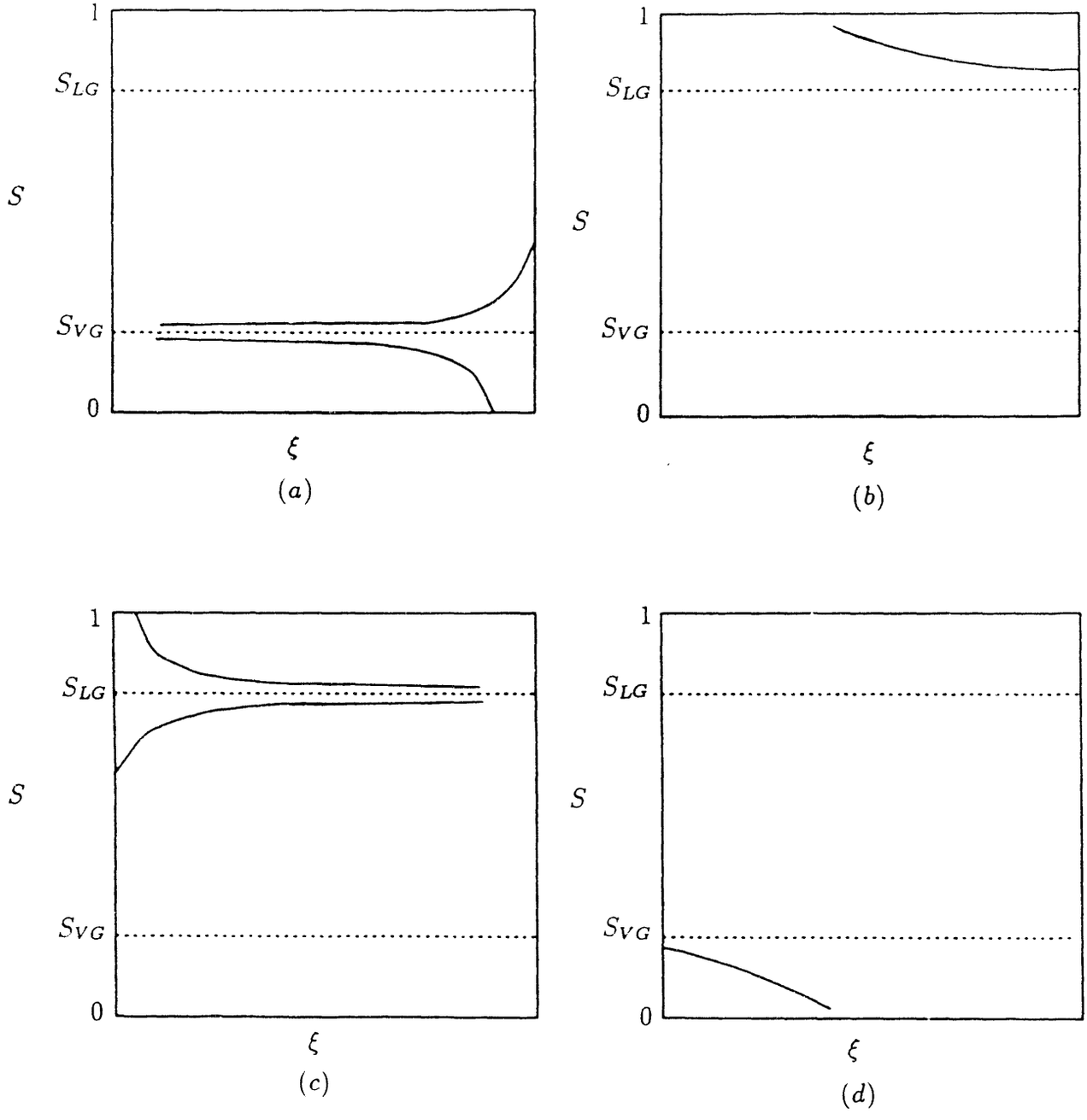

Figure 35: Steady-state selection in homogeneous heat pipes : (a) Integration upwards, $S_1 < S_{LG}$, (b) Integration upwards, $S_1 > S_{LG}$, (c) Integration downwards, $S_o > S_{VG}$, (d) Integration downwards, $S_o < S_{VG}$

where N_B is the Bond number. Although the latter is typically small, $O(10^{-6})$, one readily finds that enforcement of (54) requires large permeability variations over quite small distances. Subject to the following, this case is likely to represent continuity of capillary pressure. Thus, heterogeneity is much stronger than gravity and controls the saturation profile much like the horizontal counterflow of section A.

Consider, first, integration from the bottom within a constant permeability region (where $\omega < \omega_{cr,G}$). Then, a VD regime is rapidly reached. In a homogeneous medium this regime is predicted to continue indefinitely (although see [128] and [118]). Can this profile merge with another LD regime or with a region of subcooled liquid? The answer is negative to the first part, but not to the second. In either case, for a change in the saturation state, a region of low permeability k_t must exist somewhere at the top. Then, because a is positive and large, the response is much like in the horizontal case (46) and capillary pressure continuity applies. If k_t is such that ω remains below critical in the top (recall that $\omega_{cr,G}$ is proportional to τ^2 or k), the previous scenario (pertaining to Figures 35a-35b) is in effect and the solution is either another VD region or a rapid approach to subcooled liquid, depending on the particular conditions. On the other hand, if $\omega > \omega_{cr,G}$ at the top, only a finite two-phase zone develops that rapidly ends by merging with a subcooled liquid region.

If integration proceeds from the top (where $\omega < \omega_{cr,G}$), an LD region is rapidly approached. Again, for this flat profile to eventually change, and for a dry region to be eventually encountered, the bottom must be at a higher permeability. Since for this case we also have $a > 0$, we can employ the same reasoning as before to reach the conclusion that it is the scenario of Figures 35c-35d that is followed, namely there will be either an attraction to another LD solution or a relatively fast approach to superheated (dry) conditions.

A somewhat different way of stating the above is that in order to terminate a steady state vertical counterflow with $\theta = 3\pi/2$, it is necessary that the permeability increases somewhere in the downwards direction. If a VD region exists at the bottom, subcooled liquid dominates the top. And, if an LD region lies at the top, superheated vapor must exist at the bottom. Significantly, LD and VD branches never merge with each other, regardless of the position or form of heterogeneity. This contrasts some of the arguments of [91] in which an "unstable" VD regime becomes connected to a "stable" LD regime, and vice versa. Furthermore, if the change of permeability is in the

opposite direction ($a < 0$), capillary pressure continuity cannot bring a qualitative change in the saturation state. In this case, a VD regime would always remain vapor-dominated without reaching dryout, while an LD regime would always remain liquid-dominated, without reaching subcooled liquid conditions.

(iii) General Heterogeneity Effects

Consider, next, the more general case of heterogeneity, with normal variations in τ. Equation (51) suggests that heterogeneity enhances (makes more vapor-rich or liquid-rich) the respective VD or LD regimes when $a < 0$, and acts to diminish them in the opposite case. For concrete results, a numerical solution is necessary. For convenience, we used τ profiles that satisfy a correlated fractional Brownian motion (fBm) with $H = 0.8$, which appears to be the natural heterogeneity in many rocks [56]. Two cases were studied, a slow and a normal variation in heterogeneity, both in the unit spatial interval [0,1]. By a simple rescaling of the equations it can be readily shown that the first can be equivalently represented by a signal of the same variation as in the normal case except at much higher levels of τ.

This case of slow variation can also be analyzed asymptotically. We take $\tau \equiv \tau(\xi/\ell)$, where $\ell \gg 1$, and rescale the spatial variable using ℓ as the characteristic length, $\xi = \ell\zeta$, to obtain:

$$\frac{1}{\ell}\left(\frac{k_{r\ell}k_{rv}}{k_{r\ell}+\beta k_{rv}}\right)\left(J'\tau(\zeta)\frac{dS}{d\zeta} - J\frac{d\tau}{d\zeta}\right) = \omega - \frac{k_{r\ell}k_{rv}\tau^2(\zeta)}{k_{r\ell}+\beta k_{rv}} \tag{55}$$

For $\ell \gg 1$, the solution of the above is the saturation $S(\zeta)$ that makes the RHS vanish, thus representing a gravity driven process in a weakly heterogeneous medium. This is similar to homogeneous heat pipes, except that, because τ is now variable, there exists a continuum of curves similar to Figure 31, each for a fixed τ (or ζ). Their intersection with the line of constant ω defines a continuum of $S(\tau)$ values, which when plotted in a $S(\zeta)$ diagram give the solution to the problem. As before, there are two possible branches, a VD and an LD, to which the solution is always attracted (much like the cases in [118] and [100]). Again, VD and LD sequences are followed closely without the branches ever becoming intertwined. It follows, that given a direction of integration, there is a direct one-to-one correspondence between the heterogeneity τ and the saturation, S.

For a numerical example we used the profile of Figure 36a. Because here the combination $\tau^2 - aJ$ is always positive, it is possible for the RHS of (51) to vanish for all τ provided that ω is low enough ($\omega < \omega_{cr,min}$, where $\omega_{cr,min}$ must be obtained numerically). According to (55), the solution must follow closely the variation of τ^2, resulting into either an LD or a VD branch, depending on the

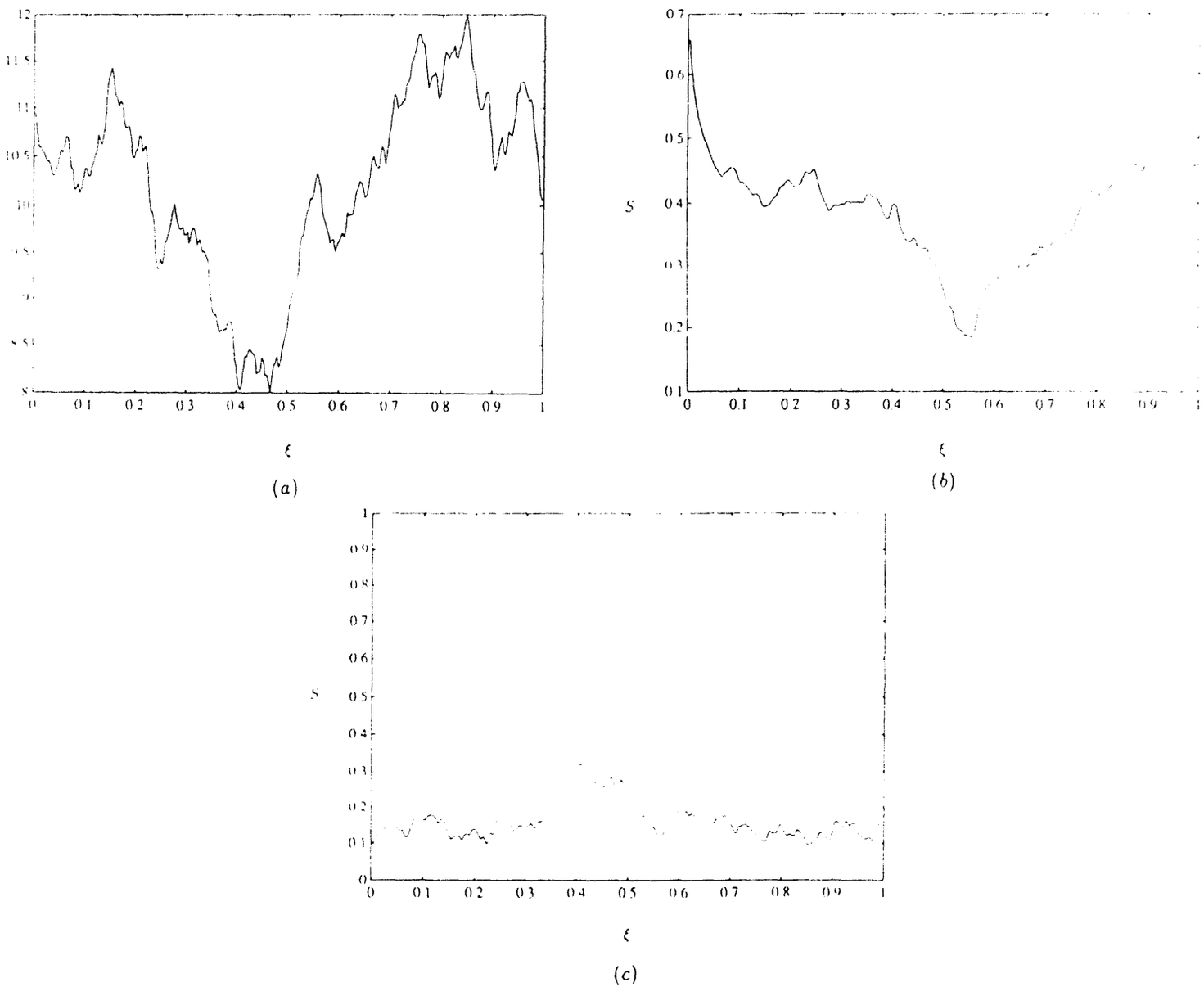

Figure 36: Weak heterogeneity (a) τ profile, (b) LD regime, $\omega = 23.0$, (c) VD regime, $\omega = 25.0$

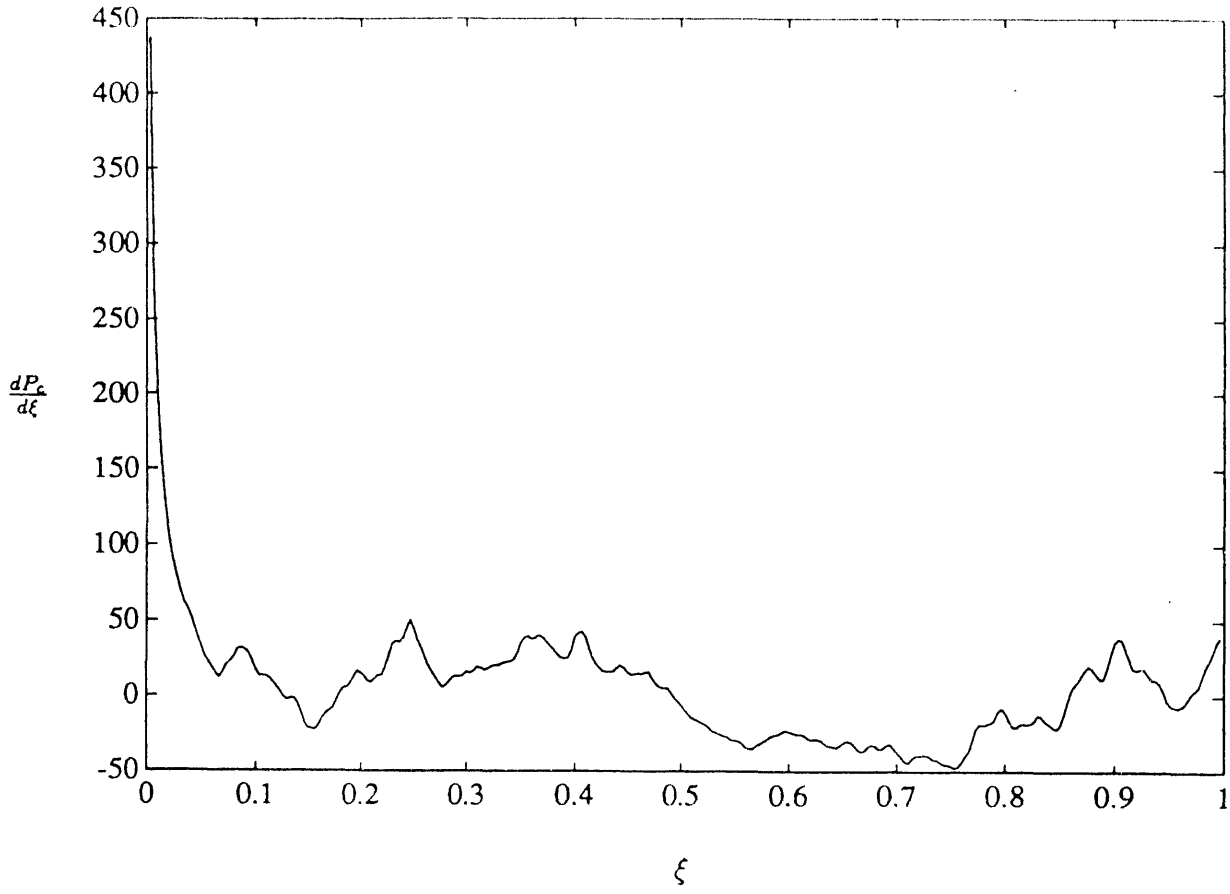

Figure 37: Capillary pressure gradient corresponding to Figure 36b

direction of integration. Numerical results shown in Figures 36b and 36c for the respective regimes verify the theoretical predictions. After a short interval, the profiles are attracted to this asymptotic state and, with a small spatial delay of about 0.05, mimic the variation of τ^2. The VD solution shows a weaker sensitivity due to the relatively narrower range of saturation values allowed. As predicted theoretically, saturations in the LD regime increase or decrease as τ increases or decreases, respectively, while the saturations in the VD regime follow opposite trends. Capillary effects are significant only near the initial boundary. The variation of the capillary pressure, corresponding to the LD state, provides a clear demonstration (Figure 37). Except near the initial boundary, where it is quite large, the capillary pressure gradient is small throughout, suggesting a gravity driven mechanism.

When the heat flux acquires larger values ($\omega > \omega_{cr,min}$), there are spatial locations where the local critical values may be exceeded ($\omega > \omega_{cr}(\xi)$). Then, the saturation departs from the corresponding regimes and becomes rapidly attracted to a single phase region (dryout in the case of an LD state, as in Figure 38a, or subcooled liquid in the case of a VD state, as in Figure 38b). On the opposite side, for very low values of ω, as is typical in geothermal reservoirs, all saturation values in the VD regime are very low, hence the profile is very nearly flat, (Figure 39), despite the variation in permeability. It is clear that the existence of a flat profile should not be taken to imply a homogeneous medium.

The second case investigated corresponds to a normal variation of τ (Figure 40a). Here, the combination $\tau^2 - aJ$ changes sign often within the interval. The solution displays hysteresis again, depending on the direction of integration. However, now capillary effects are quite significant and the one-to-one correspondence with $\tau(\zeta)$ is not obeyed. In fact, for relatively steep increases in τ, capillary pressure continuity may be in effect, as discussed above, resulting in lower saturation values. For an LD state this is contrary to the gravity effect noted in the previous. Consider, for instance, integration from the left, where an LD regime is obtained provided that ω is low enough (Figure 40b). As long as the τ variations are not too great, the saturation values are relatively constant (early part of Figure 40b). The saturation variation is mild even though regions of relative large increase in τ are traversed. This behavior is similar to the horizontal counterflow for a negative and large. At the point where a sharp increase is encountered and a becomes large (around the mid-point of Figure 40a), capillarity dominates, capillary pressure continuity is enforced and the saturation falls significantly. If the drop is not too high, a lower saturation state, still of the VD type, will be followed in the remaining part.

Under the same conditions in ω, a VD regime arises, when the integration is from the right (Figure 40c). The first part of the profile (for ξ roughly between 0.5 and 1) corresponds to heterogeneity with generally positive slope ($a > 0$), thus capillary pressure continuity applies, the saturation rising as lower permeabilities are encountered. The second part of the heterogeneity, however, involves a rather steep negative slope (between 0.15 and 0.4). As pointed out previously, the saturation response may not be given by capillary pressure continuity alone. Indeed, after the saturation falls rapidly (for ξ between 0.3 and 0.4), further large changes in permeability do not induce significant saturation response. This interpretation is supported from the variation of the

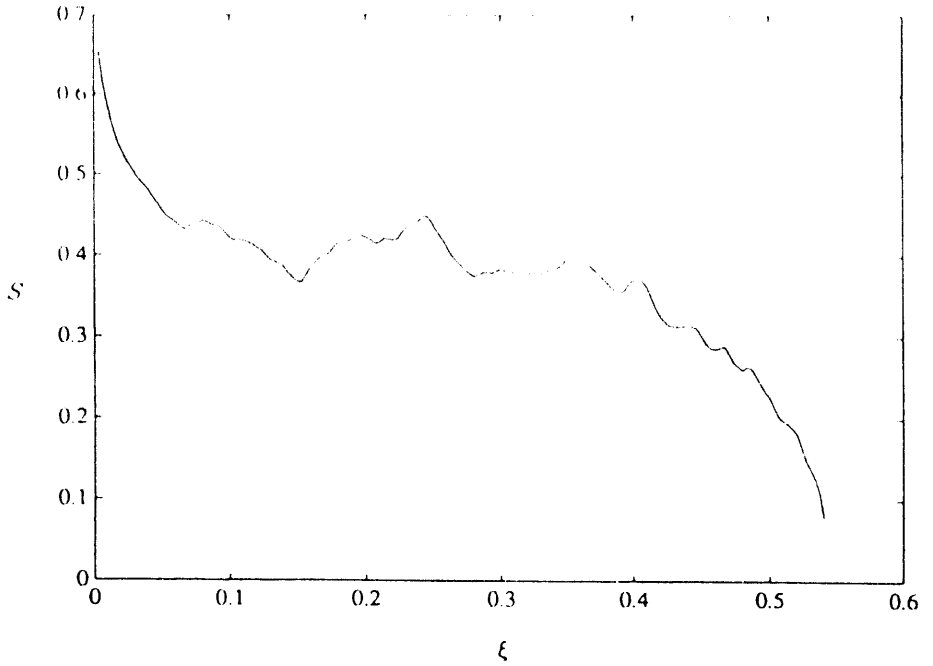

(a)

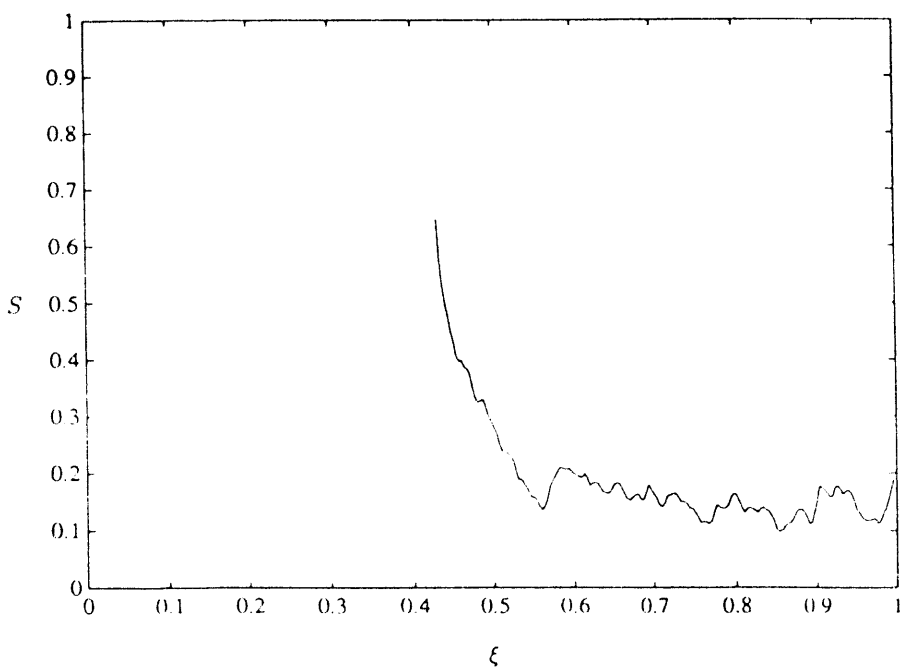

(b)

Figure 38: Weak heterogeneity for larger heat fluxes: (a) LD regime, $\omega = 24.0$, (b) VD regime, $\omega = 28.0$

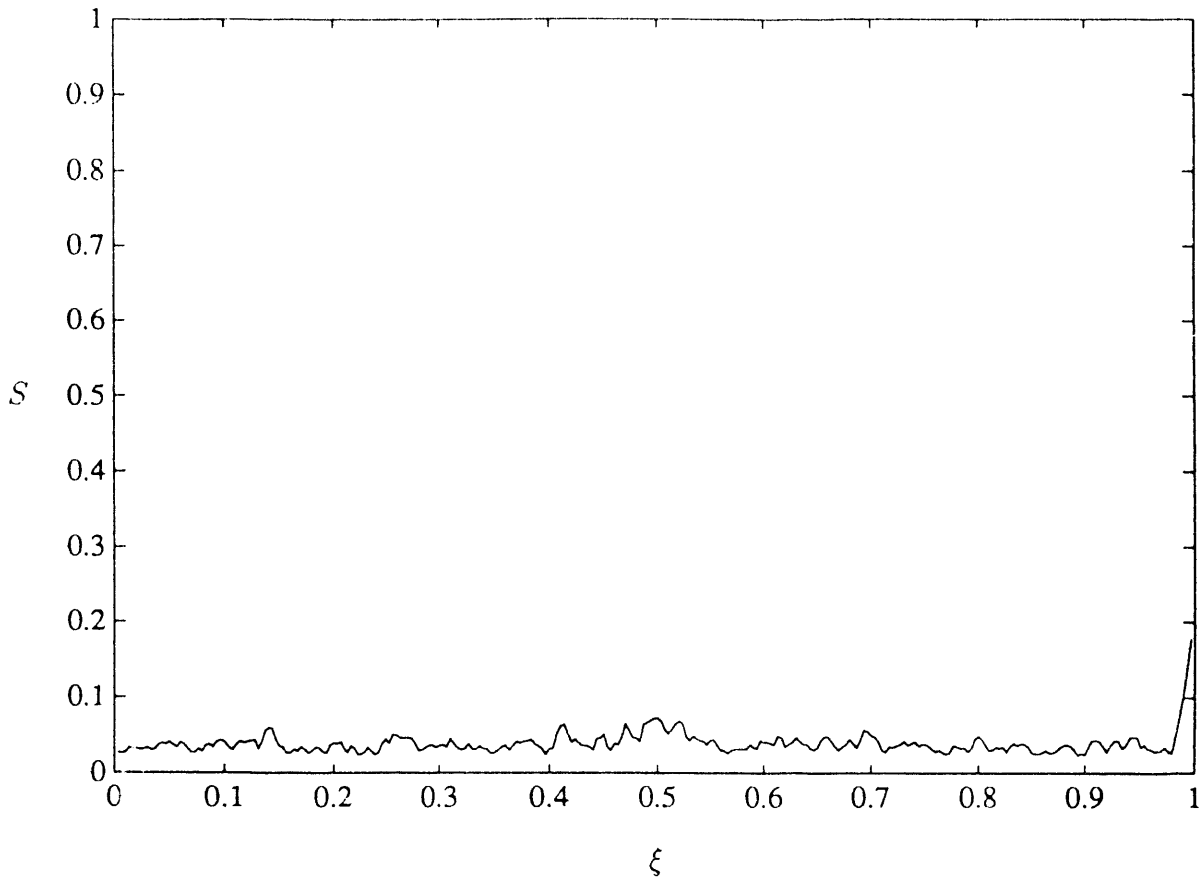

Figure 39: The VD regime corresponding to Figure 36a for $\omega = 0.6$

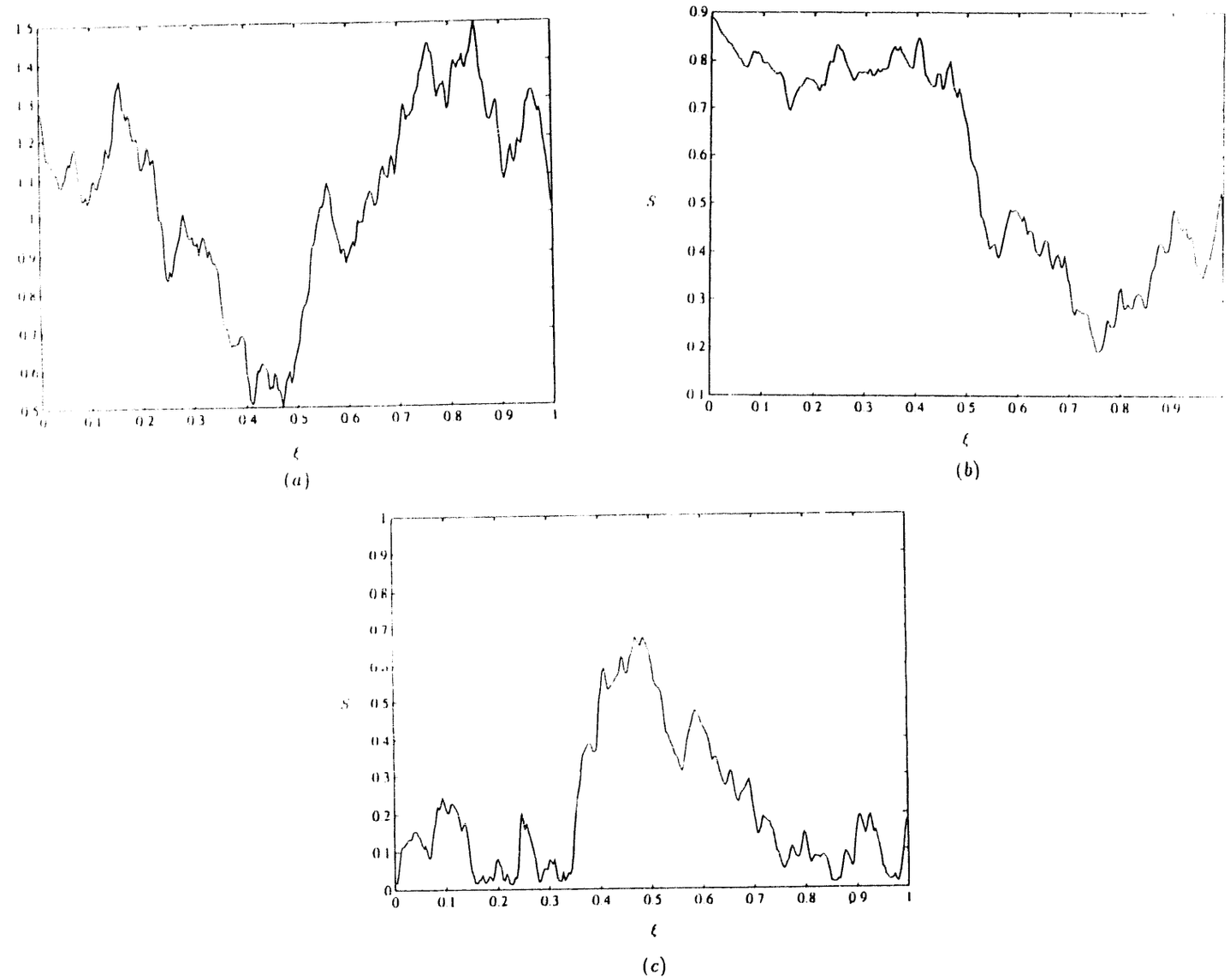

Figure 40: Normal heterogeneity: (a) τ profile, (b) LD regime, $\omega = 0.02$, (c) VD regime, $\omega = 0.02$

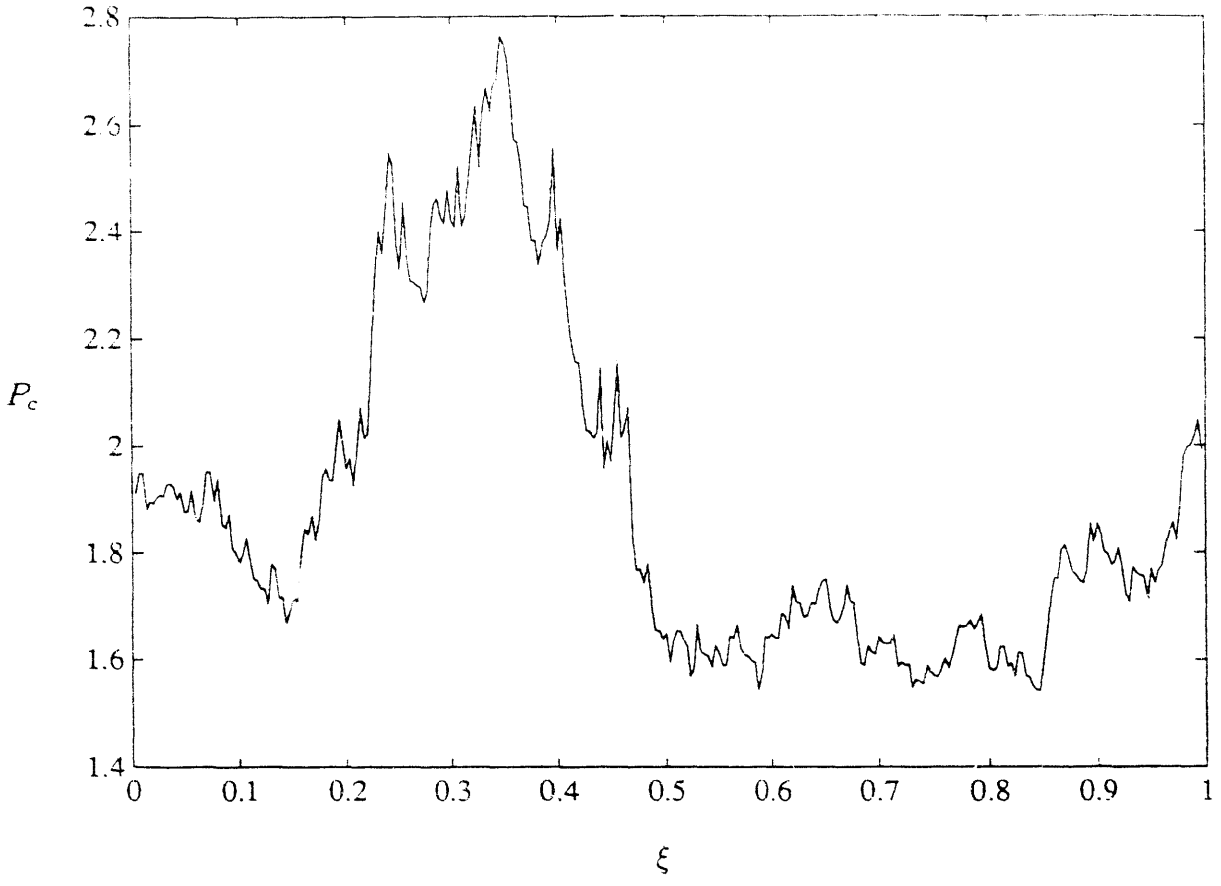

Figure 41: Capillary pressure corresponding to Figure 40a

capillary pressure (Figure 41), where the regime of capillary pressure continuity at the right half of the interval is evident. When the heat flux increases, a transition to single phase regions is possible, the LD or VD states reaching dryout (Figure 42a) or subcooled liquid (Figure 42b), respectively, in a short region. This first occurs near the location with the highest positive slope in τ (mid-point of the ξ interval). We emphasize again that no transition from an LD to a VD state or vice versa was noted, while the two regimes maintain their identity in regions of τ decreases, no matter how sharp the latter are.

2. *Top Heating*

We close by briefly noting that similar results are obtained for the case of top heating ($sin\theta = 1$).

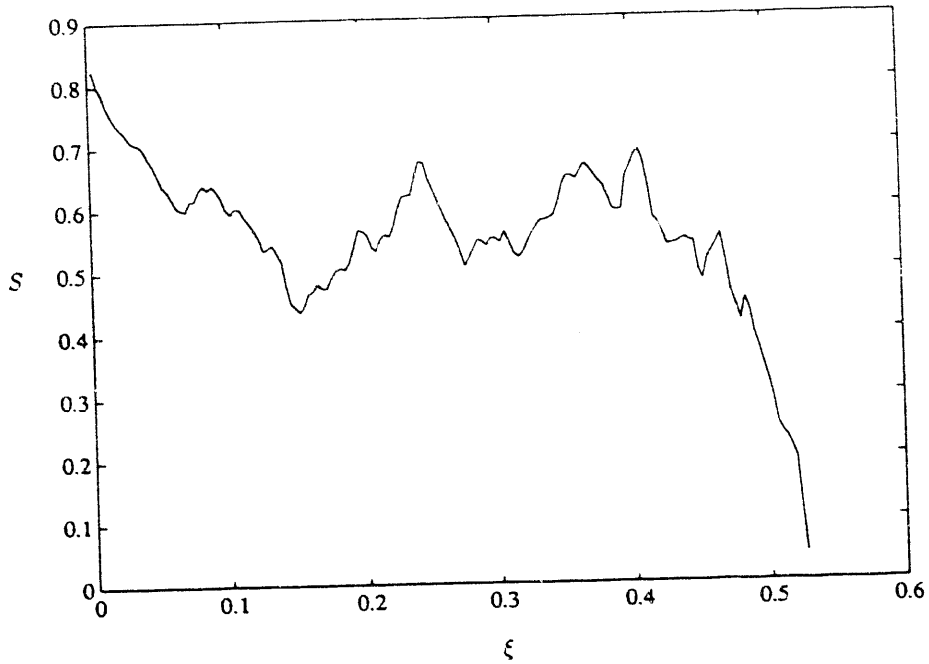

(a)

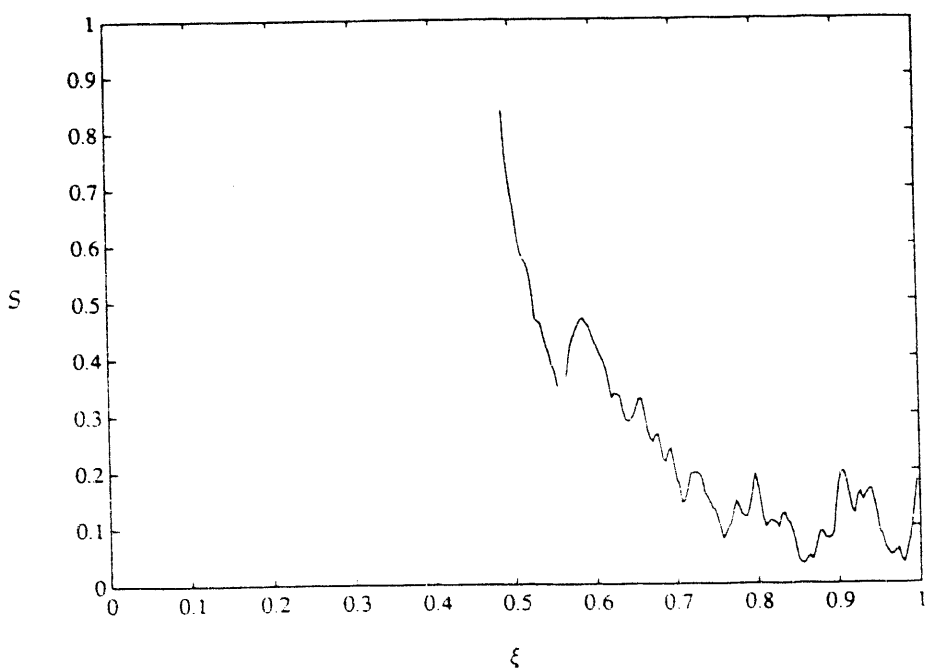

(b)

Figure 42: Normal heterogeneity for larger heat fluxes: (a) LD regime, $\omega = 0.2$, (b) VD regime, $\omega = 0.2$

Now, equation (39) yields:

$$\tau\ J'\frac{dS}{d\xi} = \omega\frac{k_{rl} + 3k_{rv}}{k_{rl}k_{rv}} + (\tau^2 + Ja) \tag{56}$$

For $a > 0$, then $dS/d\xi < 0$ throughout, and the solution follows in a straightforward fashion. Likewise, a monotonic profile (quite similar to the horizontal case) is obtained for $a < 0$ and sufficiently large ω. If the latter is low enough, however, the heterogeneity may lead to gravity-like VD and LD regimes, much like in the horizontal case. The various subcases were exhaustively treated, and we shall not elaborate further.

4.3 CONCLUSIONS

Within the framework of a continuum description, effects of permeability heterogeneity on steady state, vapor-liquid counterflow in porous media were examined. Permeability variations affect mainly two processes, gravity-driven flow and capillarity. The variations of the latter can be significant. It was shown that, as in similar previous flows [147], capillary heterogeneity acts like an external body force (such as gravity), with the additional property that it also varies spatially. For example, a multiplicity of steady states similar to gravity-driven heat pipes was found for decreasing permeabilities in horizontal counterflow and for heat fluxes lower than a critical value. Vapor-dominated and liquid-dominated regimes were obtained using selection rules that were postulated to depend on the past history (transient state) of the system. The analysis was aided by an exact solution obtained for a special heterogeneity profile.

The selection rules were next applied to determine the steady state regimes in gravity-driven heat pipes in homogeneous systems. It was shown that VD regimes originate from underlying dry regions, while LD regimes are extensions of overlying subcooled liquid regions. Significantly, the different regimes may never connect with each other, thus retaining their identity as long as the system remains in a two-phase state. The issue of the termination of the infinite two-phase zone was next analyzed. It was determined that termination requires that a sharp increase in the permeability (in the direction of increasing depth) occurs somewhere in the medium. Across this discontinuity it was shown that, depending on past history, either the overlying LD state rapidly connects with a dry region below, or the underlying VD state rapidly converts to a subcooled liquid above. The emerging picture (from top-to-bottom) is thus, subcooled liquid - LD - (discontinuity) - dry region, or subcooled liquid - (discontinuity) - VD - dry region, in the respective cases. This ordering may

be helpful in the interpretation of the nature and origin of geothermal systems. Unfortunately, this argument cannot apply for homogeneous systems, the termination of an "infinite" two-phase zone within which remains an unresolved question.

Finally, the interplay of gravity and capillarity was demonstrated in a study of two different heterogeneity modes, a slow and a normal variation. For heterogeneities that vary on a large scale, the effect is mainly on the gravity component and the saturation response closely follows the permeability variation depending, of course, on heat flux values. On the other hand, larger variations in permeability induce significant capillary effects. Often, capillary pressure continuity must be enforced, particularly for large increases in the direction of liquid flow (here, as depth increases). In contrast to both static and concurrent flow systems, capillary pressure continuity is not necessarily the condition for a decrease in prmeability, no matter how large the latter is. All these effects attribute a significant large scale hysteresis on the saturation profiles.

5 VISUALIZATION OF IMMISCIBLE DISPLACEMENT IN MICROMODEL FRACTURED SYSTEMS

M.Haghighi and Y.C. Yortsos

5.1 INTRODUCTION

Steam injection is a potentially effective method for the recovery of heavy oil from reservoirs. This is particularly important for the diatomite formations of California, which contain significant deposits of heavy oil. Unfortunately, the understanding of steam injection in fractured systems is currently based mostly on phenomenology and typically consists of applying a double porosity formalism to steam simulators. Most of these simulators use capillary imbibition as a mechanism for the exchange of fluids between the matrix blocks and the fracture network. Such a purely numerical approach offers little to further our insight into the process. A reasonable alternative is experimental studies in model geometries that mimic fractured systems, particularly good candidates of which are glass micromodels. Such a special geometry is considered in this research. The ultimate objective is to conduct steam injection experiments in these models. Unfortunately, the actual mechanisms even for isothermal displacement are not well known. Indeed, we have realized that studies even for ordinary immiscible displacement in such systems have been very limited, the understanding of the basic flow mechanisms being rather poor at present even for imbibition. Thus, before attempting to understand the more complicated case of steam injection, it was decided to experiment with the simpler, but yet unclarified, case of immiscible, isothermal displacement.

Consider the waterflooding of naturally fractured systems. Significant early work in the subject was done by Mattax and Kyte [88] who studied imbibition in fractured water-drive reservoirs. These authors experimented with a single matrix block and introduced the concept of a "critical rate" in connection with water advance in fractured-matrix reservoirs. The critical rate was defined as that for which the water advance level in the fracture is the same to the water level in the matrix. For rates less than the critical value, the water level in the matrix is above that in the fractures. Thus, all the recoverable oil will be displaced from the matrix block before the water in the fractures reaches the top of the block. Inversely, at rates greater than the critical value, the water level in the fracture will move ahead of the water in the matrix and the matrix block will be completely surrounded by water before imbibition is completed. In the first visualization study in fractured

systems, Handy and Datta [54] provided visual evidence of water imbibing in an artificially-fractured sandstone and in a heterogeneous sand pack. In the case of fractured sandstone, they observed that the water moves preferentially through the fracture, due to the low capillary pressure , while in the heterogeneous sand pack water imbibes into the fine sand because of capillary forces stronger than in the coarse sand. As rates increased, the water was seen to move preferentially through the more permeable regions.

Flow visualization is a valuable device that enables us to understand some of the complex pore level mechanisms of multiphase flow in porous media, can confirm theories and upgrade computer simulation. This is the reason why substantial efforts have been undertaken not only for fluid flow during immiscible displacement [87, 137], but also for solution gas drive [31], gravity drainage [143], and many EOR processes, such as foam flow [86] and surfactant and polymer flooding [32]. Although observing fluid flow in a single capillary tube or doublets is very useful, especially for the study of wetting phenomena [17], these tools are too simple to mimic the complex structure of capillary channels in real porous media. Therefore, investigators have been continously searching for models with closer similarity to porous media. Chatenever and Calhoun [24] were pioneers in this area by making a single layer of glass and/or lucite spheres between plates. This kind of model in general lacks the ability to show the process of individual interfaces in different geometries. Then, etched glass micromodels came into existence, in which interconnections between pore/throats were introduced. The history of the fabrication of micromodels has been reviewed by Buckley [19]. In spite of the fact that such micromodels are restricted to two dimensions, they have been very useful in understanding the complex relationship between the geometry and topology of the medium and the solid/fluid interactions [26, 79, 81, 82].

The majority of investigations so far was limited to replicas of porous media. To our knowledge a systematic study has not been undertaken for network patterns having fractures along or across the flow direction to study effects of high permeability avenues in the fluid distribution during displacement. As a result, we do not have sufficient knowlege regarding the true mechanisms of capillary imbibition for oil recovery in fractured reservoirs. Furthermore, the role of fracture in fluid distribution and the relationship between fluid/solid interactions and flow parameters are ripe subjects for visualization investigations. These issues are discussed in this chapter. Our general objective is to provide a better insight on the recovery mechanisms in naturally fractured

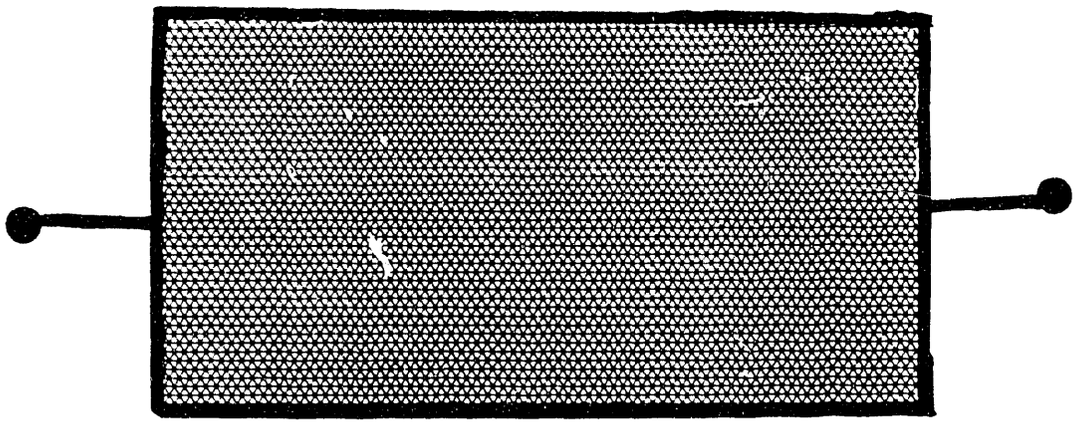

Figure 43: The pore network and fracture pattern

reservoirs during immiscible displacements, in order to improve oil recovery from such reservoirs. To achieve this goal, pore level and larger scale visualization of isothermal immiscible displacement under various conditions (drainage, imbibition, and secondary imbibition) was performed in a glass micromodel of a fracture-like structure, and a parametric experimental study of the effects of capillary number and mobility ratio was undertaken.

5.2 EXPERIMENTS

The construction of the glass micromodel in our work is basically the same as that reported in our previous DOE Report. In addition, some modifications were also implemented suitable to our material. The first pattern we used was a 3″ × 5″ inch 2 uniform triangular network with a coordination number of 6 as a matrix block and a 2 mm width strip all around the matrix as a fracture system to mimic a single matrix-fracture block (Figure 43). The width of the network channels is approximately 400 microns while the pores (region where three lines cross each other) have a linear size of about 800 microns. Inlet and outlet ports were connected to the fractures. We have employed several computer generated patterns with different pore and throat size distributions. In all these, the fracture is represented by a large size strip in the middle of the model along the

main flow direction. In recent models we have included two fractures, one along the main flow direction and another across the main flow direction. With this type of fracture configuration, the roles of direction of the fracture in the displacement process and the fluid distribution can be studied.

To estimate flow velocity in the model, which is needed for determining the capillary number, the measured volumetric rate was divided by the total cross sectional area (pore volume, 0.77 cc, divided by the length of the network, 12.7 cm). All experiments were carried out at constant rate by the use of a syringe pump.

5.3 RESULTS

So far we have carried out the following three different sequences of fluid injection into the micro-model:

1- Primary drainage

2- Primary imbibition

3- Secondary imbibition

For each displacement mode, a set of runs were made at different values of the mobility ratio and the capillary number. The objective was to probe the N_{ca}, M phase space in order to identify operating mechanisms and various aspects of the phase diagram. The various conditions employed are shown in Tables 2, 3 and 4.

5.3.1 Primary Imbibition

Systematic primary imbibition experiments were so far done only for the air-water pair. Methylene Blue water was the wetting phase. The non-wetting phase consisted of air or kerosene or viscous mineral oil in the respective experiments. For each fluid, displacements were carried out at four different capillary numbers (Table 2). However, with water displacing air, and for a capillary number lower than 10^{-5}, the water invaded the matrix first. At the pore level, both in the inlet of the model and in the matrix, two different and simultaneous mechanisms were clearly observed: 1- Water flow along the roughness of the walls. 2- Meniscus movement (Figure 44).

In the pore network, the movement of water along the pore surface roughness causes accumulation on the walls. As a result, we subsequently observed two different mechanisms: 1- When

Fluid Pair	Displacing Fluid Viscosity (cP)	Mobility Ratio	Volumetric Rate (cc/min)	Capillary Number
Water-Air	1	0.018	0.00052	2×10^{-8}
"	"	"	0.0052	2×10^{-7}
"	"	"	0.052	2×10^{-6}
"	"	"	0.52	2×10^{-5}
Water-Oil	1	"	0.00052	4×10^{-8}
"	"	1.50	0.0052	4×10^{-7}
"	"	"	0.052	4×10^{-6}
"	"	"	0.52	4×10^{-5}
Water-Oil	1	100	0.00052	4×10^{-8}
"	"	"	0.0052	4×10^{-7}
"	"	"	0.052	4×10^{-6}
"	"	"	0.52	4×10^{-5}

Table 2: Conditions for various primary imbibition experiments.

sufficient accumulation of water on the wall develops, the radius of curvature of the meniscus increases, touches the wall, and pore and adjacent channel are invaded instantaneously. 2- When there is sufficient accumulation of water on the two walls of a channel, only the channel is filled. At capillary numbers below 2×10^{-8}, both mechanisms were at work (Figure 45), resulting into a rough shaped front (Figure 46). However, at capillary numbers above 2×10^{-7}, only the first mechanism is operating and no channel filling was observed. The water invaded the network in a frontal movement that proceed line by line (Figure 47). Both these mechanisms are in agreement with earlier studies [76].

Experiments with water displacing kerosene and viscous mineral oil are currently in progress. While the water-air experiments showed indeed that the wetting phase preferentially invades the matrix block, it is not at all clear that the same will be observed during a water-oil primary imbibition.

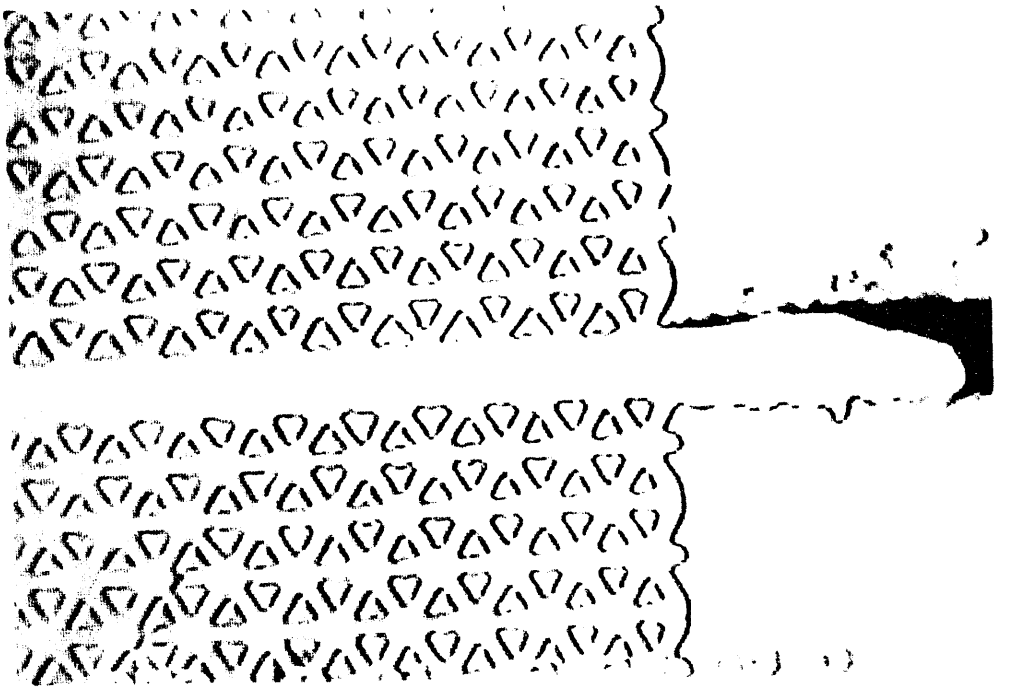

Figure 44: Primary imbibition (water-air) showing roughness flow.

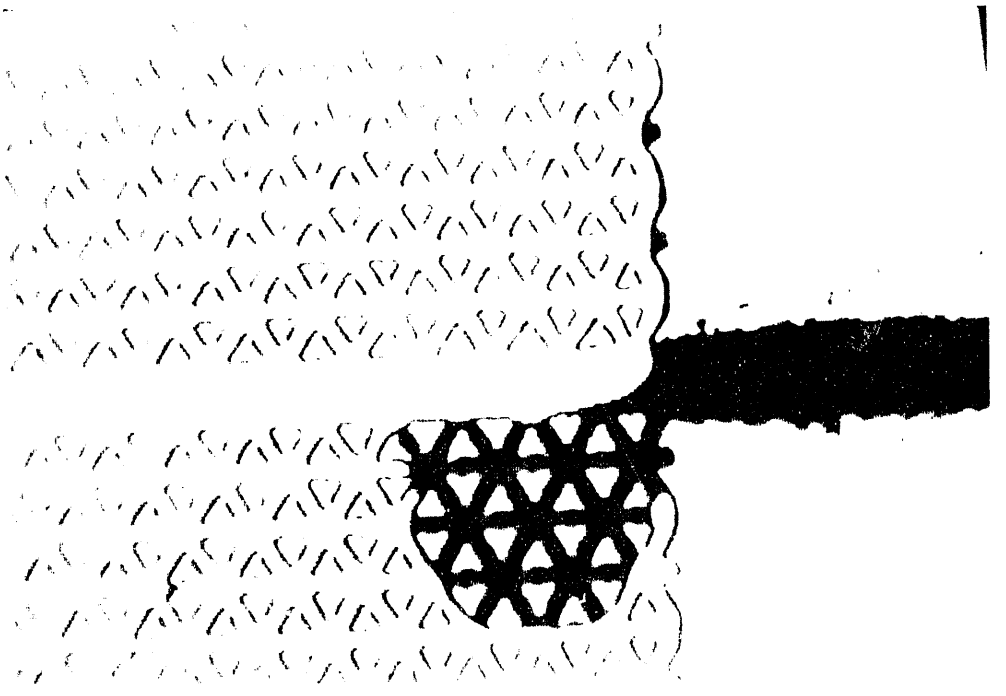

Figure 45: Primary imbibition (water-air) at $N_{ca} = 2 \times 10^{-8}$, showing both pore invasion and channel filling.

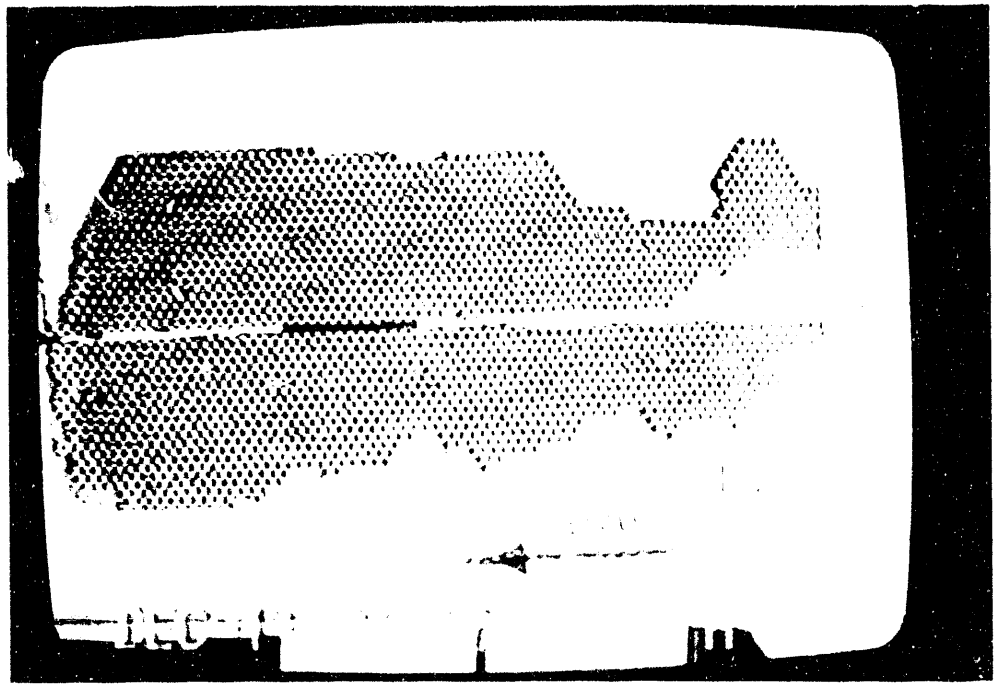

Figure 46: Primary imbibition (water-air) at $N_{ca} = 10^{-8}$, showing a rough shape of the displacement front.

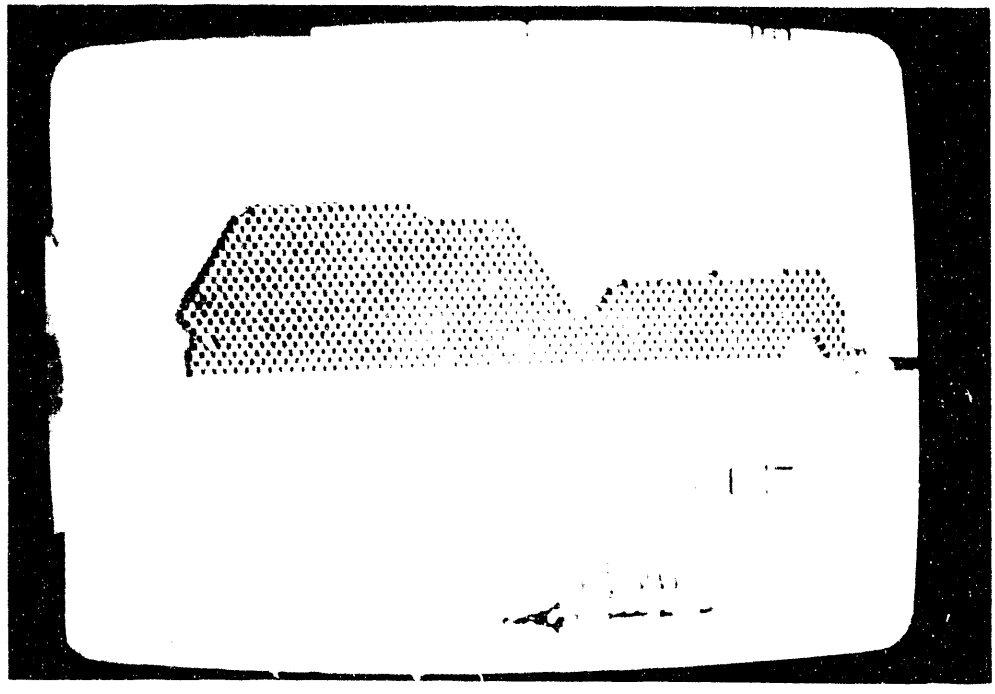

Figure 47: Primary imbibition (water-air) at $N_{ca} = 10^{-7}$, showing a flat shape of the front.

Fluid Pair	Displacing Fluid Viscosity (cp)	Mobility Ratio	Volumetric Rate (cc/min)	Capillary Number
Air-Water	0.018	55.56	0.00052	3.6×10^{-10}
"	"	"	0.052	3.6×10^{-8}
"	"	"	5.2	3.6×10^{-6}
"	"	"	40	2.8×10^{-5}
Oil-Water	1.5	0.66	0.0027	3.2×10^{-7}
"	"	"	0.054	6.3×10^{-6}
"	"	"	0.108	1.2×10^{-5}
"	"	"	0.27	3.2×10^{-5}
Oil-Water	100	100	0.0052	4.1×10^{-5}

Table 3: Conditions of various primary drainage experiments.

5.3.2 Primary Drainage

In the second set of experiments we considered primary drainage processes. In this case, the model was first saturated with water as follows. The micromodel was held vertically and water dyed with Methylene Blue was introduced through a plastic tube connected to the model inlet using a constant rate syringe pump. The flow rate was set at a very low value to completely saturate the model. Then, the model was placed horizontally for the displacement experiment to be conducted. A video camera with a close-up kit provided the desired visualization. A total of 12 runs, corresponding to three different mobility ratio values, each for four different capillary numbers were conducted (Table 3). The front movement was also recorded under a microscope for clearer visualization. In the first set of experiments, with air displacing water, for capillary numbers lower than 10^{-6}, air moves through the fracture only (Figures 48 and 49). When the flow rate is increased to 5.2 cc/min, however, where there is enough pressure to overcome the capillary threshold, air starts to also invade the matrix (Figure 50). Figure 51 shows air-water displacement at a capillary number of 2.8×10^{-5}. In this case, air moves to the fracture first, but subsequently displaces water in the network as well. The displacement has the ramified form characteristics of a percolation process. These experiments illustrate the competition between capillary and viscous forces in the fracture

and in the matrix.

Figures 52 through 55 show the displacement of water by kerosene. For capillary numbers lower than 10^{-6}, oil is shown to enter the fracture only (Figure 52). This is consistent with the previous observations. Likewise, at higher rates, oil moves to the fracture first, but after sufficient viscous pressure drop develops, the capillary threshold is exceeded and oil starts to invade the matrix as well (Figures 53 and 54). The matrix is first invaded upstream and the displaced water moves towards the fracture downstream. After oil breakthrough, the invasion of the matrix by oil terminates. At the capillary number value of 3.2×10^{-5} oil moves both in the fracture and in the matrix simultaneously (Figure 55). At this rate, oil can invade more than 90% of the network. At rates higher than this, the network is invaded almost from the start, much like in a typical displacement process. The effect of the mobility ratio is quite significant. In a typical displacement, mobility ratio affects the frontal shape, such that at high values (unfavorable mobility) the front is highly fingered, while at low values (favorable mobility) it is compact. In the case of a fractured system, the mobility ratio affects primarily the degree of penetration into the fracture before invasion of the network also commences. Clearly, as the mobility ratio decreases, penetration into the matrix may occur at rates lower than before. Indeed, for the case of heavy oil drainage, where M=0.01, even at the low rate of 0.0052 cc/min, the capillary number is of the order of 10^{-5}, thus matrix and fracture are invaded simultaneously resulting into a very compact interface (Figure 56).

During primary drainage, the interface at the pore level obeys a "go and stop" rule, such that the interface is stopped by the throat untill the capillary pressure is exceeded. After passing through this throat, the oil spontaneously invades the larger adjacent pore. Resulting water entrapment in the matrix is low because of low mobility ratio and the high connectivity of the pore network used in our experiments.

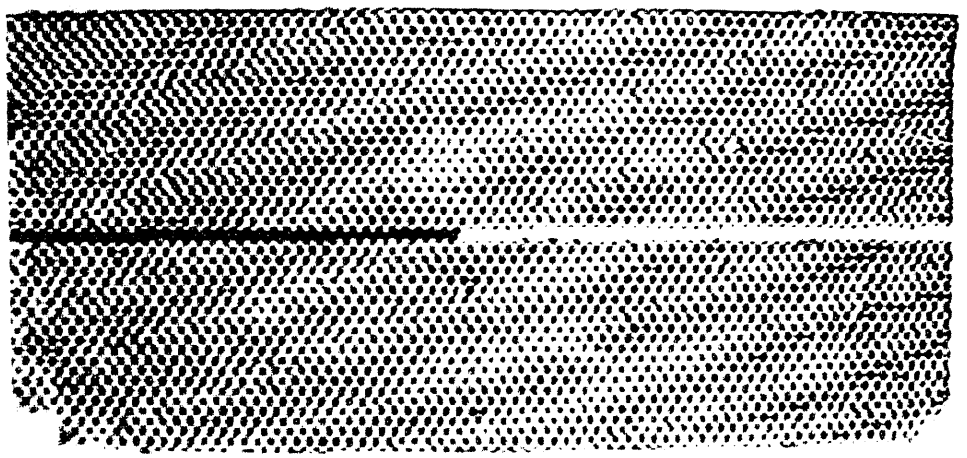

Figure 48: Primary drainage (air-water) at $N_{ca} = 3.6 \times 10^{-10}$, showing that air moves to the fracture only.

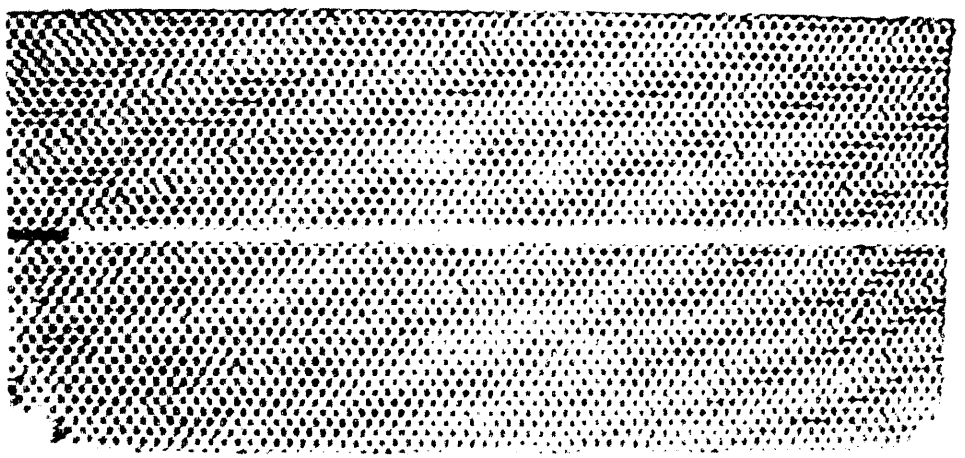

Figure 49: Primary drainage (air-water) at $N_{ca} = 3.6 \times 10^{-8}$, showing that air moves to the fracture only.

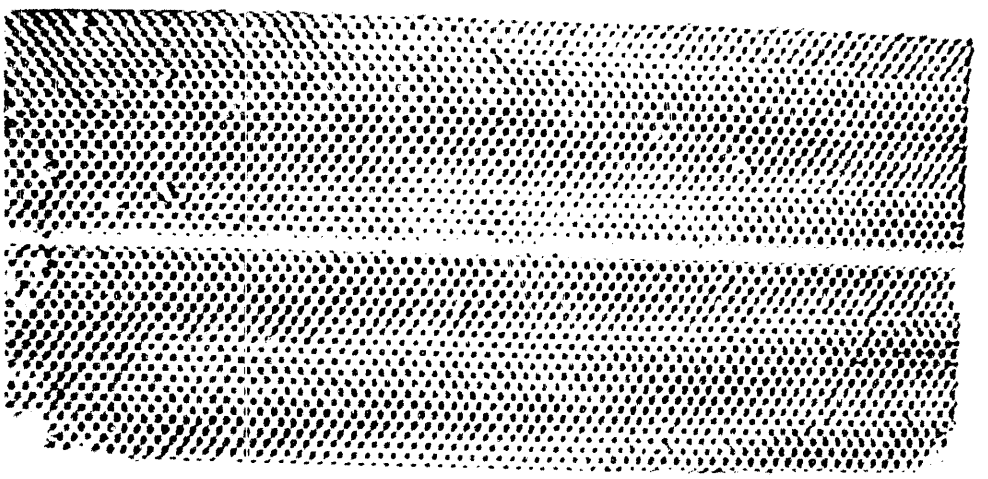

Figure 50: Primary drainage (air-water) at $N_{ca} = 3.6 \times 10^{-6}$, showing that air may also invade the matrix.

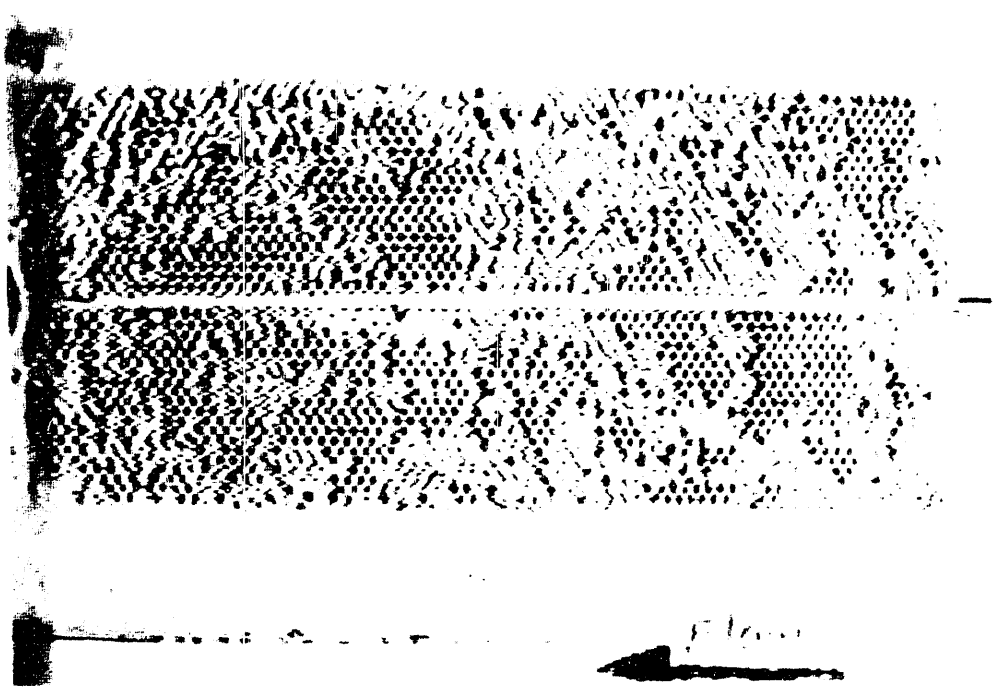

Figure 51: Primary drainage (air-water) at $N_{ca} = 2.8 \times 10^{-5}$, showing that air invades the matrix in a ramified fashion.

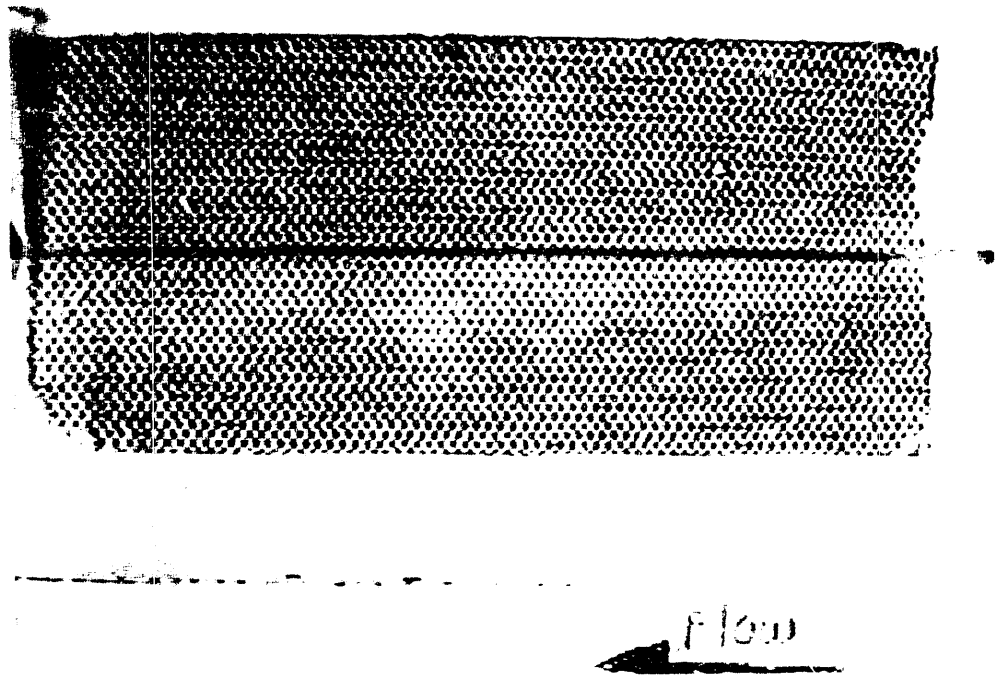

Figure 52: Primary drainage (kerosene-water) at $N_{ca} = 3.2 \times 10^{-7}$, showing that kerosene enters the fracture only.

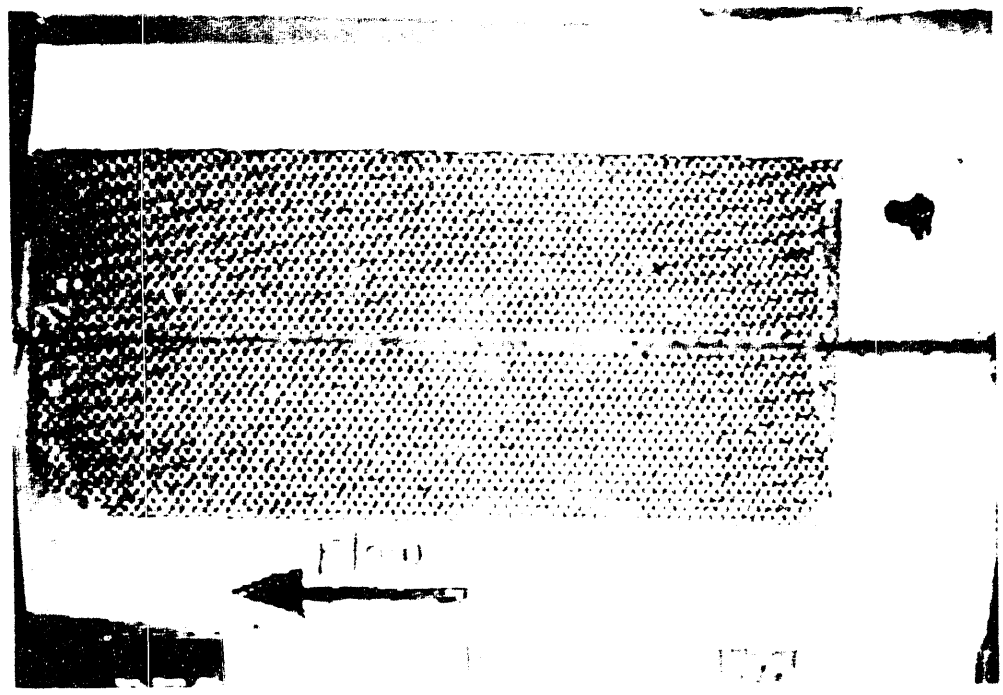

Figure 53: Primary drainage (kerosene-water) at $N_{ca} = 6.3 \times 10^{-6}$, showing that kerosene invades the matrix.

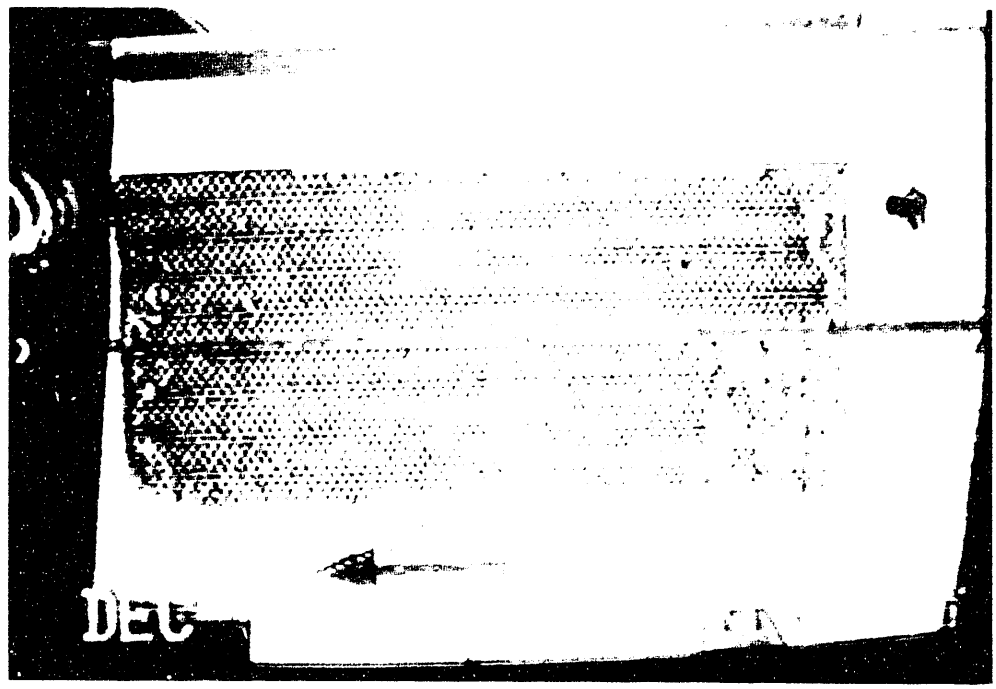

Figure 54: Primary drainage (kerosene-water) at $N_{ca} = 1.2 \times 10^{-5}$, showing that kerosene invades the matrix after entering the fracture.

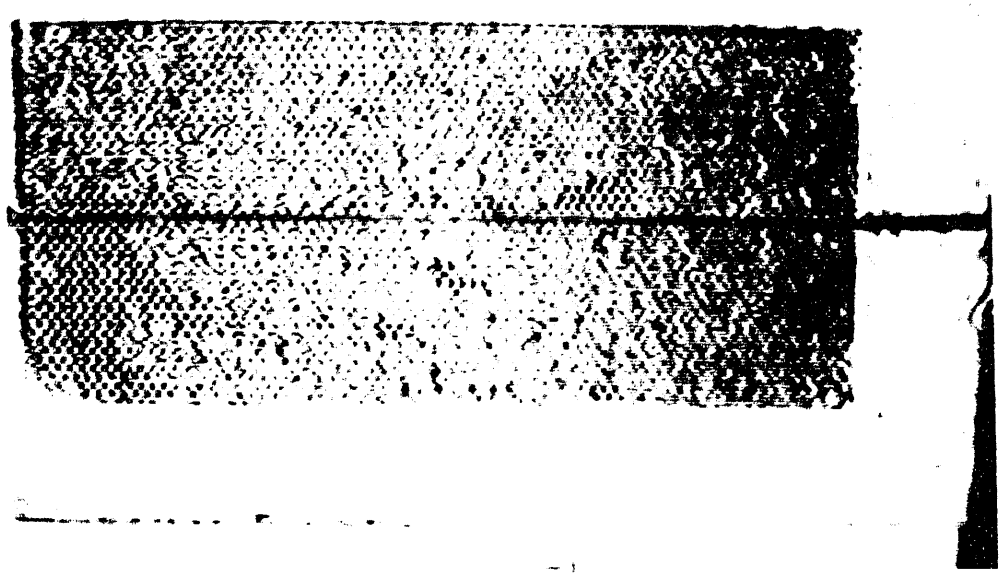

Figure 55: Primary drainage (kerosene-water) at $N_{ca} = 3.2 \times 10^{-5}$, showing that kerosene invades most of the matrix after entering the fracture.

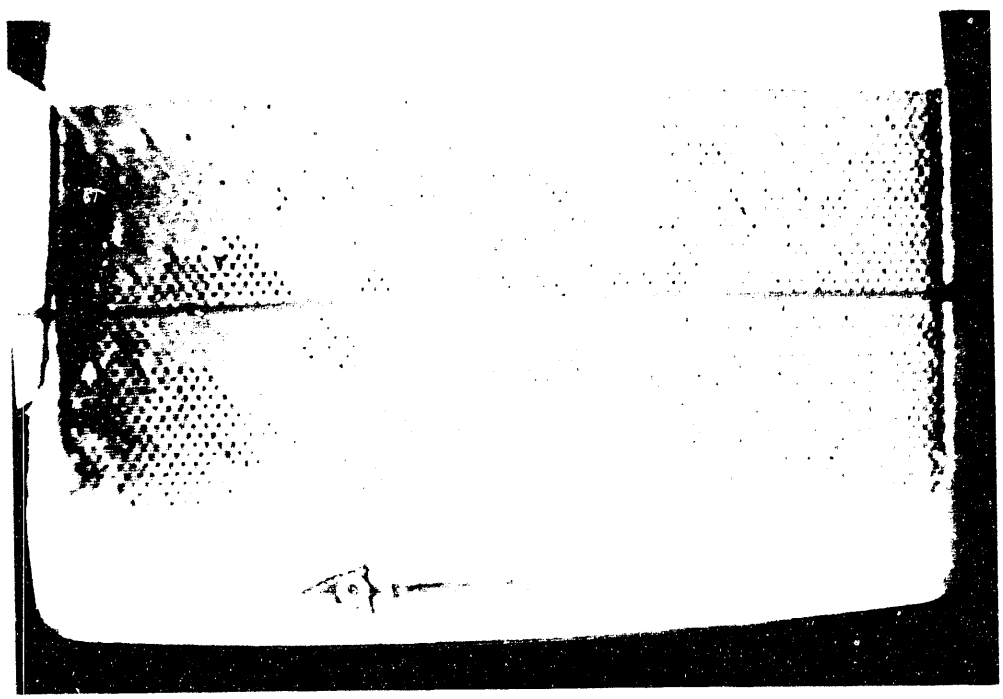

Figure 56: Primary drainage (oil-water) at $N_{ca} = 4.1 \times 10^{-5}$, showing that viscous oil invades both the fracture and the matrix.

5.3.3 Secondary Imbibition

In the last set of experiments, we considered secondary imbibition. Now the model is first saturated with water. Then, the non-wetting phase is injected at capillary number values greater than 10^{-5} in order to simulate drainage with the least amount of trapping. Obviously, the precise way drainage has taken place would substantially affect the subsequent mechanism of secondary imbibition. This set of experiments pertained to an initial drainage at relatively high capillary numbers. The resulting residual water films were not interconnected, particularly for the case of heavy oil. This has significant effects on the secondary imbibition. Table 4 shows the various parameter values used in the different runs. During the experiments involving the fluid pair water-air, water invade the matrix block following a mechanism different than for the case of primary imbibition. Now, the displacement is a succession of rapid invasion jumps that occur along the existing water films, left behind at the conclusion of primary drainage (Figure 57). This mechanism operates at low capillry numbers. At higher values, the typical meniscus displacement was also observed.

For the experiments involving the fluid pair water-kerosene, secondary imbibition was not observed at low capillary numbers (lower than 10^{-6}). Water was found to enter the fracture first, and only a few pores adjacent to the fracture were invaded (Figures 58 and 59). Only at higher values of the capillary number, 4×10^{-6} (Figure 60), an invasion similar to the previous was observed. We attribute this lack of spontaneous imbibition to the lack of connectivity between the residual water films.

In the experiments with heavy oil, where the mobility ratio was 100, water moves to the fracture first. However, before water breakthrough in the fracture, water also invades the matrix. The mechanism of displacement in both the pore throat and in the fracture is a slow uniform meniscus movement. In this experiment, we observed that if a relatively heavy oil is used for drainage, the water film left behind is apparently very thin, such that spontaneous imbibition will not take place (Figures 61, 62, 63, 64).

In general, the experiments described above provide some insight on the fluid flow in porous media when a fracture system exists. At present, the set is incomplete, particularly as it regards secondary imbibition. Future work involves further investigation on the effect of film flow and roughness flow and the computer simulation of these experiments, before steam injection is attempted.

Fluid Pair	Displacing Fluid Viscosity (cP)	Mobility Ratio	Volumetric Rate (cc/min)	Capillary Number
Water-Air	1	0.018	0.00052	2×10^{-8}
"	"	"	0.0052	2×10^{-7}
"	"	"	0.052	2×10^{-6}
"	"	"	0.52	2×10^{-5}
Water-Oil	1	"	0.00052	4×10^{-8}
"	"	1.50	0.0052	4×10^{-7}
"	"	"	0.052	4×10^{-6}
"	"	"	0.52	4×10^{-5}
Water-Oil	1	100	0.00052	4×10^{-8}
"	"	"	0.0052	4×10^{-7}
"	"	"	0.052	4×10^{-6}
"	"	"	0.52	4×10^{-5}

Table 4: Conditions for various secondary imbibition experiments.

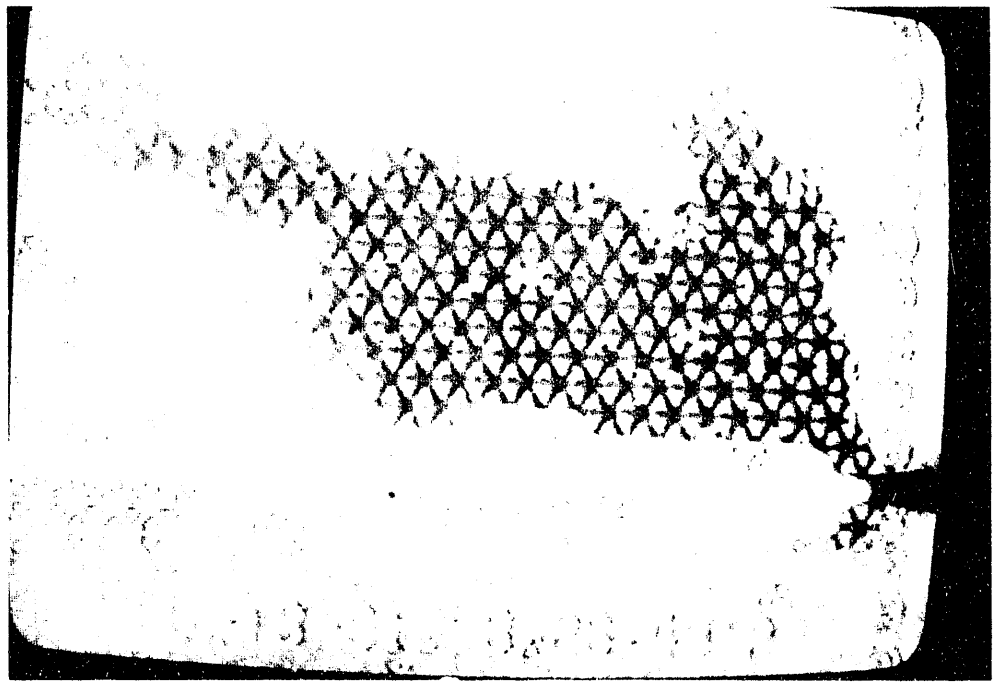

Figure 57: Secondary imbibition (water-air) at $N_{ca} = 2 \times 10^{-8}$.

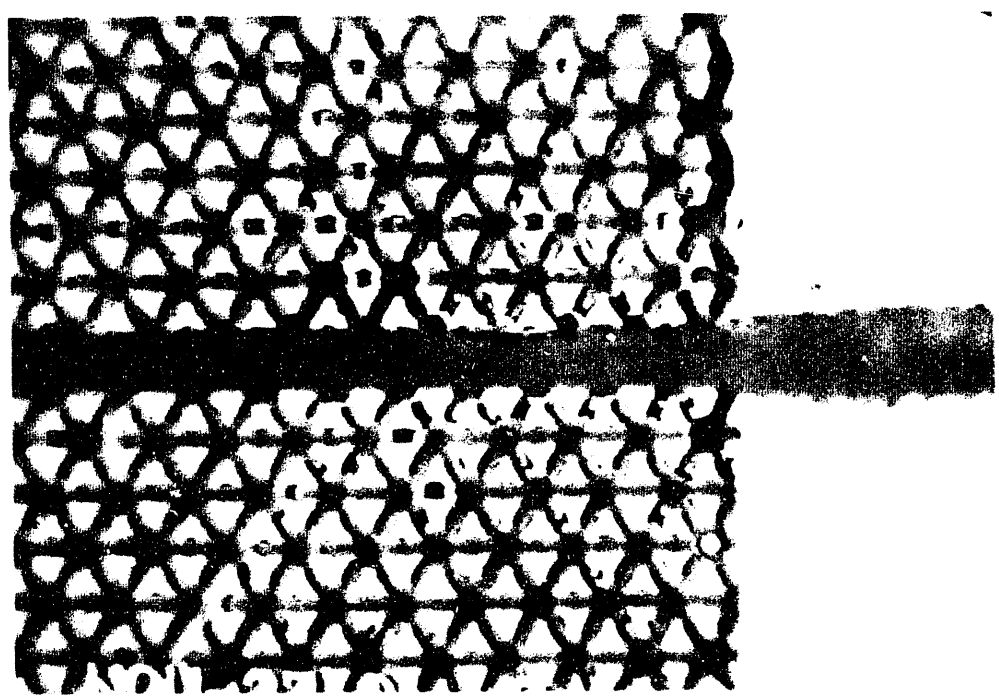

Figure 58: Secondary imbibition (water-kerosene) at $N_{ca} = 4 \times 10^{-8}$.

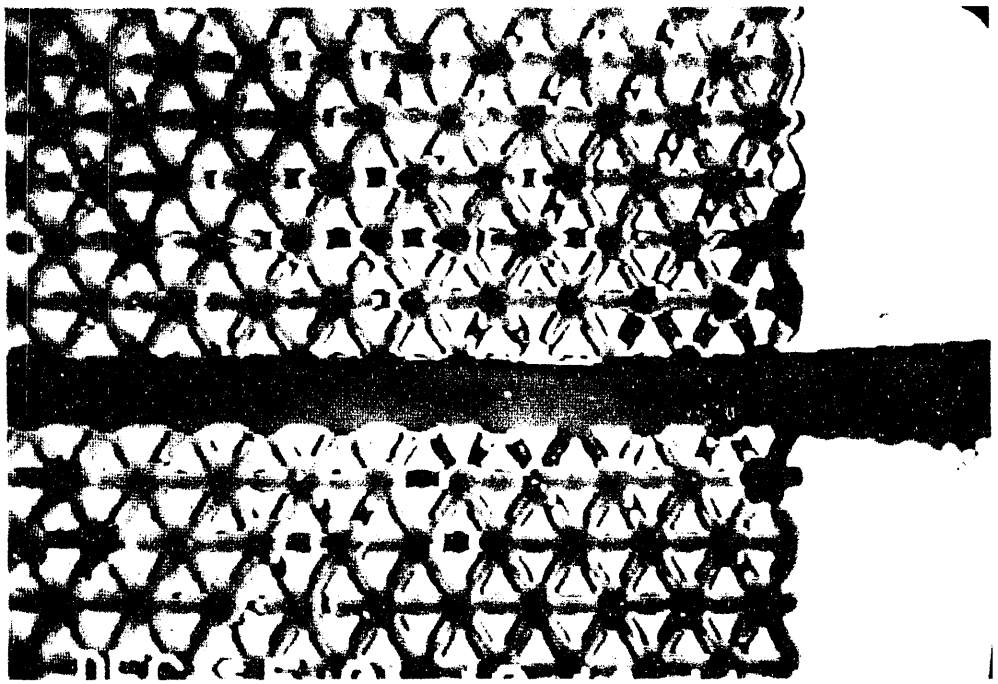

Figure 59: Secondary imbibition (water-kerosene) at $N_{ca} = 4 \times 10^{-7}$.

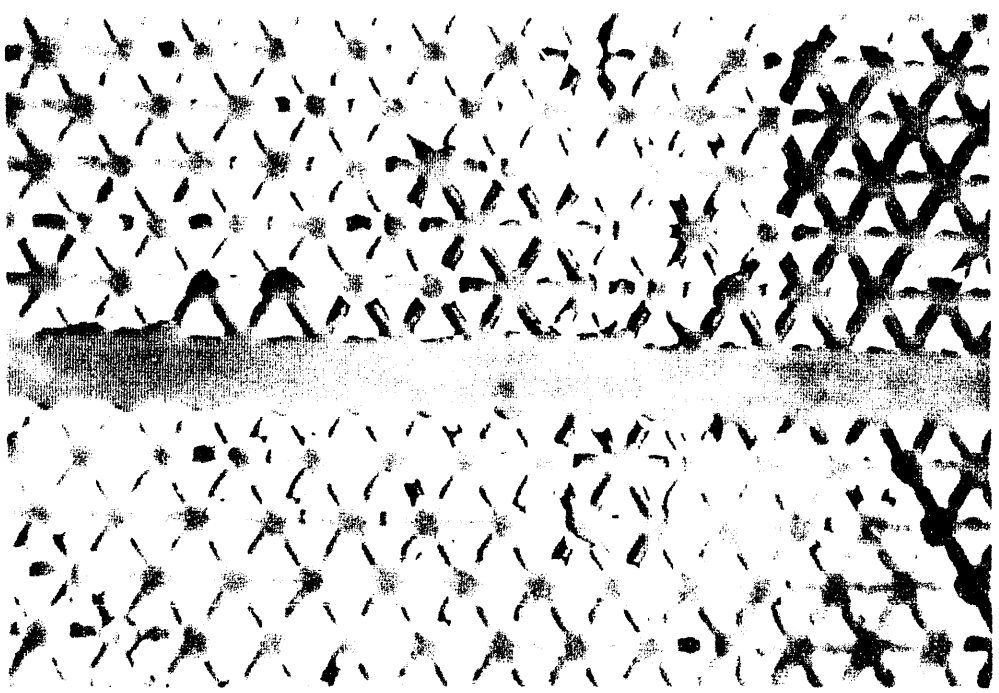

Figure 60: Secondary imbibition (water-kerosene) at $N_{ca} = 4 \times 10^{-6}$.

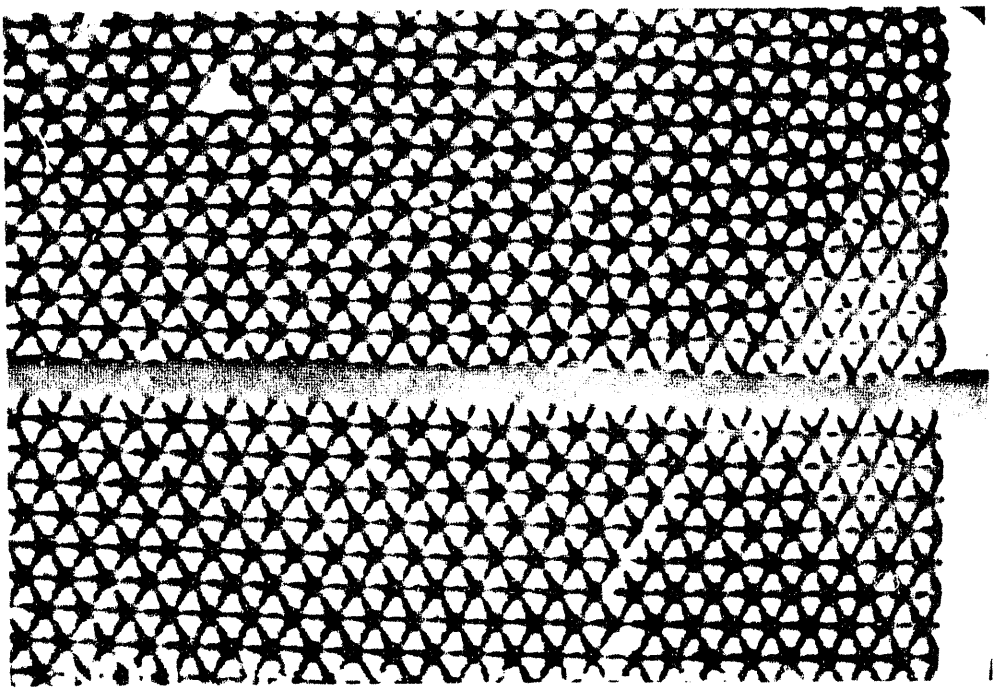

Figure 61: Secondary imbibition (water-heavy oil) at $N_{ca} = 4 \times 10^{-8}$.

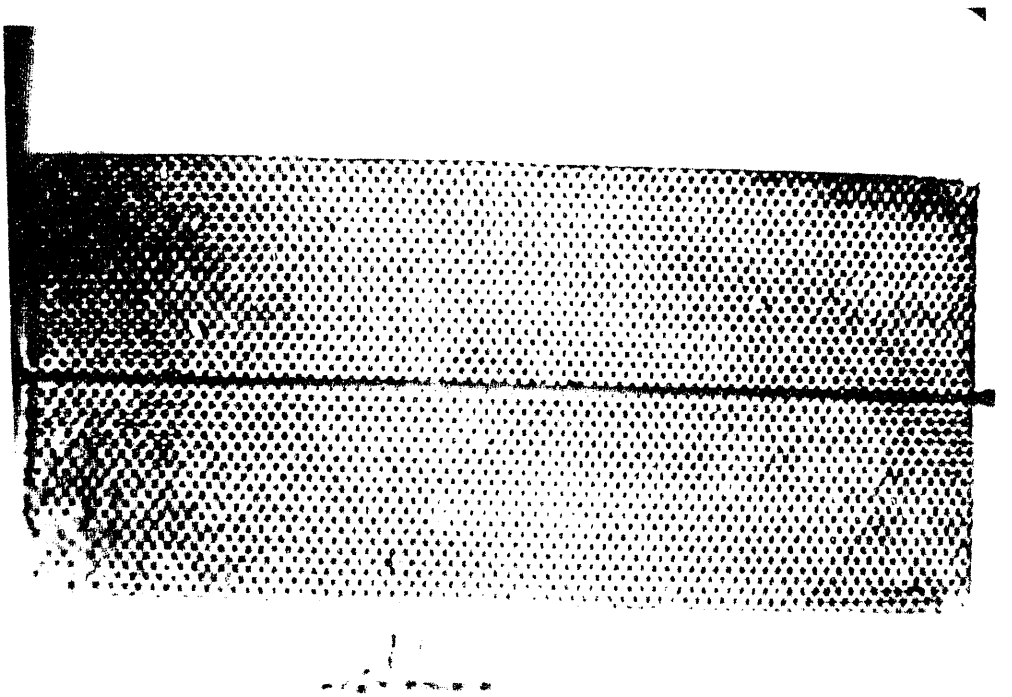

Figure 62: Secondary imbibition (water-heavy oil) at $N_{ca} = 4 \times 10^{-7}$.

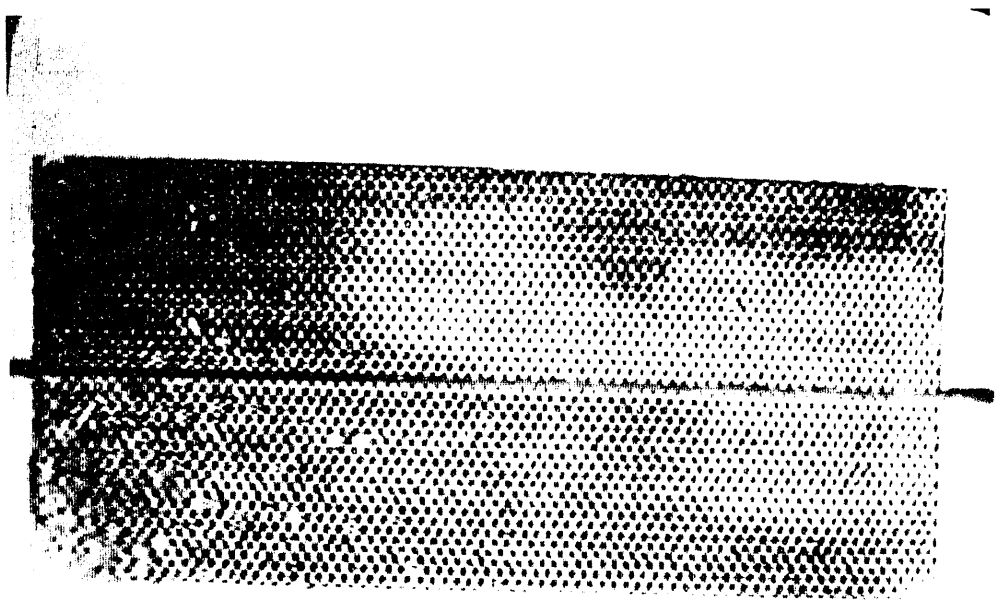

Figure 63: Secondary imbibition (water-heavy oil) at $N_{ca} = 4 \times 10^{-6}$.

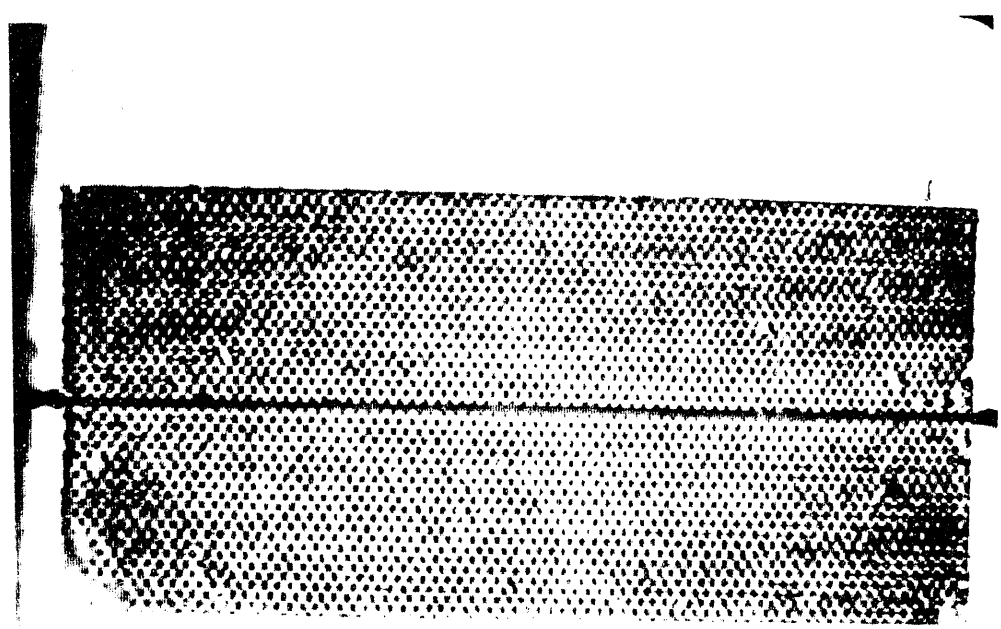

Figure 64: Secondary imbibition (water-heavy oil) at $N_{ca} = 4 \times 10^{-5}$.

6 NUMERICAL CONSTRUCTION AND FLOW SIMULATION IN NETWORKS OF FRACTURES USING FRACTAL GEOMETRY

J. Acuna and Y.C. Yortsos

6.1 INTRODUCTION

Fractal geometry is a relatively new approach for the description and modeling of complex objects and processes [46], [85]. In general, fractal images are the result of the repetition of a given geometric shape into itself over a cascade of different length scales. When coupled with random noise, the resulting complexity makes fractal images suitable for the description of a variety of natural objects. Although this should not imply that every such object is fractal, nonetheless fractals constitute a very convenient method to describe many physical processes. In particular, the application of fractals to porous media is very promising. The review by Sahimi and Yortsos [112] classifies the fractal patterns that result from various porous media processes, such as percolation, viscous fingering and fracturing. Networks of fractures in a rock are natural candidates for a fractal geometry description. This particular alternative is explored in this paper.

Conventionally, naturally fractured systems have been represented by the Warren and Root double porosity model [138] or by a random array of fractures [21], [84]. Although capturing important properties, neither of the two geometries can account for fractal characteristics recently attributed to naturally fractured systems [5], [105], [114]. The relation of fractals to fracture networks was first explored in 1985, in a study of nuclear waste disposal [5]. That study revealed that many fracture patterns at Yucca Mountain, NV, were self-repetitive over a range of scales, spanning from 0.2 to 15 meters, within which several generations of fractures were detected. Additional support for the fractal character of fracture networks can be found in recent studies of the fracture patterns of the Monterey formation [50] and of the Geysers geothermal field [115]. Prominent fractal features in the latter include the existence of a cascade of fracture scales and a self-similar structure.

It was recently proposed that the fracturing of disordered media, such as natural rocks, can be modeled using fractals [55], [134]. Indeed, fractal structures have been related to the fracture resistance of the material and to the particular fracturing process it undergoes [134]. For example, fragmentation with substantial shearing, which appears to be a dominant mechanism for many fracture networks, leads to fractal dimension values ranging between 1.2 and 1.8 [18]. Sammis et

al. have reported fractal dimensions between 1.5 and 1.7, [114].

Motivated by such findings, investigators have recently attributed fractal properties to networks of fractures and proceeded to analyze their hydraulic response (Chang and Yortsos [23], Beier [9]). These works demonstrated that the traditional solutions for single-phase fluid flow are particular cases of a more general solution, where the dimensionality (reflected in the fractal dimension) is a key variable. Significantly, this dimension can take non-integer values and characterizes the fractal response.

Current studies in the modeling of fractured systems with fractals rely on Sierpinski carpets and percolation networks [104]. In certain cases, numerical simulation has shown the expected for a fractal transient response. However, the particular networks taken represent rather special and idealized cases. Fractal models for naturally fractured systems must be consistent with the basic mechanisms of fracturing, such as shear fracturing, extension fracturing, etc. [60]. In addition, any synthetic network must honor available data, such as fracture length distribution, fracture orientation and density, etc. Real systems also possess upper and lower cutoffs, which place limits on the range of fractal behavior. Strictly speaking, rigorous methods for the construction of networks of fractures must await the successful development of fracturing theories. Recent advances in this area have been many and significant and they hold promise that a unified theory may soon emerge [55].

A practical alternative that may lack in rigor, but affords great flexibility, is possible for systems that may be described by a fragmentation process. The latter is known to lead to fractal size distributions [134]. The essential aspects of fragmentation can be simulated with the application of the IFS (Iterated Function System) approach introduced by Barnsley [4]. This technique yields networks of the desired fractal properties with much flexibility in the orientation of the fractures and in the shapes of the fragments. This approach of combining fragmentation and IFS to create fractal networks is proposed in this paper. Two issues will be addressed:

(i) The numerical construction of a synthetic network of fractures with fractal characteristics.

(ii) The simulation of transient, single-phase flow of a slightly compressible fluid and its pressure transient response in such networks.

6.2 NUMERICAL SYNTHESIS OF FRACTAL NETWORKS OF FRACTURES

6.2.1 Fragmentation and Fractals

In many fragmentation processes, the distribution of fragment sizes can be described by a power law. This fact has been known since the early 1940s, when Schuhmann's law [51] was introduced to describe the distribution in grinding operations. Turcotte [134] documents many fracturing applications, where the size distribution is described by a power law. More recently, Poulton et al. [105] postulated a power law behavior not only for the fragment size, but also for the length and spacing of discontinuities in the rock. In a related study, a power law distribution of fracture trace lengths was discovered by Barton [5].

Fragmentation was modeled in the classical work of Gilvarry [51], who used an exponential distribution to describe repetitive fracturing. A basic parameter in the analysis is the probability $p_f(l)\delta l$ that a given fragment of size in the interval between l and $l+\delta l$ will be fragmented. Recently, Turcotte [134] has showed that when p_f is constant, a power law distribution of fragment sizes is obtained. For an idealized fragmentation process, where the fragments of a given generation are all of the same relative size, the fragment size distribution is of the power law type, with an exponent related to the probability of fracturing p_f. For example, if each block creates an average of Sp_f new blocks of relative size $1/S$, the theoretical value of the exponent is

$$E = \frac{2 \ln Sp_f}{\ln S} \tag{57}$$

It can be shown that this exponent is also equal to the box fractal dimension, D, of the mosaic made up of the same pieces. Since an unfractured block represents a missing subset of fractures, the fracture length distribution will also be power law distributed with the same exponent. Equation (57) suggests that non-trivial fractals ($D < 2$) are obtained only for $p_f < 1$.

The box counting fractal dimension is one measure of a fractal structure. It is typically calculated by superposing a grid of a given cell-size on the fracture pattern and by counting the number of occupied cells. The power law relation

$$N(r) \sim r^{-D} \tag{58}$$

between the number $N(r)$ of occupied cells and the scale r, yields the dimension D. Box counting

has been routinely used to characterize the fractal properties of real networks [5], [114].

For more realistic fragmentation processes, blocks of a given generation are not all of the same relative size and a given size group may be composed by blocks of different generations. Nonetheless, as will be shown later, a power law distribution in fragment size and fracture length still persists. We should also add that fractal behavior typically holds in a finite range between an upper and a lower cutoff scale. The upper cutoff is defined by the maximum size fragment (the "largest hole" in the network). The lower cutoff is more arbitrary, usually decided from practical considerations. As shown below, finite cutoffs play an important role in the hydraulic response.

The way by which patterns are created by fragmentation, namely the initiation from a large scale and the propagation towards successively smaller scales in a systematic manner, has a close analogy with the IFS technique recently developed. In the following, we propose to mimic a natural fracturing process in the construction of a synthetic network by combining the IFS with a probability rule.

6.2.2 Generation of Fractal Networks of Fractures

Barnsley [4] has recently proposed the method of Iterated Function System (IFS) to construct fractal images. With this technique, a fractal is obtained from an initial simple shape (initiator) by applying in an iterative fashion a set of numerical transformations (propagator). Each iteration creates multiple sets of n smaller, transformed images that occupy the place of the previous image. After several generations the set converges to a fractal. The technique creates fragments of various sizes and shapes and it is well suited for the development of synthetic networks of fractures.

For the creation of the two-dimensional patterns to follow, two transformations were used. Each consists of two quadratic expressions

$$x_n = ax_{n-1} + by_{n-1} + cx_{n-1}y_{n-1} + d$$

$$y_n = ex_{n-1} + fy_{n-1} + gx_{n-1}y_{n-1} + h$$

where x_n, y_n are the coordinates of a given point of the nth generation, and a,b,c,d,e,f,g,h are the coefficients of the transformation. When $c = g = 0$ the transformation is linear (generally self-affine). If in addition $a = f$ and $b = -e$, it gives rise to self-similar fractals. The non-linear terms (c, g) are useful in controlling the geometry of the final pattern. However, control of the fractal

characteristics and the fractal dimension is mainly obtained by varying the probability p_f. As in fragmentation, we may specify that a fraction $1 - p_f$ of newly generated blocks is not allowed to further subdivide. The value of p_f affects the fractal dimension, although not necessarily according to the simple result in equation (57).

Figures 65, 66 and 67 show three typical examples of fracture networks obtained with the application of self-similar, self-affine and non-linear transformations, respectively. A fracturing probability $p_f = 0.75$ was applied every second generation.

Because of our interest on fracture networks, the objects of Figure 65 to 67 have their fractures retained. Thus, they are not strictly self-similar or self-affine. In this regard, they represent modifications of the well-known Sierpinski gasket [85]. Nevertheless, they do possess similar fractal characteristics. Figures 65b, 66b and 67b show plots of the box counting, fracture length and fragment size distributions corresponding to these objects. In all objects, box counting exhibits a power law behavior reflecting the underlying fractal structure, with an exponent varying between the values of 1.60 (for Figure 66b) and 1.62 (for Figure 67b), both very close to the theoretical value of 1.59 for a Sierpinski gasket. For the object of the self-similar transformations of Figure 65a, the other two fractal measures (fracture length and fragment size) are step-like with steps of equal size. If only the points at the edges of the step are taken, the discrete distribution so obtained is of the power law type with an exponent consistent with the theoretical value. However, this is not the case for Figure 66b, where fracture length and box counting give approximately the same exponent but the fragment size distribution hardly resembles a power law. It must be noted that finite size effects are present on all distributions. The third non-linear object of Figure 67a can be characterized as fractal, if box counting is applied ($D \sim 1.62$). Fracture length still follows a fairly well defined power law. However, fragment size distribution has a power law behavior only in segments. Certainly, as more generation are included, the distributions approach the expected power law. The above differences serve to emphasize the relevance of box counting in the characterization of the fractal structure in finite fractals.

The shape and geometry of the initiator have a significant effect on the geometry of the final pattern. Figure 68a shows a pattern of eleven generations initiated from a quadrilateral shape with a single fracture. Physically, the transformation at each stage consists of a rotation and subdivision of the original two (upper or lower, left or right) halves. The apparent relative complexity of this

(a)

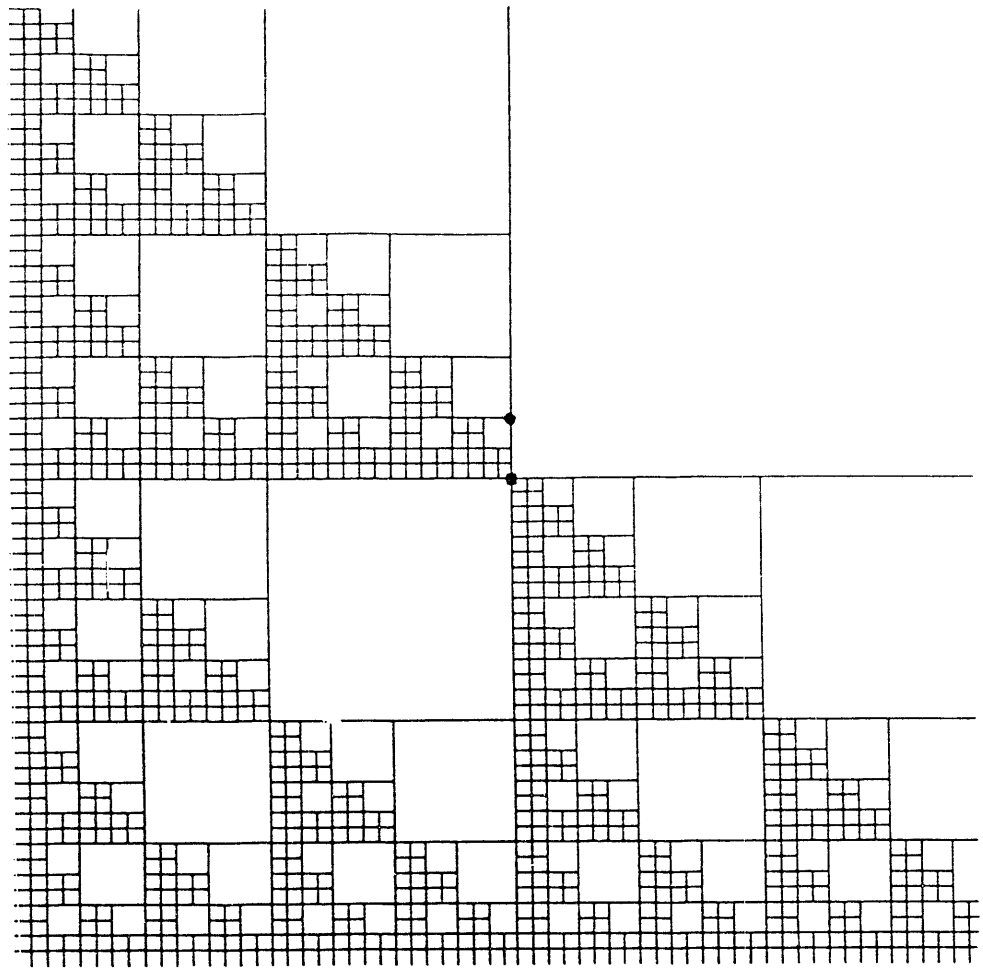

(b)

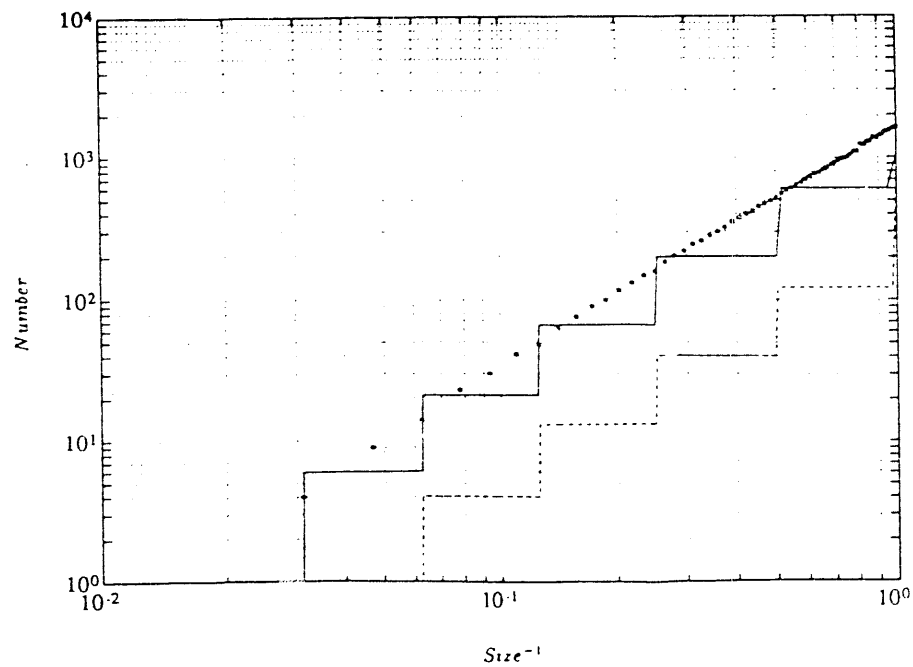

Figure 65: (a) Modified Sierpinski gasket (11 generations) with self-similar IFS. Positions A (square) and B (circle) (b) Corresponding box counting(*), fracture length (solid line) and fragment size (dashed line) distributions.

(a)

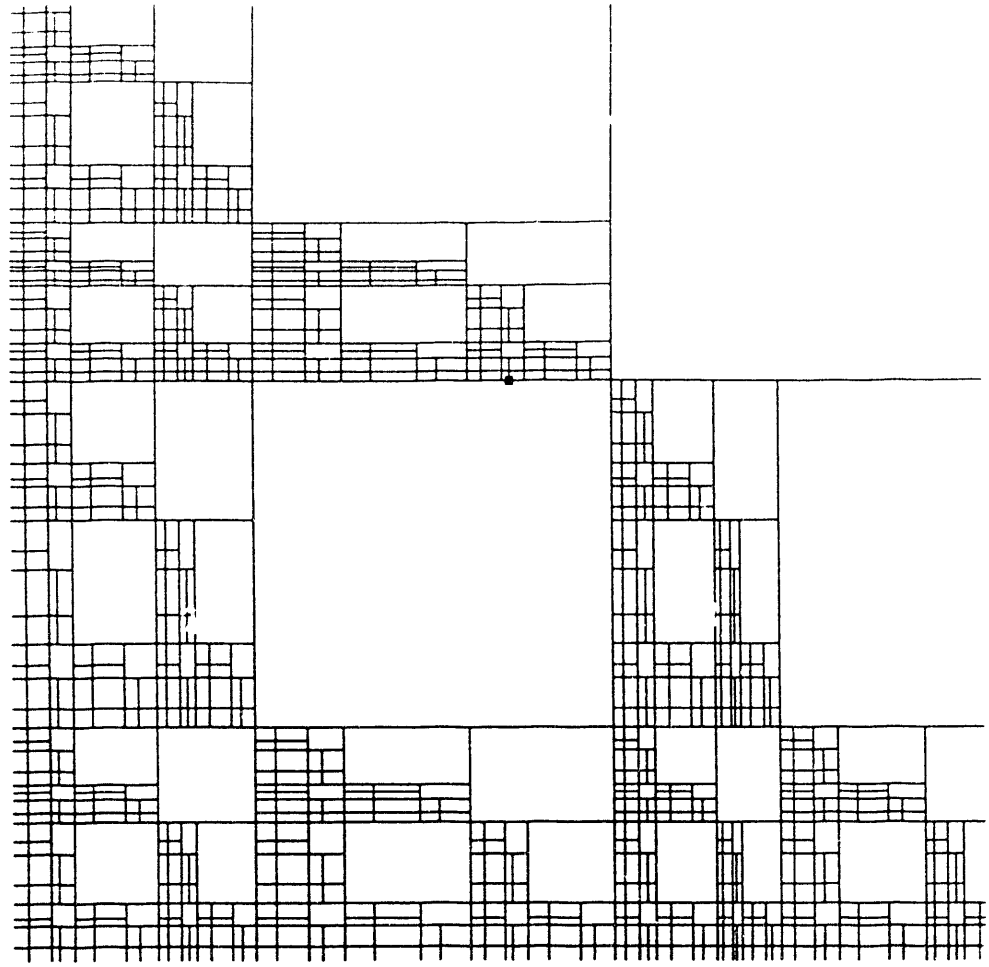

(b)

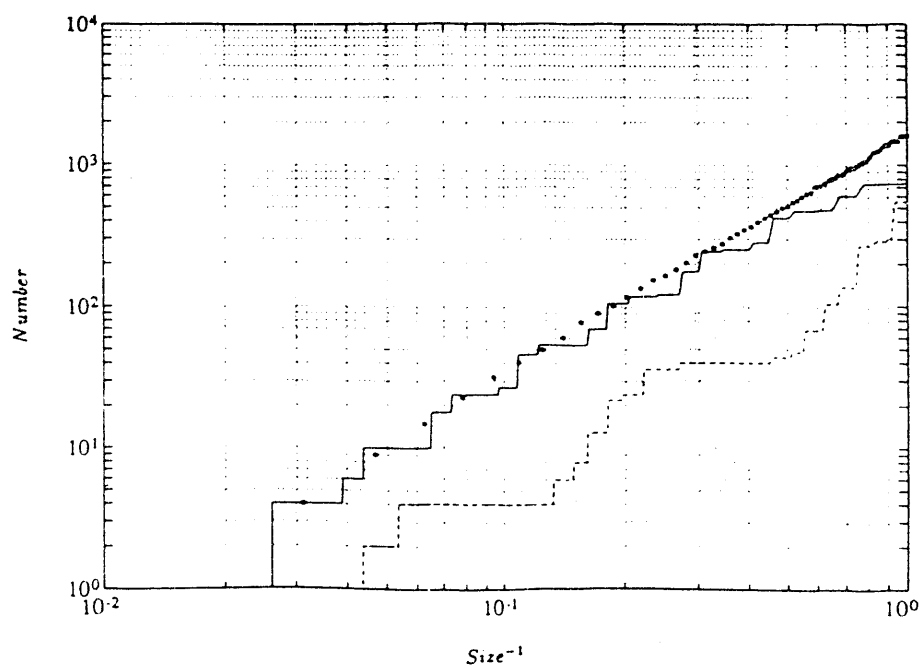

Figure 66: (a) Modified Sierpinski gasket (11 generations) with self-affine IFS. (b) Corresponding box counting(*), fracture length (solid line) and fragment size (dashed line) distributions.

(a)

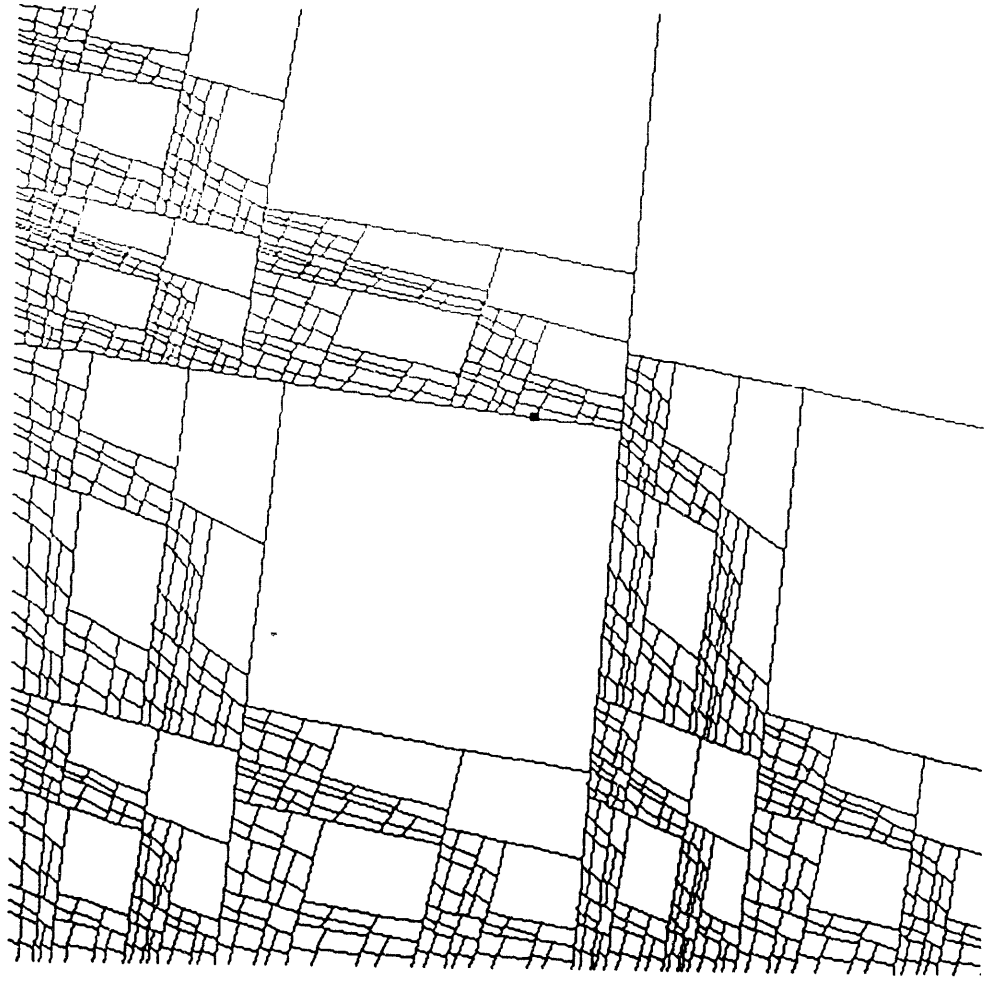

(b)

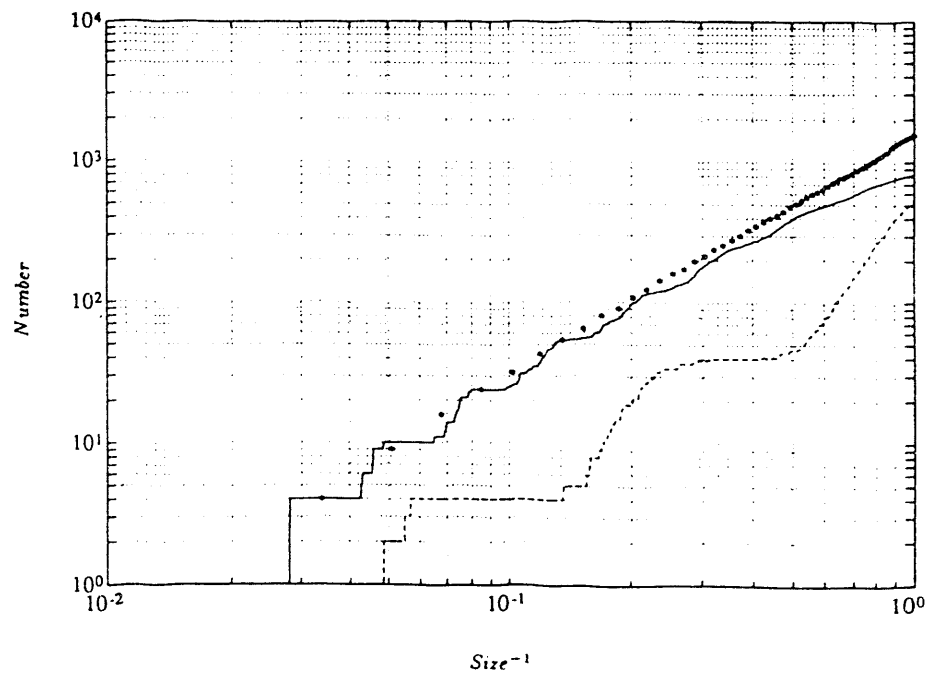

Figure 67: (a) Modified Sierpinski gasket (11 generations) with non-linear IFS. (b) Corresponding box counting(*), fracture length (solid line) and fragment size (dashed line) distributions.

pattern hides the fact that there are only minor differences with Figures 65 to 67, namely the angle of the initial fracture, the initial shape and the value of p_f (here equal to 1). In Figure 68a the initial fracture tends to be parallel to the top and bottom edges. Corresponding box counting, fracture length and fragment size distributions are shown in Figure 68b. Because the pattern is composed of pieces in a narrow size range, the box counting fractal dimension is very close to 2 in the range of interest. Changing the position of the initial fracture dramatically alters the final pattern. Figure 69a corresponds to the same initiator shape as Figure 68a, except that the initial fracture is tilted at a larger angle. In this highly distorted network, the initial fracture is hardly recognizable.

Even though Figures 68 and 69 appear realistic, as more generations are included, the fracturing process continues until the medium completely disintegrates. This results from the fact that each block was allowed to further subdivide ($p_f = 1$). To obtain non-trivial fractal patterns, the fragmentation probability must decrease, lower values in p_f resulting into lower values of the box counting dimension D. The patterns in Figures 70a and 71a were constructed as in Figure 68a, except that a fraction $(1 - p_f)$ of randomly selected fragments were left unfractured after the fourth generation. Different selections of the fragments result into different networks, although all realizations have the same box counting fractal dimension. Figure 70b and 71b show the box counting, fracture length and fragment size distributions for these patterns. The box dimensions are 1.78 and 1.65 for the two networks, respectively. As expected, the values depend on both p_f and the particular geometry. Away from the cutoffs, fragment size and fracture length distributions are of the power law type. Finite size effects are limited to sizes close to the cutoffs for regular and moderately distorted networks.

The sequence of transformations that creates a fracture also specifies its address. For example, if an IFS of two transformations, denoted by 0 and 1 respectively, is used, typical addresses of fractures are 001, 1010, 01101, etc. The number of digits in the sequence equals that of the generation to which the fracture belongs. The numbers also determine the position of a particular fracture in the map. This systematic fracture identification is especially appropriate for fluid flow simulation. The networks presented in this paper were constructed with two transformations applied to a two-dimensional initiator consisting of a single initial fracture in a quadrilateral shape. Of course, this is not a limitation of the technique, which allows for an infinite variety of transformations in any

(a)

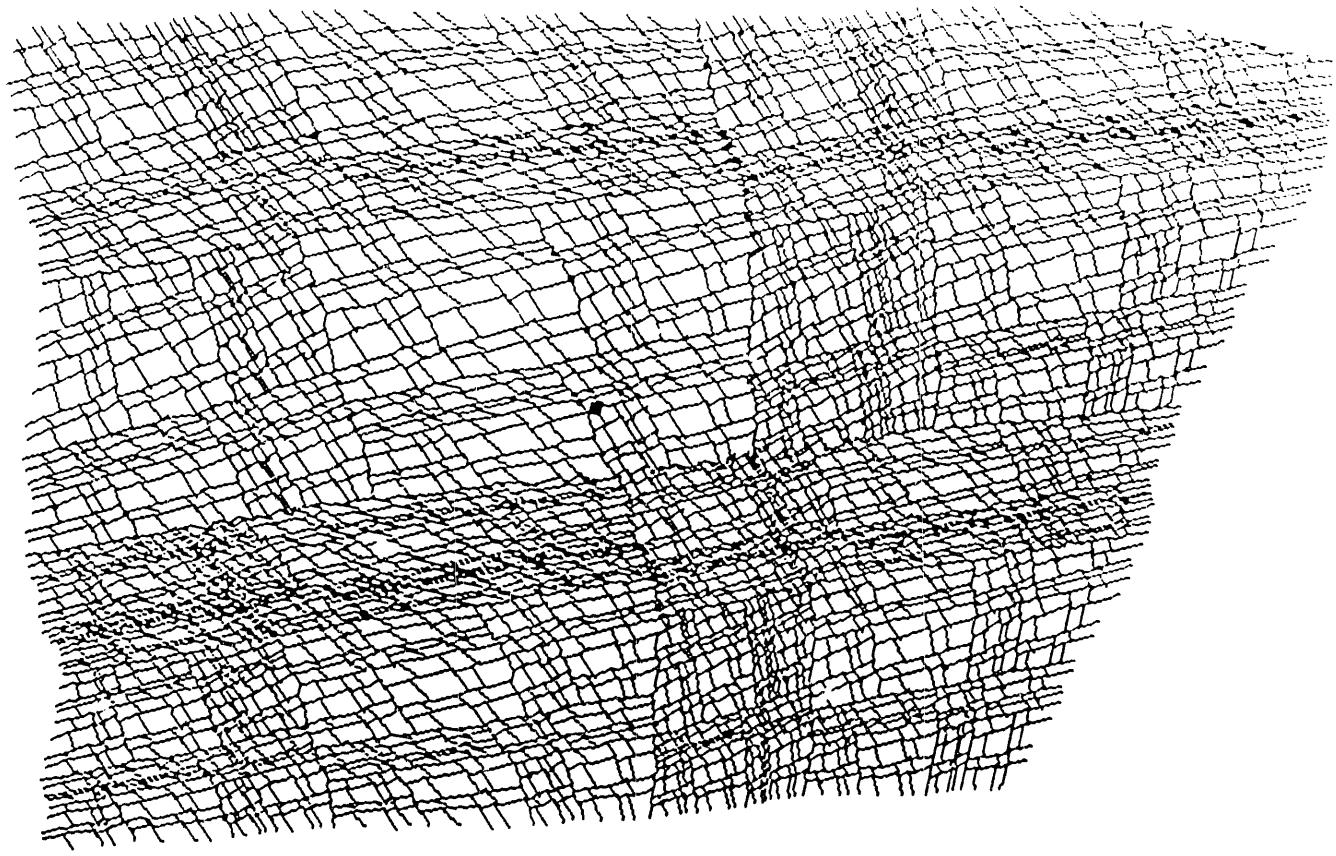

(b)

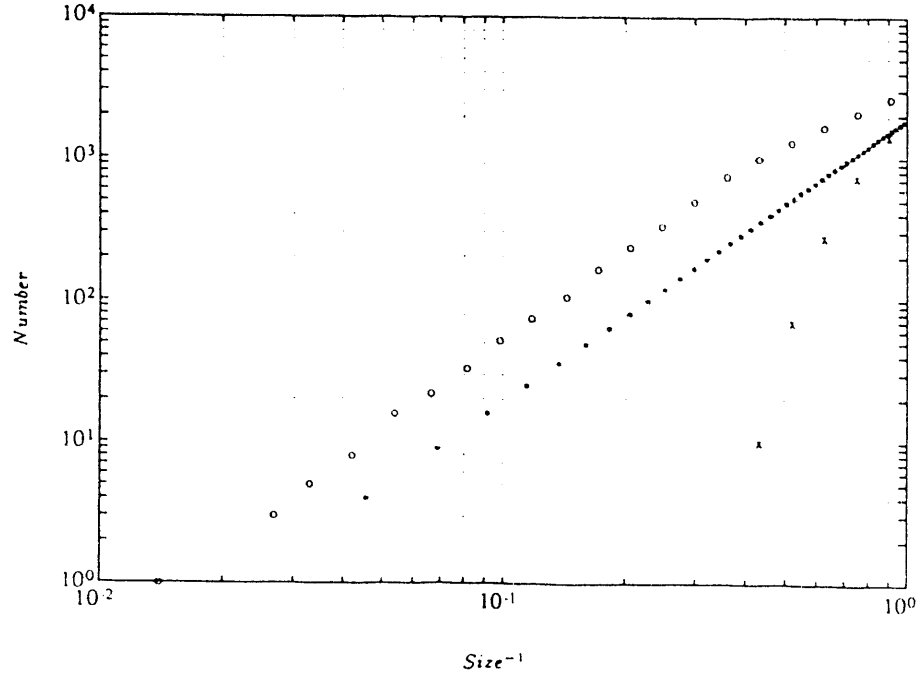

Figure 68: (a) Fracture network (11 generations) using a quadrilateral initiator and $p_f = 1$. (b) Corresponding box counting($*$), fracture length(o) and fragment size (x) distributions.

(a)

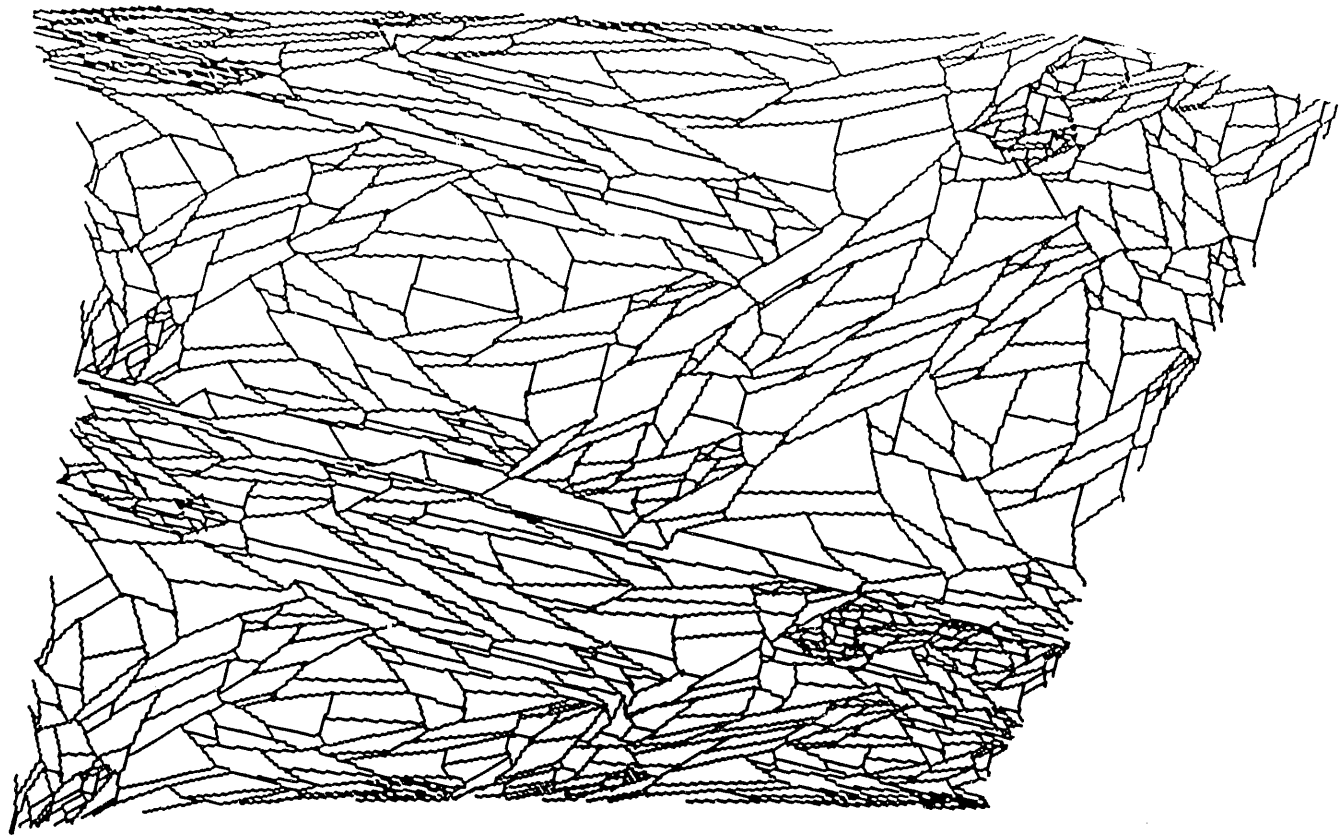

(b)

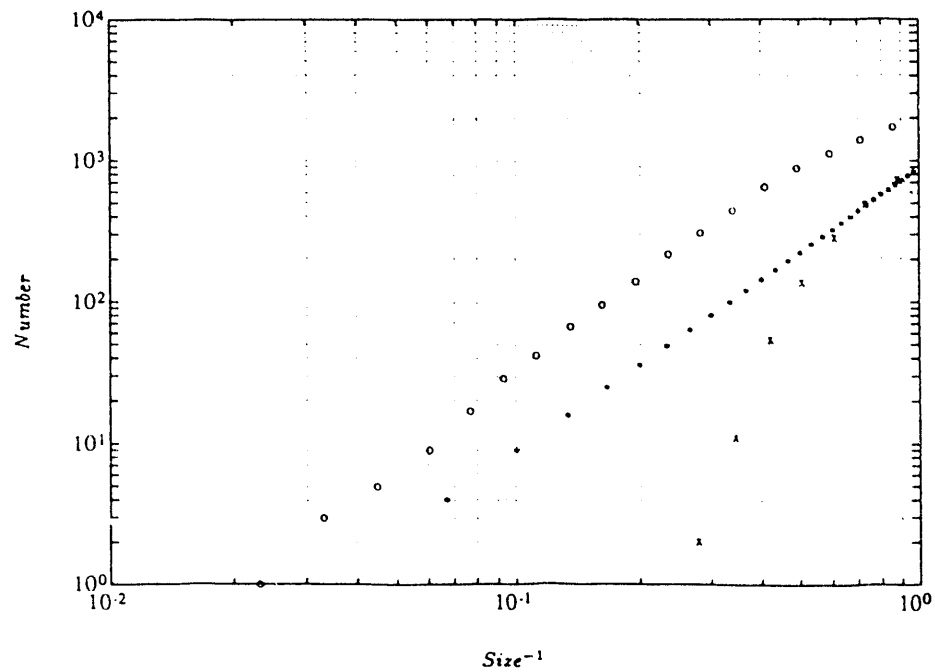

Figure 69: (a) Distorted fracture network (11 generations) using a quadrilateral initiator and $p_f = 1$. (b) Corresponding box counting ($*$), fracture length(o) and fragment size (x) distributions.

(a)

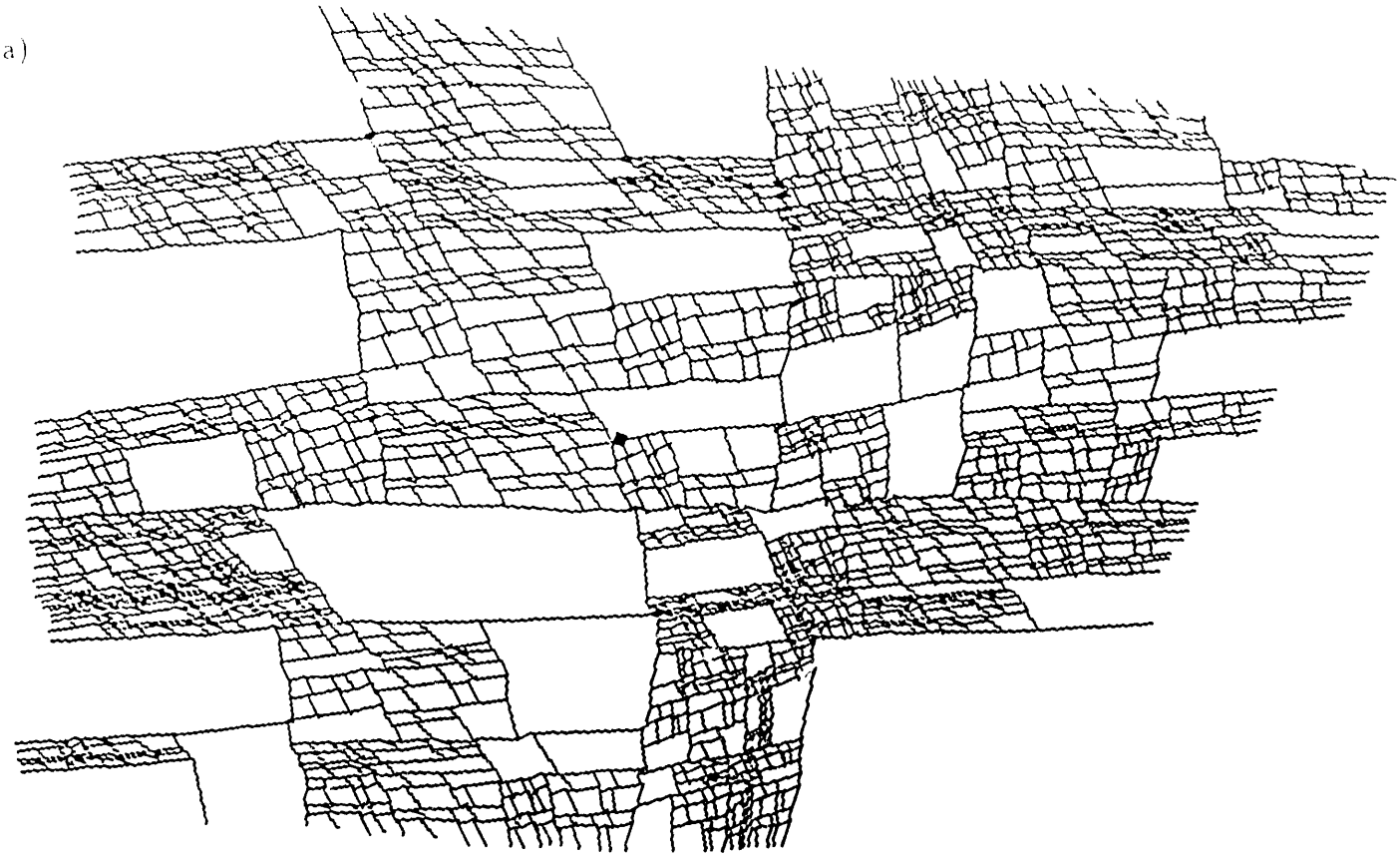

(b)

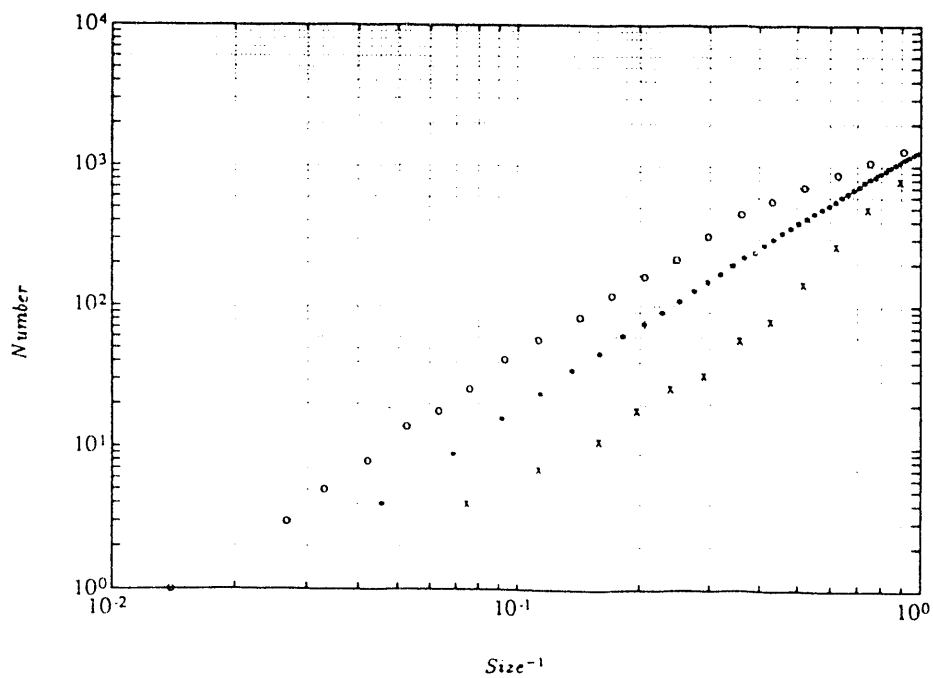

Figure 70: (a) Fracture network (11 generations) as in Figure 68 with $p_f = 0.90$. (b) Corresponding box counting($*$), fracture length(o) and fragment size (x) distributions.

(a)

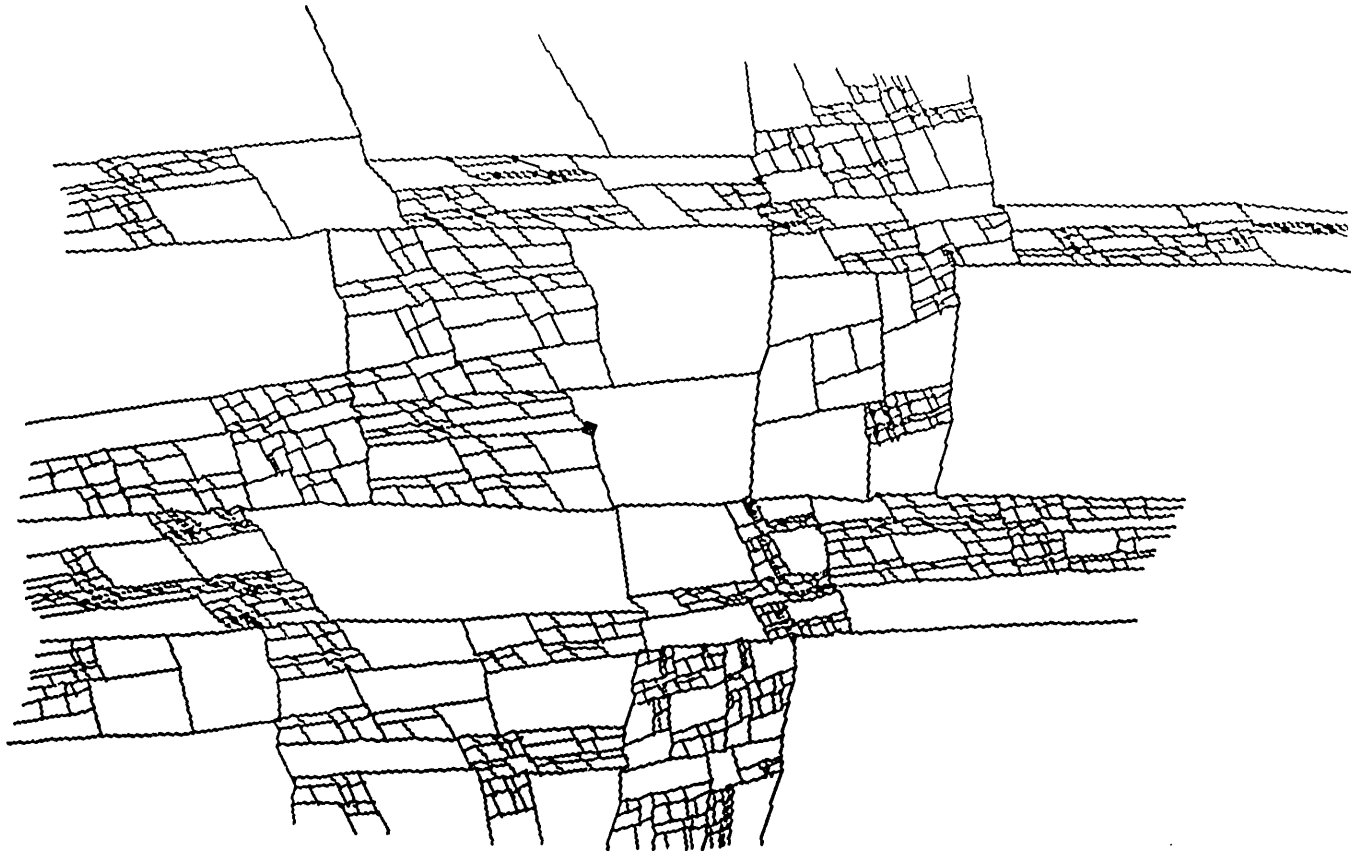

(b)

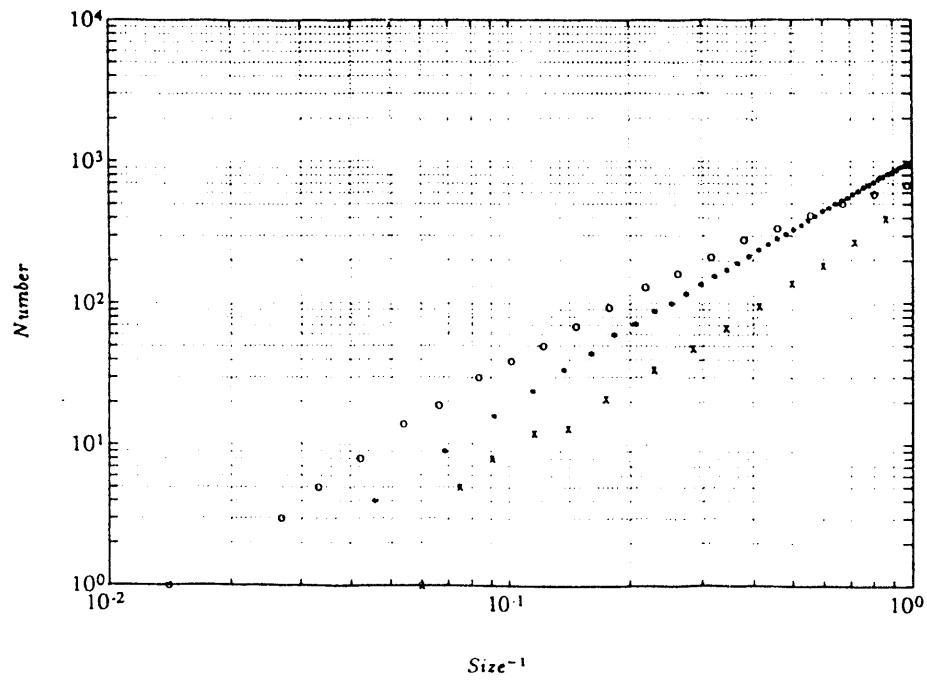

Figure 71: (a) Fracture network (11 generations) as in Figure 68 with $p_f = 0.80$. (b) Corresponding box counting($*$), fracture length(o) and fragment size (x) distributions.

dimensions and for any initiator.

6.3 FLUID FLOW SIMULATION

The usefulness of any synthetic network is tied to the ability to simulate fluid flow. In the networks under consideration, the IFS technique allows for expedient simulation. Certainly, for a numerical solution, a finite number of generations must be considered. As shown below, this imposes a significant constraint.

6.3.1 Flow Conductivity Matrix

The unique binary sequence that identifies each fracture, makes possible to precisely specify its address, shape and location, as well as to devise a numbering system for its end points. In this fashion, the nodes of the network are directly identified. This is an important development, as it alleviates the need for a finite-difference or a finite-element description. Moreover, it is uniquely related to the self-similar, nested structure of the fractal object.

To proceed with flow simulation, certain assumptions regarding the fluid flow in the fractures must be made. Consider single phase flow. Along each fracture, the usual expression applies:

$$Q = C\rho W^{\lambda}[\frac{\Delta p}{l}] \tag{59}$$

where Q is the mass flow rate, W is the width of the fracture, Δp is the pressure drop along the fracture, ρ is the fluid density and λ is the conductivity exponent, usually taken equal to three. To construct the flow conductivity matrix, we make use of the address of each fracture. The two end nodes of the initial fracture, of known coordinates, are numbered nodes 1 and 2. Each new fracture subdivides an existing block and adds two new nodes to the system. The general expression for the number of the end nodes of a fracture are α and $\alpha + 1$, respectively, where

$$\alpha = 2^{j+1} - 1 + 2 * (ad) \tag{60}$$

Here, j is the generation to which the given fracture belongs, and ad is the decimal value of the binary address. The coordinates of each such node are obtained by applying the sequence of transformations described by the address to the coordinates of nodes 1 and 2. In this fashion, we may obtain the coordinates and the number of each node in the network. Intersections between

fractures are also specified numerically in a simple manner. The final step is to calculate the conductivity of each fracture according to the assumptions made and to fill the entries of the conductivity matrix.

A true fractal pattern of fractures contains an infinite number of generations. In practice, however, only a small number of generations can be considered, since the size of the conductivity matrix doubles with every additional generation. This limitation is very significant on the response of the fractal.

6.3.2 Pressure Transients

We subsequently considered the simulation of the pressure transients during drawdown. A single well is assumed, producing at constant rate, with no flux boundary conditions imposed at the sides of the pattern. Flow occurs only in the fractures. The flow between nodes was evaluated using (59), while an appropriately weighted volume was assigned to each node. For simplicity, each fracture was assigned the same width. Denoting by g_{ij} the conductance between neighboring nodes i and j, the following discrete form for the mass balance for node i can be readily derived

$$c_f \rho_i V_i \frac{\Delta p_i}{\Delta t} = \sum_j \frac{\rho_j g_{ij}(p_j - p_i)}{\mu \ell_{ij}} - Q\delta_{i,m} \tag{61}$$

where subscript j denotes all nodes connected to node i, c_f is the fluid compressibility and m is the node number of the well. We have also used the shorthand notation $\delta_{i,j} = 1$ for $i = j$ and $\delta_{i,j} = 0$ for $i \neq j$. For further simplicity, we take the approximation $V_i = \frac{1}{2}\sum_j A\ell_{ij}$, and $g_{ij} = Ak$, where k is the fracture permeability. Defining dimensionless variables $p_D = \frac{2\pi(p_{in}-p)\rho_0 kA}{Q\ell\mu}$, $\ell_{D,i,j} = \frac{\ell_{ij}}{\ell}$ and $t_D = \frac{kt}{\ell^2 c_f \mu}$, where ℓ is the average size of fractures of the last generation and $\rho_D = \frac{\rho}{\rho_0}$, where ρ_0 is a reference density, we finally obtain

$$\frac{\rho_{D,i}}{2\Delta t_D}\sum_j \ell_{D,ij}\Delta p_{D,i} = \sum_j \rho_{D,ij}\left(\frac{p_{D,i} - p_{D,j}}{\ell_{D,ij}}\right) + \delta_{i,m} \tag{62}$$

This set of equations was solved using a fully implicit algorithm which iterates on the density term at each time step.

Of crucial importance to the solution of the above is the size ratio $N = \frac{L}{\ell}$, where L is the physical size of the domain. N is also related to the total number of nodes (approximately proportional to $\frac{2}{Z}N$, where Z is the coordination number of the network). A theoretical fractal corresponds

to $N \gg 1$ (obtained for infinitely many generations). However, as pointed out above, practical considerations restrict N to a smaller value ($O(100)$).

It is important to discuss the effect of ℓ. When the number of generations of fractures in the network increases for a fixed L, this is equivalent to a decrease in ℓ, and to an increase in N. In the dimensionless notation above, the effect will be equivalent to an increase in the size of the system, or to a delay of the boundary effect. It follows that, working with a large a number of generations is beneficial in two ways: It not only assigns stronger fractal characteristics to the network, it also serves to delay the effect of the boundary on the pressure transient. On the other hand, by decreasing ℓ, the real pressure and real time corresponding to fixed dimensionless values also decrease, the real time following an ℓ^2 dependence. It is possible that this may render more difficult the actual identification of the fractal structure, because of the demand for an increased resolution of the diagnostic instruments, particularly when the fracture permeability is high.

The solution of (61) can be expressed solely in terms of N and t_D

$$p_{D,m} = f(t_D; N) \tag{63}$$

Theoretically ($N \gg 1$), a fractal system must respond as described by the power law of Chang and Yortsos [23]

$$p_{D,m} \sim t_D^{1-\delta} \tag{64}$$

where $\delta = \frac{d_s}{2}$ and d_s is the spectral dimension. For percolation networks, d_s is related to the mass fractal dimension D and the fractal dimension of the random walk d_w [112] through

$$d_s = \frac{2D}{d_w} \tag{65}$$

Equivalently, we may use $\theta = d_w - 2$ to write

$$\delta = \frac{D}{2+\theta} \tag{66}$$

While D is an expression of the mass dimension, θ is related to the network connectivity and describes the deviation from an ordinary random walk in the fractal network. Clearly, it is the combination of both these parameters that contributes to the fractal response.

Contrary to the theoretical results, however, the numerical simulation is subject to finite size effects. These are particularly notable when the well is "off-centered" as explained below. To

analyze such effects, we focused our sensitivity studies on the number of generations, the position of the well and the randomness and irregularity of the pattern. As a diagnostic of true fractal behavior we used the pressure response in a log-log plot. According to the theory, the plots of log p_D and $dp_D/d\log t_D$ vs log t_D must both be linear. Equivalently, we may monitor the slope of these curves and test whether they are constant or not.

For a Euclidean homogeneous network, both slopes should approach zero after an early transient. This is indeed the case as shown in Figure 72. The early response with slope of $\frac{1}{2}$ is present in all our simulations, indicating flow in a single (or a few) fractures that directly feed the well. It is interesting to note that it is often the second curve (second derivative) that allows a clearer identification of the underlying structure (it approaches a constant value faster). Also shown in Figure 72c is the radial total fracture mass plot corresponding to this regular network. The plot is obtained by tracing circles of increasing radius around the well and by measuring the cumulative fracture length within each such circle. In the homogeneous case we expect a radial slope of 1 at small radii (single fractures originating from the well site) and a slope of 2 at larger values, characteristic of homogeneous systems. This is indeed displayed in Figure 72c.

For a fractal network, the theoretical fractal behavior is well displayed in Figure 73, which shows the transient response of a well at the center of the modified Sierpinski gasket of Figure 65. After an early transient, the two slopes remain constant for a significant interval of time, until boundary effects are felt (Figure 73b). The constant slope is a clear indication of an underlying fractal structure. In fact, the slope approaches the theoretical value of 0.26 ($\delta = 0.74$), for $D = 1.59$ and $\theta = 0.16$. This value of θ was obtained by random walks on the network as described by Orbach [93]. The numerical values of δ and θ are also in agreement with fluid flow simulations performed in modified Sierpinski carpets [104].

The fractal response is a consequence of the well developed radial fractal structure around the well under consideration. We confirm this in the associated radial mass plot (Figure 73c) which shows two segments, one for small radii with slope 1, related to the early transient, and another at larger radii with slope 1.59, related to the later part of the transient response. For finite size systems, radial fractal structure is necessary in order to counteract finite size effects.

The modified Sierpinski gasket was next taken to investigate the effect of the number of generations. The transient response for a gasket with nine (two less) generations is shown in Figure 74a.

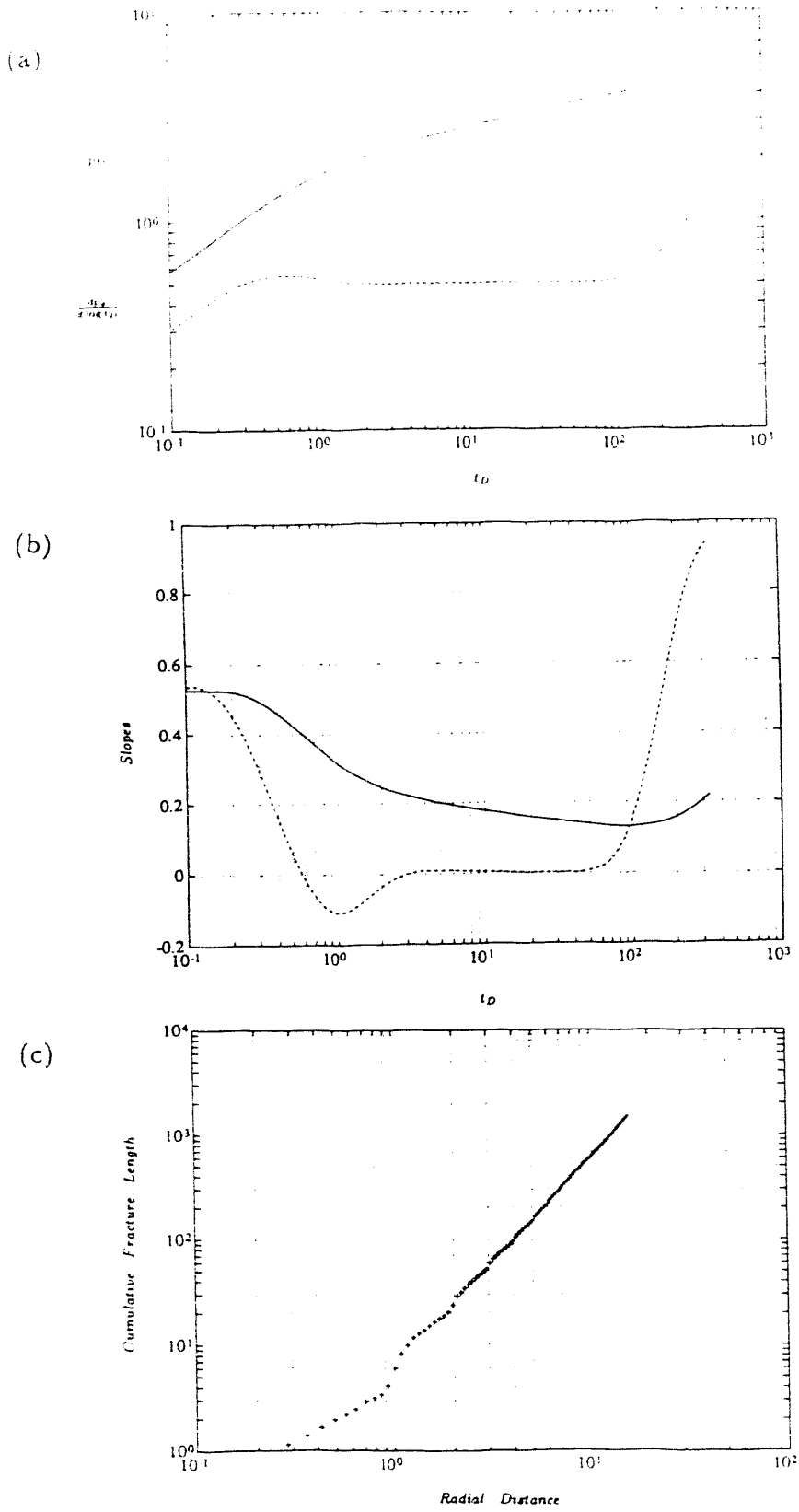

Figure 72: Pressure transient response for a homogeneous network. (a) Pressure (solid line), pressure derivative (dashed line). (b) Corresponding slopes. (c) Radial fracture mass plot.

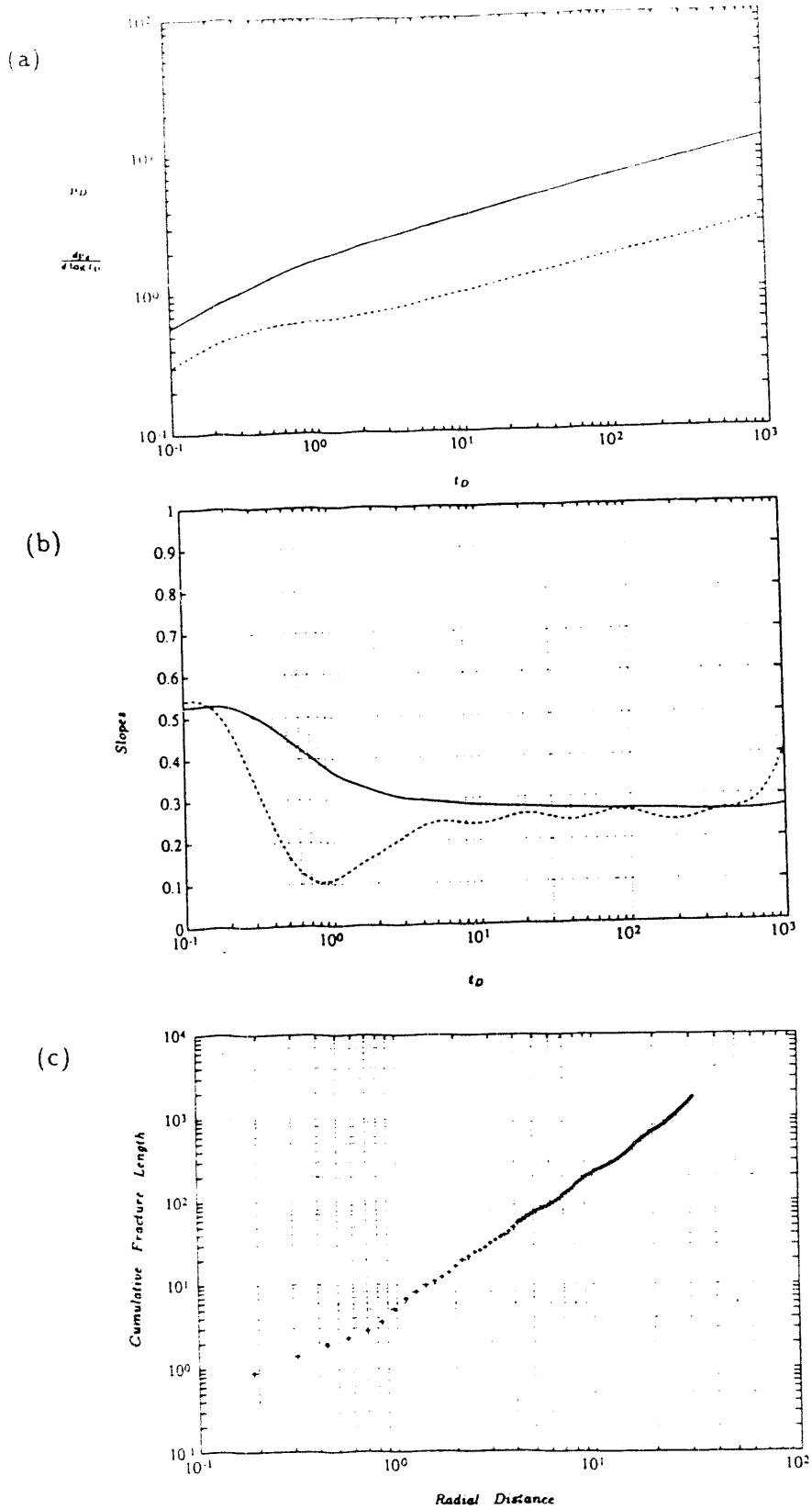

Figure 73: The response for the modified Sierpinski gasket of Figure 65a with well at A. (a), (b) Pressure transients. (c) Radial fracture mass plot for position A.

The early behavior in both Figures 73 and 74 is identical. However, because of the additional length scale, the response of Figure 73 is extended over a longer period of dimensionless time (one more cycle), thus making easier the identification of the constant slope period. This result is consistent with the previous analysis.

Finite size effects can be introduced by slight rearrangements, for instance by placing the test well at an "off-centered" position. Figure 75 shows the transient response for a test well placed at position B in the object of Figure 65a. It is observed that the early transient of $\frac{1}{2}$ slope is prolonged, while the period of constant fractal slope appears later and it has much shorter duration. The slope value is also slightly lower than in the case of position A. An explanation of this behavior is as follows. For finite systems, the development of a sharp response depends on how well a power law fits the radial mass relationship around the test well. For a perfect fractal, this relationship is of the power law type with an exponent equal to the mass dimension D ($D < 2$). This is not the case for our finite networks. For location B, the radial mass plot shows at least three segments. The first with slope of 1 is longer than the corresponding segment for position A. This accounts for the longer lasting period of the early transient at position B. The last two segments of the radial mass plot, with slopes 2.24 and 1.72 respectively, can be related to respective features in the derivative slope curve (dashed curve). However, if the network of Figure 65a were a subset of a larger self-similar network, a power law radial mass plot and a fractal transient response would still have been observed, much like in a true fractal, regardless of the position of the well.

In general, the response of finite systems vary significantly with the arrangement of the matrix blocks (computationally obtained by taking different realizations). It appears that if the blocks are arranged so that the radial structure around the well possesses fractal characteristics, the response is also fractal. This is consistent with the theoretical results, which assume radially fractal characteristics [23], and with the findings of [104].

Pressure transient tests were also conducted for the networks of Figures 70 and 71. The square dot in the middle of the pattern indicates the position of the test well. Results are shown in Figures 76 and 77, respectively. Although both pressure responses are very different from the homogeneous case (compare with Figure 72), neither test conforms exactly to the theoretical expectations for a fractal. The well of Figure 70 has a response that tends to a constant slope, this behavior being consistent with the radial mass plot which has certain power law segments. However, it cannot

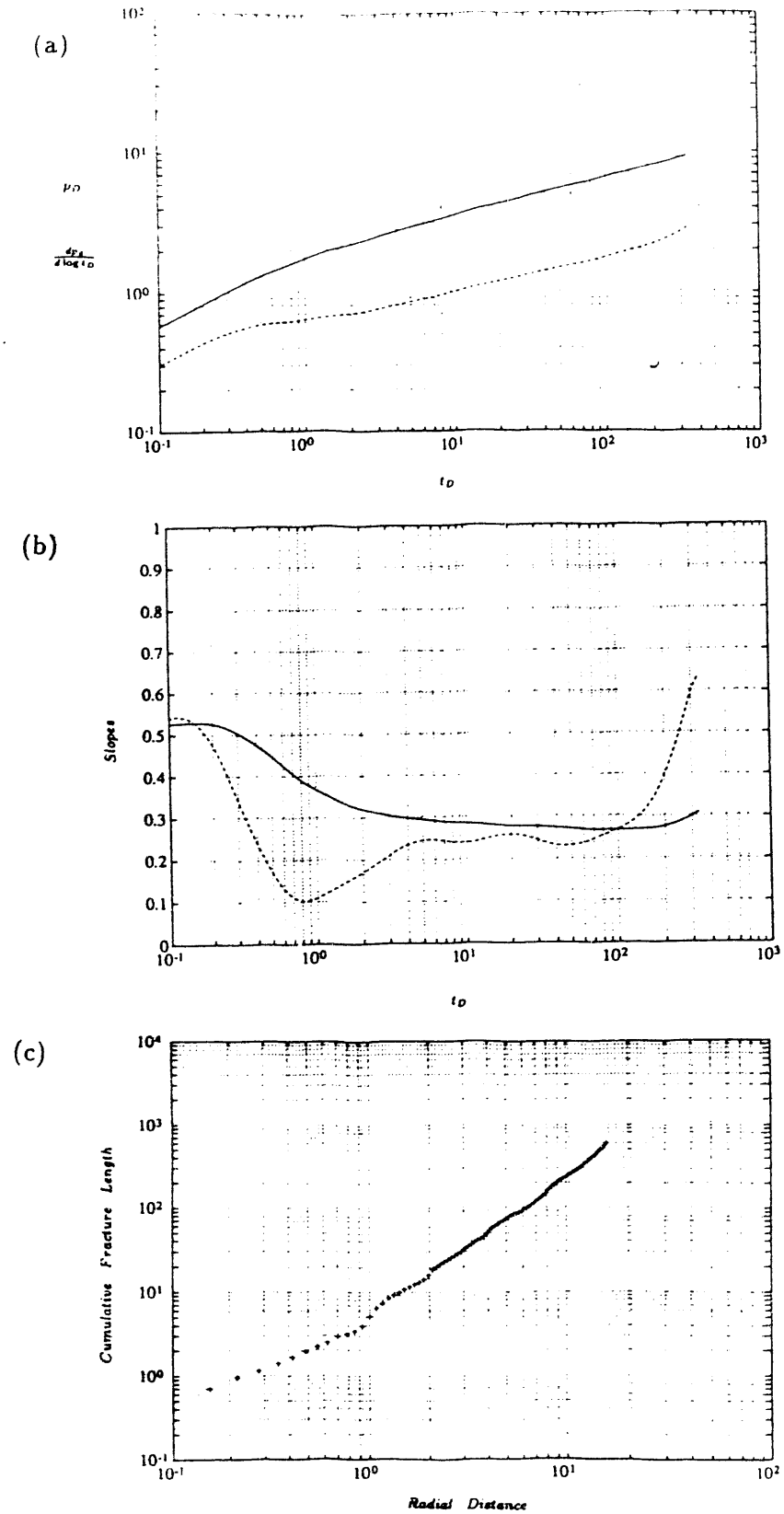

Figure 74: The response of the modified Sierpinski gasket (9 generations) with well at A. (a), (b) Pressure transients. (c) Radial fracture mass plot.

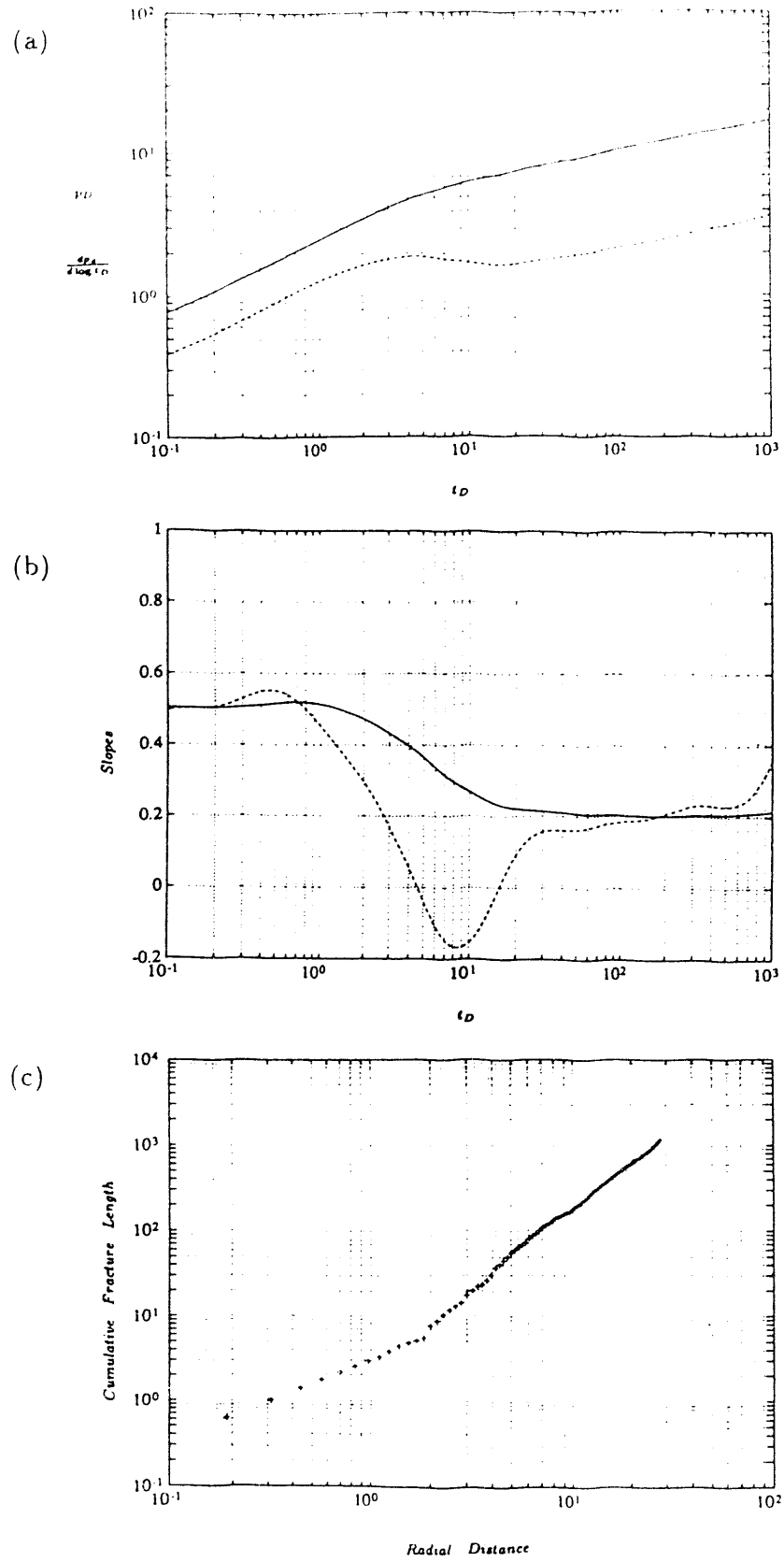

Figure 75: The response of the modified Sierpinski gasket of Figure 65a with well at B. (a), (b) Pressure transients. (c) Radial fracture mass plot for position B.

be used to unambiguously ascertain the underlying fractal. Even less revealing is the response of the well of Figure 71, where the approach to a constant value occurs late and it is interfered with boundary effects. It should be stressed again that this departure from the theoretical expectations is only a result of the limited number of generations allowed in the numerical computations (the objects of Figures 70 and 71 have fractal characteristics over a small range of scales only). Coupled with the irregularity and randomness of the patterns, this limitation prevents the identification of the fractal structure. On the other hand, many real systems are more likely than not to contain such limitations. Further work is necessary to develop better diagnostic techniques for the identification of such networks.

A variety of other tests were also performed and analyzed. The previous findings were consistently confirmed, namely that as long as the number of generations is small, the transient response is unlikely to have the theoretical characteristics, unless the arrangement of matrix blocks is such that a radially fractal structure exits.

6.4 CONCLUSIONS

A method to create fractal fracture networks with fractal characteristics was developed. The method is based on a combination of the IFS technique for constructing fractal images [4], and of a probability rule consistent with a fragmentation process. This technique allows one to create two-dimensional fractal networks with controlled fragment shape, upper and lower cutoffs, fragment sizes, and fractal dimension. Although not attempted here, the method can be generalized for the creation of three-dimensional networks.

The simulation of pressure transients showed that the identification of the fractal object with the help of existing theoretical methods is possible only if a significant number of generations is allowed, or, equivalently, if the object is fractal over a large enough range of scales. Otherwise, finite size effects and randomness may dominate the pressure response and make difficult the identification of the structure. This behavior serves to emphasize the importance of cutoff scales in fractals.

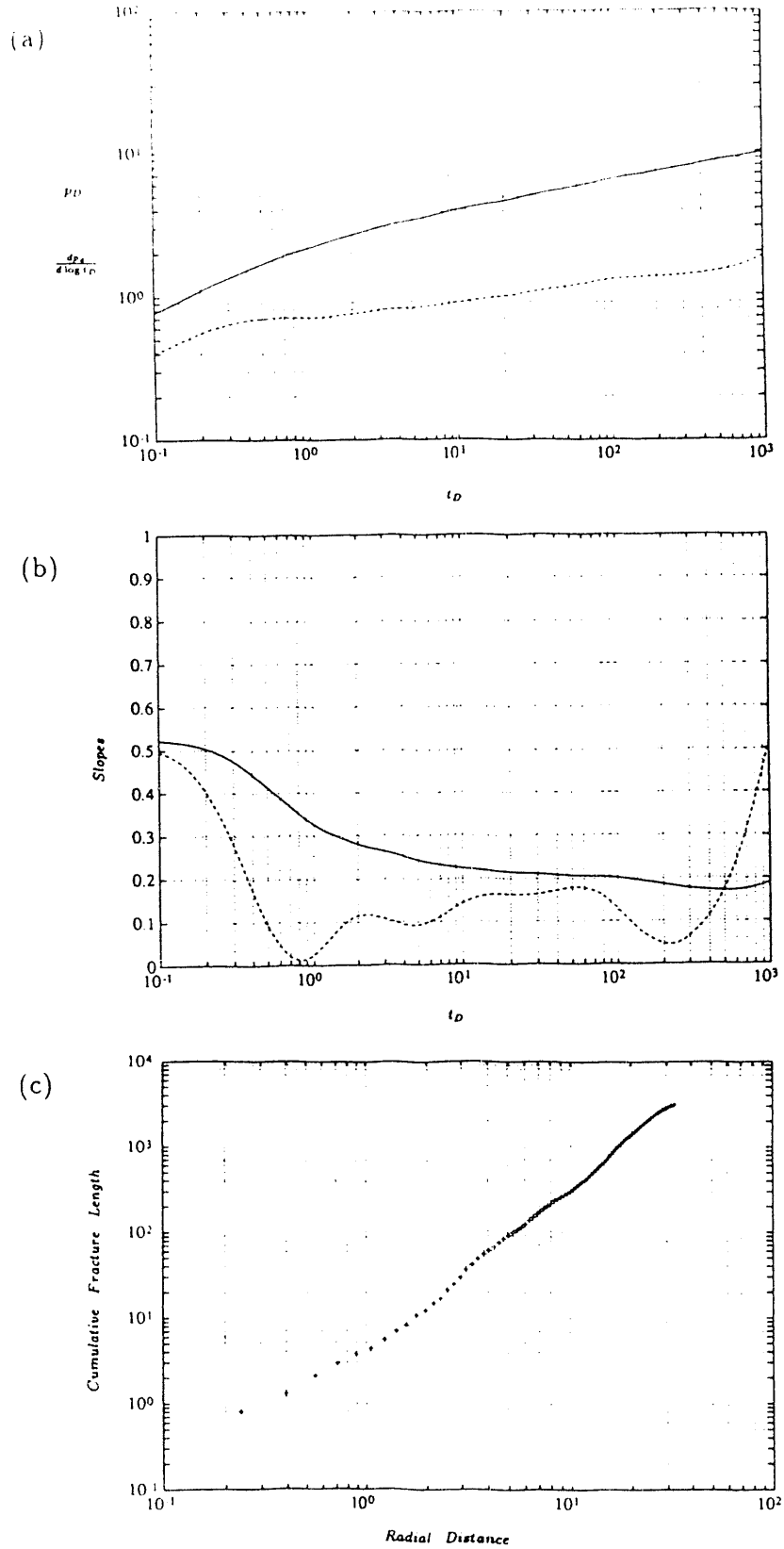

Figure 76: (a), (b) Pressure transient response for the network of Figure 70. (c) Radial fracture mass plot.

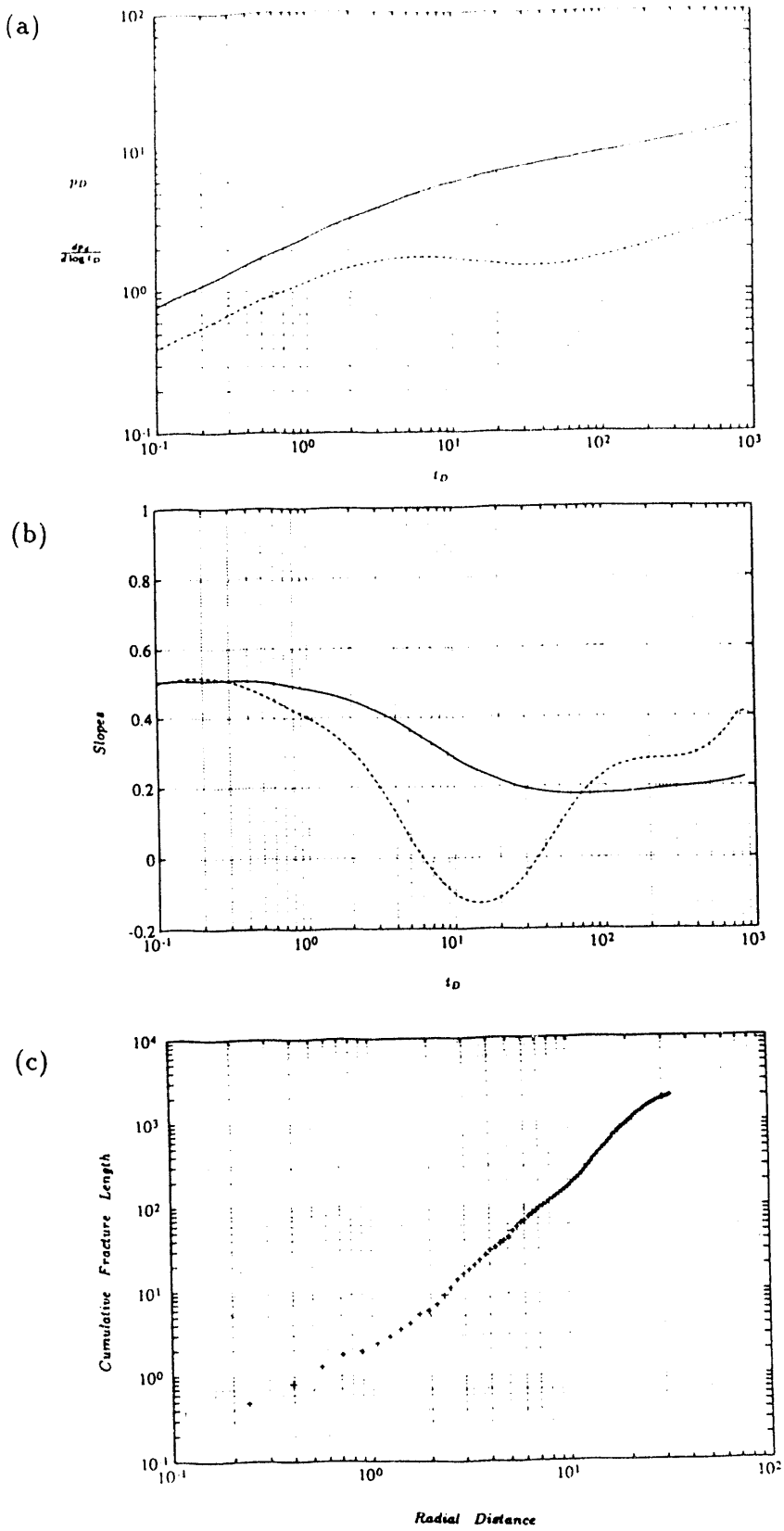

Figure 77: (a), (b) Pressure transient response for the network of Figure 71. (c) Radial fracture mass plot.

7 A THEORETICAL ANALYSIS OF VERTICAL FLOW EQUILIBRIUM

Y. C. Yortsos

7.1 INTRODUCTION

The description of displacement processes in oil reservoirs or water aquifers is often greatly simplified when the reservoir is narrow and long and the flow almost parallel. This is typically the case in many applications. Approximations under such conditions have been postulated by many researchers. In general, a Vertical Flow Equilibrium (VFE) is typically assumed (Fig. 78). Depending on the strength of gravity, the various approaches can be classified in two categories: One in which viscous forces and heterogeneity are predominant on the distribution of phases, and another in which the phases completely segregate due to gravity.

The first category is intended to capture primarily the effects of viscous forces and their interaction with heterogeneity (Fig. 79). It has been studied by several authors including Coats et al. [28], Yokoyama and Lake [144], Zapata and Lake [151], and more recently by Pande and Orr [95] and Lake et al. [72]. Since gravity is unimportant, the term vertical is meant to denote the direction along the narrow coordinate. In most of these studies a two-layer description is taken, using rather intuitive, although correct in retrospect, arguments. Extensive numerical simulation has verified the validity of the various approaches, particularly as it regards the dimensionless parameter $R_L = \frac{L}{H}\sqrt{\frac{k_V}{k_H}}$, which must take large enough values for the VFE to be applicable. Along the same lines must be considered the work by Lake and Hirasaki [71] on tracer dispersion in stratified systems, as well various phenomenological viscous fingering models, such as Koval [69], Todd and Longstaff [133] and Fayers [43]. The latter models have presently only an empirical basis, although the numerical evidence is in many cases supportive of their applicability.

The second category emphasizes gravity in addition to viscous forces and it should be more applicable to homogeneous systems of higher permeability. Not surprising, the original contributions in this direction were made in connection with groundwater aquifers, where the so-called Dupuit assumption was introduced (see [7]). Viscous, two-phase flow was studied by Dietz [35], and elaborated by Le Fur and Sourieau [73], Beckers [8] and others. A complete segregation of the immiscible phases is assumed, a sharp macroscopic interface separating the two regions (Fig. 80). Recently, Fayers and Muggeridge [44] extended this approach to tilted reservoirs with dip.

While the two classes seem to derive from the same conditions, no effort has been taken to treat them in a uniform fashion. In fact, it is not entirety clear which are the relevant parameters that demarcate in the parameter space the two regimes and where do various approximations hold. At present, most of the available evidence is numerical. While under certain conditions, this may be sufficient, it would be nonetheless desirable if a rigorous derivation were available to clearly identify the various approximations and assumptions. This is particularly the case for layered systems, where presently available formalisms are awkward and difficult to extend to many layers.

The objective of this chapter is to provide a unified approach based on a rigorous asymptotic expansion of the flow equations in long and narrow systems, where the VFE is expected to apply. First, the fundamental asymptotic analysis is developed for a model immiscible, two-phase displacement. In the absence of gravity or capillarity, an extension of the classical Buckley-Leverett equation, that also includes cross-flow terms, is obtained. Subsequently, this equation is applied to a layered systems of arbitrary number of layers. A hyperbolic non-linear system results that describes the interaction between the layers. Weak effects of capillarity and gravity are next introduced. The problem for miscible displacement is formulated in a subsequent section. Tracer dispersion in a layered system is analyzed leading to the results of [71]. Finally, we consider strong gravity and capillary effects that lead to segregated flow. The conditions for the latter are specified and we derive generalized expressions for the Dupuit and Dietz approximations. Flow segregation due to gravity-capillary equilibrium is also discussed.

7.2 ASYMPTOTIC ANALYSIS

Consider the constant rate immiscible displacement of "oil" by "water" in a long and narrow reservoir, of thickness H and length L, where $\epsilon \equiv H/L \ll 1$. For simplicity, the reservoir has no dip, but it is anisotropic and stratified with different permeabilities in the "horizontal" and "vertical" directions

$$K_H = k_H \kappa_H(X,Y) \ ; \ K_V = k_V \kappa_V(X,Y) \tag{67}$$

Here $\kappa_i > 0, (i = H, V)$ are dimensionless such that $\int_0^H \kappa_i dY = H$, when the x-dependence is neglected. Otherwise, the latter constraint is not satisfied. We normalize "horizontal" and "vertical" scales, X and Y, by L and H, respectively:

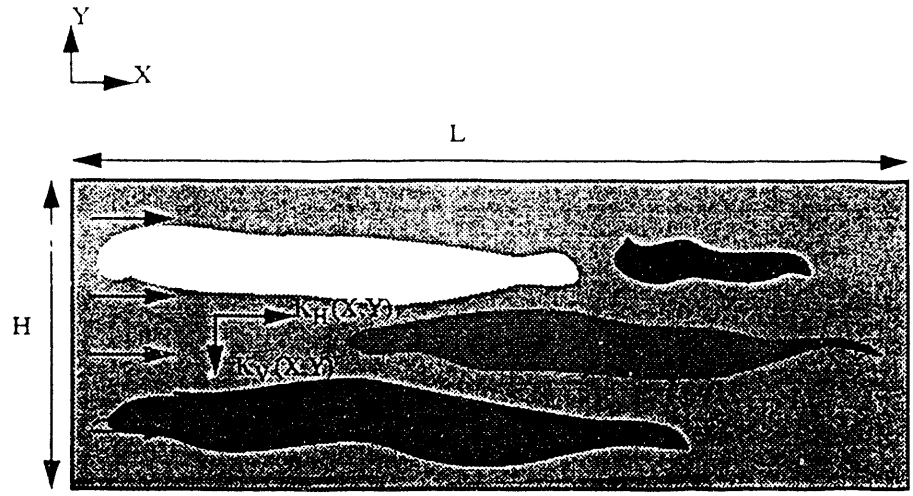

Figure 78: Schematic of heterogeneous reservoir for VFE.

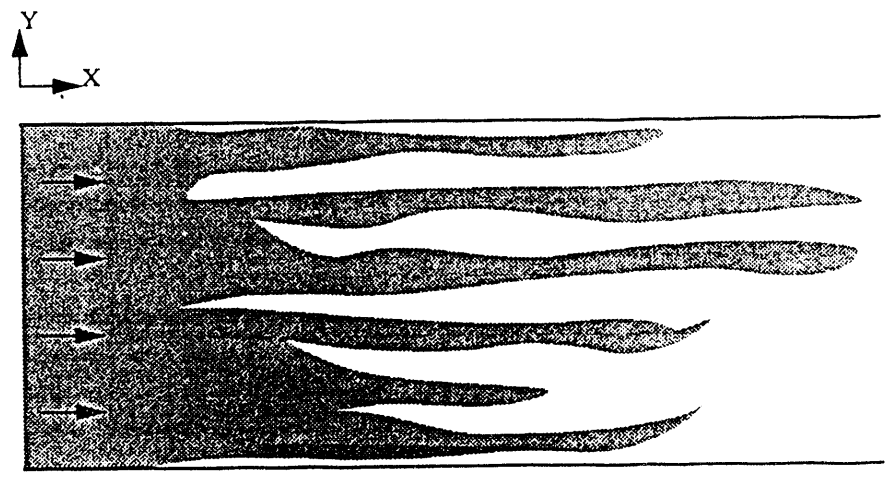

Figure 79: Schematic of viscous fingering in VFE.

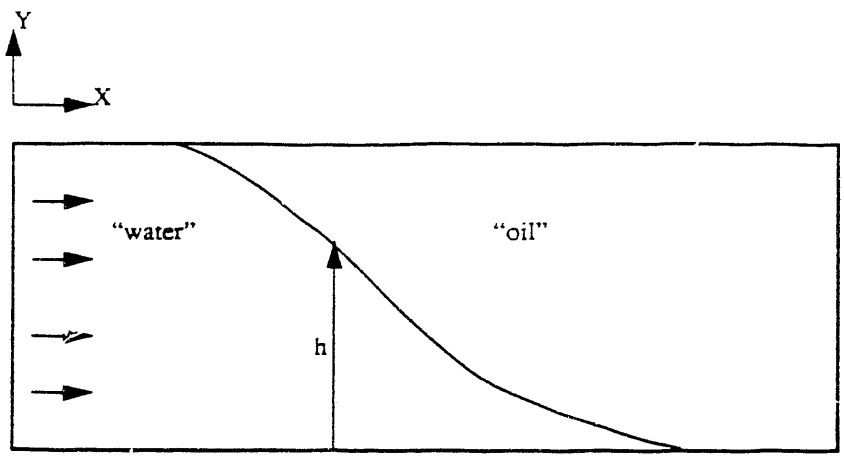

Figure 80: Schematic of gravity segregated displacement.

$$x = \frac{X}{L} \quad ; \quad y = \frac{Y}{H} \tag{68}$$

and scale all velocities by the injection velocity q, time by $\frac{L}{q}$, and the fluid pressure by $\frac{Lq\mu_o}{k_H}$. If S denotes a "water" saturation, the dimensionless balances become

$$\begin{aligned}
\epsilon[\phi\frac{\partial S}{\partial t} + \frac{\partial u_w}{\partial x}] + \frac{\partial v_w}{\partial y} &= 0 \\
\epsilon\frac{\partial}{\partial x}(u_w + u_o) + \frac{\partial}{\partial y}(v_w + v_o) &= 0 \\
u_i = -\kappa_H(x,y)\lambda_i\frac{\partial p_i}{\partial x} &\quad ; \quad i = o, w \\
\frac{\epsilon}{\delta}v_i = -\kappa_V(x,y)\lambda_i\left[\frac{\partial p_i}{\partial y} + \frac{\epsilon}{\delta}\frac{\rho_i k_V g}{q\mu_o}\right] &\quad ; \quad i = o, w
\end{aligned} \tag{69}$$

Here we defined $\delta \equiv \frac{k_V}{k_H}$, we have taken the y coordinate to increase upwards, and we have used u_i and v_i to denote the "horizontal" and "vertical" components, respectively, of the dimensionless velocity of fluid i. In the absence of capillarity and gravity, u_i and v_i can be expressed in terms of the total velocities $u \equiv u_w + u_o$ and $v \equiv v_w + v_o$, with the use of the fractional flow function $f_w(S)$.

$$u_w = u f_w(S) \ ; \ \ v_w = v f_w(S) \tag{70}$$

We recall that λ_T is the total mobility, $\lambda_T \equiv \lambda_w + \lambda_o$, where $\lambda_w \equiv \frac{\mu_o}{\mu_w} k_{rw}$ and $\lambda_o \equiv k_{ro}$, thus $f_w \equiv \lambda_w / \lambda_T$. We, then, obtain

$$\begin{aligned}
\epsilon \left[\phi \frac{\partial S}{\partial t} + \frac{\partial}{\partial x}(u f_w) \right] + \frac{\partial}{\partial y}(v f_w) &= 0 \\
\epsilon \frac{\partial u}{\partial x} + \frac{\partial v}{\partial y} &= 0 \\
u &= -\kappa_H(x,y) \lambda_T \frac{\partial p}{\partial x} \\
\frac{\epsilon}{\delta} v &= -\kappa_V(x,y) \lambda_T \frac{\partial p}{\partial y}
\end{aligned} \tag{71}$$

Since $\epsilon \ll 1$ (long and narrow reservoirs), if follows that $u = O(1)$ and $v = O(\epsilon)$, hence we may define $v = \epsilon w$, where $w = O(1)$. Substitution into (71) then yields the following

$$\begin{aligned}
\phi \frac{\partial S}{\partial t} + u \frac{\partial f_w}{\partial x} + w \frac{\partial f_w}{\partial y} &= 0 \\
\frac{\partial u}{\partial x} + \frac{\partial w}{\partial y} &= 0 \\
u &= -\lambda_T \kappa_H(x,y) \frac{\partial p}{\partial x} \\
\frac{1}{R_L^2} w &= -\lambda_T \kappa_V(x,y) \frac{\partial p}{\partial y}
\end{aligned} \tag{72}$$

where we have defined $R_L \equiv \frac{\sqrt{\delta}}{\epsilon} = \frac{L}{H}\sqrt{\frac{k_V}{k_H}}$. In this formulation, it is now evident that the only dimensionless parameter is R_L, which is precisely the parameter used in justifying the use of VFE [151]. To obtain the latter approximation, we take the limit $R_L^2 \gg 1$ and expand in a regular asymptotic expansion

$$\begin{aligned}
u &= u_0 + \frac{1}{R_L^2} u_1 + \cdots \\
w &= w_0 + \frac{1}{R_L^2} w_1 + \cdots \\
p &= p_0 + \frac{1}{R_L^2} p_1 + \cdots \\
S &= S_0 + \frac{1}{R_L^2} S_1 + \cdots
\end{aligned} \tag{73}$$

Substitution into (72) yields to leading order,

$$\begin{aligned}
\phi\frac{\partial S_0}{\partial t} + u_0\frac{\partial f_w}{\partial x} + w_0\frac{\partial f_w}{\partial y} &= 0 \\
\frac{\partial u_0}{\partial x} + \frac{\partial w_0}{\partial y} &= 0 \\
u_0 = -\lambda_T\kappa_H(x,y)\frac{\partial p_0}{\partial x} & \\
\frac{\partial p_0}{\partial y} &= 0
\end{aligned} \tag{74}$$

Eqn (74) dictates that $p_0 = p_0(x,t)$, i.e., the pressure depends on the x-coordinate only. This is the fundamental assumption of VFE or parallel flow, rigorously derived here in the limit $R_L^2 \gg 1$. Numerical evidence suggests that VFE is satisfied quite well when $R_L \geq 10$. This is consistent with our asymptotic expansion, where the next order enters at $O(\frac{1}{R_L^2})$, hence the error made by retaining only the first term is 1% or less. The rigorous identification of the parameter R_L as the relevant variable for the validity of the VFE represents the first important result of this section.

We should point out that implicit in the derivation of (74d) was the assumption $\kappa_V \neq 0$. For a layered system, where the permeability $\kappa_V = \kappa_V(y)$ may vanish somewhere, one simply needs to redefine the reservoir thickness and VFE applies without problem (Lake et al., [72]). The problem is somewhat more complicated, however, when the system is not layered. At least near the regions where κ_V vanishes, the VFE does not apply. This may complicate the analysis, thus it will not be discussed further in this section.

Unless otherwise noted, for convenience, we shall omit subscripts 0 and H. The next step is to eliminate $\frac{\partial p}{\partial x}$ by integrating (74c) along the y-coordinate, to obtain

$$u = \frac{\lambda_T(S)\kappa(x,y)}{\int_0^1 \lambda_T(S)\kappa(x,y)dy} \tag{75}$$

where we have assumed a constant injection rate (although the extension to a variable rate is straightforward). Subsequently, we eliminate w by integrating (74b)

$$w = -\int_0^y \frac{\partial u}{\partial x}dy \tag{76}$$

where a no-flow boundary condition was used. Final substitution into (74a) yields the result

$$\phi\frac{\partial S}{\partial t} + \frac{\lambda_T\kappa}{\int_0^1 \lambda_T\kappa dy}\frac{\partial f_w}{\partial x} - \frac{\partial}{\partial x}\left[\frac{\int_0^y \lambda_T\kappa dy}{\int_0^1 \lambda_T\kappa dy}\right]\frac{\partial f_w}{\partial y} = 0 \tag{77}$$

This equation represents the second important result of this chapter. The equation is a first-order, hyperbolic PDE, but in two spatial dimensions (x, y), and it contains only saturation S as the dependent variable. When κ and S are independent of y, it naturally reduces to the traditional 1-D Buckley-Leverett (B-L) equation

$$\phi \frac{\partial S}{\partial t} + \frac{\partial f_w}{\partial x} = 0 \tag{78}$$

In this sense, equation (77) is a 2-D generalization of the B-L equation under the conditions of VFE. We must point out, however, that because of the reduction in the dimensionality, equation (77) cannot satisfy all boundary conditions, thus it is not expected to hold near all boundaries. This becomes more apparent below.

Before we proceed, let us recall the conditions for the validity of the above. It was derived in the limit $R_L \gg 1$ in the absence of gravity and capillarity. The latter condition requires that the gravity terms in (69d) are small, or

$$N_G \ll 1 \tag{79}$$

where the gravity number was defined, $N_G \equiv \frac{H k_H g(\rho_w - \rho_o)}{L \mu_o q}$ (note the difference in notation with Fayers and Muggeridge, [44]. This allows for both equations (74d) and (75) to remain valid. However, in order for gravity and capillarity to be also absent from (70) and (77), one needs the stronger constraints (see also below)

$$N_G \ll \frac{1}{R_L^2} \text{ and } N_{CT} \ll \epsilon \tag{80}$$

where the transervse capillary number is $N_{CT} \equiv \frac{\sqrt{k_V}}{H N_{ca}}$ (see [144]). As pointed out in the introduction, under these conditions, equation (77) is a VFE approximation that emphasizes viscous cross-flow and heterogeneity. It is assumed, therefore, to control viscous fingering in such systems.

7.3 LAYERED RESERVOIRS

While the full solution of (77) is possible, it is more practical to consider a discrete treatment of the y-dependence instead. For example, this would be the case of a layered reservoir (Fig. 81). We

Figure 81: Schematic of layered reservoir for VFE.

take

$$\begin{aligned} \kappa(x,y) &\simeq \kappa_i(x) \\ S(x,y) &\simeq S_i(x) \end{aligned} \; ; \frac{i-1}{N} < y < \frac{i}{N}; \quad i = 1,\ N \tag{81}$$

Here, N is the number of equal thickness layers of the system. For simplicity, we shall denote $\psi = \lambda_T \kappa / \int_0^1 \lambda_T \kappa dy$. We may then integrate (77) over y from $\frac{i-1}{N}$ to $\frac{i}{N}$, to obtain the system

$$\phi_i \frac{\partial S_i}{\partial t} + \psi_i \frac{\partial f_i}{\partial x} - (f_i - f_{i-1}) \frac{\partial}{\partial x} \sum_1^{i-1} \psi_j = 0 \ ; \ i = 1, N \tag{82}$$

Here, we have approximated y-integrals by sums, have denoted $f_i \equiv f_w(S_i), \psi_i \equiv \psi(S_i; \kappa_i)$ and defined $f_o \equiv \psi_o \equiv 0$. We may recast (82) in terms of a hyperbolic system

$$\frac{\partial \mathbf{S}}{\partial t} + \mathbf{A} \frac{\partial \mathbf{S}}{\partial x} = \mathbf{B} \frac{\partial \kappa}{\partial x} \tag{83}$$

where $\mathbf{S} = [S_1, S_2, \ldots, S_N]^T$ and $\kappa = [\kappa_1, \kappa_2, \ldots, \kappa_N]^T$ are $(N \mathrm{x} 1)$ vectors. $\mathbf{A} = [a_{ij}]$ and $\mathbf{B} = [b_{ij}]$ $(i, j = 1, N)$ are N x N square matrices with the following coefficients. Matrix $\mathbf{A}$ consists of two terms $\mathbf{A} = \mathbf{D} - \mathbf{E}$, where

$$\begin{aligned} d_{ii} &= \frac{\lambda_T(S_i)\kappa_i}{\phi_i \Lambda} \left(\frac{\partial f_w}{\partial S} \right)_i \\ d_{ij} &= 0, i \neq j \end{aligned} \tag{84}$$

and

$$
\begin{aligned}
e_{ij} &= \frac{(f_w(S_i) - f_w(S_{i-1}))}{\phi_i \Lambda^2} \kappa_j \times \\
&\left(\frac{\partial \lambda_T}{\partial S}\right)_j \begin{cases} \frac{1}{N}\sum_{i}^{N} \lambda_T(S_m)\kappa_m & ; \quad j \leq i-1 \\ -\frac{1}{N}\sum_{1}^{i-1} \lambda_T(S_m)\kappa_m & ; \quad j \geq i \end{cases} \\
&e_{ii} = 0
\end{aligned}
\tag{85}
$$

The inhomogeneous matrix **B** has coefficients

$$
\begin{aligned}
b_{ij} &= \frac{(f_w(S_i) - f_w(S_{i-1}))}{\phi_i \Lambda^2} \times \\
&\lambda_T(S_j) \begin{cases} \frac{1}{N}\sum_{i}^{N} \lambda_T(S_m)\kappa_m & ; \quad j \leq i-1 \\ -\frac{1}{N}\sum_{1}^{i-1} \lambda_T(S_m)\kappa_m & ; \quad j \geq i \end{cases}
\end{aligned}
\tag{86}
$$

In the above we have denoted $\Lambda \equiv \frac{1}{N}\sum_{i}^{N} \lambda_T(S_m)\kappa_m$.

This general formulation in discrete form is free of empirical arguments and represents a rigorous result, apparently also obtained here for the first time.

We observe the following:

1. Matrix **A** is neither diagonal nor symmetric. This is because of the coupling between adjacent layers of different properties. The coupling is due to the variation of the mobility with saturation.

2. When the layer permeabilities also depend on position ($\frac{\partial \kappa}{\partial x} \neq 0$) a source (sink) term arises on the RHS of (83). Thus, in this case, heterogeneity acts in the form of a reaction term. This feature is also due to the coupling between the layers and it is absent in the single layer case.

3. When all layer properties are the same, the system reduces to the B-L equation, as expected.

4. For a two-layer system, we may further simplify ($\Lambda = \lambda_T(S_1)\kappa_1 + \lambda_T(S_2)\kappa_2$) to obtain

$$d_{11} = \frac{\lambda_T(S_1)\kappa_1}{\phi_1\Lambda}\left(\frac{\partial f_w}{\partial S}\right)_1 \tag{87}$$

$$d_{22} = \frac{\lambda_T(S_2)\kappa_2}{\phi_2\Lambda}\left(\frac{\partial f_w}{\partial S}\right)_2 \tag{88}$$

$$d_{12} = d_{21} = 0 \tag{89}$$

$$e_{11} = e_{12} = 0 \tag{90}$$

$$e_{21} = \frac{1}{2}\left(\frac{f_w(S_2) - f_w(S_1)}{\phi_2\Lambda^2}\right)\kappa_1\kappa_2\left(\frac{\partial\lambda_T}{\partial S}\right)_1\lambda_T(S_2) \tag{91}$$

$$e_{22} = -\frac{1}{2}\left(\frac{f_w(S_2) - f_w(S_1)}{\phi_2\Lambda^2}\right)\kappa_1\kappa_2\left(\frac{\partial\lambda_T}{\partial S}\right)_2\lambda_T(S_1) \tag{92}$$

$$b_{11} = 0, \quad b_{12} = 0 \tag{93}$$

$$b_{21} = \frac{1}{2}\left(\frac{f_w(S_2) - f_w(S_1)}{\phi_2\Lambda^2}\right)\lambda_T(S_1)\lambda_T(S_2)\kappa_2 \tag{94}$$

$$b_{22} = -\frac{1}{2}\left(\frac{f_w(S_2) - f_w(S_1)}{\phi_2\Lambda^2}\right)\lambda_T(S_1)\lambda_T(S_2)\kappa_1 \tag{95}$$

The above contains the formulation of Zapata and Lake [151] and [95], but it is here also augmented by permeability heterogeneity along the x-direction. The latter result is also new.

7.4 EFFECTS OF CAPILLARITY AND GRAVITY

When the injection rates are low enough for capillary and gravity effects to be of some importance, but not very low for the phases to be segregated, equations (70) must be reformulated. We obtain

$$\begin{aligned} u_w &= uf_w(S) + \frac{N_{CT}}{R_L}\kappa_H\lambda_o f_w\frac{\partial\Pi_c}{\partial x} \\ v_w &= vf_w(S) + \kappa_V\lambda_o f_w\left\{N_{CT}\frac{\partial\Pi_c}{\partial y} - \frac{\delta}{\epsilon}N_G\right\} \end{aligned} \tag{96}$$

where a J-function representation was used for the capillary pressure, and Π_c is the dimensionless capillary pressure.

Equations (71), (77) are appropriately modified. For instance, (71a) becomes

$$\epsilon\left[\phi\frac{\partial S}{\partial t}+\frac{\partial}{\partial x}(uf_w+\frac{N_{CT}}{R_L}\kappa_H\lambda_o f_w\frac{\partial\Pi_c}{\partial x})\right]+$$
$$\frac{\partial}{\partial y}\left[vf_w+\kappa_V\lambda_o f_w\left\{N_{CT}\frac{\partial\Pi_c}{\partial y}-\frac{\delta}{\epsilon}N_G\right\}\right]=0 \tag{97}$$

We may proceed in exactly the same way as before, by substituting $v=\epsilon w$, identifying the large parameter as $R_L^2=\frac{\delta}{\epsilon^2}$ and expanding appropriately. In order for the flow not to be segregated, condition (79) must still hold, $N_G \ll 1$. The longitudinal capillary term can be reglected, except near sharp fronts, much like in the classical Buckley-Leverett problem. However, transverse capillarity and gravity can be retained, if the following conditions are valid, $N_{CT}\sim O(\epsilon)$ and $N_G\sim O(\frac{1}{R_L^2})$. Then, the following equation is obtained

$$\phi\frac{\partial S}{\partial t}+\frac{\lambda_T\kappa}{\int_0^1\lambda_T\kappa dy}\frac{\partial f_w}{\partial x}-\frac{\partial}{\partial x}\left[\frac{\int_0^y\lambda_T\kappa dy}{\int_0^1\lambda_T\kappa dy}\right]\frac{\partial f_w}{\partial y}=$$
$$-\frac{\partial}{\partial y}\left[\kappa_V\lambda_o f_w\left\{\frac{N_{CT}}{\epsilon}\frac{\partial\Pi_c}{\partial y}-R_L^2N_G\right\}\right] \tag{98}$$

The relative importance of gravity over capillarity depends on the dimensionless ratio

$$\frac{\epsilon R_L^2 N_G}{N_{CT}}=\frac{g\Delta\rho H\sqrt{k_V}}{\gamma} \tag{99}$$

which is rate-independent. For thin beds of low vertical permeability, capillarity dominates. Then, if the typical assumption is made about Π_c as a single function of S, the RHS above represents capillary spreading (one should keep in mind, however, that permeability heterogeneity is likely to also imply capillary heterogeneity as well, see Yortsos and Chang, [147]. This case is of interest but will not be considered in this study). As shown below in the case of miscible displacement, capillary spreading can be equivalently represented in terms of a macro-dispersivity. Capillary effects in VFE were considered by Yokoyama and Lake [144].

When gravity dominates over capillarity in (98), then

$$\phi\frac{\partial S}{\partial t}+\frac{\lambda_T\kappa}{\int_0^1\lambda_T\kappa dy}\cdot\frac{\partial f_w}{\partial x}-\frac{\partial}{\partial x}\left[\frac{\int_0^y\lambda_T\kappa dy}{\int_0^1\lambda_T\kappa dy}\right]\frac{\partial f_w}{\partial y}=$$
$$+\Theta_G\frac{\partial}{\partial y}\left[\kappa_V\lambda_o f_w\right] \tag{100}$$

where we defined $\Theta_G=\frac{k_V g}{\mu_o g}(\rho_w-\rho_o)$. Upon integration over y between $\frac{i-1}{N}$ and $\frac{i}{N}$ the contribution of the gravity term acts as a source/sink. Then, equation (83) must be modified as follows

$$\frac{\partial\mathbf{S}}{\partial t}+\mathbf{A}\frac{\partial\mathbf{S}}{\partial x}=\mathbf{B}\frac{\partial\kappa}{\partial x}+\mathbf{G} \tag{101}$$

where the ith element of the $\mathbf{G}$ vector is

$$g_i=N\Theta_G[\kappa_V\lambda_o(S_i)f_w(S_i)-\kappa_V\lambda_o(S_{i-1})f_w(S_{i-1})] \tag{102}$$

If the flow rates are quite low, such that $N_G\sim O(1)$, the phases are likely to segregated. This case is described in a later section.

7.5 MISCIBLE DISPLACEMENT

Consider, next, a first-contact miscible process in the limit of negligible gravity, $N_G\ll 1$. The mathematical description consists of equations (71b) - (71d), where the total mobility is now a normalized inverse viscosity, $\lambda_T(C)=\frac{1}{\mu(C)}$, and where the dimensionless concentration C is the dependent variable. The latter satisfies an advection-dispersion equation, which reads in dimensional notation

$$\epsilon\left(\phi\frac{\partial C}{\partial t}+u\frac{\partial C}{\partial x}\right)+v\frac{\partial C}{\partial y}=$$
$$\frac{\epsilon}{Pe_L}\cdot\frac{\partial^2 C}{\partial x^2}+\frac{\alpha_T}{\alpha_L}\frac{1}{\epsilon Pe_L}\frac{\partial^2 C}{\partial y^2} \tag{103}$$

This equation is the analogue of (71a) to miscible displacement. In the above, we have denoted with α_L and α_T the longitudinal and transverse dispersivities, respectively, and we expressed longitudinal dispersion with the Peclet number, Pe_L. In the case of mechanical dispersion only,

$$Pe_L\simeq\frac{L}{\alpha_L} \tag{104}$$

Typically, $L \gg \alpha_L$, thus longitudinal dispersion can be neglected (except near sharp fronts). To obtain asymptotic results we follow the same procedure as above to get the final result

$$\phi\frac{\partial C}{\partial t} + \frac{\lambda\kappa}{\int_0^1 \lambda\kappa dy}\frac{\partial C}{\partial x} - \frac{\partial}{\partial x}\left[\frac{\int_0^y \lambda\kappa dy}{\int_0^1 \lambda\kappa dy}\right]\frac{\partial C}{\partial y} = N_{TD}\frac{\partial^2 C}{\partial y^2} \tag{105}$$

where, subscript T was omitted for simplicity. In (105) we have neglected longitudinal dispersion, but have retained transverse dispervion by assuming that $N_{TD} \equiv \frac{\alpha_T}{\alpha_L}\frac{1}{\epsilon^2 Pe_L} \simeq \frac{\alpha_T}{\epsilon H}$ remains finite in the limit of small ϵ. When transverse dispersion is neglected, the previous equation (77) is recovered, if the identification is made $S \leftrightarrow C$, $\lambda_T \leftrightarrow \lambda$, and $f_w \leftrightarrow C$.

In the latter case, the equivalent of (83) reads

$$\frac{\partial \mathbf{C}}{\partial t} + \mathbf{A}\frac{\partial \mathbf{C}}{\partial x} = \mathbf{B}\frac{\partial \kappa}{\partial x} \tag{106}$$

where $\mathbf{C} = [C_1, C_2, \cdots, C_N]^T$. The representation becomes simpler if we take the approximate mobility dependence $\lambda(C) = e^{rC}$, where r measures the mobility ratio, $r = \ell n M$. Then, for constant $\phi_i = \phi$, which can subsequently be absorbed in the dimensionless time, the coefficient matrices reduce to the following

$$\begin{aligned} d_{ii} &\equiv d_i = \frac{\kappa_i e^{rC_i}}{\frac{1}{N}\sum_1^N \kappa_j e^{rC_j}}, \\ e_{ij} &= r(C_i - C_{i-1})d_j \begin{cases} \frac{1}{N}\sum_i^N d_m, & j \le i-1 \\ -\frac{1}{N}\sum_1^{i-1} d_m, & i \le j \end{cases} \end{aligned} \tag{107}$$

and

$$b_{ij} = \frac{e_{ij}}{r\kappa_j} \tag{108}$$

One notes the interesting property that the sum of all the elements of each column of E vanishes, $\sum_{j=1}^N e_{ij} = 0$.

When the solute is not passive, an exact solution to the system is not available. Some interesting remarks can be made in the two limits where $r \to +\infty$ (unstable displacement, $M \gg 1$) or when $r \to -\infty$ (stable displacement, $M \ll 1$). In these two cases it can be shown readily that the matrix

C becomes diagonal and, furthermore, that the only element with non-zero velocity is the layer with the highest ($r \to \infty$) or the lowest concentration ($r \to -\infty$), respectively. To show this, consider (107a) and rearrange as follows

$$d_i = \frac{\kappa_i}{\frac{1}{N}\sum_1^N \kappa_j e^{r(C_j - C_i)}} \tag{109}$$

It is then straightforward that, in the limit $r \to \infty$, then $d_i \to 0$ for all i, except for $i = max$, where C_{max} is the maximum concentration, hence $d_{max} \to N$. The opposite applies for the case $r \to \infty$, in which $d_i \to 0$ for all i, except for $i = min$, where C_{min} is the minimum concentration, hence $d_{min} \to N$. In summary, in the case of very unstable displacement ($M \gg 1$), the highest concentration travels the fastest, in accord with viscous fingering notions. While, for very stable displacement ($M \ll 1$), it is the lowest concentration that travels the fastest, also as expected. Besides this simple result, however, equation (106) contains a much richer structure. This is currently under study.

7.6 TRACER DISPERSION

In the passive solute case, where the viscosity is constant ($r = 0$), the off-diagonal terms e_{ij} vanish and we obtain the linear system

$$\frac{\partial C_i}{\partial t} + \kappa_i \frac{\partial C_i}{\partial x} = -(C_i - C_{i-1})\frac{\partial}{\partial x}(\sum_i^N \kappa_m) \tag{110}$$

where, in the above κ_i is to be interpreted as normalized with the average permeability of a cross section. When $\frac{\partial \kappa_i}{\partial x} = 0$, this has the solution

$$C_i = H(t\kappa_i - x) \tag{111}$$

where $H(z)$ is the step function. In the continuum limit

$$\bar{C} = \lim_{n\to\infty} \frac{1}{N}\sum_1^N C_i \tag{112}$$

we further get

$$\bar{C} = \int_{\kappa_{min}}^{\kappa_{max}} f(\kappa) H(\kappa t - x) d\kappa \tag{113}$$

where $f(\kappa)$ is the *pdf* of κ. If we define the cumulative distribution $F(\kappa) = \int_{\kappa_{min}}^{\kappa} f(\kappa)d\kappa$, then we may rearrange to get

$$\bar{C} = H(t\kappa_{max} - x) - F(\frac{x}{t}) \tag{114}$$

For a more general result in the case $\frac{\partial \kappa_1}{\partial x} = 0$, we consider transverse dispersion. We shall make use of the continuum formulation (104) and write (for ϕ = const.)

$$\frac{\partial C}{\partial t} + \kappa(y)\frac{\partial C}{\partial x} = N_{TD}\frac{\partial^2 C}{\partial y^2} \tag{115}$$

This equation represents Taylor-Aris dispersion as applied to porous media flows [71]. One can readily show that it tends asymptotically to macro-dispersion. Indeed, by using a coordinate moving with the average speed $\xi = x - t$, one gets [132]

$$(\kappa(y) - 1)\frac{\partial C}{\partial \xi} \cong N_{TD}\frac{\partial^2 C}{\partial y^2} \tag{116}$$

which can be integrated to

$$C = \frac{1}{N_{TD}}\frac{\partial \bar{C}}{\partial \xi}\int_0^y \int_0^{y'} (\kappa(y'') - 1)dy''dy' \tag{117}$$

In the moving frame of reference the mass flux over a cross-section is

$$\int_0^1 (\kappa(y) - 1)Cdy =$$

$$\frac{1}{N_{TD}}\int_0^1 (\kappa(y) - 1)\int_0^y \int_0^{y'} (\kappa(y'') - 1)dy''dy'dy \cdot \frac{\partial \bar{C}}{\partial \xi} \tag{118}$$

thus, yielding the macro-dispersion approximation

$$\frac{\partial \bar{C}}{\partial t} + \frac{\partial \bar{C}}{\partial x} = D_m\frac{\partial^2 \bar{C}}{\partial x^2} \tag{119}$$

where

$$D_m \equiv \frac{1}{N_{TD}}\int_0^1 (\kappa(y) - 1)\int_0^y \int_0^{y'} (\kappa(y'') - 1)dy''dy'dy \tag{120}$$

In dimensional notation, the macrodispersity is expressed as

$$\alpha_m = \frac{1}{H\alpha_T(k_H)^2}\int_0^H (K_H(y) - k_H)$$
$$\int_0^y \int_0^{y'} (K_H(y'') - k_H)dy''dy'dy \tag{121}$$

This result was first derived by Lake and Hirasaki [71] by different means.

7.7 GRAVITY SEGREGATED FLOW

Consider, next, the case where the gravity terms in (69) are strong, $N_G \sim O(1)$. Here, the approach is somewhat different. Gravity effects must be also considered in the distribution of pressure, not only in the equation for the mass balance. Consider, first, negligible capillarity in the immiscible displacement case. The general expression for the vertical flow velocity was derived before

$$\frac{\epsilon}{\delta} v = -\kappa_v \left[\lambda_T \frac{\partial p}{\partial y} + N_G(\lambda_w \bar{\rho}_w + \lambda_o \bar{\rho}_o) \right] \tag{122}$$

where $\bar{\rho}_i \equiv \frac{\rho_i}{\rho_w - \rho_o}$. In view of the fact that $v = \epsilon w$, we must take

$$\lambda_T \frac{\partial p}{\partial y} + N_G(\lambda_w \bar{\rho}_w + \lambda_o \bar{\rho}_o) = 0 \tag{123}$$

thus gravity terms must be considered in the distribution of pressure. This is a true VFE. However, the fluids now become segregated and the previous analysis is not necessary. To show that flow segregation occurs we consider (96b) in the absence of capillary effects

$$v_w = \epsilon \left[w f_w(S) - \kappa_V \lambda_o f_w N_G R_L^2 \right] \tag{124}$$

All terms above must be $O(1)$ or less. However, since we assumed $N_G \sim O(1)$, the last term on the RHS would diverge at large R_L, unless $k_V \lambda_o f_w$ vanishes, thus

$$\lambda_o f_w \to 0 \tag{125}$$

The solution of equation (125) is segregated flow

$$S = \begin{cases} S_{wr} & ; \quad h < y < 1 \\ 1 - S_{or} & ; \quad 0 < y < h \end{cases} \tag{126}$$

where the location of the "macroscopic interface" $h \equiv h(x,t)$ is to be determined as a function of position and time (Fig. 79). This is the classical case of gravity tonguing which as shown above, holds under the conditions $R_L \gg 1, N_G \sim O(1)$. The first is a geometric condition, while the second also involves flow rates. To our knowledge, this is the first time that flow segregation was proved analytically.

To obtain the evolution of h, one needs to consider an integral balance. For this, equation (72a) is integrated over y between 0 and 1 to yield

$$\phi\frac{\partial}{\partial t}\int_0^1 S dy + \int_0^1 \frac{\partial}{\partial x}(u f_w) dy = 0 \tag{127}$$

Next, we use (123) to solve with respect to p. We obtain after considerable algebra

$$\frac{\partial p}{\partial x} = N_G \frac{\partial}{\partial x}\left[\int_1^y \frac{(\lambda_w \bar{\rho}_w + \lambda_o \bar{\rho}_o) dy}{\lambda_T}\right] + \frac{\partial \Pi}{\partial x} \tag{128}$$

where $\Pi \equiv \Pi(x,t)$ is the presure at $y = 1$ and depends on x and t only. Our ultimate goal is to obtain an expression for u. By subsequent substitution of (128) into (69b) and (127), we finally get

$$\phi\frac{\partial}{\partial t}\int_0^1 S dy + N_G \int_0^1 \frac{\partial}{\partial x}$$
$$\left\{\kappa_H \lambda_T f_w \frac{\partial}{\partial x}\left(\int_1^y \left(\frac{\lambda_w \bar{\rho}_w + \lambda_o \bar{\rho}_o}{\lambda_T}\right) dy' - \Pi\right)\right\} dy = 0 \tag{129}$$

Next, the total mass balance is considered. In a straightforward manner it can be shown that the following equation results

$$N_G \int_0^1 \frac{\partial}{\partial x}$$
$$\left\{\kappa_H \lambda_T \frac{\partial}{\partial x}\left(\int_1^y \left(\frac{\lambda_w \bar{\rho}_w + \lambda_o \bar{\rho}_o}{\lambda_T}\right) dy' - \Pi\right)\right\} dy = 0 \tag{130}$$

The two equations must be solved in conjection with the distribution (126). We illustrate this application below.

7.8 THE DUPUIT AND DIETZ APPROXIMATIONS

Under the full segregation assumption, consider that the "oil" phase is "air" (switch for a moment to subscript a) so that we take $\mu_a \ll \mu_w$ and Π =const. This conveniently eliminates the last terms in (129) and (130). Expression (126) can be used to evaluate all the integrals. For example, we have

$$\frac{\lambda_w \bar{\rho}_w + \lambda_a \bar{\rho}_a}{\lambda_T} = \begin{cases} \bar{\rho}_a & ; \quad h < y < 1 \\ \bar{\rho}_w & ; \quad 0 < y < h \end{cases} \tag{131}$$

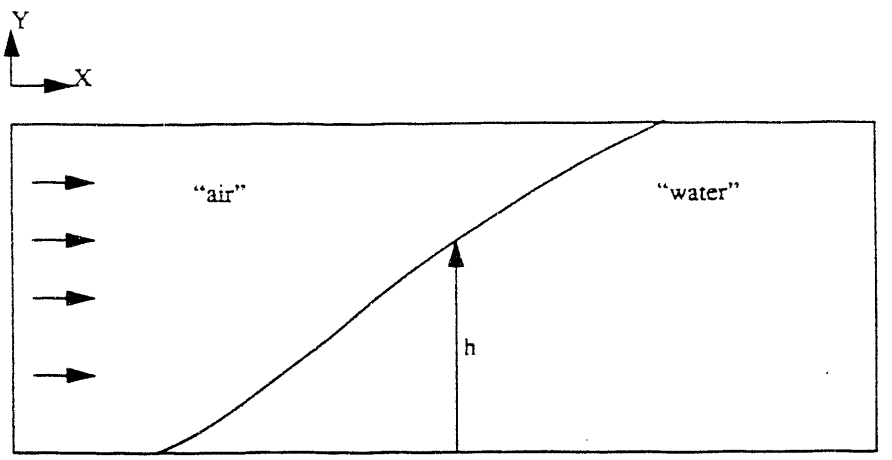

Figure 82: Schematic of air-water system for Dupuit assumption.

Hence,

$$\int_1^y []dy' = \begin{cases} (y-1)\bar{\rho}_a & ; \quad h < y < 1 \\ (h-1)\bar{\rho}_a + (y-h)\bar{\rho}_w & ; \quad 0 < y < h \end{cases} \tag{132}$$

thus,

$$\frac{\partial}{\partial x}\int_1^y []dy' = \begin{cases} 0 & ; \quad h < y < 1 \\ (\bar{\rho}_a - \bar{\rho}_w)\frac{\partial h}{\partial x} & ; \quad 0 < y < h \end{cases} \tag{133}$$

Proceeding similarly with the evaluation of the other integrals the final result is obtained

$$\phi\frac{\partial h}{\partial t} = N'_G\frac{\partial}{\partial x}\left[\int_0^h \kappa_H(x,y)dy \cdot \frac{\partial h}{\partial x}\right] \tag{134}$$

where $N'_G = N_G/M$ and M is the ratio of the mobilities of the displacing to the displaced phase, (here $M = \frac{\mu_w k_{ra}(S_{wr})}{\mu_a k_{rw}(1-S_{ar})}$). This is the standard, non-linear diffusion equation used traditionally in the water infiltration literature (Fig. 82). It usually arises under the so-called Dupuit approximation where $\kappa_H = 1$ (see [7]). Here, it was derived explicity, rigorously, and more generally.

In the more general case, a similar approach applies. The evaluation of the various integrals is much simplified, if generalized functions (like step and delta functions and their derivatives) are used. For instance, we can take

$$\lambda_T = \frac{1}{M} H(y-h) + H(h-y) \tag{135}$$

so that the integral in (129) is expressed in the compact form $\bar{\rho}_o(y-1)H(y-h) + (\bar{\rho}_o(h-1) + \bar{\rho}_w(y-h))H(h-y)$, etc. The properties of the generalized functions needed are $H'(z) = \delta(z)$ and $z\delta'(z) = -\delta(z)$, where $\delta(z)$ is the delta function of z. Without going into the considerable details, we shall only present the final results. The total mass balance yields

$$\begin{aligned} &N_G \frac{\partial}{\partial x}\left[\int_0^h \kappa_H dy \cdot \frac{\partial h}{\partial x}\right] - \\ &\frac{\partial}{\partial x}\left[\left(\int_0^h \kappa_H dy + \frac{1}{M}\int_h^1 \kappa_H dy\right) \cdot \frac{\partial \Pi}{\partial x}\right] = 0 \end{aligned} \tag{136}$$

while the "water" mass balance becomes

$$\begin{aligned} &\phi \frac{\partial h}{\partial t} + M N_G \frac{\partial}{\partial x}\left[\int_0^h \kappa_H dy \cdot \frac{\partial h}{\partial x}\right] - \\ &M \frac{\partial}{\partial x}\left[\int_0^h \kappa_H dy \cdot \frac{\partial \Pi}{\partial x}\right] = 0 \end{aligned} \tag{137}$$

Here, $M = \frac{\mu_o k_{rw}(1-S_{or})}{\mu_w k_{ro}(S_{wr})}$. We can integrate (136) once with respect to x to get

$$\begin{aligned} &N_G \int_0^h \kappa_H dy \cdot \frac{\partial h}{\partial x} - \\ &\left(\int_0^h \kappa_H dy + \frac{1}{M}\int_h^1 \kappa_H dy\right) \frac{\partial \Pi}{\partial x} = C \end{aligned} \tag{138}$$

where $C = 1$, without loss, and then eliminate $\frac{\partial \Pi}{\partial x}$ between (137) and (138) to obtain the final equation

$$\begin{aligned} &\phi \frac{\partial h}{\partial t} + \frac{\partial}{\partial x}\left[\frac{\int_0^h \kappa_H dy}{\int_0^h \kappa_H dy + \frac{1}{M}\int_h^1 \kappa_H dy}\right] = \\ &N_G \frac{\partial}{\partial x}\left[\frac{\int_0^h \kappa_H dy \int_h^1 \kappa_H dy}{\int_0^h \kappa_H dy + \frac{1}{M}\int_h^1 \kappa_H dy} \frac{\partial h}{\partial x}\right] \end{aligned} \tag{139}$$

This is the generalization of the well known parallel flow approximation, derived by Dietz [35] for the case of constant permeability. The process can be approximated as an 1 - D displacement

with equivalent "saturation" $\bar{S} = S_{wr} + h(1 - S_{or} - S_{wr})$, equivalent relative permeabilities given by $\bar{k}_{rw} = k_{rw}(1 - S_{or}) \int_0^h \kappa_H dy$ and $\bar{k}_{ro} = k_{ro}(S_{or}) \int_h^1 \kappa_H dy$, and a straight line "capillary pressure" with dispersion coefficient N_G.

The pseudofunctions become straight-lines when the permeability is constant [35]. In any other case, they are non-linear functions of $\bar{S}$, and, in fact, they may also vary with position x. Clearly, because of the integral form, the order of the layers affects drastically the shape of the pseudofunctions (Lake et al., [72]).

7.9 CAPILLARITY-GRAVITY SEGREGATION

When the dimensionless ratio in (99) is not large, capillarity is also of importance. The equivalent of (124) is now

$$v_w = \epsilon \left[w f_w(S) + \kappa_V \lambda_o f_w \left(\frac{N_{CT}}{\epsilon} \frac{\partial \Pi_C}{\partial y} - N_G R_L^2 \right) \right] \tag{140}$$

Following the same arguments as before, when N_{CT} and N_G are not small, we are led to the capillary equilibrium condition

$$N_{CT} \frac{\partial \Pi_c}{\partial y} = \frac{\delta}{\epsilon} N_G \tag{141}$$

which can be integrated to yield

$$\Pi_c = \Pi_{co} + y \frac{\delta N_G}{\epsilon N_{CT}} \tag{142}$$

where Π_{co} is the capillary pressure at $y = 0$. If Π_c is assumed to be a single function of saturation, the above determines the vertical distribution of saturation, given its value $S_0(x,t)$ at $y = 0$.

Again, an integral approach is needed. However, the problem here is quite simpler. Indeed, it can be readily shown that the "water" pressure is hydrostatic, such that

$$p_w = -N_G \bar{\rho}_w (y - 1) + \Pi(x,t) \tag{143}$$

hence, the total flow rate u is described by expression (75) (assuming negligible capillarity along the x-direction). Thus, we can use directly equation (127) to get

$$\phi\frac{\partial}{\partial t}\int_0^1 S dy + \frac{\partial}{\partial x}\left\{\frac{\int_0^1 \kappa_H \lambda_w(S)dy}{\int_0^1 \kappa_H \lambda_T(S)dy}\right\} = 0 \tag{144}$$

Equations (142) and (144) completely specify the problem. For example, all integrals in (144) can be explicitly calculated from the solution of (142), in terms of $S_0(x,t)$, the evolution of which can be obtained from (144). The result would be an equivalent to the Buckley-Leverett equation, this time in terms of $S_0(x,t)$. Whether, however, appropriate pseudofunctions can be defined remains to be investigated.

Finally, if capillarity predominates in equation (142), the saturation profiles along the vertical direction follow the capillary heterogeneity. Specifically, if k_V does not vary greatly with y, then the saturation profile is flat, $S = S_0(x,t)$, and equation (144) becomes the traditional Buckley-Leverett equation (78).

7.10 SUMMARY

In this section, using a formal approach, the various manifestations of Vertical Flow Equilibrium were derived. Key to the analysis was the identification of the parameter R_L as the proper asymptotic variable and the development of a formal asymptotic method in terms of $1/R_L^2$. The analysis confirms previously known numerical results and, for the first time, it rigorously establishes their validity in the limit of large R_L^2. Because the condition is geometric-structural it applies independently of flow and process parameters, hence it can be used regardless of the particular displacement process. Due to the ensuing reduction in the dimensionality of the problem, the process description is facilitated significantly. To our knowledge, this is one of the few cases in multiphase flow in porous media where such a reduction is possible.

The formal approach presented has many advantages, as it allows for a plethora of special cases to be readily derived. An analysis along these lines is also possible for any EOR process, and we hope to report on this in the future. In all cases, heterogeneity is the key variable of the description and it is only the relative interplay of viscous to other forces that dictates the various approximations. Viscous, gravity and capillary effects were considered in the case of immiscible displacement. The classification of the various regimes depends on the wrelative importance of these forces, as described by the dimensionless parameters. We should point out that the above

can be readily extended to include a second "horizontal" dimension by appropriate, but perhaps laborious, modifications.

Many of the results obtained here are new, in the sense that they extend previous approximate analyses. Thus, eqns. (77) and (83) are an extension of Zapata and Lake [151], eqns (98) and (100) extend the work of Yokoyama and Lake [144], eqns (106) and (119) are extensions of Lake and Hirasaki [71], and eqns (134), (139) and (144) extend the Dupuit and Dietz approximations. In addition to their formal aspects, our results also ofter insight on effects of viscous cross-flow, as in (84)-(86), and they suggest directly the relevant pseudofunctions for each case. Finally, it is the hope that a more detailed analysis of equation (106) would lead to improved approximations and to rigorously establishing the validity of the various empirical viscous fingering models (such as Koval, [69], Todd and Longstaff, [133] and Fayers, [43]).

8 PARALLEL FLOW IN HELE-SHAW CELLS

M. Zeybek and Y.C. Yortsos

8.1 INTRODUCTION

During the past several years the flow of immiscible fluids in Hele-Shaw cells and porous media has been investigated extensively. Of particular interest to most studies has been frontal displacement, specifically viscous fingering instabilities and finger growth. This can be readily understood in view of the many interesting theoretical and practical problems associated with such fronts. For Hele-Shaw cells, we mention the selection problems and the singular perturbation associated with the high capillary number limit [10, 30], and the relation of viscous fingers to crystal growth [101] and flame front dynamics [152]. In porous media, unstable frontal displacement has been highlighted with the use of Diffusion-Limited-Aggregation (DLA) [140] and other probabilistic growth models [68]. Issues of capillarity, heterogeneity, randomness and spatial correlation, including fractal statistics [41, 75, 77, 78], have been extensively explored, although several outstanding questions still remain unanswered [145]. The practical ramifications regarding oil recovery, as well as many other industrial processes in porous media, have served as the primary driving force for most of these investigations.

By contrast, little attention has been paid to the motion of lateral fluid interfaces, which are parallel to the main flow direction. Parallel flow is an often encountered, although much overlooked regime. In the context of Hele-Shaw displacement, it is the theoretical limit of fully developed fingers (e.g. the Saffman-Taylor finger [111]) (see Figure 83). Parallel flow conditions have been invoked in qualitative support of the scaling properties of unstable, non-capillary displacement in porous media. Concerning the latter, it has been shown [67, 74] that as long as the viscosity ratio M is finite, the initially fractal displacing fluid cluster eventually evolves into a compact Euclidean object (although its perimeter may be a self affine fractal [67, 68, 74]). In a different context, parallel flow is often realized in thin and long reservoirs, typically masked under the assumption of vertical flow equilibrium (VFE) [28, 144, 151]. Recent studies on viscous fingering in porous media have invoked parallel flow to develop approximate models that satisfy numerical experiments [43, 45]. Finally, we mention that parallel flow is routinely encountered in yet other contexts, for example the steady-state, con-current flow in relative permeability measurements [29], as well as

in processes involving counter-current imbibition [64]. Although not directly relevant to this work, the pore-level analysis of such flows is very much incomplete at present, despite recent advances in the understanding of viscous coupling between phases [3] and efforts to ascribe a viscosity ratio dependence on steady-state relative permeabilities [110].

It is well known, that under the typical conditions of low $Re = \frac{\rho g b}{\mu}$ (where b denotes cell spacing), the flow of a single phase in Hele-Shaw cells and porous media, (and more generally, multi-phase, multi-component flow, but in the absence of spatial and concentration gradients) is potential. Such purely viscous flow exists on either side of the interface between immiscible fluids in a Hele-Shaw cell (Figure 83), and sufficiently far from the interface region in the case of porous media. We recall that potential flow (although in the opposite, inviscid limit) also governs the fluid flow in water waves [83]. We surmise that the dynamics of the lateral interfaces in parallel flow are likely to be related to those of shallow water waves [53].

It is with this idea in mind that we examine the dynamics of fluid interfaces in parallel flow in Hele-Shaw cells. In particular, the possibility of sustained wave propagation and the existence of solitons form the main subject of this chapter. We present both theoretical and experimental evidence that, subject to certain conditions, supports the existence of dispersive waves in the parallel flow of two immiscible fluids. In the theoretical part, we first proceed with a linear analysis, which shows that small disturbances are dispersive, if the viscosity ratio M is different than unity and the spacing of the "inner" fluid does not correspond to the Saffman-Taylor finger configuration. Subsequently, a weakly non-linear analysis is presented for long-wave, small amplitude disturbances. The asymptotic description of the general problem is ultimately formulated in terms of a set of KdV and Airy equations. The solution of the former is obtained numerically, although analytical results are also used for comparison purposes. A brief summary of this work was given in a recent article [154]. This chapter presents a more detailed account, as well as the extension to the more general (non-symmetric) case.

We must point out that although there are many similarities with shallow water waves, there are also many differences. First, the use of two immiscible liquids in a Hele-Shaw cell invariably raises issues of wettability and capillarity. The latter acts to dissipate high frequency waves, while under certain conditions the former may completely dominate the process. Such issues do not arise in shallow water waves, where it is viscous dissipation that results into an amplitude decrease.

Secondly, for flat steady-state interfaces to develop between the two immiscible fluids, a parallel flow condition ($q_a\mu_a = q_b\mu_b$) at high values of the modified capillary number, N'_{ca}, must be first met. This requires a somewhat elaborate experimental procedure. Finally, solitary waves in shallow water wave experiments are typically detected by special probes due to their very small amplitude. Hele-Shaws cells make difficult the use of such probes. Therefore, the experiments were restricted to simple flow visualization.

To test the theoretical predictions, several experiments were conducted. First, we considered a configuration of two fluids separated by one interface. For reasons that will become apparent, we refer to this as the symmetric case. This configuration allows us to test and improve our experimental technique, but also to compare with well known analytical results. After satisfactory results were obtained, experiments were carried out for the non-symmetric case, where two interfaces are involved. In all experiments, we attempted to generate single solitons on both interfaces as well as to seek the interaction of solitons. Compared to frontal displacement in Hele-Shaw experiments, the experiments are well reproduced. Flat interfaces are readily recovered, after the disturbance leaves the cell, and experimental runs can be easily reproduced. We shall point out that in our experiments, the viscosity ratio was finite, contrary to most Hele-Shaw experiments reported in the literature, which are carried out at large viscosity ratio.

8.2 THEORY

We examine the lateral interfaces between two immiscible and incompressible fluids of different viscosities in the parallel Hele-Shaw flow shown schematically in Figure 83. The cell is horizontal and has half-width W. Parallel flow requires flat interfaces and the absence of pressure gradients in the transverse (Y) direction. This condition is satisfied by the requirement $\mu_b q_b = \mu_a q_a \equiv Q$, where μ_i denotes viscosity and q_i the flow velocity of fluid i. Under the above, steady-state interfaces are flat. We denote the normalized interface positions by λ_1 and λ_2 ($-1 \leq \lambda_2 \leq \lambda_1 \leq 1$), where transverse lengths are scaled with the half-width W. The basic governing equations follow from the usual Hele-Shaw assumptions. In each fluid, Darcy's law applies and the pressure satisfies the Laplace equation

$$\nabla^2 P_i = 0 \quad \Rightarrow \quad \nabla^2 \Phi_i = 0 \quad ; \quad i = a, b \tag{145}$$

Here, subscript a denotes the "inner" fluid. We shall point out that fluid b flows in two different,

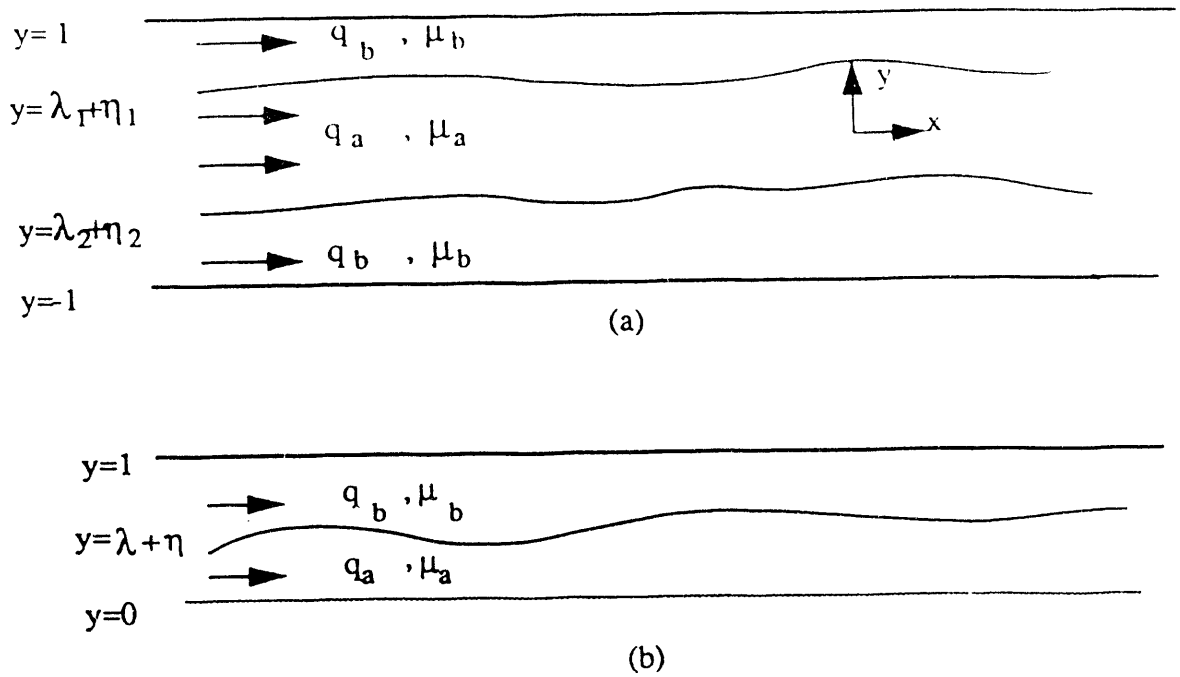

Figure 83: Flow geometry for (a) Non-symmetric and (b) Symmetric case

separated regions, thus two different pressures are needed for a full description. We describe the interfaces in dimensional notation by

$$\mathcal{F}_i(X,Y,T) \equiv Y - F_i(X,T) = 0 \quad ; \quad i = 1,2 \tag{146}$$

On each interface, the usual kinematic conditions apply, that fluid velocities normal to the interfaces are equal to each other and to the normal velocity of the interface itself

$$\vec{U}_b.\vec{n}_i = \vec{U}_a.\vec{n}_i \quad ; \quad i = 1,2 \tag{147}$$

$$\vec{U}_a.\vec{n}_i = -\frac{\mathcal{F}_{iT}}{|\nabla \mathcal{F}_i|} \quad ; \quad i = 1,2 \tag{148}$$

where $\vec{n}_i = \frac{\nabla \mathcal{F}_i}{|\nabla \mathcal{F}_i|}$ is the normal vector. With the use of Darcy's law the above transform into

$$\nabla P_b.\nabla \mathcal{F}_i = M\, \nabla P_a.\nabla \mathcal{F}_i \quad ; \quad i = 1,2 \tag{149}$$

$$\vec{U}_a.\nabla \mathcal{F}_i = -\frac{\partial \mathcal{F}_i}{\partial T} \quad ; \quad i = 1,2 \tag{150}$$

Finally, across each interface the pressure drop is due to curvature, thus

$$\Delta P_j = \gamma\, \frac{F_{iXX}}{|\nabla \mathcal{F}_i|^3} \quad ; \quad j = a,b \quad ; \quad i = 1,2 \tag{151}$$

where γ is the interfacial tension. Since the present interest is in long waves, higher order corrections to pressure drop are of secondary importance. We point out briefly that this problem is different than the two problems by Park and Homsy [97] for frontal displacement and by Burgess and Foster [20] for flow at the side of a Hele-Shaw bubble, where capillarity dominates the leading order approximations in the thin dimension. Thus, the present case requires a novel formulation, which is currently under consideration.

8.2.1 Linear Analysis

The dynamics of flat interfaces parallel to the flow direction is next obtained by following an analysis in terms of normal modes. As a preliminary step, we investigate one interface only, corresponding to the symmetric problem $\lambda_1 = -\lambda_2$, $\eta_1 = -\eta_2$, where η_1 and η_2 describe the dimensionless disturbances of the two interfaces ($0 < y < 1$) (see Figure 83b). Using lower case letters to denote dimensionless quantities, the dimensionless base interface is at location

$$\overline{f}_1 = \lambda_1 \tag{152}$$

while the base pressure satisfies

$$\overline{p}_i = -x \quad ; \quad i = a, b \tag{153}$$

Here, we have scaled pressure by $\frac{q_a \mu_a L}{k}$, where $k = \frac{b^2}{12}$ is the permeability of the Hele-Shaw cell, L is a streamwise length and time is scaled by L/q_a. Perturbations are next taken for the pressure and the interface as follows

$$p_i = \overline{p}_i + p' = -x + \varepsilon\, e^{i(\omega t - kx)}\, \varphi_i(y) \quad ; \quad i = a, b \tag{154}$$

$$f_1 = \overline{f}_1 + B\varepsilon\, e^{i(\omega t - kx)} \tag{155}$$

After linearization and use of no-flow boundary conditions at $y = 1$ and $y = 0$, the following results for the potential disturbances

$$\varphi_b = K_1 \cosh(k(y-1)) \quad ; \quad \lambda_1 < y < 1$$
$$\varphi_a = K_2 \cosh ky \quad ; \quad 0 < y < \lambda_1$$

Substitution into the interface conditions yields after some algebra, the following result for the complex frequency ω

$$\omega = 2\,\frac{k\,sinhk}{(1+M)sinhk + (1-M)sinhk(1-2\lambda_1)} + \frac{i}{6N'_{ca}}\,\frac{2k^3 sinh(k\lambda_1)sinhk(1-\lambda_1)}{(1+M)sinhk + (1-M)sinhk(1-2\lambda_1)} \tag{156}$$

Here, $M \equiv \frac{\mu_b}{\mu_a}$ is defined as the ratio of the viscosity of the "outer" fluid b, to the viscosity of the "inner" fluid a (Figure 83). We note that in the above relation, capillarity first enters at $O(k^4)$. Hence, for long waves (small k) and for a sufficiently large value of the modified capillary number, $N'_{ca} = q_a\mu_a L^2/\gamma b^2$ [58], capillarity can be neglected, although it should be cautioned that 3-D effects may become important when the capillary number is too large [90]. Under these conditions, the frequency is strictly real and the long wave speed $c \equiv \omega/k$ can be expanded as

$$c = c_0[1 - \frac{k^2}{3}\,\frac{(M-1)\lambda_1(1-2\lambda_1)(1-\lambda_1)}{1-\lambda_1+\lambda_1 M} + \cdots] \tag{157}$$

where $c_0 = 1/(1-\lambda_1+\lambda_1 M)$. For $M \neq 1$, the above relation predicts dispersive waves [1], i.e., waves with different wavelength travel with different speed. This result is quite different from the linear stability relations of frontal displacement, which yield either constant growth (viscous fingering) or constant decay. The existence of oscillatory modes in Hele-Shaw displacements was first reported in a previous communication [149] and it is also in agreement with recent marks by Xu [142] and by Meiburg [92]. As expected, the waves become non-dispersive when the fluids have equal viscosity ($M = 1$). Interestingly, non-dispersive waves are also predicted for the Saffman-Taylor conditions ($\lambda_1 = \frac{1}{2}$), although the latter have infinitesimal velocity when $M \gg 1$.

An analysis similar to the above gives the dispersion relation for the non-symmetric case, where now two interfaces are involved (Figure 83a). As expected, the dispersion relation is substantially more complicated. The final result is

$$tanh(k(1-\lambda_1))[e^{-k\lambda_1}aD + e^{k\lambda_1}aE] - aMe^{-k\lambda_1}D - be^{-k\lambda_1}D + be^{k\lambda_1}E + aMe^{k\lambda_1}E = 0 \tag{158}$$

where

$$D = e^{k\lambda_2}[(d-b)\,sinh(k(1+\lambda_2)) - M\,d\,cosh(k(1+\lambda_2))]$$
$$E = e^{-k\lambda_2}[(b-d)\,sinh(k(1+\lambda_2)) - M\,d\,cosh(\alpha(1+\lambda_2))]$$
$$a = i[1 - \tfrac{\omega}{k}]$$

$$b = i\,[1 - M]$$
$$d = i\,[1 - \tfrac{\omega}{k} M]$$

For our purposes, we shall consider only the asymptotic expansion at small wave numbers, by taking $c = x_0 + x_1 k + x_2 k^2 + \cdots$. Two solutions arise

$$c_m = x_{0,m} + x_{2,m} k^2 + \cdots \qquad ; \qquad m = 1, 2 \tag{159}$$

where

$$x_{0,1} = \frac{1}{M}$$

$$x_{0,2} = \frac{2}{\Delta}$$

$$x_{2,1} = \frac{(M-1)(\lambda_1-1)(\lambda_2+1)(\lambda_1-\lambda_2)}{M^2(2+\lambda_2-\lambda_1)}$$
$$x_{2,2} = \frac{4}{3}\,\frac{(M-1)}{\Delta^2}\,\frac{(\lambda_1-\lambda_2)(1+\lambda_2-\lambda_1)[(\lambda_2+1)^2+(\lambda_1-1)^2+(\lambda_2+1)(\lambda_1-1)]}{(2+\lambda_2-\lambda_1)}$$

and where we have defined $\Delta \equiv 2+(M-1)(\lambda_1-\lambda_2)$. The two roots correspond to the two different amplitude equations for the two interfaces. As in the symmetric case, the waves are dispersive as long as $M \neq 1$.

8.2.2 Weakly Non-Linear Analysis

The linear analysis is limited to the description of the onset of motion. The subsequent dynamics can be obtained by a non-linear analysis that includes higher order effects. In this section, the evolution of these dispersive waves is investigated.

We shall apply a perturbation analysis similar to that used for shallow water waves, valid for small amplitudes and long wavelengths. We consider the initial value formulation as described in [66]. First, two key dimensionless parameters are defined: $\delta \equiv W/L$, where L is the initial length of the disturbance, and $\epsilon \equiv A/W$, where A is a measure of the initial disturbance amplitude. In this notation, the Laplace equation in each flow region is

$$\delta^2 \phi_{ixx} + \phi_{iyy} = 0, \qquad ; \qquad i = a, 1, 2 \tag{160}$$

In the above, we have used subscripts 1 and 2 to denote the velocity potential of fluid b in the "upper" and "lower" regions, respectively. Correspondingly, the interface positions are at $y_i =$

$\lambda_i + \eta_i$ $(i = 1, 2)$. The interface conditions now read

$$\delta^2(\phi_{ix} - 1)\eta_{ix} - \phi_{iy} = \delta^2 M(\phi_{ax} - 1)\eta_{ix} - M\phi_{ay} \quad ; \quad i = 1, 2 \tag{161}$$

$$\delta^2(\eta_{it} - \eta_{ix}(\phi_{ax} - 1)) = -\phi_{ay} \quad ; \quad i = 1, 2 \tag{162}$$

and in the absence of surface tension

$$\phi_a = \phi_i \quad ; \quad i = 1, 2$$

The problem is fully specified with the no flow boundary conditions at the side walls

$$\frac{\partial \phi_1}{\partial y} = 0 \quad at \quad y = 1$$
$$\frac{\partial \phi_2}{\partial y} = 0 \quad at \quad y = -1$$

a sufficiently fast far-field decay of the disturbances

$$\eta_i \to 0 \quad at \quad |x| \to \infty$$

and the initial condition:

$$\eta_i(x, 0) = \epsilon h_i(x)$$

To implement an asymptotic approach, a long wave, long time and small amplitude approximation is considered, $\delta \ll 1$, $\tilde{t} = \epsilon t$, $\epsilon \ll 1$. Then, the following asymptotic expansions are taken

$$\phi_i = \epsilon\phi_{i0} + \epsilon\delta^2\phi_{i1} + \epsilon\delta^4\phi_{i2} + \cdots \quad ; \quad i = 1, 2 \tag{163}$$

$$\eta_i = \epsilon\eta_{i0} + \epsilon^2\eta_{i1} + \cdots \quad ; \quad i = 1, 2 \tag{164}$$

where the various terms of the expansion also depend on $\tilde{t}$, e.g. $\eta_i \equiv \eta_i(x, t, \tilde{t})$. For non-trivial results to be obtained, the relation $\delta = \kappa\sqrt{\epsilon}$ is necessary, as can be readily shown with the method of dominant balance [66]. Use of this in (163)-(164) and substitution into the field equations and in the interfaces conditions (161)-(162) yield the following results. At the 0th order

$$\boldsymbol{\eta}_{0,t} + \mathbf{A} \cdot \boldsymbol{\eta}_{0,x} = 0, \tag{165}$$

where the matrix

$$\mathbf{A} = \begin{bmatrix} \frac{M+1-(M-1)\lambda_2}{M\Delta} & \frac{(M-1)(\lambda_1-1)}{M\Delta} \\ \frac{-(1+\lambda_2)(M-1)}{M\Delta} & \frac{M+1+(M-1)\lambda_1}{M\Delta} \end{bmatrix}$$

has eigenvalues $\frac{2}{\Delta}$ and $\frac{1}{M}$. This system is diagonalized if we introduce the variable

$$\mathbf{v}_0 = -\mathbf{L} \cdot \boldsymbol{\eta}_0 \tag{166}$$

where

$$\mathbf{L} = \frac{1}{(2-\lambda_1+\lambda_2)} \begin{bmatrix} -1 & 1 \\ 1+\lambda_2 & 1-\lambda_1 \end{bmatrix}$$

The components of $\mathbf{v}_0 = \begin{bmatrix} v_{10}\ , & v_{20} \end{bmatrix}^T$ can be expressed in terms of η_{i0},

$$\begin{aligned} v_{10} \equiv U &= \frac{\eta_{10}-\eta_{20}}{2-\lambda_1+\lambda_2} \\ v_{20} \equiv V &= -\frac{(1+\lambda_2)\eta_{10}+(1-\lambda_1)\eta_{20}}{2-\lambda_1+\lambda_2} \end{aligned} \tag{167}$$

It follows that variable U is proportional to the net transverse displacement of fluid a. From (165) and (166) we obtain

$$\mathbf{v}_{0,t} + \mathbf{D} \cdot \mathbf{v}_{0,x} = 0 \tag{168}$$

where

$$\mathbf{D} = \mathbf{L}^{-1}\mathbf{A}\mathbf{L} = \begin{bmatrix} \frac{2}{\Delta} & 0 \\ 0 & \frac{1}{M} \end{bmatrix}$$

The solution of the initial value problem (168) is

$$v_{10} = f_0(\sigma, \tilde{t}) \tag{169}$$

$$v_{20} = g_0(\xi, \tilde{t}) \tag{170}$$

where the two moving coordinates $\sigma \equiv x - \frac{2t}{\Delta}$, $\xi \equiv x - \frac{t}{M}$, were introduced, and $f_0(\sigma, 0) = h_1(0)$, $g_0(\xi, 0) = h_2(0)$.

To obtain the dependence on σ, ξ and $\tilde{t}$, the next order in the expansion is considered. After considerable algebra, one finds

$$\boldsymbol{\eta}_{1,t} + \mathbf{A} \cdot \boldsymbol{\eta}_{1,x} = -\boldsymbol{\eta}_{0,\tilde{t}} + \mathbf{C} \cdot \begin{bmatrix} \eta_{10}\eta_{10,x}\ , & \eta_{20}\eta_{20,x} \end{bmatrix}^T + (\eta_{10}\eta_{20})_x \mathbf{d} - \kappa^2 \mathbf{e}_{xx} \tag{171}$$

where

$$\mathbf{C} = \frac{2(M-1)}{M\Delta^2} \begin{bmatrix} M+1-(M-1)\lambda_2 & -(M-1)(\lambda_1-1) \\ -(1+\lambda_2)(M-1) & -(M+1+\lambda_1(M-1)) \end{bmatrix}$$

$$\mathbf{d} = \frac{(M-1)}{M\Delta^2}\begin{bmatrix} (M-1)(\lambda_1+\lambda_2)-2M \\ (M-1)(\lambda_1+\lambda_2)+2M \end{bmatrix}$$

and the vector $\mathbf{e}$ is a complicated expression involving $\phi_0, \eta_0, \ldots$ and their spatial derivatives [153]. Equivalently, we may use transform (166) to obtain

$$\mathbf{v}_{1,t} + \mathbf{D}\cdot\mathbf{v}_{1,x} = -\mathbf{v}_{0,\bar{t}} - \mathbf{L}\cdot\mathbf{C}\cdot\begin{bmatrix} \eta_{10}\eta_{10,x}, & \eta_{20}\eta_{20,x} \end{bmatrix}^T - (\eta_{10}\eta_{20})_x\mathbf{L}\cdot\mathbf{d} + \kappa^2\mathbf{L}\cdot\mathbf{e}_{xx} \tag{172}$$

Use of (167)-(170) into (172) leads after considerable algebra to

$$\begin{aligned}(\frac{2}{\Delta}-\frac{1}{M})v_{11,\xi} = -v_{10,\bar{t}} &+ \frac{4(M-1)}{\Delta^2}(2+\lambda_2-\lambda_1)v_{10}v_{10,\sigma} \\ &+\frac{\kappa^2(M-1)}{M\Delta}(a_{11}v_{10,\sigma\sigma\sigma}+a_{12}v_{20,\xi\xi\xi})\end{aligned} \tag{173}$$

and

$$\begin{aligned}-(\frac{2}{\Delta}-\frac{1}{M})v_{12,\sigma} = -v_{20,\bar{t}} &+ (\frac{M-1}{M\Delta})(2+\lambda_2-\lambda_1)(v_{20}v_{10,\sigma}+v_{10}v_{20,\xi}) \\ &+\frac{\kappa^2(M-1)}{M\Delta}[a_{21}v_{10,\sigma\sigma\sigma}+a_{22}v_{20,\xi\xi\xi}]\end{aligned} \tag{174}$$

After integration of (173) with respect to ξ, all secular terms vanish if the terms containing v_{10} also vanish, thus ($U \equiv v_{10}$)

$$U_{\bar{t}} = \frac{4(M-1)}{\Delta^2}(2+\lambda_2-\lambda_1)UU_\sigma + \frac{(M-1)\kappa^2}{M\Delta}a_{11}U_{\sigma\sigma\sigma} \tag{175}$$

Similarly working for the other component in (174) and eliminating secular terms yields

$$V_{\bar{t}} = \frac{(M-1)\kappa^2}{M\Delta}a_{22}V_{\xi\xi\xi} \tag{176}$$

assuming sufficiently fast decay to zero. The two coefficients in (175) and (176) are given by

$$a_{11} = \frac{4M}{3\Delta}\,\frac{(\lambda_2-\lambda_1)(1+\lambda_2-\lambda_1)[(\lambda_2+1)^2+(\lambda_1-1)^2+(\lambda_2+1)(\lambda_1-1)]}{(2+\lambda_2-\lambda_1)}$$

$$a_{22} = \frac{(1-\lambda_1)(\lambda_1-\lambda_2)(1+\lambda_2)\Delta}{M(2+\lambda_2-\lambda_1)}$$

and they are related to $x_{2,1}$ and $x_{2,2}$ by $a_{ii} = \frac{M\Delta x_{2,i}}{M-1}$ $(i = 1,2)$. The various parameters in (175)-(176) are functions of the undisturbed interface positions λ_1, λ_2, and the mobility ratio M. For the full problem, the solution of both (175) and (176) is required. We may note the following: (*i*) Purely translational motion occurs when $M = 1$, as expected; (*ii*) There are two long wave

speeds, $2/\Delta$ and $1/M$, both decreasing to zero as the viscosity ratio increases. The long wave speed $1/M$ corresponding to variable V is simply the dimensionless (undisturbed) velocity of fluid b; (*iii*) As anticipated, the linearized equations yield the leading order of the linear analysis; (*iv*) The dispersive term in the KdV equation vanishes when $1 + \lambda_2 - \lambda_1 = 0$ (which, for the symmetric case $\lambda_1 = -\lambda_2$, coincides with the Saffman-Taylor finger width $\lambda_1 = 1/2$); (*v*) Anti-symmetric disturbances ($\eta_1 = \eta_2$) are governed by the Airy equation (176) alone; (*vi*) Finally, when both initial and disturbed interfaces are symmetric ($\lambda_1 = -\lambda_2$ and $\eta_1 = -\eta_2$), the interface motion is governed by the KdV equation alone. The latter is of great interest for the subsequent experiments. This case may be recast in terms of the original variables as follows ($\lambda \equiv \lambda_1$)

$$\eta_t + c_0\,\eta_x - 2(M-1)c_0^2\eta\,\eta_x + \epsilon\,\frac{c_0^2}{3}\,\kappa^2\,(M-1)\lambda(1-2\lambda)(1-\lambda)\eta_{xxx} = 0 \qquad (177)$$

Equation (177) can be interpreted as follows: Due to parallel flow, any initial disturbance travels with a long wave speed c_0. The latter always lies between the velocities of the two fluids (e.g., $1 < c_0 < 1/M$ for $M < 1$). For an observer traveling with speed c_0 the fluid flow is counter-current, the lower viscosity fluid flowing towards the right and the higher viscosity towards the left in the schematic of Figure 84 (where one must recall that in the Hele-Shaw context, viscous shear is not relevant to long waves). Because of unequal viscosities, the long wave disturbances also disperse, to the left if $(M-1)(1-2\lambda) > 0$, and to the right, otherwise. We note that shorter wavelength dispersion, although possible, is likely to be damped by capillarity and wettability effects. Sustained wave propagation is possible only if amplitudes are small and the non-linearity is weak. Strong non-linear effects must be excluded. They violate parallel flow conditions and are likely to lead to frontal motion and viscous fingering. Nonetheless, weakly non-linear waves also tend to break, to the left if $(M-1)\eta > 0$, and to the right, otherwise. For the positive disturbance of Figure 84, dispersion will oppose breaking if $1 - 2\lambda < 0$. Under this condition, a permanent form wave would develop, that propagates to the left or to the right, depending on whether $M > 1$ or $M < 1$, respectively. Analogous conclusions can be drawn for all other possibilities.

In the symmetric case we may use classical results [39] to predict in advance the possibility of solitary waves, in terms of M, the interface position λ_1 and the initial shape of the disturbance. With the use of the rescaling

$$u \to \alpha\eta \quad ; \quad x \to \beta\sigma \quad ; \quad t \to t$$

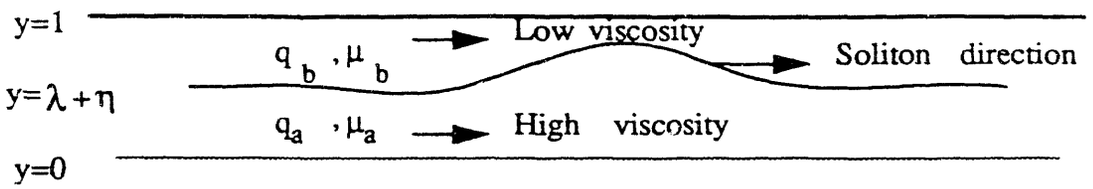

Figure 84: Counterflow of the two fluids in a moving frame of reference

where

$$\beta = -[\epsilon \frac{c_0^2}{3} \kappa^2 (M-1)\lambda(1-2\lambda)(1-\lambda)]^{-1/3}$$

$$\alpha = -\frac{1}{3}(M-1)c_0^2\beta$$

Equation (177) can be mapped into the standard form

$$u_t - 6uu_x + u_{xxx} = 0 \tag{178}$$

with initial condition

$$u(x,0) = -u_0 sech^2(b(x-x_0))$$

Then, the theory predicts the following: (*i*) When $\lambda_1 > 0.5$, $M < 1$, $\eta > 0$, and $\lambda_1 < 0.5$, $M > 1$, $\eta < 0$, solitons develop and propagate in the positive σ direction. (*ii*) When $\lambda_1 > 0.5$, $M > 1$, $\eta > 0$, and $\lambda_1 < 0.5$, $M < 1$, $\eta < 0$, solitons propagate in the negative σ direction. (*iii*) No solitons would form in any other case. Based on the above, the phase diagram of Figure 85 can be constructed. Both the existence of solitons and their direction of propagation, in a frame of reference moving with speed $2/\Delta$, are shown. The map will be repeatedly used below in the comparison between experiment and theory.

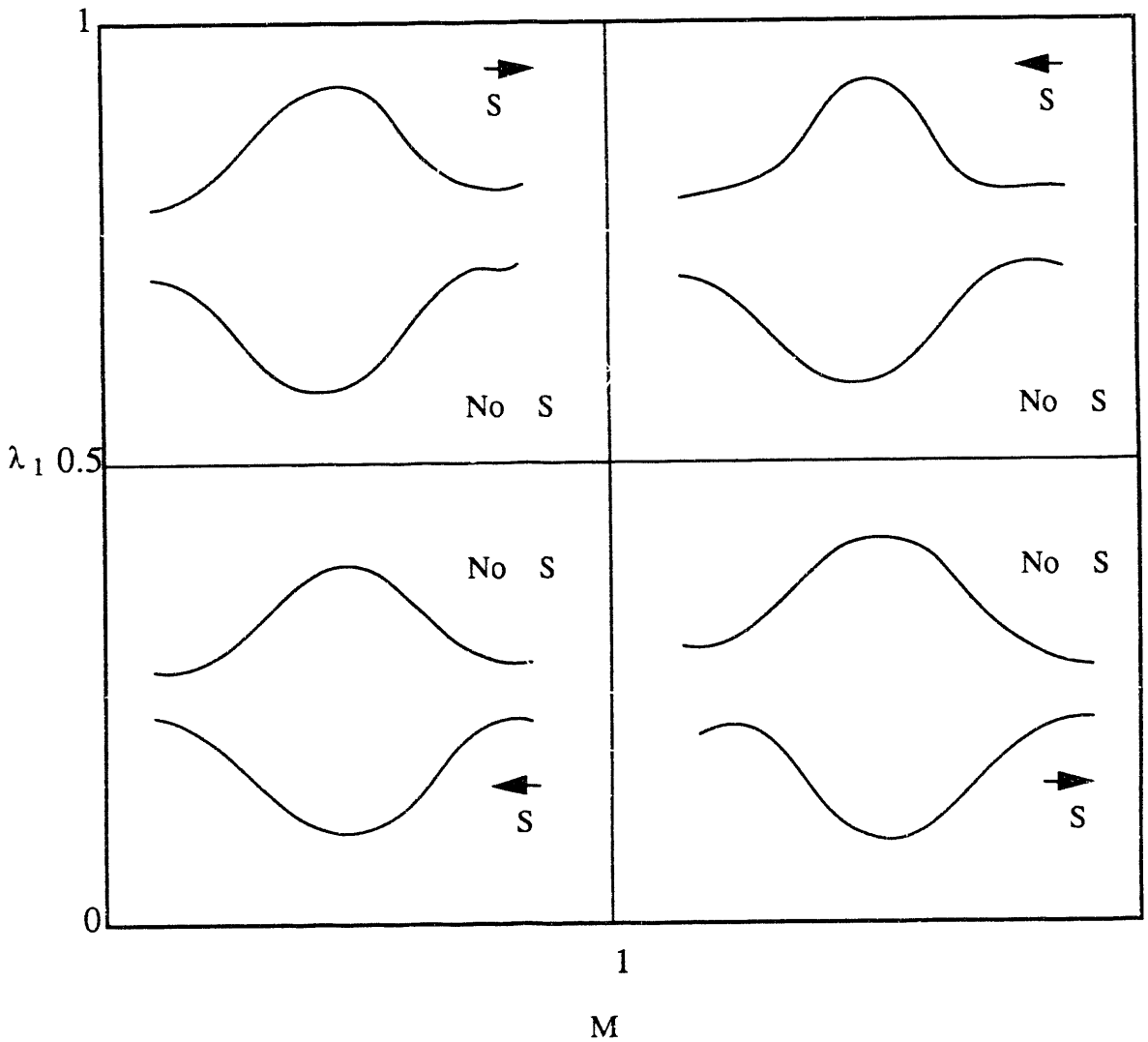

Figure 85: M vs. λ_1 diagram for formation of solitons

8.2.3 Numerical Method

Although we shall often use general exact results, we shall rely for illustration purposes on numerical results, obtained with the pseudospectral technique of Fornberg and Whitham [48]. The method combines a Fourier transform treatment of the space dependence with a leapfrog scheme for the time evolution and it is well suited for non-linear dispersive waves. The interval l is discretized into N equidistant points, with spacing $\Delta x = l/N$ (N was taken as 128, 256 or 512). The function $\eta(x,t)$ is discrete Fourier-transformed with respect to x by the use of a fast Fourier transform algorithm. Thus equation (177) is discretized as follows

$$\eta_i^{n+1} - \eta_i^{n-1} = -\,2i\Delta t c_0 \mathcal{F}^{-1}[(\frac{2\pi}{N} n\mathcal{F}(\eta)] + 2i(2(M-1)c_0^2)(\eta_i^n)\Delta t\, \mathcal{F}^{-1}[(\frac{2\pi}{N} n\mathcal{F}(\eta)]$$
$$-\,2i\,(\epsilon\frac{\kappa^2 c_0^2}{3})\,(M-1)\lambda(1-2\lambda)(1-\lambda)\;\mathcal{F}^{-1}[sin((\frac{2\pi}{N})^3 n^3\Delta t)\mathcal{F}(\eta)] \qquad (179)$$

The numerical scheme was tested favorably with an exact soliton solution, as well as with the test example of Zabusky and Kruskal [150]. A similar discretization was implemented for the Airy equation.

In the experiments that follow, the existence of solitons was tested by direct comparison with simulation, but also by looking for the following key properties [39]: (*i*) Arbitrary initial disturbances evolve into one or more solitons and into dispersive waves of substantially smaller amplitude: (*ii*) The speed of a soliton depends on its amplitude, which increases with an increase in amplitude; (*iii*) Solitons regain their identity after interaction with other solitons. For a given initial condition, the number of solitons and their amplitude can be predicted from the standard theory of the KdV equation [39, 139]. For example, the number of solitons obeys the condition

$$N \leq [(\frac{u_0}{b^2} + \frac{1}{4})^{1/2} - \frac{1}{2}] + 1 \qquad (180)$$

while the soliton amplitude is

$$a_n = 2\kappa_n^2 \qquad (181)$$

where

$$\kappa_n = \frac{1}{2}b[(1 + \frac{4u_0}{b^2})^{1/2} - (2n-1)] \qquad (182)$$

These were used in the subsequent comparison with the experiments.

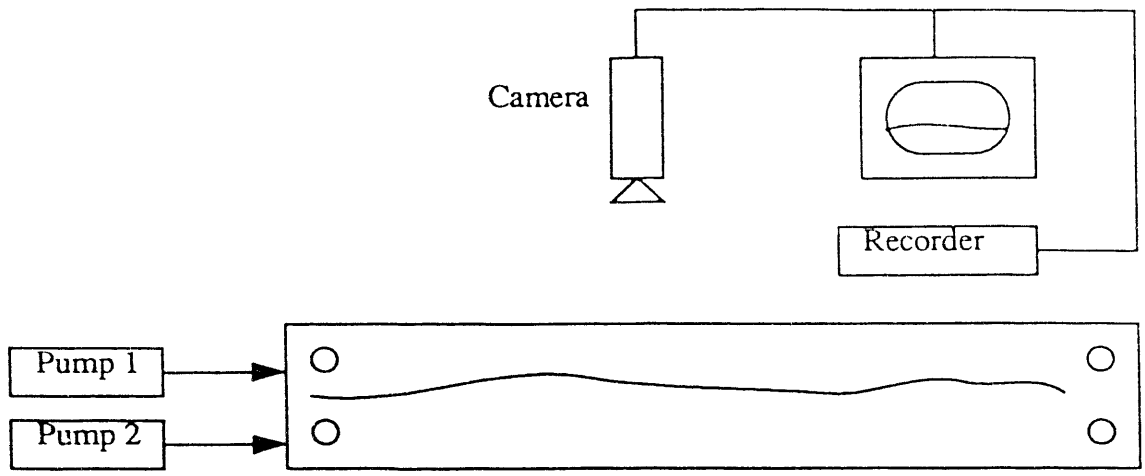

Figure 86: Experimental set up

8.3 EXPERIMENTAL

As in shallow water wave experiments, the two small parameters δ and ϵ play a critical role. The conditions $\delta, \epsilon \ll 1$ suggest that for a satisfactory resolution (larger A) requires larger cell width, which in turn requires proportionally larger length. Therefore, the construction of a narrow and long Hele-Shaw cell was necessary in order to observe possible solitary waves [89, 96, 111, 131]. The cell consisted of two plexiglass plates, $\frac{1}{2}$ *in.* thick, of dimensions 230 × 27 *cm*, and of a rubber gasket spacer 0.08 *cm* thick. Since interferometric methods [131] were not available, the uniformity of the gap was estimated by the indirect method of [96]. The linear regression coefficient of the data was 0.999, indicating a good uniformity of the cell. The plates were held together using C-clamps. The experimental set up consists of the Hele-Shaw cell in horizontal position, three integral variable speed peristaltic pumps, a video camera, a video recorder and a monitor (see Figure 86). The frame of the cell was constructed such that it can be tilted both with respect to the transverse and to the longitudinal axes. This was necessary in order to establish the steady-state interfaces.

Experiments reported below were conducted with two different fluid pairs. The first pair is mineral oil and glycerol/water solution with corresponding viscosities 170 cp and 860 cp, respec-

tively, while the second pair is DC 200 silicon fluid and glycerol/water solution with corresponding viscosities 1060 cp and 500 cp, respectively. Mineral oil is the wetting fluid in the first pair, while DC 200 silicone fluid is the wetting fluid in the second pair. The viscosities of the fluids were measured by both a Cannon-Fenske and a Brookfield spindle viscometers. Since the parallel flow condition is one on fluid viscosities, ($q_a\mu_a = q_b\mu_b$), the accuracy of these measurements play an important role in establishing the flat interface. Relatively high flow rates were used, such that the modified capillary number was typically $O(10^2)$. No sustained wave propagation was observed for substantially lower N'_{ca} values. This is consistent with the theory. The experiments were conducted with configurations involving both one and two interfaces. The single interface case corresponds to the symmetric case ($\lambda_1 = -\lambda_2$, $\eta_1 = -\eta_2$). This configuration can be viewed either as the top or the bottom half of the symmetric problem. It can be easily checked that the solution of (177) is invariant to the change $\lambda_1 \to 1 + \lambda_2$, $\eta_1 \to \eta_2$, $M \to 1/M$ (please note also the rescaling of time), thus without loss we may view the flow as the top half of a symmetric problem with the "lower" fluid being fluid a. In our experiments, this was the more viscous fluid for the case $M = 0.2$ and the less viscous fluid for the case $M = 2.1$.

Conducting the flow experiments consists of two stages. The first stage is to establish a flat lateral fluid interface and parallel flow conditions for the two fluids. For the single interface case, this was accomplished by a displacement process with the aid of gravity. The cell was first filled with one fluid. While the cell is tilted on its side, the lighter fluid is slowly injected at the top. Subsequently, the cell is slowly returned to horizontal position. The parameter λ, which is the dimensionless location of the interface, is controlled by the relative amounts of fluids injected. For the non-symmetric case, flat interfaces were established by the simultaneous injection of both fluids, while the cell was slightly tilted on the transverse axis. We were unable to independently vary the locations of both top (λ_1) and bottom (λ_2) interfaces, which shifted together according to the amounts of the fluids injected. We stress that in the two interface problem, the parallel flow condition, $\mu_b q_b = \mu_a q_a$, was found essential for the establishment of a parallel interface. Under conditions such that the modified capillary number is relatively large, flat interfaces were obtained with an accuracy of ± 1 mm.

The second stage is to introduce a disturbance as an initial condition, typically obtained by interrupting momentarily the flow of one fluid, and to monitor the motion of the disturbance. The

wave length and the amplitude of the disturbances were controlled by the speed of the interruption. Although results obtained with such initial conditions were generally satisfactory, questions may arise as to the effect of flow interruption and end effects. This will be discussed in a later section.

8.4 RESULTS AND DISCUSSION

8.4.1 Symmetric Case

Three different cases were considered corresponding to three different viscosity ratio regimes ($M < 1$, $M \sim 1$, $M > 1$).

8.4.2 M < 1

Here, the first pair of fluids (mineral oil and water/glycerol solution) was used with $M = 0.2$. Figure 87 shows typical experimental results in digitized pictures taken from a videotape. A hump-like initial disturbance taken to satisfy the small amplitude and long wave conditions was imposed on the parallel interface ($\lambda = 0.69$) (Figure 87a). The cell width here is 6 cm. For the particular initial conditions of wavelength $L = 20$ cm, and amplitude 1 cm, the theory predicts a single soliton traveling forward ($\lambda > 1/2, M < 1, \eta > 0$) (see Figure 85). Indeed, upon restoration of the flow rate to the initial level, the disturbance was advected by the flow, and it started developing into a wave of constant shape followed by a wiggly interface of small amplitude and short wavelength behind it. Typically, this constant amplitude wave has taken a permanent form after traveling about 45 cm, and appeared to possess all the characteristics of a soliton (Figure 87b). The amplitude is clearly different from the initial and remains constant for a substantial distance traveled (Figure 87c), as long as 150 cm, beyond which end effects seem to become appreciable. Numerical simulations corresponding to these conditions and for the initial shape of Figure 87a are shown in Figure 88.

The comparison between theory and experiment shows a quite satisfactory agreement, despite the ambiguity on the suitability of the initial condition for the experiment (recall that the disturbance is imposed by flow interruption). Theoretical and experimental number of solitons coincide (equal to 1), while computed and observed final amplitudes were 0.81 cm and 0.76 cm, respectively. The wave velocity with respect to a fixed observer was calculated to be 0.28 cm/sec, which compares well with the experimental value of 0.26 cm/sec. Due to the particular scales selected to match one-to-one the experimental pictures, certain typical characteristic features of soliton and

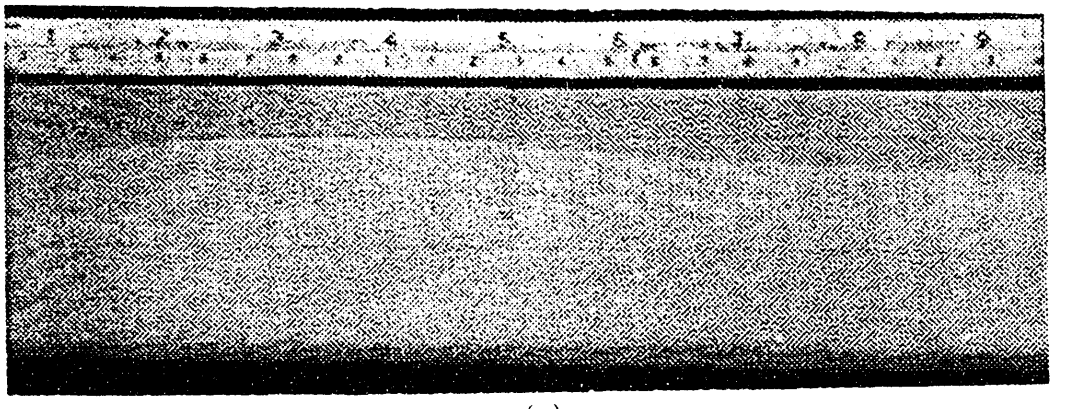

(a)

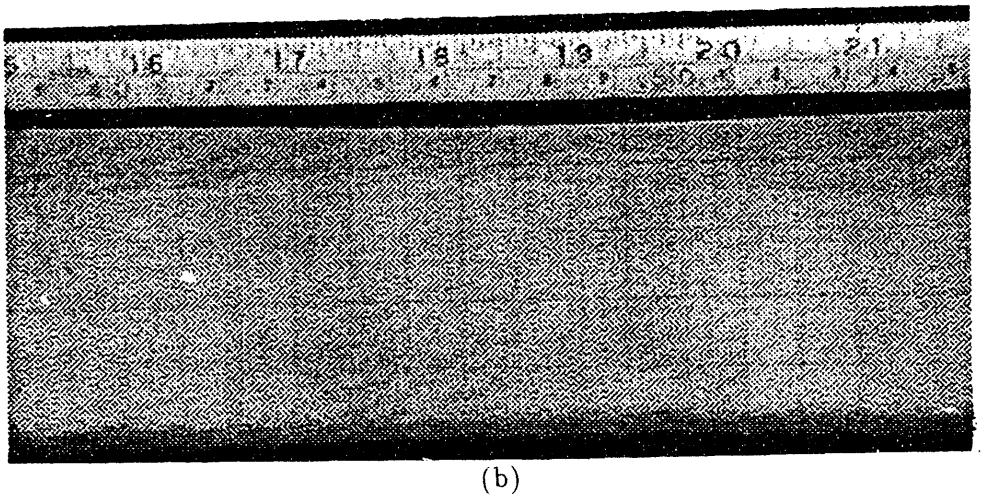

(b)

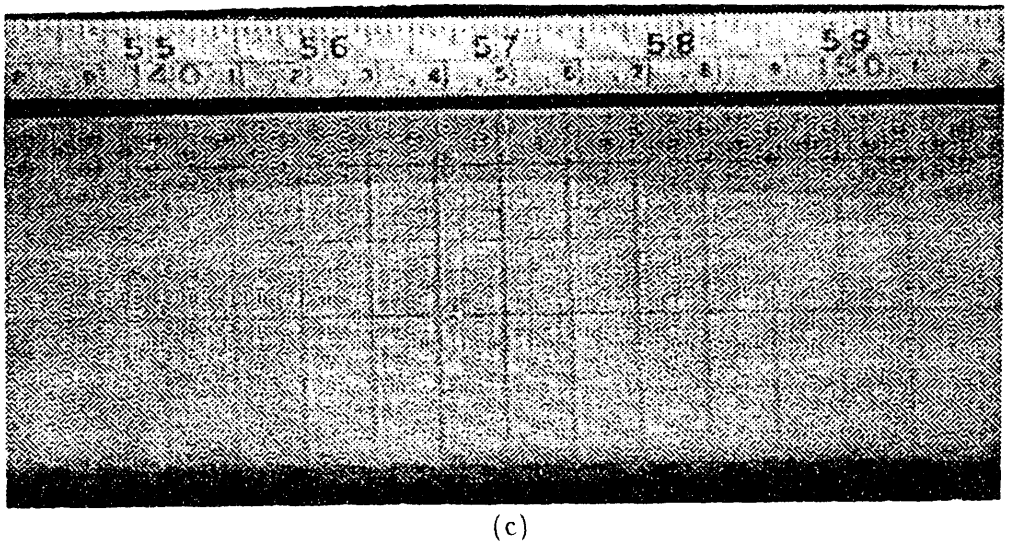

(c)

Figure 87: Single solitary wave (a) Initial condition (b) and (c) Subsequent stages

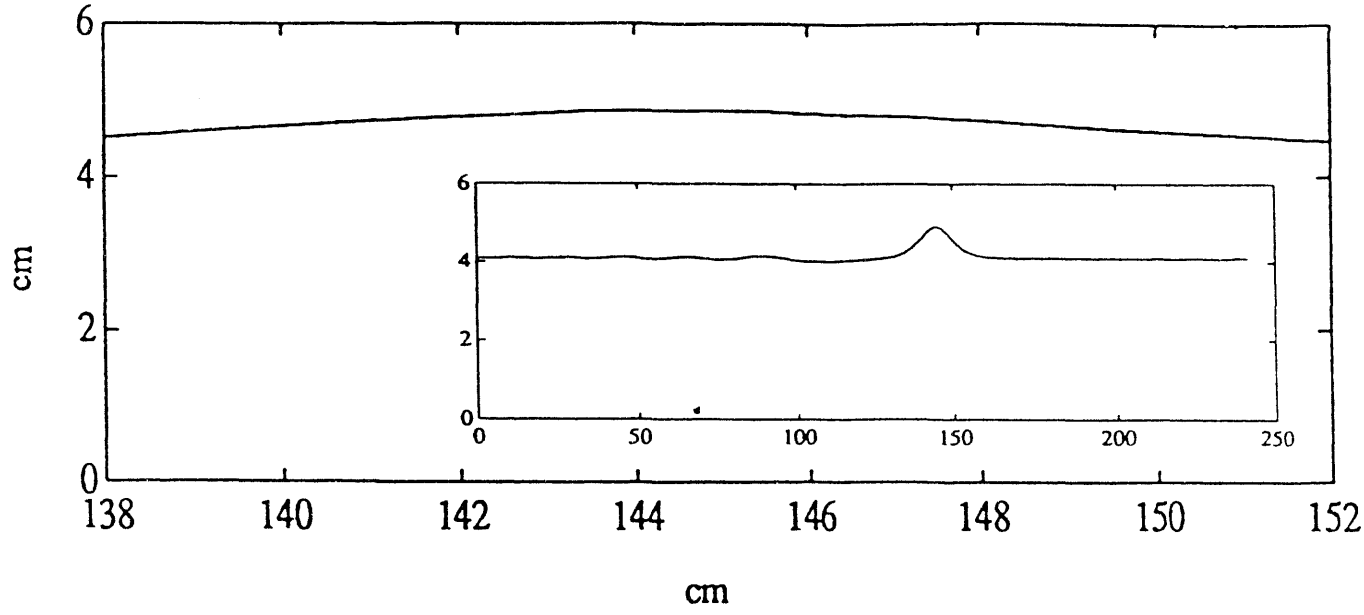

Figure 88: Numerical simulation of figure 87c. Inset: Profile in different scales

dispersive waves are suppressed in Figure 88. To illustrate this point, the profile of Figure 88 is replotted in the inset with different scales. Nonetheless, motion of dispersive waves was actually not observed to our satisfaction in the experiments. Typically, a noisy and wiggly interface of small wave length and amplitude formed soon after the main wave evolved. However, we suspect that wettability and surface tension have likely played major roles on its subsequent development.

Figure 89 shows the emergence of two solitons arising from an initial disturbance of longer wavelength ($L \sim 45\ cm$). According to the theoretical predictions, two solitary waves of different amplitudes (and speed) should arise, in order of descending amplitudes (Figure 89). As time progresses, the two solitons are clearly separated, the higher amplitude soliton moving faster and away from the trailing lower amplitude soliton. Figure 89b is a picture of the trailing wave. A typical characteristic of the emergence of more than one solitons is an increase in the amplitude after the onset of the initial disturbance. This feature was clearly observed. Comparison with the numerical simulations is again quite satisfactory (see Figure 90 and the inset with different scales).

Under the same conditions, soliton interaction is shown in Figure 91. To create the two solitary waves, two disturbances of different amplitude were sequentially introduced. The second disturbance is of higher initial amplitude and evolves into a faster soliton, that eventually takes over the preceding slower one. After this nonlinear interaction, tall and short solitons reappear, but in reverse order and propagate with their original speed (Figure 91b). All these features are consistent with the theory. Corresponding numerical simulations are in good agreement as shown in Figure 92. Some additional effects were also considered. For instance, short wave disturbances, typically corresponding to $\delta \geq 0.5$, were found to dissipate after their onset, as predicted by the theory. Figure 93 shows such a short wave disturbance and its subsequent stage, where the amplitude has significantly decreased over a rather short distance. Numerical simulations are also in agreement.

For disturbances in the opposite negative direction ($\eta < 0$), no solitons are predicted by the theory (compare Figure 85). This prediction was tested in the experiments. Consistent with the theory, any such disturbances (whether of long or short wavelength) dissipated continuously, although it is quite likely that wettability may have also interfered with the interface dynamics in this case (see below). Similarly, for $0 < \lambda < 1/2$, but with a positive initial disturbance, no solitons are theoretically predicted. A typical experimental run for such conditions ($\lambda = 0.3$) is shown in

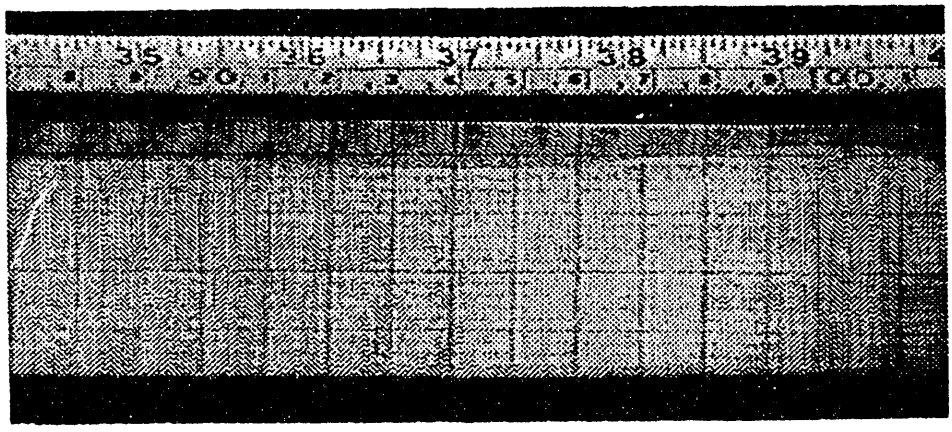

(a)

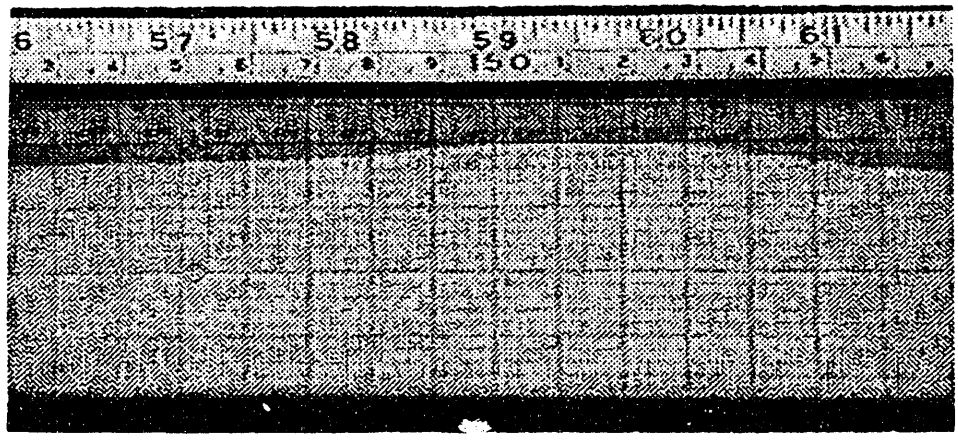

(b)

Figure 89: Two solitary waves at two different stages

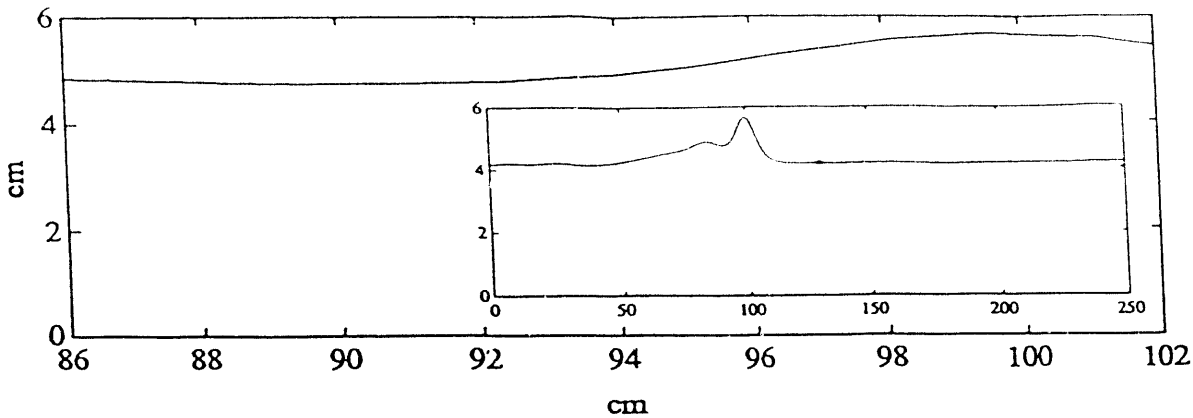

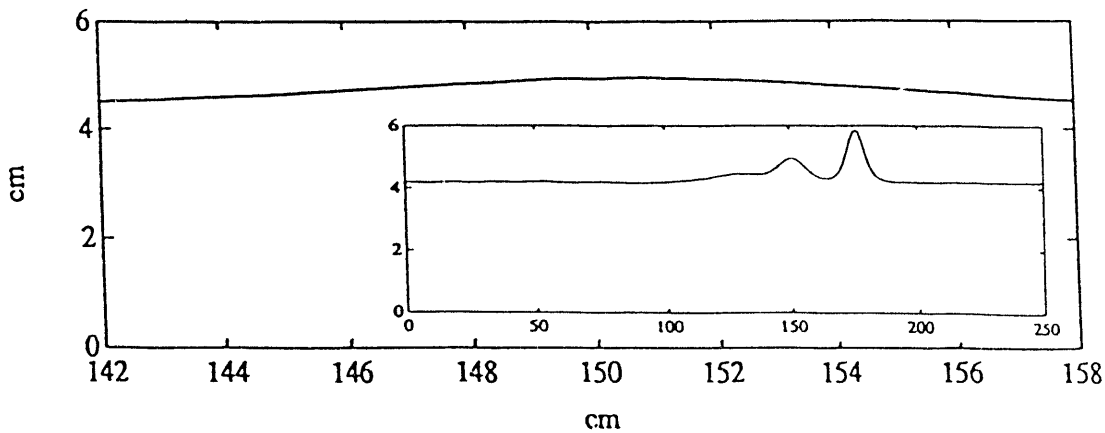

Figure 90: Numerical simulation of figure 89 Inset: profile in different scales

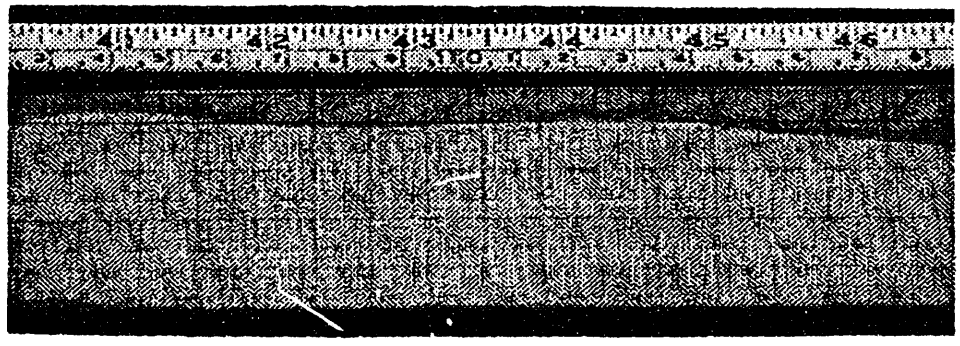

(a)

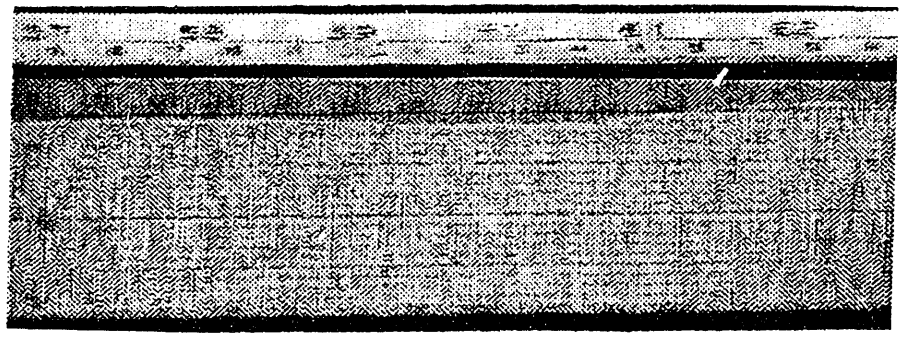

(b)

Figure 91: Two solitary waves (a) Before and (b) After interaction

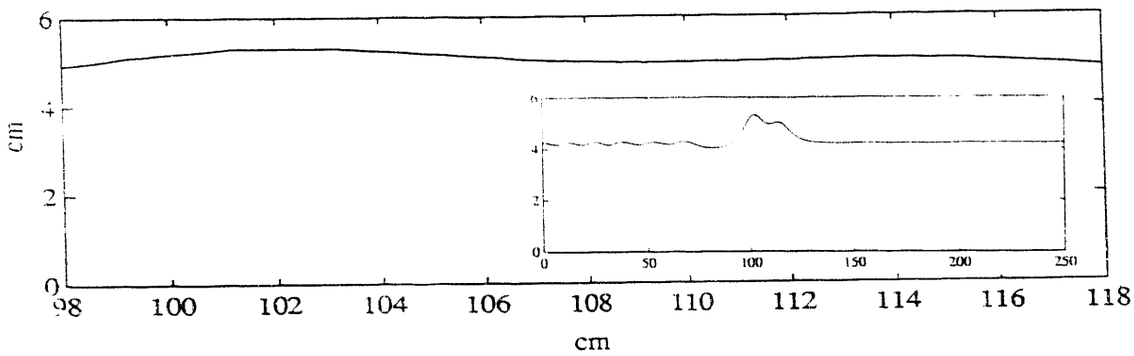

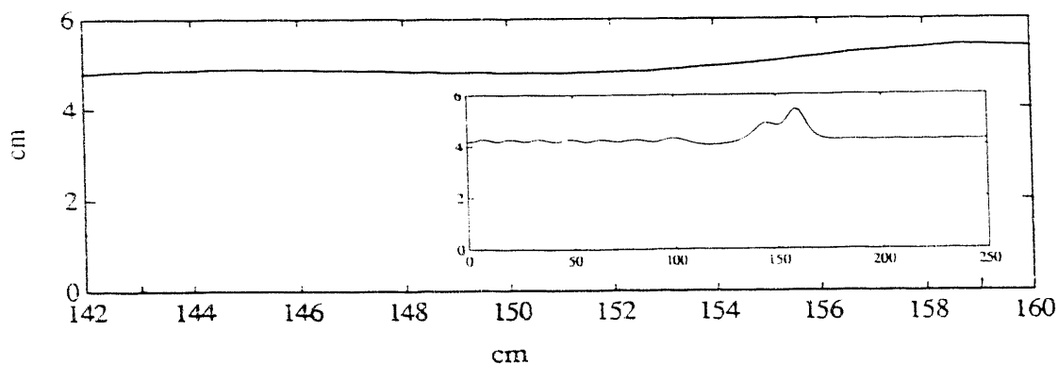

Figure 92: Numerical simulation of figure 91 Inset: Profile in different scales

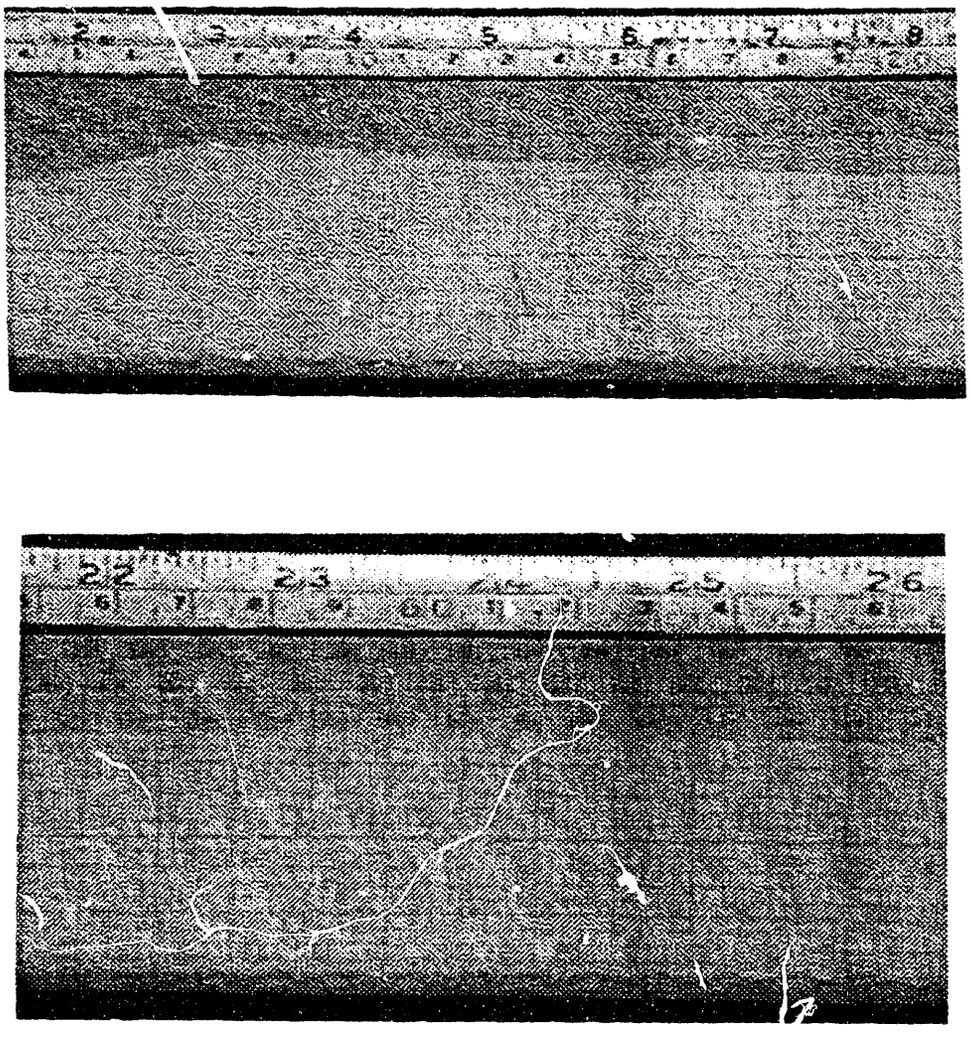

Figure 93: Short wave initial disturbance and subsequent stage

Figure 94. The corresponding simulation result was also in good agreement with the experiment. Finally, when $0 < \lambda < 1/2$, and the initial disturbance is negative, solitons are predicted to propagate in the negative σ direction (Figure 85). Unfortunately, this disturbance could not be introduced clearly and solitons were not observed, although dispersive-like waves traveling ahead of the main disturbance were noticed and the advective velocity agreed with the theory to some degree. We strongly believe that the reason for this discrepancy is wettability. Indeed, soliton propagation in the negative σ direction (which is equivalent to this case) was observed, when we experimented with a different pair of fluids of different viscosity ratio ($M > 1$), but with reverse wettability.

8.4.3 M ~ 1

The second region of interest in Figure 85 corresponds to equal viscosity fluids. Experiments were carried out with a pair of mineral oil and water/glycerol solution of nearly equal viscosity ($M = 0.97$). In this case, both the non-linear and the dispersive terms in the KdV equation (177) are very small, hence we expect constant wave speed and translational motion independent of the wave amplitude. In the experiments, disturbances similar to Figure 87 were introduced. However, neither a change in shape nor a wiggly interface were observed.The disturbance simply propagated with a constant speed, equal to the fluid velocities [153]. As a second test, two disturbances with different amplitudes were sequentially introduced, in a way analogous to the soliton interaction case discussed above. It was observed that the distance between the two disturbances remained constant and that no further interaction occurred. This behavior is fully consistent with the theory.

8.4.4 M > 1

Finally, for completeness, we also considered the case with $M > 1$. As pointed out above, this case is symmetric to $M < 1$, thus results identical to the previous should be obtained under the appropriate conditions. The condition $M > 1$ required a different pair of fluids, however, the wettability was not altered (the top fluid was still wetting the surface). We used DC 200 silicon fluid and glycerol/water solution with $M = 2.1$. Solitons are predicted to move to the left on the σ axis for $M > 1$, $\lambda > 1/2$ and $\eta > 0$ (Figure 85).

The first experiment was to generate a single soliton. As in the previous case, it was satisfactory

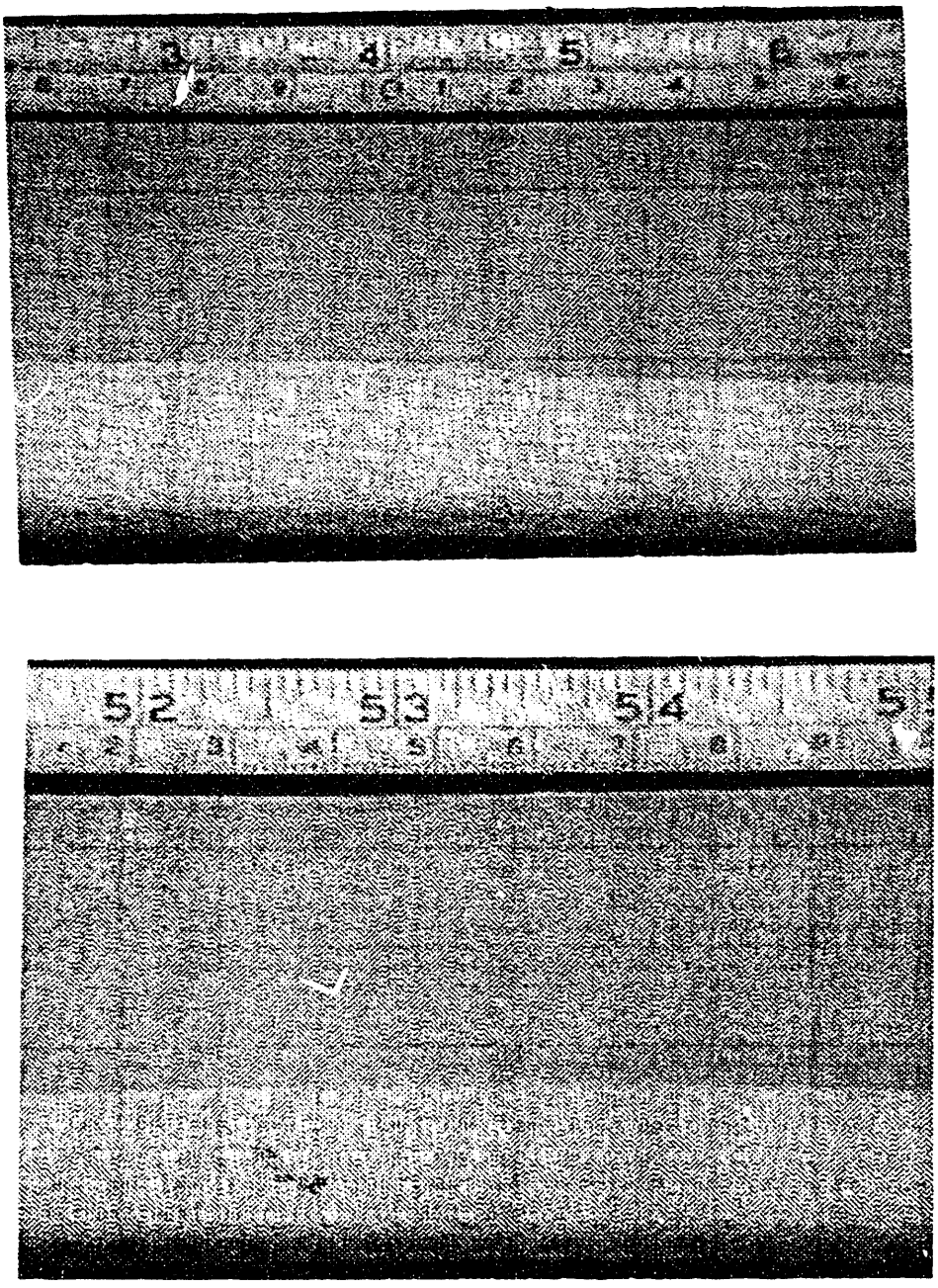

Figure 94: Experiment with $\lambda < 1/2$ and positive initial disturbance

[153]. Interaction of solitons was sought in a subsequent experiment. Contrary to the case $M < 1$, we first introduced the higher amplitude disturbance, which evolves into a higher amplitude soliton, to be followed by the lower amplitude disturbance, which evolves into a lower amplitude soliton. According to the theory, for a fixed observer, the lower amplitude soliton travels faster and eventually overtakes the higher amplitude soliton. This was clearly observed. Because of limitations on the length of the cell, however, complete reappearance of the lower amplitude soliton after the interaction was not possible. As before, the experimental run and the corresponding numerical simulation were in good agreement [153].

8.4.5 Non-Symmetric Case

Although the experiments in the symmetric case appear to support the theory, we also experimented with the non-symmetric configurations. Two different channel widths ($2W = 9\ cm$ and $12\ cm$) were used. As in the first set of experiments, the pair of fluids consisted of mineral oil (outer fluid) and glycerol/water solution (inner fluid). The flat lateral interfaces were established by the simultaneous injection of the two fluids.

In the experiments below, we used $\lambda_1 = 0.65$ and $\lambda_2 = -0.76$. Two disturbances, of initial amplitude $1.2\ cm$ and $-0.75\ cm$, respectively, were simultaneously generated on each interface. Figure 95 shows the solitary waves developed on each interface. The two waves retained their shapes even after they traveled a distance of about $140\ cm$. Wiggly interfaces suggesting dispersive waves were observed in the back of the waves. Figure 96 shows the corresponding numerical simulations.

Interaction of solitons was also studied. Here, two different amplitude disturbances were sequentially introduced on each interface. Numerical simulations confirmed the experimental findings. Other conditions were also tested for different values of λ_1 and λ_2. In the non-symmetric case, the value of the parameter $\lambda_1 - \lambda_2$ is critical. When $\lambda_1 - \lambda_2 < 1$ (interfaces are closer to each other), all other conditions remaining the same the disturbances dissipated. For additional details, reference [153] should be consulted. Unfortunately, the experimental amplitudes were too small for satisfactory identification and comparison. Further work on this and related issues is currently underway.

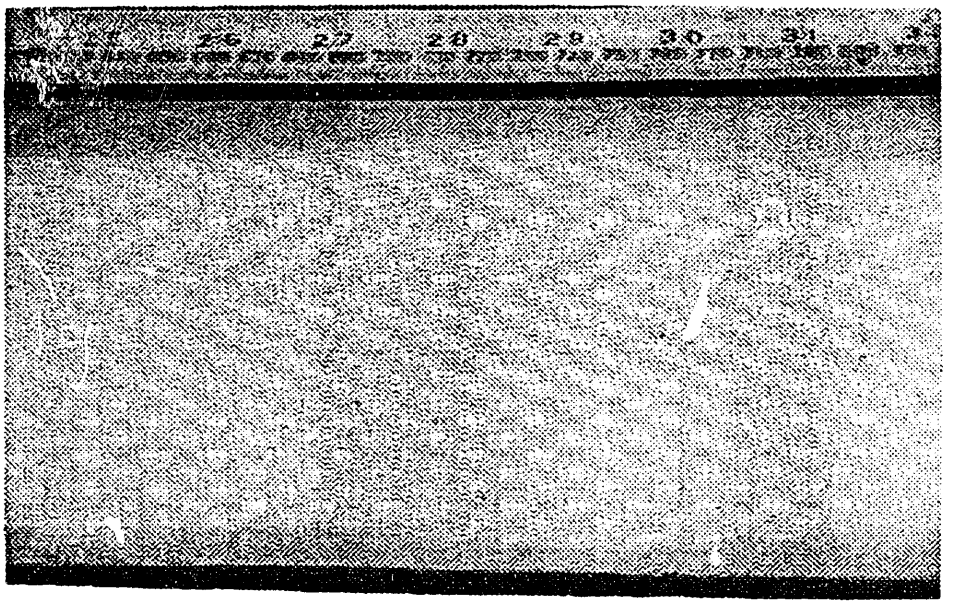

(a)

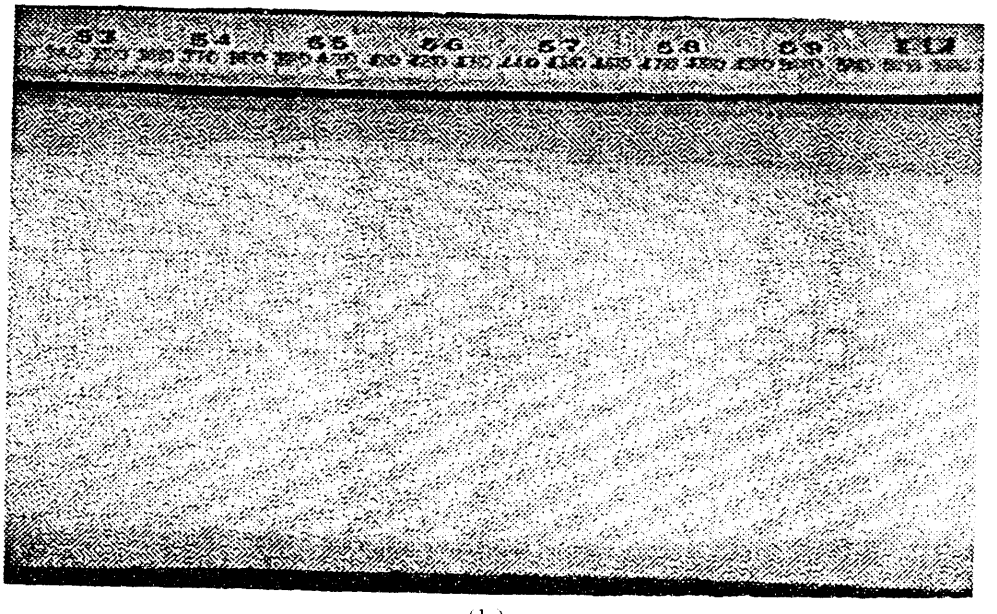

(b)

Figure 95: The non-symmetric case: Single soliton at two different stages

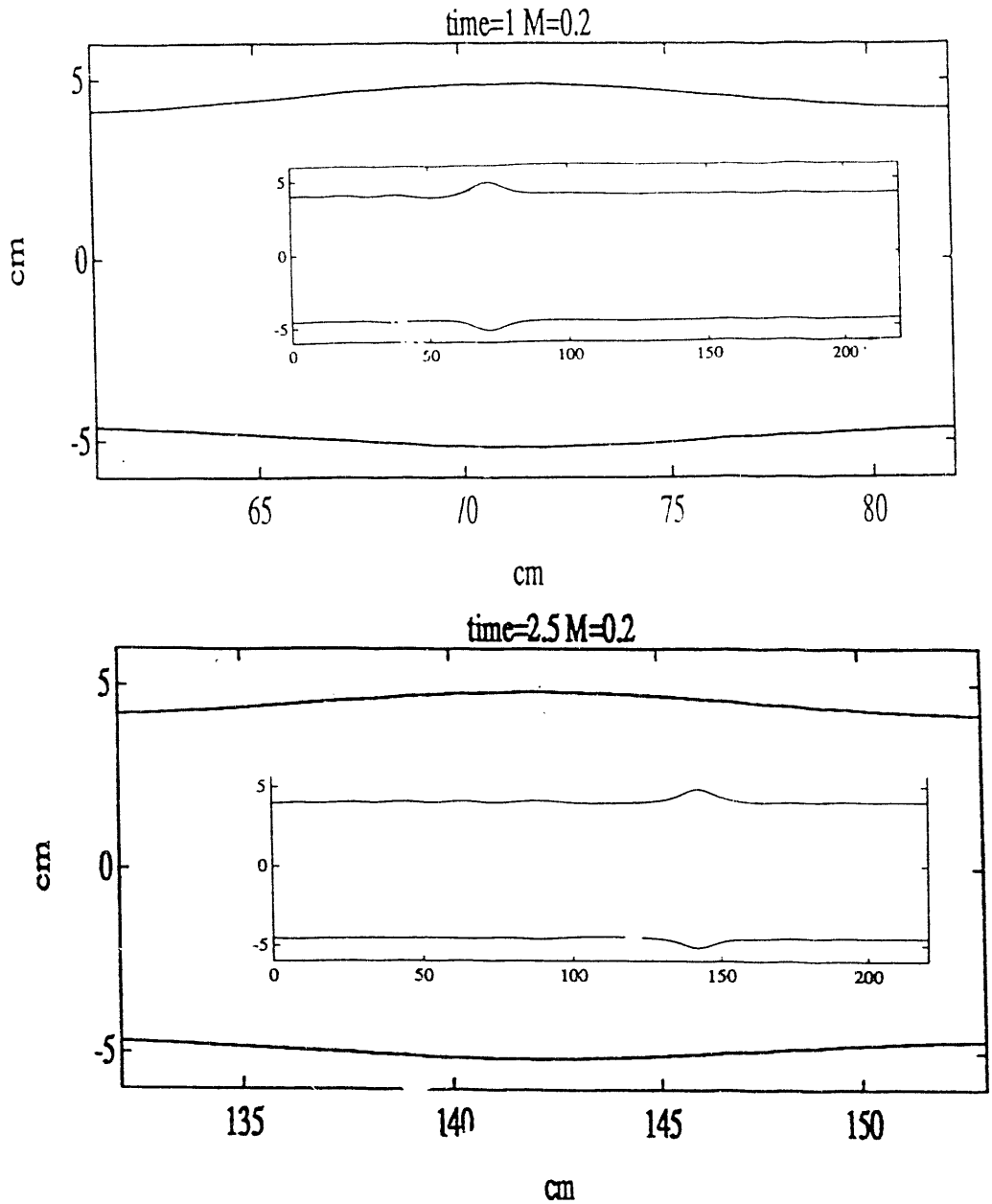

Figure 96: Numerical Simulation of Figure 95

8.5 CONCLUDING REMARKS

The small amplitude, long wave motion of lateral interfaces in parallel flow was investigated at large values of N'_{ca} in a long, horizontal Hele-Shaw cell. The asymptotic theory for the case of two fluids was formulated in terms of a set of KdV and Airy equations. The findings of the theory were validated by experiments involving both one (symmetric case) and two interfaces (non-symmetric case). Under the condition $\mu_b q_b = \mu_a q_a$, flat interfaces pertaining to parallel flow were successfully established in either case. Experimental results supported, for the most part, the theoretical predictions including the existence of solitons. It is important to point out that this is the first time that Hele-Shaw (and, perhaps porous media) flows have been reported to contain KdV dynamics (although see also [63] in a different context). However, some experimental aspects still remain unclear.

It was pointed out that dispersive waves associated with solitons should appear in the experiments. These waves can be identified in the simulations, although only at a high resolution. However, they were not observed in the experiments. A wiggly shape did develop at the points where it was supposed to be present. This was observed in both forward and backward moving solitons. We believe that it is indeed the initial motion of the dispersive waves that initiates these noisy interfaces. However, the subsequent motion is largely controlled by surface tension and wettability effects which become important at small wavelengths. Significantly, no wiggly interface was observed in the experiments with equal viscosity fluids ($M \sim 1$).

Along the same lines, it was pointed out that the direction of the initial disturbance was critical to the development of wave motion. In all cases, the experiments were successful when the initial disturbance was in the direction of drainage (non-wetting displacing wetting). Inconclusive were the results of experiments when the disturbance was introduced in the opposite (imbibition) direction. For the latter, it was observed that the shape of disturbance was not as well defined as in the drainage case. We demonstrated this for the simplest case of equal viscosities, $M \sim 1$. Quite satisfactory results were obtained when the disturbance was positive (from non-wetting to wetting). Results much different than expected, and generally not in agreement with the theory, were obtained when the disturbance was in the opposite direction (from wetting to non-wetting fluid). Wettability and related effects are certainly in need of further investigation.

Finally, in some cases the velocity of the frame of reference was quite larger than the soliton

speed, thus we were not able to monitor the full extent of the wave motion. With the aid of gravity, this velocity of the frame of reference can be reduced to zero. However, now the flow directions must be opposite to each other. Such experiments are currently underway. Parallel theoretical developments involving waves in the presence of gravity in Hele-Shaw flows are reported in [92].

9 FLOW OF POWER-LAW FLUIDS IN POROUS MEDIA

C. Shah and Y. C. Yortsos

9.1 INTRODUCTION

An important industrial application of non-Newtonian fluids in porous media is in the area of Enhanced Oil Recovery(EOR). In such processes, various non-Newtonian fluids, such as low concentration polymer solutions, emulsions etc. are simultaneously injected to increase the viscosity of injected water or other driving agents that displace oil from reservoirs. A variety of rheologically complex fluids are used to improve sweep efficiencies, divert displacing fluids and block swept zones. To describe the viscosity (η) versus shear rate ($\dot{\gamma}$) behavior of such fluids in the bulk, various empirical models have been proposed. A commonly used is the power law model[12]

$$\eta = K\dot{\gamma}^{n-1} \tag{183}$$

where K is a consistency index and the difference between n and unity indicates the degree of departure from Newtonian behavior. The fluid behavior is shear thinning for $n < 1$ and shear thickening for $n > 1$.

In contrast to Newtonian fluids, the state of the art in understanding the flow of power-law fluids, either single- or multiphase, in porous media is incomplete. As a rule, the interplay of the nonlinear rheology with the porespace geometry results in complex problems, that prohibit the direct passage from the micro-(pore) to the macroscale (Salman et al. [113], Sorbie et al. [124]). Thus, with few exceptions, laws analogous to Darcy's for flow of non-Newtonian fluids in porous media have not been rigorously established. Indeed, although frequently used in practice, capillary tube models based on a bundle of capillary tubes do not represent adequately the true physical phenomena in porous media. Although sophisticated approaches have recently appeared (Canella et al. [22], Sorbie et al. [124]), Similar issues arise in the simultaneous flow of a pair of immiscible non-Newtonian fluids in porous media. Fortunately, when one or both of these fluids are of the power-law type, and at conditions of capillary control at the porescale ($N_{ca} << 1$), the concept of saturation-dependent relative permeability may be applicable, perhaps in a modified form, to account for possible effects of the power-law rheology (Salman et al. [113]). Despite the considerable

extent of applications, however, little is known at present about such dependences.

To obtain a better insight on the flow of non-Newtonian fluids in porous media, we have considered simulation of flow in network-like 2-D porous media with distributed sizes. First, the single phase flow of both shear thinning and shear thickening fluids is simulated. It is shown that the critical path approach of Katz and Thompson [65] as extended by Yortsos [146] is well suited for power-law fluids except for very small values of the power law index n. Subsequently, the immiscible displacement of Newtonian fluid by a non-Newtonian fluid is simulated and some initial results are reported. The chapter is completed by an analysis of the importance of converging-diverging geometries in porous media to pressure drop during flow of viscoelastic fluids. The latter is important in certain cases, and shall be included in future simulation.

9.2 POWER-LAW FLUIDS

The problem considered in this section involves single- and multi-phase flow of power-law fluids in porous media, the latter modelled as a network of capillaries. An important limitation imposed in the subsequent analysis is that such elements are of uniform cross-section, so that the contribution of converging-diverging geometries to the pressure drop is not significant. Hence, overall pressure drop across a capillary is still related to the average flow rate through the capillary by a power-law. We caution, however, that this may not be necessarily the case in porous media, particularly at sufficiently high flow rates as discussed later in this chapter. Proceeding under the above assumption, the porescale relation for a power-law fluid becomes

$$q = g(\Delta P)^{1/n} \tag{184}$$

where q is the volume flow rate in a pore of conductance q, across which there is an applied pressure drop ΔP. Under the above qualification, which renders the problem to one of power-law resistors, the following aspects will be addressed: (i) Effective Medium Averages and (ii) Critical Path Analysis. Both these issues were briefly discussed theoretically in a previous report [146]. In this chapter, we shall test the validity of the previous theory by the use of numerical simulation.

For the simulation of single phase flow of a power-law fluid in a single capillary, the following expression was used

$$q = \frac{\pi R^{\frac{3n+1}{n}} n \Delta P^{1/n}}{(2L)^{1/n}(3n+1)K} \tag{185}$$

where R and L denote radius and length of the capillary, respectively. Appropriately rescaled, the dimensionless form of the above equation is

$$Q^* = R^{*\frac{3n+1}{n}} (\Delta P^*)^{1/n} \tag{186}$$

The pressure field in the network was calculated by applying a mass balance at each node of the network which allows us to calculate the flow in each bond. Successive relaxation iterations using under-relaxation were found to lead to convergence for this highly non-linear problem. The convergence criteria used for the iterative method was of the order of $1 * 10^{-5}$, both for shear thinning and for shear thickening fluids. Results for the flow and conductance distribution have been obtained both for shear thinning ($n < 1$) and for shear thickening ($n > 1$) fluids in a network of size 21*21. These results were used to test the previous theories on EMA and critical path analysis.

9.2.1 Effective Medium Averages

Yortsos [146] obtained the following analytical expression for the Effective Medium Approximation (EMA) in the flow of power-law fluids in a Bethe lattice (a tree-like network)

$$\int_0^\infty G(g)[\frac{(z-1)g}{g^n + (((z-1)^n - 1)g_m^n)^{1/n}} - 1]dg = 0 \tag{187}$$

where $G(g)$ is the distribution of the conductances of the bonds, g_m is the effective conductance, the value of which we are seeking, and z is the coordination number of the network.

The above is an integral equation for g_m, the solution of which allows for the average and total conductances $< g >$ and $< g_T >$, respectively, to be evaluated

$$< g >= ((z-1)^n - 1)^{1/n} g_m \tag{188}$$

$$< g_T >= \frac{z}{z-1} < g > \tag{189}$$

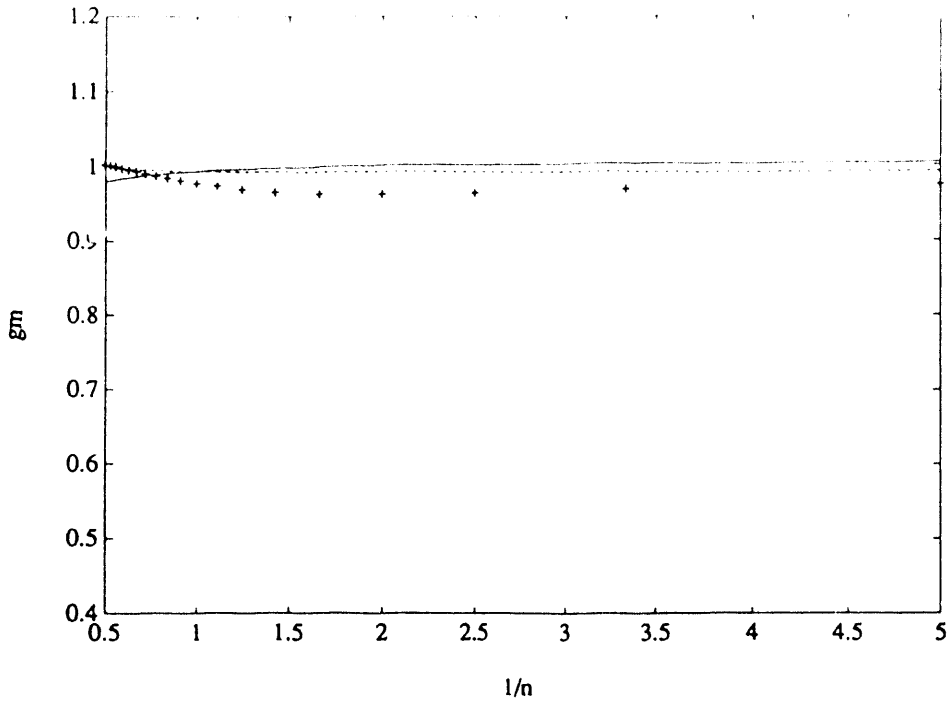

Figure 97: Effective conductances for power-law fluids for a uniform pore size distribution in [0.9-1.1]

In a previous publication, Canella et al [22] obtained a different EMA expression for power-law fluids over a regular lattice that reads as follows

$$\int_0^\infty G(g)[(\frac{z/2g_m}{g+(z/2-1)g_m})^n - 1]dg = 0 \tag{190}$$

The two expressions (187) and (190) are clearly different. In order to test their validity, we obtained the respective values of g_m along with numerical results from direct simulation in a square lattice. Figures 97-99 show plots of the values of the effective conductances g_m vs. the power-law index n for various size distributions ranging from narrow to wide. Solid lines indicate values of g_m obtained from expression (190), dotted lines show the values calculated from expression (187), while numerical values are plotted as crosses. For comparison purposes, three different bond size distributions were used. As shown in Figure 97, the two analytical expressions give values comparable to the numerical values for a wide range of n. To a certain degree, this is anticipated. Expression (187) appears to be in a better agreement in comparison to expression (190) and also has the proper trend. One should recall that (187) is a rigorous asymptotic EMA expression for Bethe lattices. Figure 97 suggests that it may be also approximately valid for porous media as

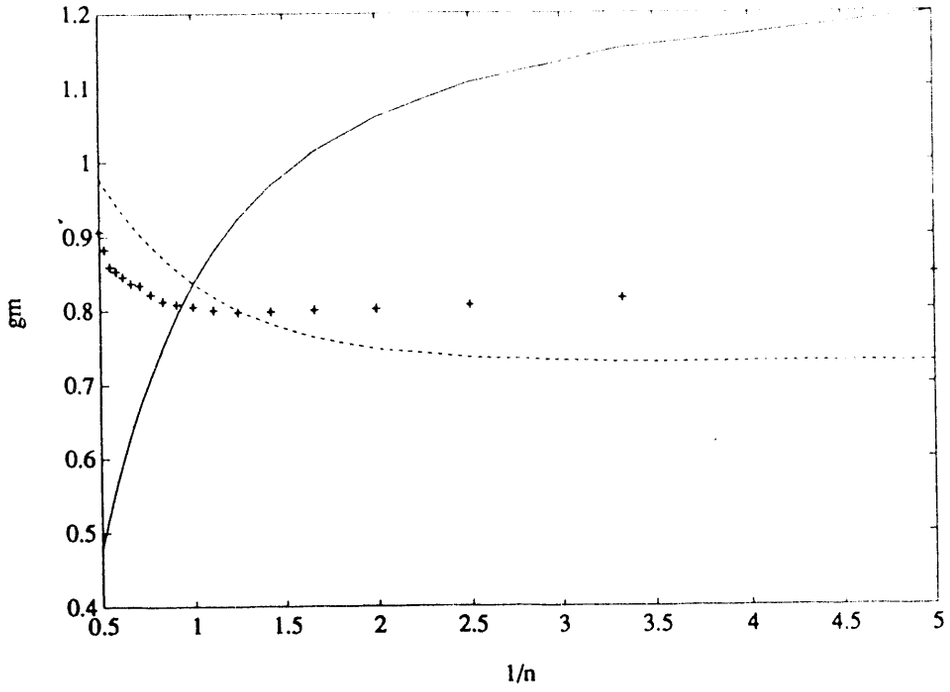

Figure 98: Effective conductances for power-law fluids for a uniform pore size distribution in [0.4-1.6]

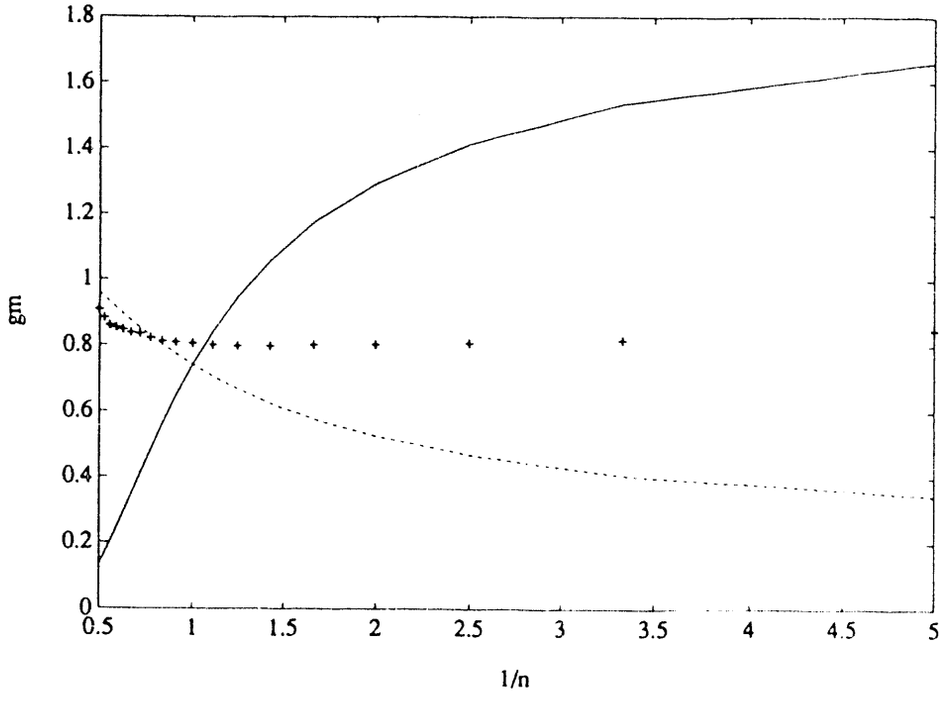

Figure 99: Effective conductances for power-law fluids for a uniform pore size distribution in [0.01-1.99]

well. We point out that rigorous EMA results for general network for power-law fluids are not currently available. The close agreement between EMA and numerical results is attributed to the narrow size distribution of Figure 97. As this distribution becomes wider, the agreement between analytical and numerical results deteriorates, particularly for low values of n (Figures 98 and 99). Nonetheless, expression (187) appears to be a better choice, provided that the distribution is not very wide. For wider distributions, EMA theories are not expected to be valid. Instead, a critical path analysis is more likely to be applicable. This is discussed below.

9.2.2 Critical Path Analysis

Based on the method of Katz and Thompson [65], Yortsos [146] extrapolated the concept of critical path analysis to power-law fluids and derived the following macroscopic law

$$q^n = \frac{k_1 A k_1^{(n-1)/2} \Delta P}{mL} \tag{191}$$

where the constant A is related to the formation factor σ/σ_o and the exponent n

$$A = [(\sigma/\sigma_o)^{0.38})\phi^{0.12}]^{n-1} \frac{(7.84)^{1-n} 3^{1+n} (23.57 t_n)^{t_n}}{2^{2n+1}(1+3n)^n (3+t_n)^{2+t_n}}] \tag{192}$$

and for a 3-d network

$$t_n \approx 1.76 + 0.24/n \tag{193}$$

In the above, k_1 is the Newtonian permeability

$$k_1 = \frac{1}{226} l_c^2 \frac{\sigma}{\sigma_o} \tag{194}$$

where l_c is a percolation length obtained from mercury porosimetry. The concept of critical path requires a wide conductance distribution such that substantial flow occurs only over a subset of the pore network, which can be taken to be the percolation cluster. To test this approach, we rearranged the above as follows

$$\log(q^n/D) = \frac{1}{2}[\log k_1 + \log c^2]n + \log B \tag{195}$$

where we have defined for simplicity

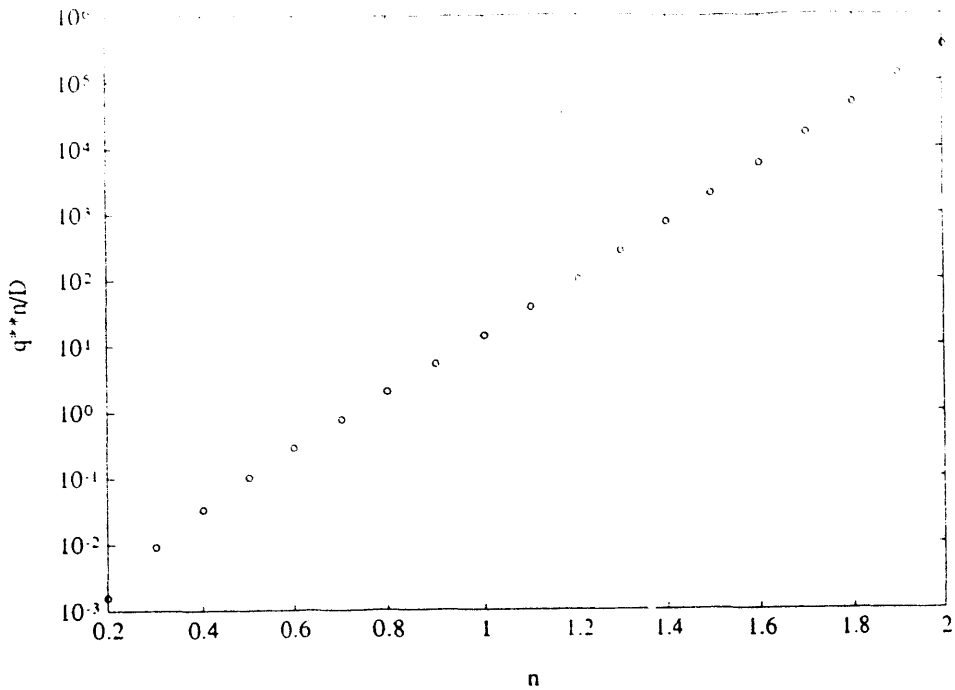

Figure 100: Test of critical path analysis for a uniform pore size distribution in [0.4-1.6]

$$B = \frac{k_1^{1/2}\Delta P}{cmL}, \tag{196}$$

$$c = (\sigma/\sigma_o)^{0.38}\phi^{0.12}, \tag{197}$$

and

$$D = \frac{(7.84)^{1-n}3^{1+n}(23.57t_n)^{t_n}}{2^{2n+1}(3n+1)^n(3+t_n)^{2+t_n}} \tag{198}$$

By rearranging in the form of equation (195), we can directly test the critical path analysis by searching for a linear relation between q^n/D and n in a semilog plot. Figures 100 and 101 show semilog plots of q^n/D against the power-law index n for two different distributions of bond sizes obtained by numerical simulation in a 3-D 11*11*11 cubic lattice. As can be shown, the theoretical prediction of a straight line in (195) is quite well satisfied for values of n that are not too small. We do observe, however, a deviation from the straight line behaviour for small values of n. The effect of the pore size distribution is not very significant, both Figures 100 and 101 displaying approximately the same behavior. Indeed, despite the relatively narrow pore size distribution used in Figure 100,

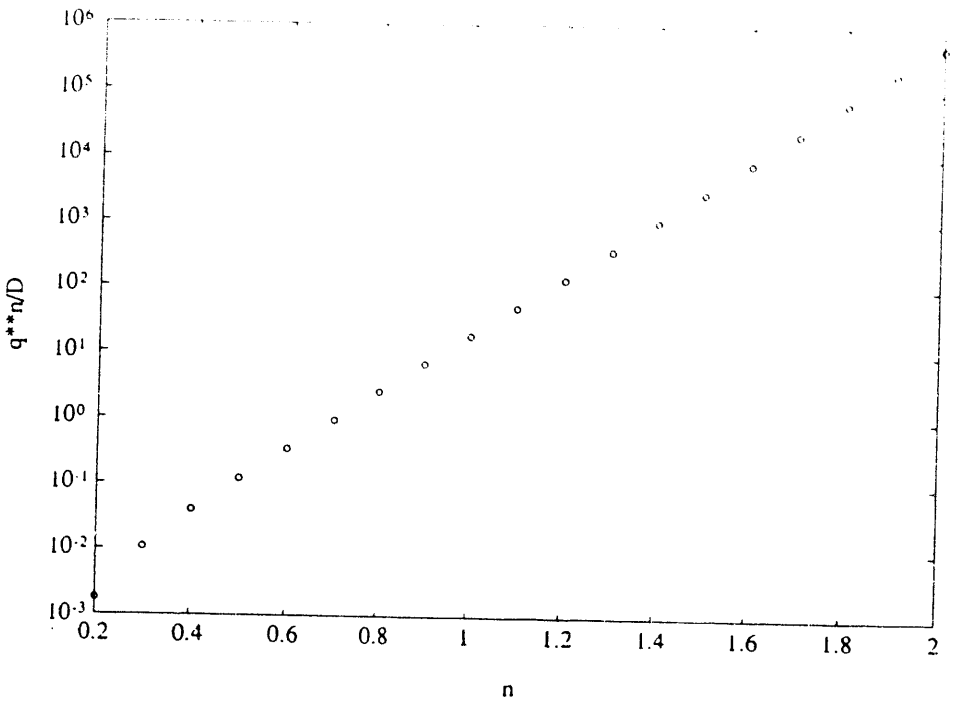

Figure 101: Test of critical path analysis for a uniform pore size distribution in [0.01-1.99]

the corresponding conductance distribution, which scales as $r^{3+1/n}$, is still wide, thus satisfying the conditions for the critical path analysis.

The different behaviour of single phase flow in porous media when the values of n are small raises the possibility of a different kind of flow mechanism compared to that of critical path. In a preliminary investigation, we examined in more detail the actual flow pattern as obtained from the numerical simulation.

9.2.3 `Flow Patterns

Typical results of single-phase flow in the network for various values of n are shown in Figures 102-105. In all these simulations, fluid flow occurs from left to right at a constant pressure difference. The two boundaries are held at a fixed pressure, with periodic boundary conditions applied to the lateral two boundaries. In the Figures, black color represent the maximum flow rate, while white color squares correspond to little or no flow through the bonds of the network. Only the flow through the bonds is shown, flow through the node connecting two bonds depicted in white. Shades between black and white indicate flow rates distributed proportionately betweeen a maximum and zero respectively. In all plots, a uniform distribution of bond sizes in the interval [0.01-1.99] was

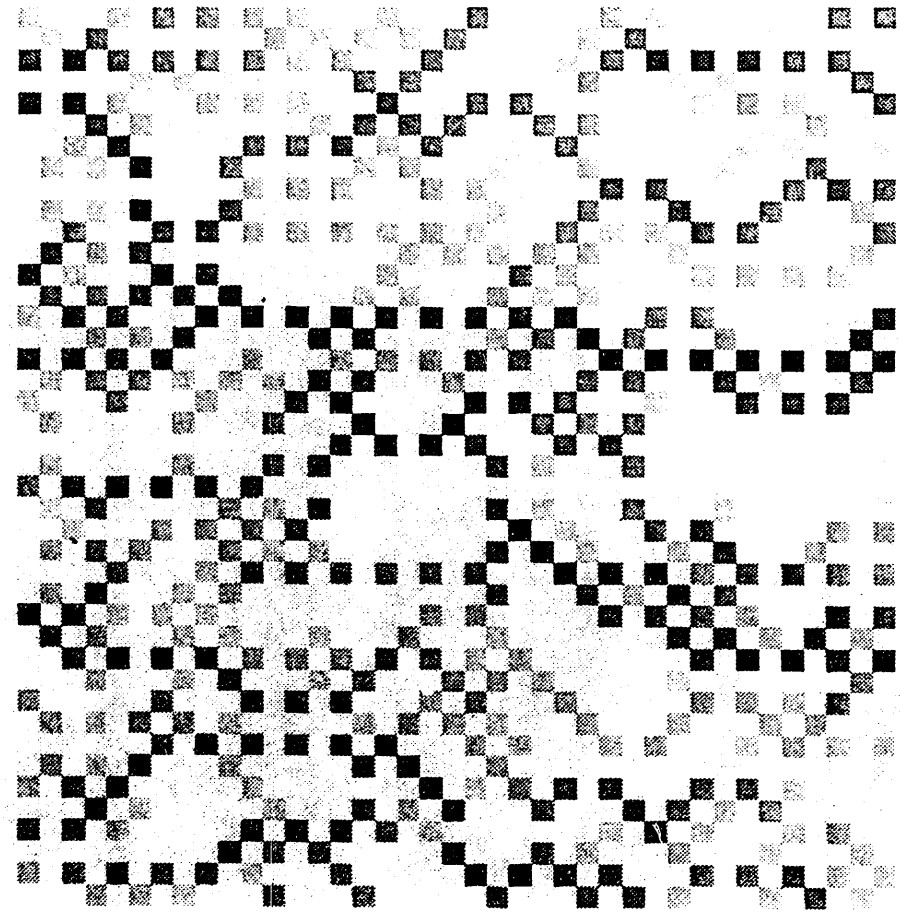

Figure 102: Flow Pattern for n=1

used.

Figure 102 shows the flow of a Newtonian fluid ($n = 1$). We observe that the flow is distributed over the entire network, and we may identify a connected cluster, resembling a percolating cluster, through which most of the flow is taking place. Indeed, there exist empty pockets (holes), where flow is very small and bonds are not conducting. Similar results were also obtained for n=0.8 to 0.4 (not shown), indicating that shear thinning fluids in this range of power-law index flow through the network much as expected from the critical path theory. It should be pointed out, though, that more empty pockets appear in the network as the value of n decreases. A typical example of this flow distribution obtained when n=0.2 is shown in Figure 103. In this case, the flow occurs only through a limited network of connecting bonds. We may identify large empty

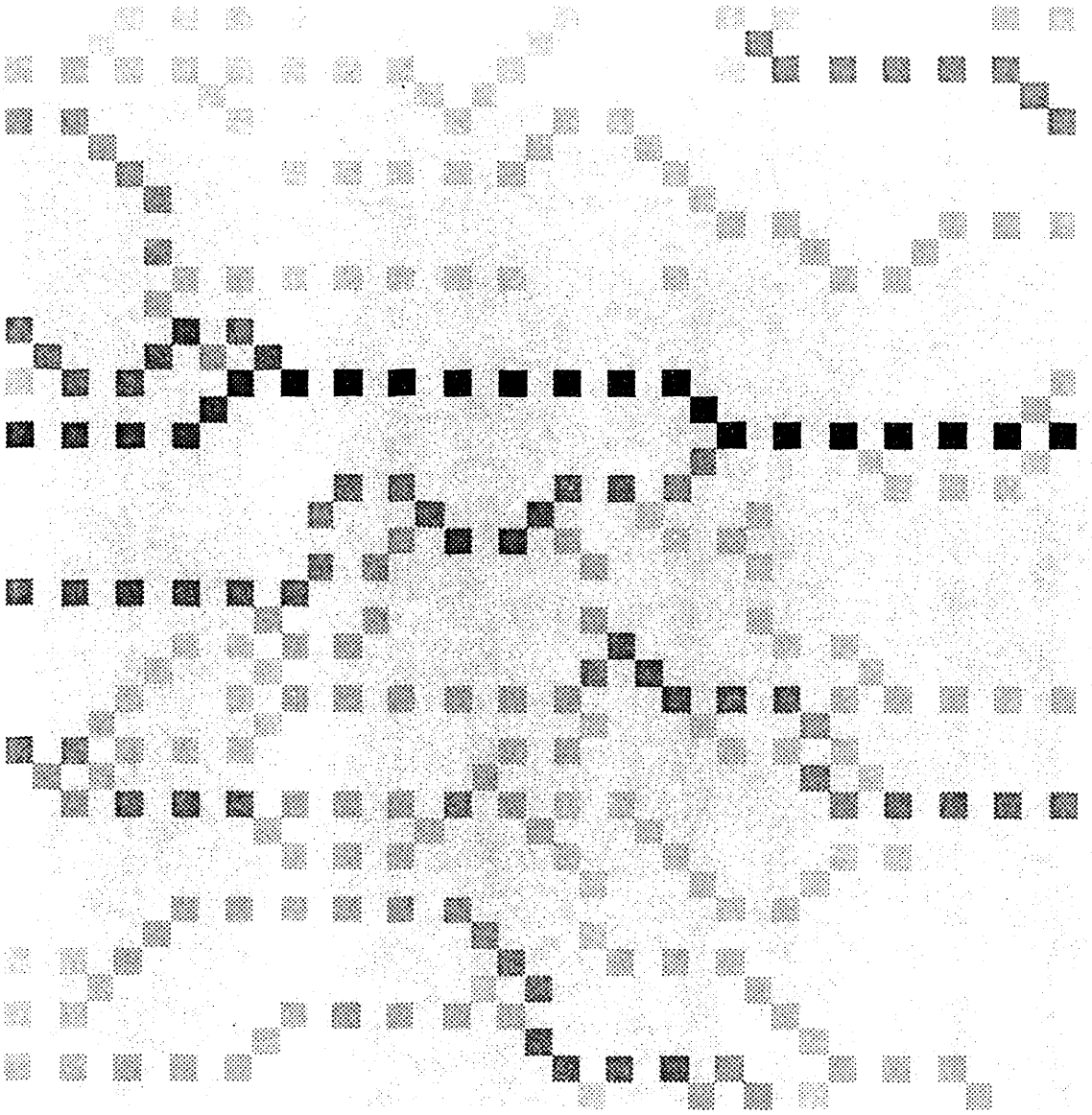

Figure 103: Flow Pattern for n=0.2

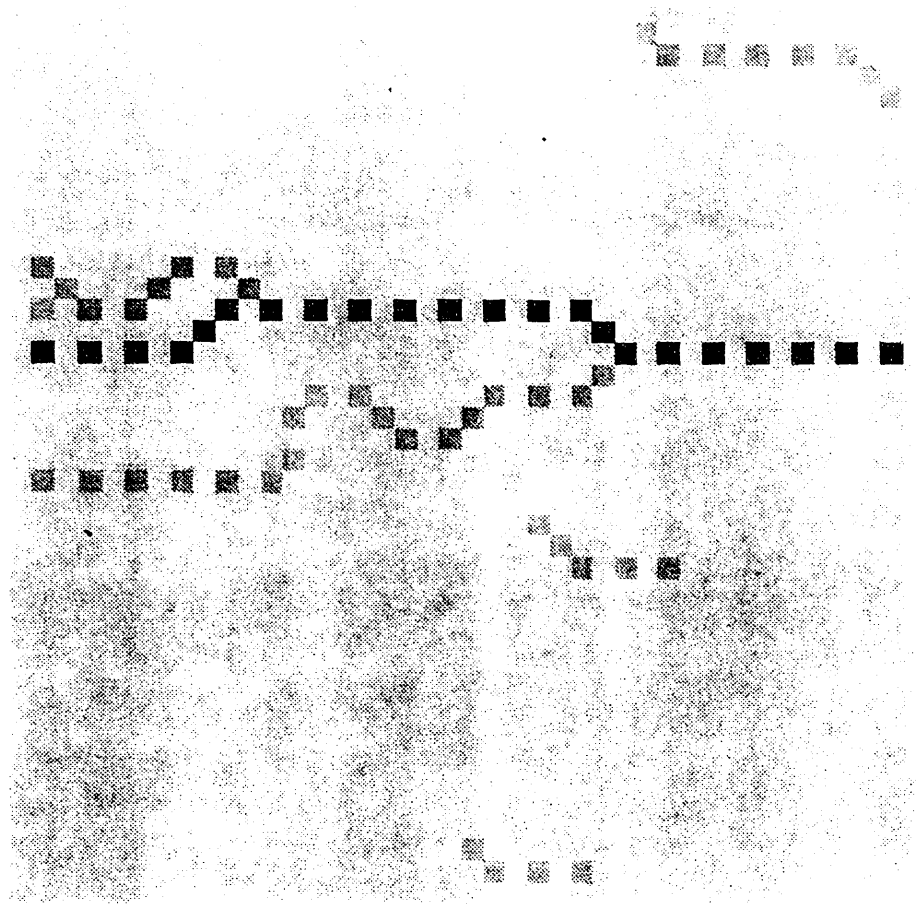

Figure 104: Flow Pattern for n=0.07

pockets, where no flow occurs. This is still in accordance with the theory. At smaller values of n, the conductance distribution is very wide and flow occurs only through a small subset of the percolating cluster corresponding to the highest conducting bonds. The subset becomes smaller as n decreases [13, 14]. We observe a more pronounced effect when n=0.07 (figure 104). In this case, the entire flow occurs through a very small number of connected bonds. The remaining network participates very little to flow and acts like an empty pocket. Clearly, the application of effective medium theories would be fruitless in such situations.

In the above, the key concept is the existence of a critical path, which in turn requires that conductance distributions are wide enough. Since the conductance is related to the bond size through $g \approx r^{3+1/n}$, it follows that such a hypothesis is satisfied better as n decreases. Nonetheless,

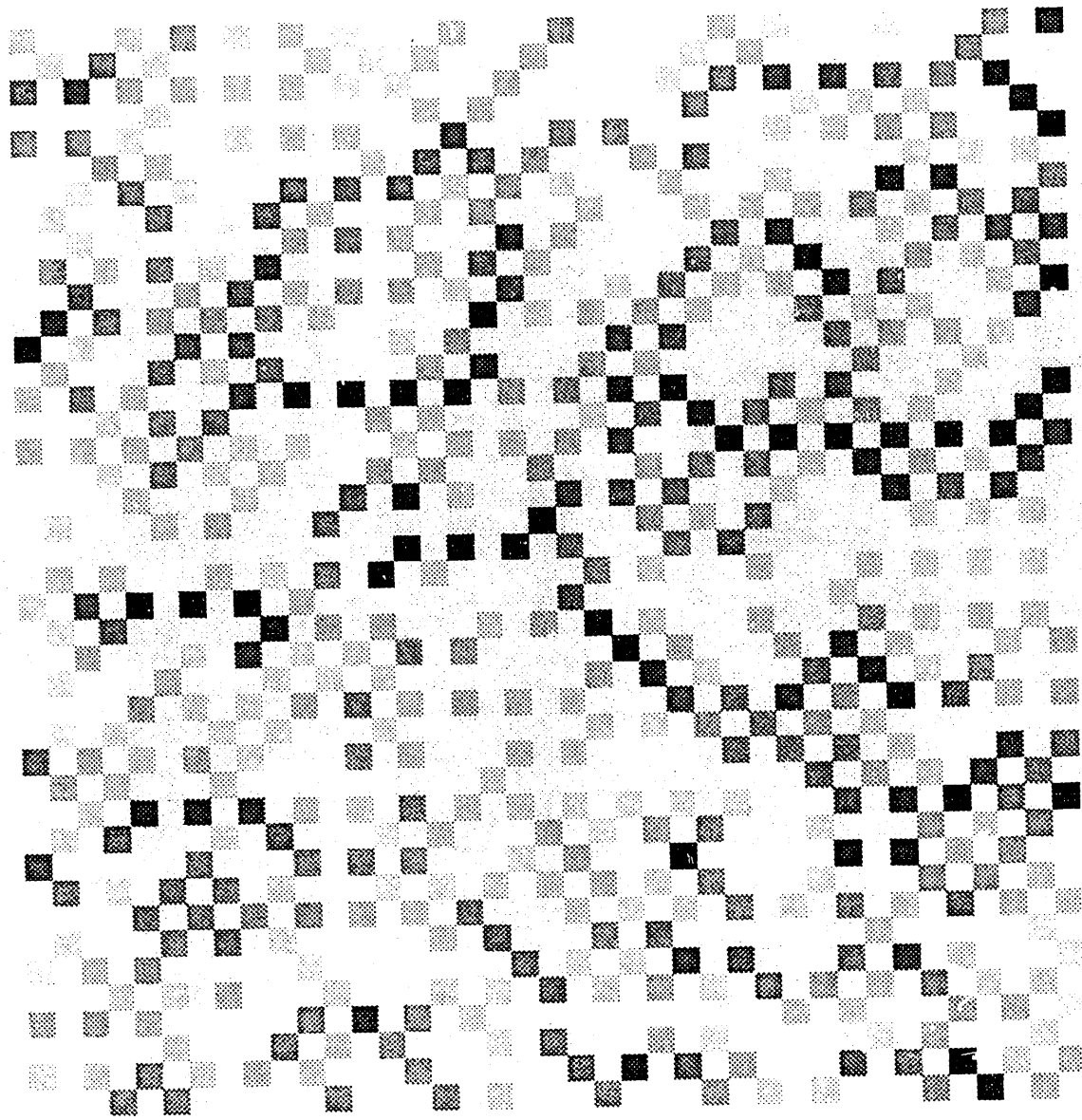

Figure 105: Flow Pattern for n=5

shear thickening fluids also qualify for the same critical path analysis. Figure 105 shows the flow pattern for a shear thickening fluids (with $n = 5$), where the flow distribution resembles the Newtonian case ($n = 1$).

The above confirm quantitatively the validity of the critical path analysis, particularly for shear thinning fluids. When n becomes very low, however, the application of the theory is questionable. This was already anticipated in [146]. Additional research is necessary in order to understand the behavior in this low n range. In fact, because of the close similarity of the flow at small n with the flow of Bingham plastics, a common treatment of these two cases may be necessary. We hope to report on this in future publication.

9.3 TWO-PHASE FLOW

With the increasing application of non-Newtonian fluids in EOR processes, it is important to develop an understanding of pore level displacement. At present, very little is available in this area, most of the studies, concentrating instead on phenomenological description. To remedy this situation, we performed computer simulations at the pore level, involving a non-Newtonian power-law fluid displacing a Newtonian fluid. This displacement was studied under constant pressure conditions across the network and for a drainage process. In modeling the displacement of the immiscible Newtonian fluids through the network, we have used the following assumptions [15]

(i)Volume calculations apply to pore bodies only, the pressure drop occuring in pore throats. (ii)Throats are filled by either invading or displaced fluids, while bodies may contain both fluids. (iii)The capillary pressure in a throat is inversely proportional to the tube radius, while the capillary pressure drop in a node is negligible. (iv)Poiseuille's law for the flow rate Q_{ij} across the bond connecting adjacent nodes i and j for a Newtonian fluid reads

$$Q_{ij} = \frac{\pi R_{ij}^4 (P_i - P_j)}{8\mu L_{ij}} = g_{ij}(P_i - P_j) \tag{199}$$

where P_i is nodal pressure, R_{ij} and L_{ij} are the radius and length of the bond respectively and μ is the viscosity of the Newtonian fluid. For the non-Newtonian power law fluids, the above reads

$$Q_{ij} = \frac{\pi R_{ij}^{(3n+1)/n} n (P_i - P_j)^{1/n}}{(2L)_{ij}^{1/n}(3n+1)K} = g_{ij}\Delta P_{ij}^{1/n} \tag{200}$$

As the fluids are incompressible, the following mass balance applies

$$\sum_j Q_{ij} = 0 \tag{201}$$

We can calculate the pressure field by using the iterative method described in the simulation of single-phase flow, except that we use a combination of linear and nonlinear pressure drop equations, depending on the type of fluid present in the bond.

Initially, the network is occupied by the Newtonian fluid. A non-wetting, non-Newtonian fluid is injected through the left side of the 2-D network, held at a fixed pressure. Fluid escapes through the right side of the network, also held at a constant pressure. The capillary pressure condition is applied to determine when a particular bond is invaded. The node saturation is updated each time by using the above equations for Q_{ij}. In time Δt, the nodal saturation $S_i(t)$ increases following

$$S_i(t + \Delta t) = S_i + \Delta t V_i \sum_j Q_{ij} \tag{202}$$

where V_i is the volume of node i. The time interval Δt is calculated such that only one node is filled at each time step. For the next time step, the above calculations are repeated and the flow of the two immiscible fluids is modelled.

Preliminary results were obtained for immiscible displacement at a fixed pressure difference for two different values of the power-law index. Figure 106 shows a sequence of the interface motion for the case of a shear thinning fluid (n=0.2). Here 1 and 0 refer to pores occupied by invading and initial fluids, respectively. We observe significant fingering, trapping and bypassing. These results are expected based on the previous flow patterns of single-phase flow (Fig. 102-105). Indeed, one would anticipate that the shear-thinning fluid would show a pronounced tendency for fingering, selecting a very narrow path. The same is observed in Figure 106. To some degree, the pattern is reminiscent of flow distribution in a single phase flow under shear-thinning conditions.

On the other hand, the opposite picture develops for the shear-thickening case (n=2). Figure 107 shows corresponding results. It is observed that the interface is quite compact, the front moving with a small amount of trapping at the indicated capillary number.

Work is currently in progress in order to understand the particular machanisms which lead to the features of these displacement processes.

1	1	0	0	0	0	0	0	0	0	0	0	0	0	0	0	0	0	0
1	1	0	0	0	0	0	0	0	0	0	0	0	0	0	0	0	0	0
1	1	0	0	0	0	0	0	0	0	0	0	0	0	0	0	0	0	0
0	0	0	0	0	0	0	0	0	0	0	0	0	0	0	0	0	0	0
0	0	0	0	0	0	0	0	0	0	0	0	0	0	0	0	0	0	0
1	0	0	0	0	0	0	0	0	0	0	0	0	0	0	0	0	0	0
1	0	0	0	0	0	0	0	0	0	0	0	0	0	0	0	0	0	0
0	0	0	0	0	0	0	0	0	0	0	0	0	0	0	0	0	0	0
1	0	0	0	0	0	0	0	0	0	0	0	0	0	0	0	0	0	0
1	0	0	0	0	0	0	0	0	0	0	0	0	0	0	0	0	0	0
1	0	0	0	0	0	0	0	0	0	0	0	0	0	0	0	0	0	0
1	1	1	1	1	0	0	0	0	0	0	0	0	0	0	0	0	0	0
1	1	0	0	1	0	0	0	0	0	0	0	0	0	0	0	0	0	0
0	0	0	0	0	0	0	0	0	0	0	0	0	0	0	0	0	0	0
1	1	0	0	0	0	0	0	0	0	0	0	0	0	0	0	0	0	0
1	0	0	0	0	0	0	0	0	0	0	0	0	0	0	0	0	0	0
1	0	0	0	0	0	0	0	0	0	0	0	0	0	0	0	0	0	0
1	0	0	0	0	0	0	0	0	0	0	0	0	0	0	0	0	0	0
1	1	0	0	0	0	0	0	0	0	0	0	0	0	0	0	0	0	0
1	1	0	0	0	0	0	0	0	0	0	0	0	0	0	0	0	0	0
1	0	0	0	0	0	0	0	0	0	0	0	0	0	0	0	0	0	0

1	1	0	0	0	0	0	0	0	0	0	0	0	0	0	0	0	0	0
1	1	1	1	0	0	0	0	0	0	0	0	0	0	0	0	0	0	0
1	1	0	0	0	0	0	0	0	0	0	0	0	0	0	0	0	0	0
0	0	0	0	0	0	0	0	0	0	0	0	0	0	0	0	0	0	0
0	0	0	0	0	0	0	0	0	0	0	0	0	0	0	0	0	0	0
1	1	0	0	0	0	0	0	0	0	0	0	0	0	0	0	0	0	0
1	0	0	0	0	0	0	0	0	0	0	0	0	0	0	0	0	0	0
1	0	0	0	0	0	1	0	0	0	0	0	0	0	0	0	0	0	0
1	1	0	0	0	0	1	1	1	1	0	0	0	0	0	0	0	0	0
1	1	0	0	0	1	1	1	1	0	0	0	0	0	0	0	0	0	0
1	1	0	0	1	1	1	1	1	0	0	0	0	0	0	0	0	0	0
1	1	1	1	1	1	1	0	1	0	0	0	0	0	0	0	0	0	0
1	1	0	0	1	1	1	1	1	0	0	0	0	0	0	0	0	0	0
0	0	0	0	0	0	0	0	0	0	0	0	0	0	0	0	0	0	0
1	1	0	0	0	0	0	0	0	0	0	0	0	0	0	0	0	0	0
1	0	0	0	0	0	0	0	0	0	0	0	0	0	0	0	0	0	0
1	0	0	0	0	0	0	0	0	0	0	0	0	0	0	0	0	0	0
1	0	0	0	0	0	0	0	0	0	0	0	0	0	0	0	0	0	0
1	1	1	0	0	0	0	0	0	0	0	0	0	0	0	0	0	0	0
1	1	1	0	0	0	0	0	0	0	0	0	0	0	0	0	0	0	0
1	0	0	0	0	0	0	0	0	0	0	0	0	0	0	0	0	0	0

1	1	0	0	0	0	0	0	0	0	0	0	0	0	0	0	0	0	0
1	1	1	1	0	0	0	0	0	0	0	0	0	0	0	0	0	0	0
1	1	0	0	0	0	0	0	0	0	0	0	0	0	0	0	0	0	0
0	0	0	0	0	0	0	0	0	0	0	0	0	0	0	0	0	0	0
0	0	0	0	0	0	0	0	0	0	0	0	0	0	0	0	0	0	0
1	1	0	0	0	0	0	0	0	0	1	0	0	0	0	0	0	0	0
1	0	0	0	0	0	0	0	0	0	1	0	0	0	0	0	0	0	0
1	0	0	0	0	1	1	0	0	0	1	1	1	0	1	1	0	0	0
1	1	0	0	0	0	1	1	1	1	1	1	1	1	1	1	0	0	1
1	1	0	0	0	1	1	1	1	1	0	0	0	0	0	1	1	1	1
1	1	0	0	1	1	1	1	1	1	0	0	0	0	0	0	0	0	0
1	1	1	1	1	1	1	0	1	0	0	0	0	0	0	0	0	0	0
1	1	0	0	1	1	1	1	1	0	0	0	0	0	0	0	0	0	0
0	0	0	0	0	0	0	0	0	0	0	0	0	0	0	0	0	0	0
1	1	0	0	0	0	0	0	0	0	0	0	0	0	0	0	0	0	0
1	1	1	0	0	0	0	0	0	0	0	0	0	0	0	0	0	0	0
1	0	1	1	0	0	0	0	0	0	0	0	0	0	0	0	0	0	0
1	0	1	1	1	1	0	0	0	0	0	0	0	0	0	0	0	0	0
1	1	1	1	0	0	0	0	0	0	0	0	0	0	0	0	0	0	0
1	1	1	0	0	0	0	0	0	0	0	0	0	0	0	0	0	0	0
1	0	0	0	0	0	0	0	0	0	0	0	0	0	0	0	0	0	0

Figure 106: Simulation of drainage for n=0.2 at three different times (N_{ca}=0.03)(1 denotes injected and 0 denotes displaced fluids)

1	1	1	1	1	1	1	1	0	0	0	0	0	0	0	0	0	0	0
1	1	1	1	1	1	1	1	0	0	0	0	0	0	0	0	0	0	0
1	1	1	1	1	1	0	1	1	0	0	0	0	0	0	0	0	0	0
0	1	1	1	1	1	0	0	0	0	0	0	0	0	0	0	0	0	0
0	0	1	1	1	0	0	0	0	0	0	0	0	0	0	0	0	0	0
1	1	1	1	1	1	1	0	0	0	0	0	0	0	0	0	0	0	0
1	1	1	1	1	1	0	0	0	0	0	0	0	0	0	0	0	0	0
1	1	1	1	1	1	1	0	0	0	0	0	0	0	0	0	0	0	0
1	1	1	1	1	0	1	0	0	0	0	0	0	0	0	0	0	0	0
1	1	1	0	0	0	0	0	0	0	0	0	0	0	0	0	0	0	0
1	0	1	0	1	0	0	0	0	0	0	0	0	0	0	0	0	0	0
1	1	1	1	1	0	0	0	0	0	0	0	0	0	0	0	0	0	0
1	1	1	1	1	0	0	0	0	0	0	0	0	0	0	0	0	0	0
1	1	1	1	1	1	0	0	0	0	0	0	0	0	0	0	0	0	0
1	1	0	1	1	0	0	0	0	0	0	0	0	0	0	0	0	0	0
1	1	1	1	1	1	1	1	0	0	0	0	0	0	0	0	0	0	0
1	1	1	1	1	1	1	1	0	0	0	0	0	0	0	0	0	0	0
1	0	1	1	1	1	1	0	0	0	0	0	0	0	0	0	0	0	0
1	1	1	1	0	0	0	0	0	0	0	0	0	0	0	0	0	0	0
1	1	1	1	1	1	0	0	0	0	0	0	0	0	0	0	0	0	0
1	0	1	1	0	0	0	0	0	0	0	0	0	0	0	0	0	0	0

1	1	1	1	1	1	1	1	1	0	0	0	0	0	0	0	0	0	0
1	1	1	1	1	1	1	1	0	0	0	0	0	0	0	0	0	0	0
1	1	1	1	1	1	0	1	1	0	0	0	0	0	0	0	0	0	0
0	1	1	1	1	1	1	1	0	0	0	0	0	0	0	0	0	0	0
0	0	1	1	1	1	1	1	0	0	0	0	0	0	0	0	0	0	0
1	1	1	1	1	1	1	1	0	0	0	0	0	0	0	0	0	0	0
1	1	1	1	1	1	0	1	1	0	0	0	0	0	0	0	0	0	0
1	1	1	1	1	1	1	1	1	0	0	0	0	0	0	0	0	0	0
1	1	1	1	1	1	1	1	0	0	0	0	0	0	0	0	0	0	0
1	1	1	1	1	0	1	1	0	0	0	0	0	0	0	0	0	0	0
1	0	1	1	1	1	0	0	0	0	0	0	0	0	0	0	0	0	0
1	1	1	1	1	1	0	0	0	0	0	0	0	0	0	0	0	0	0
1	1	1	1	1	1	1	0	0	0	0	0	0	0	0	0	0	0	0
1	1	1	1	1	1	1	0	0	0	0	0	0	0	0	0	0	0	0
1	1	0	1	1	1	0	0	0	0	0	0	0	0	0	0	0	0	0
1	1	1	1	1	1	1	1	0	0	0	0	0	0	0	0	0	0	0
1	1	1	1	1	1	1	1	1	0	0	0	0	0	0	0	0	0	0
1	0	1	1	1	1	1	1	1	0	0	0	0	0	0	0	0	0	0
1	1	1	1	1	1	0	1	0	0	0	0	0	0	0	0	0	0	0
1	1	1	1	1	1	0	0	0	0	0	0	0	0	0	0	0	0	0
1	0	1	1	1	0	0	0	0	0	0	0	0	0	0	0	0	0	0

1	1	1	1	1	1	1	1	1	0	0	0	0	0	0	0	0	0	0
1	1	1	1	1	1	1	1	0	0	0	0	0	0	0	0	0	0	0
1	1	1	1	1	1	0	1	1	0	0	0	0	0	0	0	0	0	0
0	1	1	1	1	1	1	1	0	0	0	0	0	0	0	0	0	0	0
0	0	1	1	1	1	1	1	0	0	0	0	0	0	0	0	0	0	0
1	1	1	1	1	1	1	1	0	0	0	0	0	0	0	0	0	0	0
1	1	1	1	1	1	0	1	1	0	0	0	0	0	0	0	0	0	0
1	1	1	1	1	1	1	1	1	0	0	0	0	0	0	0	0	0	0
1	1	1	1	1	1	1	1	0	0	0	0	0	0	0	0	0	0	0
1	1	1	1	1	0	1	1	0	0	0	0	0	0	0	0	0	0	0
1	0	1	1	1	1	0	0	0	0	0	0	0	0	0	0	0	0	0
1	1	1	1	1	1	0	0	0	0	0	0	0	0	0	0	0	0	0
1	1	1	1	1	1	1	0	0	0	0	0	0	0	0	0	0	0	0
1	1	1	1	1	1	1	0	0	0	0	0	0	0	0	0	0	0	0
1	1	0	1	1	1	0	0	0	0	0	0	0	0	0	0	0	0	0
1	1	1	1	1	1	1	1	0	0	0	0	0	0	0	0	0	0	0
1	1	1	1	1	1	1	1	1	0	0	0	0	0	0	0	0	0	0
1	0	1	1	1	1	1	1	1	0	0	0	0	0	0	0	0	0	0
1	1	1	1	1	1	0	1	0	0	0	0	0	0	0	0	0	0	0
1	1	1	1	1	1	0	0	0	0	0	0	0	0	0	0	0	0	0
1	0	1	1	1	0	0	0	0	0	0	0	0	0	0	0	0	0	0

Figure 107: Simulation of drainage for n=2.0 at three different times (N_{ca}=0.03)(1 denotes injected and 0 denotes displaced fluids)

9.4 VISCOELASTIC EFFECTS

The above were confined to fluids of power-law type where other elastic effects were suppressed. However, shear thinning fluids used in EOR applications rarely exhibit inelastic characteristics. Most such fluids do exhibit shear thinning but in addition they also display extensional viscosity effects. In our analysis, we have neglected such issues. Complications, however, are certain to arise when the pressure drop in porous media is large enough for extensional viscosity effects to be important [61]. Indeed, Jones and Walters [61, 62] have reported that above a critical set of conditions, a significant increase in the flow resistance in a porous media is observed. This has been attributed to the high extensional viscosities, which are found in many dilute polymer solutions at moderate to high strain rates. It is obvious that the question of extensional viscosity would be important near the wellbore, where strain rates are the highest. Moreover, extensional viscosity becomes important whenever the flow of non-Newtonian fluids occurs through geometries such that the crosssectional area is not uniform. This section summarizes the pertinent literature on the subject.

Typical porous media consist of converging-diverging geometries, which are likely to contribute to the overall pressure drop due to the generation of extensional flow. It is important, therefore, to understand the critical conditions at which extensional flow can be significant. Jones and Walters [61] studied both extensional as well as shear flows for the determination of the rheological properties of very dilute aqueous solutions of Xanthan Gum and Polyacrylamide, both of which are of potential use in EOR. For polyacrylamide solution, a critical strain rate region was identified, beyond which extensional viscosity effects are likely to be important for practical polymer flooding. Figure 108 shows the general flow behaviour of viscoelastic fluids in geometries which can induce extensional viscosity effects. Critical flow rates between 0.02 to 0.4 cc/sec were reported based on the type of geometries shown in Figure 109. The corresponding Reynolds numbers are quite low and range between 0.04 to 0.06. In contrast, Xanthan Gum solution, which is both shear thinning and tension thinning has an extensional viscosity behaviour which is different from that of the high molecular weight polyacrylamide.

In examining the flow of non-Newtonian elastic fluids, Boger [16] pointed out that vortex enhancement is linked with an increased pressure loss through the contraction region. Binding and Walters [11] carried out a study to measure pressure drops in contraction flow geometries for the

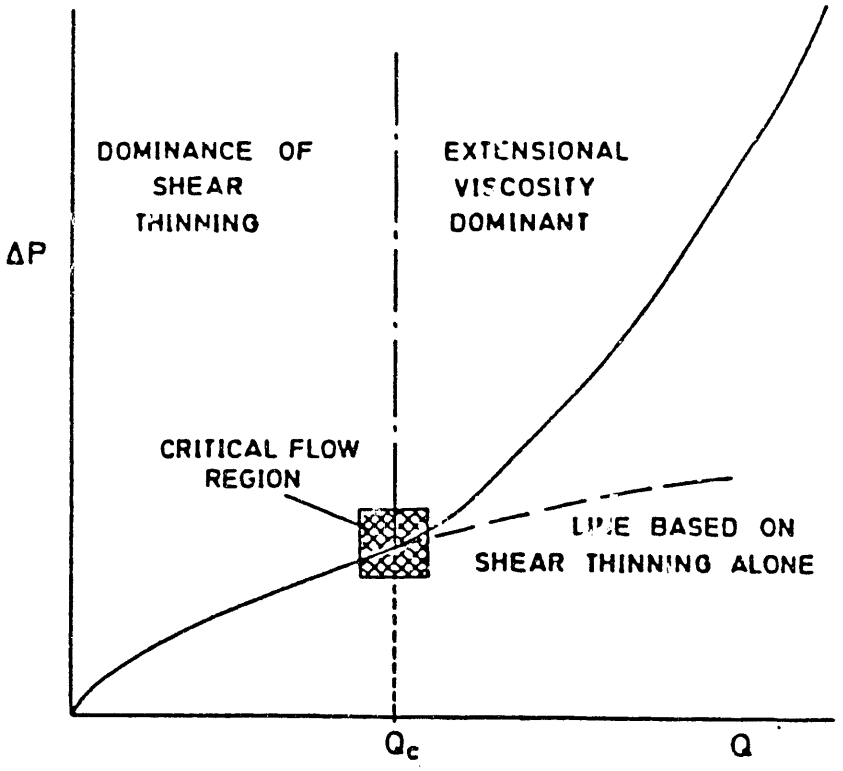

Figure 108: Flow behavior of viscoelastic fluids in porous media (from [61])

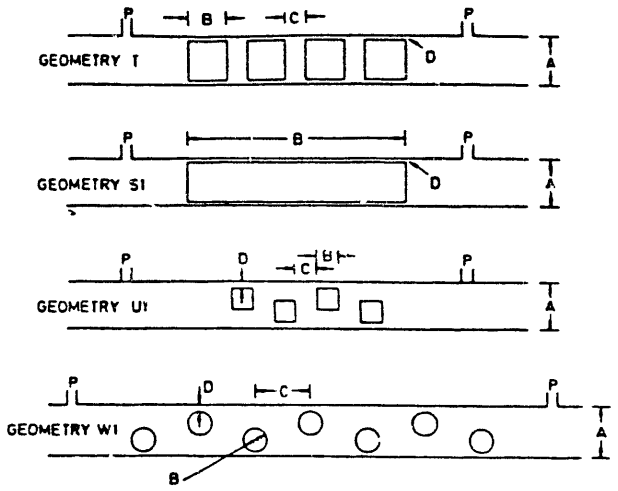

Geometry	A	B	C	D
U1	25	12.5	12.5	3
W1	23	12.5	33.75	2.5

Geometry	A	B	C	D
T1	28	24.5	12.5	1.45
T2	13.5	12.5	6.75	0.75
T3	6.2	5.9	3.2	0.4
S1	28	137	–	1.4

Dimensions of model geometries

Figure 109: Typical model geometries studied in [61]

determination of the extensional behaviour of polymer solutions. The flow rates used during their study were in the range of $10^{-7} - 10^{-4} m^3/s$. They reported that Boger fluids (which are highly-elastic, constant-viscosity non-Newtonian fluids) displayed vortex enhancement in axisymmetrical contraction, but not in plannar contractions, while aqueous solutions of polyacrylamide exhibited vortex enhancement in both these geometries. On the other hand, Evans and Walter [42] carried out experiments with a wide variety of geometries to examine the flow of aqueous polyacrylamide solutions and reported that the flow characteristics in contraction flows are difficult to generalize from one type of contraction to another, or from one type of non-Newtonian fluids to another. Durst [40] studied porous media flows of dilute polymer solutions and showed that the small addition of high molecular weight polymers to a Newtonian solvent trigger pressure drops if the flow rate exceeds an onset flow rate corresponding to a critical Deborah number of the porous media-polymer solution matrix. The critical Deborah number was identified as 0.5 in that study.

Another important viscoelastic effect identified is the Trouton ratio, given by [61, 62]

$$T_R = \frac{\eta_E(\dot{\varepsilon})}{\eta(\dot{\gamma})} \tag{203}$$

where η_E is the extensional viscosity based on the srain rate $\dot{\varepsilon}$ and η is the shear viscosity at the shear rate $\dot{\gamma}$. For Newtonian fluids, the Trouton ratio is constant ($T_R = 3$), whereas highly-elastic fluids are noted for having high T_R. Jones et al [62] reported that the Trouton ratio increases with increase in strain rate both for a Boger fluid and for an aqueous solutions of polyacrylamide at constant shear viscosity.

The above studies indicate that extensional viscosity may contribute significantly to the overall pressure drop for viscoelastic fluids in convergence-divergence flow geometries, even at low Reynold numbers for viscoelastic fluids. For this reason, it would be worthwhile to incorporate the associated pressure drop from convergent-divergent porous medium models in order to identify the contribution of extensional flow to the overall pressure drop. This work is currently underway.

SUMMARY AND FUTURE WORK

Our work on network models to describe vapor-liquid flow is near completion. To test and validate the approach, experimental flow visualization is planned. Upon the satisfactory match of theory and experiment, efforts will be taken for process scale-up, in which effects of temperature gradients on the growth of the vapor (steam) phase and relative permeability effects will be particularly considered. In parallel, we shall modify the existing code to describe steam injection.

The experiments on steam injection in Hele-Shaw cells and micromodels identified several interesting phenomena regarding the interplay between steam injection, condensation, frontal stability and the viscoelastic response of heavy oils. Our subsequent research on this subject will involve the analysis and modeling of these observations. We shall proceed to investigate the steam front dynamics in both Hele-Shaw and porous media geometries. Particular attention will be paid to the rheology of heavy oils in porous media, a subject that has not been adequately addressed previously.

The work on pore level modeling will be coupled with our continuum models of both concurrent and countercurrent flow. Process scale up will be attempted in order to understand in detail the origin of the capillary and permeability characteristics of macroscopic vapor-liquid flows. Effects of heterogeneity will be further explored, particularly as the latter affects frontal displacement. This work is also expected to enhance our understanding of the onset of nucleate boiling, a process still incompletely understood. Finally, we plan to explore the solution of various problems related to the injection of steam from horizontal wells and the concommitant problems of gravity drainage.

Reservoir heterogeneity will be further explored in the continuation of our work on the representation of fracture networks using fractal geometry. We shall pursue the development of diagnostic methods based on multiple wells and interference testing. In parallel, investigations will continue on the understanding and the modeling of steam injection in fractured systems. Experimental studies will be conducted for steam injection in the micromodel geometries taken to represent a fracture-matrix element. The focus of this work will be on steam displacement mechanisms in fractured reservoirs. Additionally, we shall proceed with scale up, where the large scale description using fractals will be coupled with the pore-level analysis.

The development of a rigorous framework for the description of flow processes under the assumption of VFE has enabled us to model various EOR processes. An important application in the present context is steam injection. Various models of steam injection have appeared in the litera-

ture, typically under severe simplifying assumptions. The availability of our VFE framework can lead to the proper formalism and to the development of more appropriate models where many of the previous assumptions can be relaxed. In particular, effects of heterogeneity and gravity segregation will be probed. In parallel, we shall investigate the properties of simple systems, such as one-phase miscible and two- phase immiscible flow under VFE conditions, to determine the behavior of the system obtained, particularly whether it admits chaotic solutions or not and how does it lead to simplifying average models, such as the Koval, Todd-Longstaff, and Fayers approximations. This research is necessary for a better understanding of viscous fingering in unstable displacement, a subject of interest to heavy oils.

The final part of this work involves investigations on chemical additives. Previous efforts have been in the area of foam formation and propagation. At present, work needs to be done to interpret some of the previous experimental findings in the area of foam formation. Work is under way to develop a mechanism of foam formation in a pore network, using recent advances in the field. Experimental work is also planned to test these hypotheses using micromodels. Because of the similarity of foam flow with the flow of Bingham plastics, we plan to continue our previous study of non-Newtonian fluids by concentrating on shear-thinning behavior and on the flow of viscoplastic fluids. In addition, in view of their possible relevance to the rheology of heavy oils, viscoelastic effects in porous media flows will be studied.

PUBLICATIONS

The following publications have resulted from this research during the period reported:

1. Satik, C., and Yortsos, Y.C., "Percolation Models for Boiling and Bubble Growth in Porous Media", paper presented at the 1991 ASME Annual Meeting, Atlanta, GA (Dec. 4, 1991).

2. Satik, G., and Yortsos, Y.C., "Simulation of Pattern Formation and Percolation Using Fractional Brownian Statistics", paper presented at the 1991 AIChE Annual Meeting, Los Angeles, CA (November 20, 1991).

3. Kong, X., Haghighi, M., and Yortsos, Y.C., "Flow Visualization of Steam Injection in Hele-Shaw Cells", paper presented at the Heavy Oils and Tar Sands Symposium, Lexington, KY (Nov. 14, 1991).

4. Yortsos, Y.C., "A Theoretical Analysis of Vertical Flow Equilibrium", paper SPE 22612, presented at the 66th SPE Annual Fall Meeting, Dallas, TX (Oct. 6-9, 1991).

5. Acuna, J., and Yortsos, Y.C , "Numerical Construction and Flow Simulation in Networks of Fractures Using Fractal Geometry", paper SPE 22703, presented at the 66th SPE Annual Fall Meeting, Dallas, TX (Oct. 6-9, 1991).

6. Zeybek, M. and Yortsos, Y.C., "Interface Dynamics in Parallel Flow In Hele-Shaw Cells", J. Fluid Mech., in press (1992).

7. Stubos, A.K., Satik, G., and Yortsos, Y.C., "Critical Heat Flux Hysteresis in Vapor-Liquid Counterflow in Porous Media", Int. J. Heat Mass Transf., in press (1992).

8. Stubos, A.K., Satik, G., and Yortsos, Y.C., "Effects of Heterogeneity on Vapor-Liquid Counterflow in Porous Media", Int. J. Heat Mass Transf., submitted (1991).

9. Chang, J. and Yortsos, Y.C., "Effect of Capillary Heterogeneity on Buckley-Leverett Displacement," SPERE, in press (1992).

10. Yortsos, Y.C., Satik, C., Bacri, J.-C., and Salin, D., "Large-Scale Percolation Theory of Drainage", Transport in Porous Media, in press (1992).

11. Zeybek, M. and Yortsos, Y.C., "Long Waves in Parallel Flow In Hele-Shaw Cells", Phys. Rev. Lett., 67, 1430-1433 (1991).

12. Satik, G., Parlar, M., and Yortsos, Y.C., "A Study of Steady- State, Steam-Water Counterflow in Porous Media", Int. J. Heat Mass Transf., 34, 1755-1771 (1991).

13. Baghdikian, S.Y., Ph.D Thesis, University of Southern California (1991).

14. Zeybek, M., Ph.D Thesis, University of Southern California (1991).

References

[1] M.J. Ablowitz and H. Segur. *Solitons and the Inverse Scattering Transform.* SIAM, 1981.

[2] P. Armitage and R.A. Dawe. *Paper SPE 18495, Presented at the SPE International Symposium on Oilfield Chemistry, Houston, TX*, February 8-10, 1989.

[3] R.W. Aul and W.L. Olbright. *J. Fluid Mech.*, 215:585, 1990.

[4] M.F. Barnsley. *Fractals Everywhere.* Academic Press, Boston, 1988.

[5] C.C. Barton and P.A. Hsieh. Physical and hydrologic-flow properties of fractures. field trip guidebook t385. In *28th International Geological Congress.* American Geophysical Union, 1989.

[6] H.H. Bau and K.E. Torrance. *Int. J. Heat Mass Transfer*, 25:45, 1982.

[7] J. Bear. *Dynamics of Fluids In Porous Media.* American Elsevier, 1972.

[8] H.L. Beckers. *Appl. Science Res. Annual*, 14:101, 1965.

[9] R.A. Beier. *SPE Paper 20582 presented at the 65th Annual SPE Fall Meeting, New Orleans, LA, Sept. 23-26*, 1990.

[10] D. Bensimon, L.P. Kadanoff, S. Liang, B.I. Shraiman, and C. Tang. *Rev. Mod. Phys.*, 58:977, 1986.

[11] D.M. Binding and K. Walters. *J. of Non-Newtonian Fluid Mechanics*, 30:233, 1988.

[12] R.B. Bird, Steward W.E., and Lightfoot E.N. *Transport Phenomena.* John Wiley and Sons, New York, 1990.

[13] R. Blumenfeld and A. Aharony. *J. Phys.A:Math. Gen.*, 18:L443, 1985.

[14] R. Blumenfeld, Meir Y., Harris B., and A. Aharony. *J. Phys.A:Math. Gen.*, 19:L791, 1986.

[15] M. Blunt and P. King. *Transp. in Porous Media*, 6:407, 1991.

[16] D.V. Boger. *Ann. Rev. Fluid. Mech.*, 19:157, 1987.

[17] C. E. Brown and E.L. Neustadter. *J. Can. Pet. Technology*, 19:100, July-Sept. 1980.

[18] W.K. Brown, R.R. Karpp, and D.E. Grady. *Astrophysics and Space Science*, 94:401, 1983.

[19] J.S. Buckley. In *Interfacial Phenomena in Petroleum Recovery, Chapter 5*, Marcel Dekker Inc., New York, 1990.

[20] D. Burgess and M.R. Foster. *Phys. Fluids*, 2:1105, 1990.

[21] M.C. Cacas, E. Ledoux, G. deMarsily, and B. Tillie. *Water Resouces Research*, 26:479, 1990.

[22] W.J. Canella, C. Huh, and R.S. Seright. Paper SPE 18089, presented at the 63rd Annual SPE Fall Meeting, Houston, TX, Sept. 1988.

[23] J. Chang and Y.C. Yortsos. *SPE Formation Evaluation*, page 631, 1990.

[24] A. Chatenever and J.C. Calhoun, Jr. *Trans. AIME*, 195:149, 1952.

[25] A. Chatenever, M.K. Indra, and J.R. Kyte. *JPT*, page 13, June 1959.

[26] I. Chatzis and F. A. L. Dullien. *J. Colloid Interface Sci.*, 91:199, 1983.

[27] Y.K. Chuah and V.P. Carey. *Int. J. Heat Mass Transfer*, 28:147, 1985.

[28] K.H. Coat, J.R. Dempsey, and J.H. Anderson. *SPEJ*, page 63, 1971.

[29] R.E. Collins. *Flow of Fluids Through Porous Media.* Petroleum Publishing Co. Tulsa, OK, 1976.

[30] R. Combescot, T. Dombre, V. Hakim, Y. Pomeau, and A. Pumir. *Phys. Rev. Let.*, 56:2036, 1986.

[31] A. Danesh, J.M. Peden, D. Krinis, and G.D. Henderson. *Paper SPE 16956, Presented at the 62nd Annual Technical Conference and Exhibition of the SPE, Dallas, TX*, September 27-30, 1987.

[32] J.A. Davis and S.C. Jones. *J. Pet. Tech.*, 20:1415, 1968.

[33] D.C.Brock and F.M. Orr Jr. *Paper SPE 22614, Presented at the 66th Annual Technical Conference and Exhibition of the SPE*, Oct.6-9, 1991.

[34] B.M.R. Demiral, L.M. Castanier, and W.E. Brigham. *Paper SPE 22644, Presented at the 66th Annual Technical Conference and Exhibition of the SPE*, Oct.6-9, 1991.

[35] D.N. Dietz. *Akad. van Wetenschappen*, 56-B:83, 1954.

[36] T.M. Doscher. Technical Report DOE/ET/12075-1, Univ. of Southern California, 1980.

[37] C. Doughty and K. Pruess. *Int. J. Heat Mass Transfer*, 31:79, 1988.

[38] C. Doughty and K. Pruess. *Int. J. Heat Mass Transfer*, 33:1205, 1990.

[39] P.G. Drazin and R.J. Johnson. *Solitons: An Introduction.* Cambridge University Press, 1989.

[40] F. Durst. *J. of Non-Newtonian Fluid Mechanics*, 22:169, 1987.

[41] A.S. Emanuel, G.K. Alameda, R.A. Behrens, and T.A. Hewett. *SPERE*, 4:311, 1989.

[42] R.E. Evans and K. Walter. *J. of Non-Newtonian Fluid Mechanics*, 20:11, 1986.

[43] F.J. Fayers. *SPERE*, page 551, 1988.

[44] F.J. Fayers and A.H. Muggeridge. *SPERE*, page 487, 1990.

[45] F.J. Fayers and T.M.J. Newley. *SPERE*, page 542, 1988.

[46] J. Feder. *Fractals.* Plenum Press, New York, 1988.

[47] T.W. Forest. *J. Appl. Phys.*, 53:6191, 1982.

[48] B. Fornberg and G.B. Whitham. *Proc Roy. Soc. Lond.*, 289:373, 1978.

[49] F.P.Bretherton. *J.Fluid Mech.*, 10:166, 1961.

[50] R.E. Garrison, editor. *The Monterey Formation and Related Silicieous Rocks of California.* The Pacific Section Society of Economic Paleontologists and Mineralogists, Los Angeles, 1981.

[51] J.J. Gilvarry. *Solid State Communications*, 2:9, 1964.

[52] J.F. Gouyet, M. Rosso, and B. Sapoval. *Phys. Rev. B*, 37:1832, 1988.

[53] J. Hammack, N. Scheffner, and H. Segur. *J. Fluid Mech.*, 209:567, 1989.

[54] L.L. Handy and P. Datta. Fluid distribution during immiscible displacement in porous media. *Chevron California Research Center*, 1964.

[55] H.J. Herrmann and S. Roux. *Statistical Models for the Fracture of Disordered Media*. North Holland, 1990.

[56] T.A. Hewett. *Paper SPE 15386, presented at the 61st Annual SPE Fall Meeting, New Orleans, LA*, 1986.

[57] G.J. Hirasaki, D.J. O'Meara, and J.A. Rohan. *Paper SPE 18592 Presented at the 63rd Annual Meeting of SPE, Houston, TX, Oct. 2-5*, 1988.

[58] G.M. Homsy. *Ann. Rev. Fluid Mech*, 19:271, 1987.

[59] V. Hornof and N.R. Morrow. *SPERE*, page 251, 1988.

[60] J.C. Jaeger and N.G.W. Cook. *Fundamentals of Rock Mechanics*. Chapman and Hall, London, 1979.

[61] D.M. Jones and K. Walter. *Rheological Acta*, 28:482, 1989.

[62] D.M. Jones, K. Walter, and Williams P.R. *Rheological Acta*, 26:20, 1987.

[63] L.P. Kadanoff. *Phys. Rev. Lett.*, 65:2986, 1990.

[64] F. Kalaydjian and B. Legait. *C.R.A.S.*, 304:869, 1987.

[65] A.J. Katz and A.H. Thompson. *J. Geophys. Res.*, 92:599, 1987.

[66] J. Kevorkian and J.D. Cole. *Perturbation Methods in Applied Mathematics*. Springler-Verlag, 1980.

[67] M.J. King and H. Sher. *Phys. Rev. A*, 41:874, 1990.

[68] P.R. King. *J. Phys.*, 20:L529, 1987.

[69] E. J. Koval. *SPEJ*, page 145, 1963.

[70] S.A. Kovalev, S.L. Solov'yev, and O.A. Ovodkov. *Heat Transfer - Sov. Res.*, 19(3):109, 1987.

[71] L.W. Lake and G.J. Hirasaki. *SPEJ*, 21:459, 1981.

[72] L.W. Lake, E. Kasap, and M. Shook. *North Sea Oil and Gas Reservoirs-II, The Norwegian Institute of Technology, Graham and Trotman*, 2:297, 1990.

[73] B. Le Fur and P. Sourieau. *Rev. Inst. Fr. Petrol.*, 18:325, 1963.

[74] J. Lee, A. Coniglio, and H.E. Stanley. *Phys. Rev. A*, 41:4589, 1990.

[75] R. Lenormand. *Proc. Roy. Soc. A.*, 423:159, 1989.

[76] R. Lenormand. *J. Phys.:Condens. Matter*, 2:70, 1990.

[77] R. Lenormand, F. Kalaydjian, M.T. Bieber, and J.M. Lombard. *Paper SPE 20475 presented at the 66th SPE Annual Fall Meeting, New Orleans, LA, Sept. 22-26*, 1990.

[78] R. Lenormand, E. Touboul, and C. Zarcone. *J. Fluid Mech.*, 189:165, 1988.

[79] R. Lenormand, C. Zarcone, and A. Sarr. *J. Fluid Mech.*, 135:337, 1983.

[80] X. Li and Y.C. Yortsos. *Paper SPE 22589, Presented at the 66th Annual Technical Conference and Exhibition of the SPE*, October 6-9, 1991.

[81] Y. Li and N.C. Wardlaw. *J. Collid Interface Sci.*, 109:461, 1986.

[82] Y. Li and N.C. Wardlaw. *J. Collid Interface Sci.*, 109:473, 1986.

[83] J. Lighthill. *Waves in Fluids.* Cambridge University Press, 1978.

[84] J.C.S. Long and K. Hestir. *Lawrence Berkeley Laboratory Earth Sciences Division Annual Report 1989*, page 45, 1990.

[85] B.B. Mandelbrot. *The Fractal Geometry of Nature.* W.H. Freeman, New York, 1983.

[86] R. F. Mast. SPE 3997, 1972.

[87] C.C. Mattax and J.R. Kyte. Ever see a water flood. *Oil and Gas J.*, 59:115-128, 1961.

[88] C.C. Mattax and J.R. Kyte. *Soc. Pet. Eng. J.*, 225:177, 1962.

[89] T. Maxworthy. *J. Fluid Mech*, 177:207, 1987.

[90] T. Maxworthy. *Phys. Rev. A*, 39:5863, 1989.

[91] M.J. McGuinness, M. Blakeley, K. Pruess, and M.J. O'Sullivan.

[92] E. Meiburg and T. Maxworthy. *submitted*, 1991.

[93] R. Orbach. *Science*, 231:814, 1986.

[94] S. Owete and E. Brigham. *SPERE*, page 315, 1987.

[95] K.K. Pande and F.M. Orr. *paper, SPE 19668 presented at the Society of Petroleum Engineers Fall Technical Conference and Exhibition, San Antonio, TX*, 1989.

[96] C.W. Park, S. Gorell, and G.M. Homsy. *J. Fluid Mech*, 141:257, 1984.

[97] C.W. Park and G.M. Homsy. *J. Fluid Mech*, 139:291, 1984.

[98] M. Parlar and Y.C. Yortsos. *J. Colloidal Interface Sci.*, 132:425, 1989.

[99] M. Parlar and Y.C. Yortsos. *Paper SPE 16969 presented at the 62nd Annual SPE Fall Meeting, Dallas, TX*, Sept. 1987.

[100] M. Parlar, M. Zeybek, and Y.C. Yortsos. *Paper SPE 20054, SPE California Regional Meeting, Ventura, CA, April 4-6*, 1990.

[101] P. Pelcé. *Dynamics of Curved Fronts.* Academic Press, 1988.

[102] M.S. Plesset and A. Prosperetti. *Ann. Rev. Fluid Mech.*, 9:145, 1977.

[103] M.S. Plesset and S.A. Zwick. *J. Appl. Phys.*, 25:493, 1954.

[104] J. Polek, K. Karasaki, J.C.S. Long, and J. Barker. *Earth Sciences Division Annual Report 1989 Lawrence Berkeley Laboratory*, page 74, 1990.

[105] M.M. Poulton, N. Mojtabai, and I.W. Farmer. *Intl.J. Rock Mech. Min.Sci. and Geomech.*, 27:219, 1990.

[106] M. Prats. Thermal Recovery, SPE Monograph, Vol. 7, Dallas, Texas (1982).

[107] P.S. Ramesh and K.E. Torrance. *Int. J. Heat Mass Transfer*, 1990:1895, 33.

[108] M. Rosso, J.F. Gouyet, and B. Sapoval. *Phys. Rev. B*, 32:6053, 1985.

[109] M. Rosso, J.F. Gouyet, and B. Sapoval. *Phys. Rev. Letters*, 57:3195, 1986.

[110] D.H. Rothman. *J. Geophys. Res. B*, 95:8663, 1990.

[111] P.G. Saffman and G.I. Taylor. *Proc. Roy. Soc. London Ser. A*, 245:312, 1958.

[112] M. Sahimi and Y.C. Yortsos. *Paper SPE 20476 presented at the 65th Annual SPE Fall Meeting, New Orleans, LA, Sept. 23-26*, 1990.

[113] M. Salman, S. Baghdikian, L.L. Handy, and Y.C. Yortsos. submitted. *SPERE*, 1989.

[114] C. Sammis, G. King, and R. Biegel. *PAGEOPH*, 125:777, 1987.

[115] C. Sammis, J. Lin, and I. Erhsaghi. *Proceedings of the 16th Workshop on Geothermal Reservoir Engineering Stanford, CA, Jan. 23-25*, 1991.

[116] J.M. Sanchez and Schechter R.S. *Paper SPE 16967 presented at the 62nd Annual SPE Fall Meeting, Dallas, TX*, Sept. 1987.

[117] B. Sapoval, M. Rosso, and J.F. Gouyet. *J. Phys. (Paris) Lett.*, 46:L149, 1985.

[118] C. Satik, M. Parlar, and Y.C. Yortsos. *Int. J. Heat Mass Transf.*, 34:1755, 1991.

[119] G. Schubert and J.M. Straus. *J. Geophysical Res.*, 84:1621, 1979.

[120] G. Schubert and J.M. Straus. *J. Geophysical Res.*, 85(B11):6505, 1980.

[121] L.E. Scriven. *Chem. Eng. Sci.*, 10:1, 1959.

[122] A.K. Singhal. Technical Report PR-38, Petroleum Research Institut, Canada, November 1978.

[123] S.L. Solov'yev and S.A. Kovalev. *Tepl. Vysok. Temp.*, 22(3):528, 1984.

[124] K.S. Sorbie. *Paper SPE 19651 presented at the 64th SPE Annual Fall Meeting, San Antonio, October 8-11*, 1989.

[125] G.L. Stegmeier, D.D. Laumbach, and C.W. Volek. *Paper SPE 6787. Presented at the 52nd Annual Technical Conference and Exhibition, Denver, October 9-12*, 1977.

[126] G. Straus, J.M.and Schubert. *J. Geophysical Res.*, 86(B10):9433, 1981.

[127] A.K. Stubos and J-M. Buchlin. *in "Convective Heat and Mass Transfer in Porous Media", S. Kakac, B. Kilkis, F.A. Kulacki and F. Arinc Eds., NATO ASI Series E, Applied Sciences, Vol. 196, Kluwer Academic Publishers*, 1991.

[128] A.K. Stubos, C. Satik, and Y.C. Yortsos. *Submitted to the Int. J. Heat Mass Transfer*, 1991.

[129] M.A. Styrikovich, S.P. Malyshenko, A.B. Andrianov, and I.V. Talaev. *Heat Transfer - Sov. Res.*, 11(1):23, 1987.

[130] J. Szekely and G.P. Martins. *Chem. Eng. Sci.*, 26:147, 1971.

[131] P. Tabeling, G. Zocchi, and A. Libchaber. *J. Fluid Mech*, 177:67, 1987.

[132] G.I. Taylor. *Proc. Roy. Soc. A*, 219:186, 1953.

[133] M.R. Todd and W.J. Longstaff. *JPT*, page 874, 1972.

[134] D.L. Turcotte. *Journal of Geophysical Research*, 91(B2):1921, 1986.

[135] K.S. Udell. *J. Heat Transfer*, 105:485, 1983.

[136] K.S. Udell. *Int. J. Heat Mass Transfer*, 28:485, 1985.

[137] P. van Meurs. *Trans.AIME*, 210:295, 1959.

[138] J.E. Warren and P.P. Root. *SPEJ*, page 245, 1963.

[139] G.B. Whitham. *Linear and Nonlinear Waves*. John Wiley, 1974.

[140] T.A. Witten and L.M. Sanders. *Phys. Rev. Let.*, 47:1400, 1981.

[141] R.A. Wooding. *J.Fluid Mech.*, 7:501, 1960.

[142] J.J. Xu. *paper, presented at the 44th Annual APS Meeting, Tampa, AZ, Nov. 24-26*, 1991.

[143] D. Yang, N.C. Wardlaw, and M. Mckeller. *AOSTRA J. of Research*, 6:123, 1990.

*U.S.GPO:1992-661-026/60011

[144] Y. Yokoyama and L.W. Lake. *paper, SPE 10109 presented at the 56th Annual SPE Fall Meeting, San Antonio, TX*, 1981.

[145] Y.C. Yortsos. *J. Phys.: Condens. Matter*, 2:SA443, 1990.

[146] Y.C. Yortsos. *Modification Of Chemical and Physical Factors in Steamflood to increase Heavy Oil Recovery*. Annual DOE Report, April 1991.

[147] Y.C. Yortsos and J. Chang. *TiPM*, 5:399, 1990.

[148] Y.C. Yortsos and M. Parlar. *Paper SPE 19697 presented at the 64th Annual SPE Fall meeting, San Antonio, TX, Oct 8-11*, 1989.

[149] Y.C. Yortsos and M. Zeybek. *Paper presented at the 1989 AIChE Fall Meeting, San Francisco, CA, Nov. 5-10*, 1989.

[150] N.J. Zabusky and M.D. Kruskal. *Phys. Rev. Lett.*, 15:6, 1965.

[151] V.J. Zapata and L.W. Lake. *Paper SPE 10111 presented at the 56th Annual SPE Fall Meeting, San Antonio, TX*, 1981.

[152] Y.B. Zeldovitch, A.G. Istratov, N.I. Nidin, and V.B. Librovich. *Comb. Sci. and Tech.*, 24:1, 1980.

[153] M. Zeybek. PhD thesis, University of Southern California, 1991.

[154] M. Zeybek and Y.C. Yortsos. *Phys. Rev. Lett.*, 67:1430, 1991.

END

DATE
FILMED
5/1/92